Acoustical Physics, Vol. 48, No. 4, 2002, pp. 379–387. Translated from Akusticheskiĭ Zhurnal, Vol. 48, No. 4, 2002, pp. 437–446.

Anomalous Phenomena in Sound Propagation Near the Sea Floor: A Review

B. A. Kasatkin

Institute of Marine Technology Problems, Far-East Division, Russian Academy of Sciences, ul. Sukhanova 5a, Vladivostok, 690950 Russia

e-mail: kasatkas@marine.febras.ru

Received March 1, 2000

Abstract—A review is presented of numerous experimental data that exhibit anomalies in sound transmission through the water–sand interface of the sea bottom at overcritical angles of incidence. These data are complemented with those of in-sea experiments performed with a side-scan sonar for low grazing angles. It is shown that the explanations given by different researchers for the anomalous phenomena are insufficient, and a development of a new theoretical model is required to allow for all aspects of the problem. *© 2002 MAIK "Nauka/Interperiodica".*

In applied acoustics, a class of problems exists whose solutions are based on that of a simpler classical problem of sound reflection and refraction at an interface between two media. Such problems primarily include the problems of sound propagation in a waveguide [1], where the phenomenon of total internal reflection plays a key role.

Muir, Horton, and Thomson [2], 1979, were the first to express doubts about the validity or at least about the completeness of the classical theory for describing the reflection and refraction processes. Their paper considers an experiment on the reflection and refraction at the interface between water and sand at a sea bottom for bounded beams generated by a parametric sound source. The authors argued that the experimental data agree well with the theory only for undercritical angles of incidence. For overcritical angles, the experiment led to anomalous results, namely:

—the amplitude of the transmitted wave was by 10–15 dB higher than the calculated one (the amplitude anomaly);

—the sound field in the refracted wave was spread over a wide angular range (the anomaly of the refraction angle).

The aforementioned paper gave rise to a number of publications and discussions in which mainly experts in parametric sound sources participated. The conclusion of the discussion was summarized by Williams and Satkoviak [3] in 1989, who attributed the amplitude anomaly to the specificity of calculating the performance of the parametric projector. In their opinion, even in the far-field zone, the sound field of the parametric source retains its sensitivity to the structure of the transverse aperture factor, which is governed by the distribution of the boundary function at the pump projector; when this factor is appropriately chosen, the theory can be corrected and brought into agreement with the experiment. However, even the corrected theory lacks in explaining the anomaly of the refraction angle.

The conclusions formulated in [3] seemed to be unconvincing for Chotiros [4], whose paper appeared in the same year and caused a new wave of publications and discussions. In his paper, Chotiros both confirmed the anomalous results of the previous studies [2] and obtained the frequency dependence for the observed phenomena. By using linear but well directed sound sources, Chotiros nearly excluded the errors in the theoretically estimated signal level of the transmitted wave and, respectively, in the anomaly of the level.

The experiments of Chotiros were performed in a shallow-water sea with sandy bottom, with a technique that was thereafter repeatedly used by other researchers. According to this technique, the transmitted waves were received by a system of hydrophones distributed along orthogonal axes of a cubic array. The vertically distributed hydrophones served to analyze the vertical structure of the transmitted wave, while the hydrophones distributed over the three axes of the array were used to determine the relative time delays and the propagation direction for the transmitted wave. The sound beam was generated by a source that was at a distance of 4.5 m from the bottom surface. The angular position of the tower-mounted projector relative to the receiving array could be changed so that the grazing angle of the incident wave took the values 90°, 59°, 39°, 29°, and 22°.

The amplitude anomaly, i.e., the offset of the measured amplitude from the calculated value, along with its frequency dependence, is illustrated by Fig. 1a taken from [4], where the tower positions *3* and *5* correspond to undercritical and overcritical incidence angles, respectively (the corresponding grazing angles are 39° and 22°). At the frequency band f = (5–80) kHz, the estimated amplitude anomaly is A = (0–60) dB, while

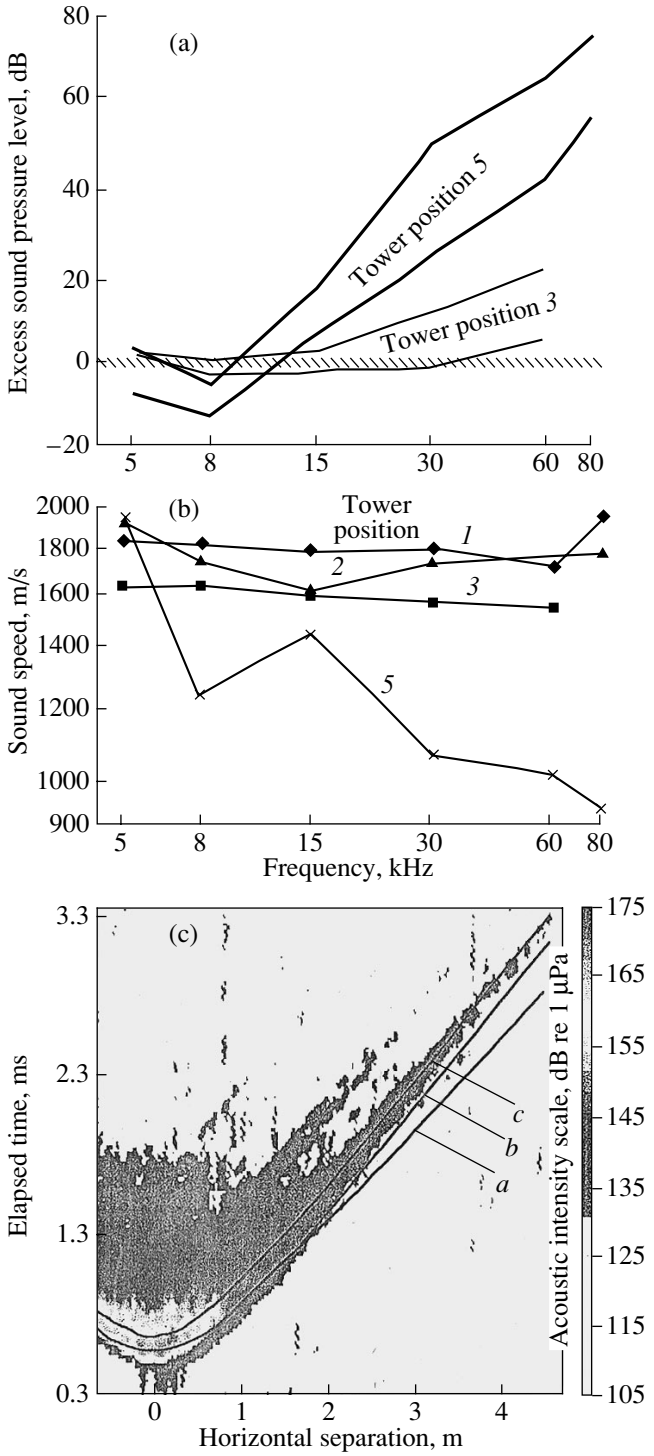

Fig. 1. Experimental characteristics of sound waves refracted at the water–sand interface: (a) amplitude anomaly of the transmitted wave; (b) anomaly of the sound speed (the refraction angle); and (c) anomaly of the propagation velocity.

A = (10–15) dB at f = 20 kHz, which agrees with the estimate of [2].

Figure 1b [4] illustrates the anomaly of the refraction angle. Here, the frequency dependences are presented for the apparent and effective sound speeds in the bottom material, which are calculated in accordance with the Snell law from the refraction angle, sound speed in water, and incidence angle specified by the experimental layout. In the model representation, the sandy bottom itself is treated as an equivalent fluid. For tower positions *1–3* that correspond to undercritical incidence angles, the experimental sound speed in the sea floor agrees well with the model one, while, in position *5*, which corresponds to overcritical angles, the effective sound speed decreases from the expected value C = 1742 m/s to 1100–1000 m/s at higher frequencies of the band f = (5–80) kHz.

Among the later publications of Chotiros [5–8], paper [6] should be mentioned on detecting the low-velocity wave component in the field of the transmitted waves. In this work, a technique was proposed that was subsequently used by other experimenters. According to this technique, the experiment was carried out in a hydroacoustic tank whose bottom was covered with sand, which was prepared in a specific manner to get minimal surface roughness. A bottom-moored vertical chain of hydrophones was used for the signal reception. An omnidirectional source of pulsed sound signals could horizontally move at a distance of 0.5 m from the bottom. From the measured amplitude and arrival time of the pulsed signal, the parameters of transmission were obtained and compared with the calculations. The calculated dependences of the arrival times were plotted for both refracted and diffracted components [1] of the transmitted signal, with the sound speeds C = 1742 m/s and C = 1200 m/s in the bottom material, on the assumption that the Snell law was valid at the interface.

These experiments clearly showed that the signal arrival times satisfactorily corresponded to the calculated sound speed, C = 1742 m/s, for the undercritical incidence angles (curves *a* and *b*). However, as the horizontal distance and incidence angle increase, the arrival time consistently shifts to the plot (curve *c*) that corresponds to the speed C = 1200 m/s in the bottom material, thereby exhibiting the anomaly of propagation velocity (Fig. 1c [4]).

The same technique was used in [8] to measure the angular distribution of acoustic intensity in the transmitted wave. According to these measurements, the maximum of the angular distribution changes in accordance with the Snell law at undercritical angles, as if the sound speed in the bottom material took the calculated value 1675 m/s. However, in the domain of critical angles, another peak appears in the angular distribution that remains predominant as the grazing angle decreases down to 9.7°. This peak corresponds well to sound speeds of 1100–1200 m/s in the bottom material, and the angle of anomalous refraction is 45°–55° (Fig. 2 [8]).

The anomalies of the refraction angle and propagation speeds were used by Chotiros to propose an explanation for the anomalous phenomena by applying the theory of sound propagation in two-phase media, which

was earlier developed by Biot [9]. According to the Biot theory, three types of waves can exist in a two-phase medium like sea sand: two longitudinal waves and a shear wave. Among these waves, the second longitudinal one has an anomalously low velocity, $C_{L2} \approx 400$ m/s, and two other waves propagating with quite "normal" velocities, C_{L1} = (1700–1750) m/s and C_t = 1000 m/s, which correspond to the experimental data. According to Chotiros, the second (slow) longitudinal wave is just what can be responsible for the anomaly of the refraction angle, because it implies no phenomenon of full internal reflection at all. However, to agree with the experimental data, this wave should have a velocity of 1000–1200 m/s. To come to the quantitative agreement, Chotiros varied the parameters of the two-phase medium of the sea-sand type to obtain a specific dispersion dependence for the velocity of the slow longitudinal wave. The resulting dispersion proved to be so strong that it yielded a value of about 400 m/s at low frequencies and the desired value 1000–1200 m/s at the experimental frequencies 5–60 kHz.

In this connection, paper [10] should be mentioned, which reports on acoustic measurements of the elasticity of various bottom materials, including sandy ones under load. As the quantity to be measured, the velocity of the slow longitudinal wave was used. It proved to be 250–500 m/s for different loads at frequencies of 5–60 kHz, but no dispersion was observed. In the latest papers of Chotiros [11–13], interesting additional experimental data are presented. However, no new arguments or information on the directly measured velocity and dispersion of the slow longitudinal wave can be found there.

On the other hand, an alternative point of view appeared in recent years, and it was proposed in [14–21]. The proposed explanation is based on the well-known theory of sound refraction by the randomly rough surface of the sea bottom. This theory has been successfully used in [14–17] to explain the anomaly of the refraction angle and the apparent decrease in the effective sound speed in the bottom material. In [18], quantitative estimates are given for the amplitude anomaly and its dependence on the depth of the observation point, as related to the diffraction-caused insonification of the bottom halfspace. However, the unique experimental data obtained in [19–21] with the techniques earlier tested in a shallow sea and a hydroacoustic tank offers convincing evidence that the proposed explanation of the anomalous phenomena is at least not the only one.

Let us consider the aforementioned experimental data in more detail. In [19], an improved technique is reported for the measurements in a hydroacoustic tank whose bottom is covered with a layer of sea sand prepared in a specific manner. The surface of the sand was either smoothed to a condition of an even plane or brought to a condition of roughness. The measuring technique included variation of the horizontal position

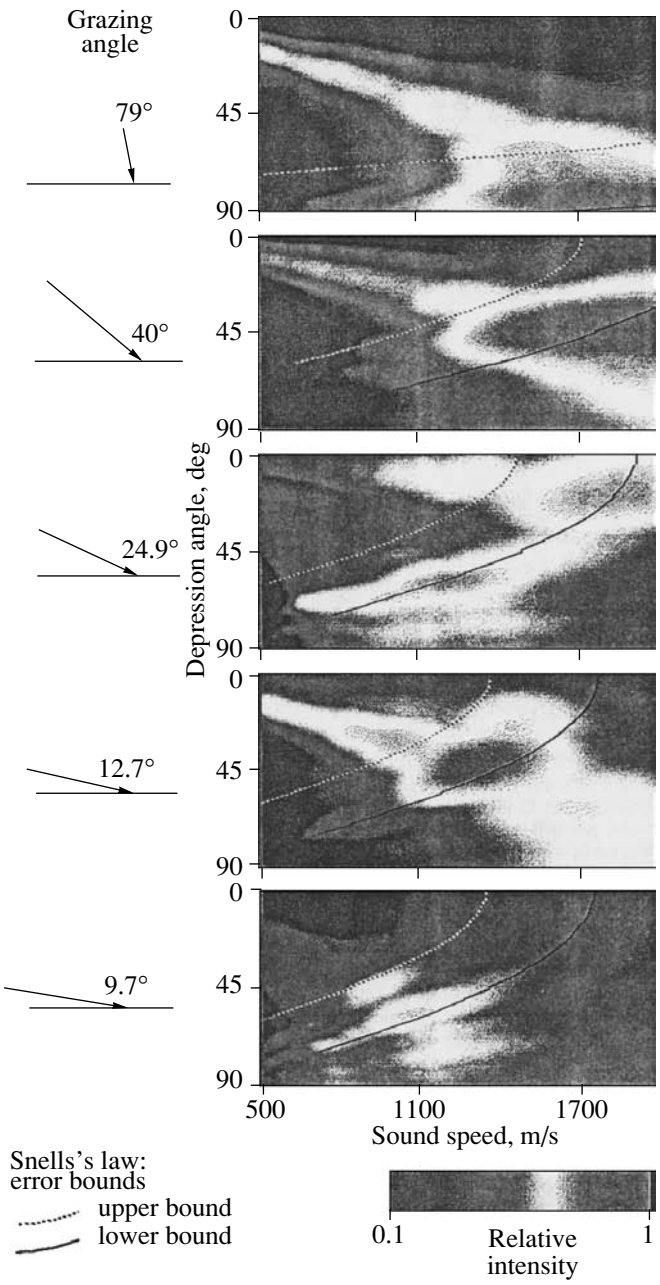

Fig. 2. Angular distributions of intensity of the transmitted wave as functions of the grazing angle and the sound speed in the bottom material.

of the omnidirectional sound source at a distance of 0.5 m from the bottom and sequential changes in the depth of the receiving hydrophone within the bottom bulk down to a depth of 90 cm with a step of 1.5 cm. Upon processing the amplitude-phase information, the technique provides the cross sections of the sound field in the bottom, which take the form of wave fronts in the depth–distance coordinates. These fronts characterize the complex pattern of sound refraction and diffraction for the entire range of incidence angles, including the overcritical ones. Figures 3a and 3b illustrate the exper-

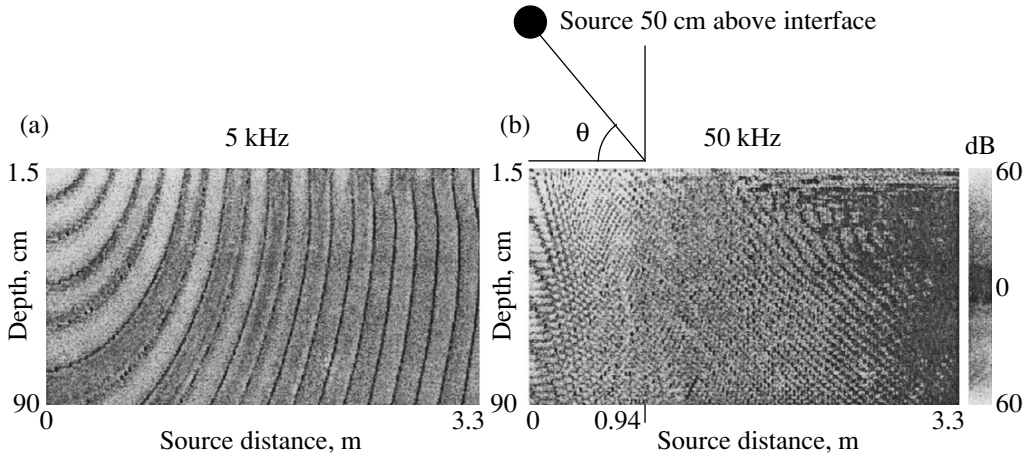

Fig. 3. Real part of the measured sound pressure in the sandy bottom with a smooth surface.

imental pattern of the sound field for the smoothed surface, both at low and high frequencies (5 and 50 kHz, respectively).

At a frequency of 5 kHz, the sound field structure is represented by a set of quasi-spherical wave fronts, which corresponds to the refracted waves. The propagation velocity of the waves along the interface corresponds well to the water wave: there are no traces of the bottom (lateral) wave. The absence of any anomalies in the sound field structure at 5 kHz fully agrees with the earlier conclusions of Chotiros [4].

A quite different pattern of the sound field is observed at a frequency of 50 kHz, which is illustrated by Fig. 3b. Two subsystems of wave fronts are visible, one of which corresponds to the quasi-spherical (refracted) waves in the domain of undercritical angles and the other corresponds to a surface source located in the domain of overcritical incidence angles. The two subsystems interfere to produce a maximum in the sound pressure at the apparent refraction angles 45°–55°, the corresponding apparent sound speed in the bottom material being 1100–1200 m/s.

It is clear that these apparent values, although agreeing well with those observed in [4–8], have nothing in common neither with the slow wave predicted by the Biot theory nor with diffraction-type sound scattering by the bottom surface, which is treated as smooth in the case at hand. At the frequency 50 kHz, the sound field structure itself is anomalous in the sense that it does not follow the classical description [1].

In [19], the sound field pattern is also presented for a bottom with a rough surface, for both low and high frequencies. At 50 kHz, the diffraction sound scattering naturally deformed the structure of the wave fronts corresponding to the surface source in the domain of overcritical angles, because this domain is most sensitive to the state of the surface. The structure and position of the interference maximum remained nearly unchanged at the apparent refraction angles 45°–55°. The direct measurements of the spatial spectrum of the sound field [19] and sound speed in the sandy bottom [20] did not reveal the slow wave with a velocity of 1100–1200 m/s, which is predicted by the Chotiros–Biot theory [8].

The measurements in a hydroacoustical tank with the technique proposed in [6] also allow one to obtain the transmission characteristics from the measured propagation times and to detect wave components that have different effective velocities of propagation. Such characteristics were found in [19], and the slow component with an effective velocity of 1200 m/s was reliably detected from the experimental data obtained for the model sand with a rough surface. This component proved to have a low level when the surface was sufficiently smooth.

The aforementioned data show that the diffraction-scattering mechanism increases the level of the low-velocity component in the total wave field. However, these data are insufficient to unambiguously determine the nature of the slow component and, hence, the origin of the propagation time anomaly.

For example, the quantitative estimate $C = 1200$ m/s for the effective velocity of the transmitted wave, at which the slow component manifests itself, is obtained on the assumption that the refraction mechanism acts and the Snell law is valid. If one supposes that the slow component is the surface wave with a synchronous excitation, the effective propagation velocity $C =$ (1380–1420) m/s will correspond to the same delay times, the specific value of the velocity depending on the parameters of the sand. It is clear that, for a wave with such characteristics to exist, one needs either some other model for the bottom material which differs from that of Biot, or another mathematical model for the bottom halfspace which differs from the classical one.

The important information required for understanding the time anomaly is carried by the impulse responses presented in [13], [18], and [20]. In these works, the technique from [4] was applied to a shallow

sea with the use of delta-like probing pulses at various incidence angles and horizons of observation. From the entire body of the data obtained, one can conclude that the impulse response is considerably distorted for lower grazing angles and deeper horizons of observation. The distortion of the impulse response consists in its broadening, the tail part of the pulse nearly always having a discrete structure, with pronounced arrival times of separate wave components.

According to [13], the tail components of the impulse response can be attributed to the slow wave predicted by the Biot–Chotiros theory. However, as we have mentioned above, these components can be related to the surface wave as well. The discrete structure of the impulse response can be hardly explained by the diffraction mechanism of insonifying the bottom halfspace with the incoherent signals scattered by the random roughness of the bottom.

Finally, the unique experimental data reported in [13], [18], and [20] complement the results reported in [4] on estimating the amplitude anomaly of the transmitted wave and its dependence on the parameters of the problem. These experiments were performed in the sea, with the use of a parametric projector and broadband (delta-like) pulses, for wide ranges of reception depths and grazing angles. The following conclusions can be drawn from the aforementioned publications:

—the amplitude anomaly grows as the reception depth increases and the grazing angle decreases;

—the amplitude anomaly exhibits an intricate interference-caused dependence on the frequency and grazing angle (see [18] and [20]) and on the reception depth [13];

—at the experimental frequencies 5–15 kHz, the amplitude anomaly is estimated as 30–80 dB at the low grazing angles 30°–15° (see [18] and [20]).

Note that, according to [4], the amplitude anomaly changes by 30–40 dB per decade within the frequency band 5–80 kHz when the reception horizon is fixed and the grazing angle is equal to 22°.

The undoubtedly unique estimates were obtained in [13] for the amplitude anomaly at a grazing angle of about 4.3°, with different reception depths. To simplify the analysis, we present these data in Fig. 4, with curve *1* corresponding to the calculated signal level in the inhomogeneous wave of the lower halfspace and curve *2* corresponding the experimental data given in [13]. It is evident that the amplitude anomaly exhibits an intricate interference-caused dependence on the reception depth, and the signal level reaches its maximum at some horizon under the surface. One can suppose that, at such small grazing angles, the decrease in the signal amplitude does not follow the exponential law in the near-bottom layer, as the model requires: it rather increases up to some horizon, remains inhomogeneous within the near-bottom layer, and spherically diverges outside this layer.

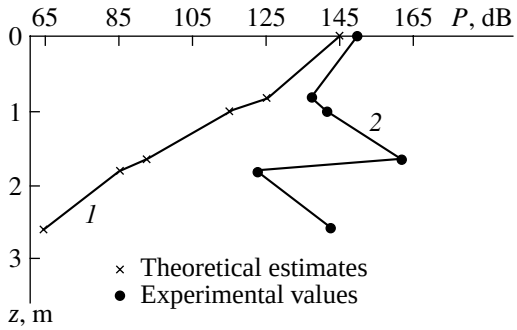

Fig. 4. Signal levels in the transmitted wave versus observation depth: (*1*) calculated and (*2*) experimental dependences.

Let us consider the spectra of the received signals, which are shown in Fig. 5 [13]. Figure 5a presents the calculated and experimental power densities for the signals received by hydrophones *7* and *8*, which were located directly at the interface, $z = 0$. One can see that the experimental spectrum significantly differs from the calculated one in its low-frequency part, this difference being the evidence of a considerably broadened signal. Figures 5b–5d correspond to hydrophones *3*, *2*, and *1*, whose depths are 1.0, 1.8, and 2.6 m, respectively. We can see that the spectrum of the model signal rapidly looses its high-frequency components in accordance with the exponential decay of the signal amplitude when the attenuation coefficient in the inhomogeneous wave increases with growing frequency. In contrast, the spectra of the signals received at certain horizons are enriched with high-frequency components whose level increases with increasing frequency, thereby compensating for the losses caused by the geometric spread and signal broadening. As a result, the spectra of the signals received by the deeper hydrophones remain nearly uniform. The only possibility for such a behavior is an inhomogeneous wave whose amplitude exponentially increases in depth.

Another feature of the experimental data [13] consists in the interference-caused variability of the signal level from –20 to +9 dB relative to the calculated value at points *4*, *7*, and *8*, which are located either in the water bulk near the bottom or at the bottom but are separated by 1.5–2.0 m in distance.

Unfortunately, the aforementioned discussion of more that 20 years in duration had no appropriate representation in Russian publications. However, it is really interesting for those who use in practice underwater acoustic systems that operate near the sea bottom with overcritical (small) incidence angles. Side-scan sonars (SSS) can be primarily attributed to such systems. In the Institute of Marine Technology Problems, Far-East Division, Russian Academy of Sciences, rich experience had been accumulated in operating the SSS of a self-contained unmanned underwater vehicle (SCUUV). With the optimal operational modes of an

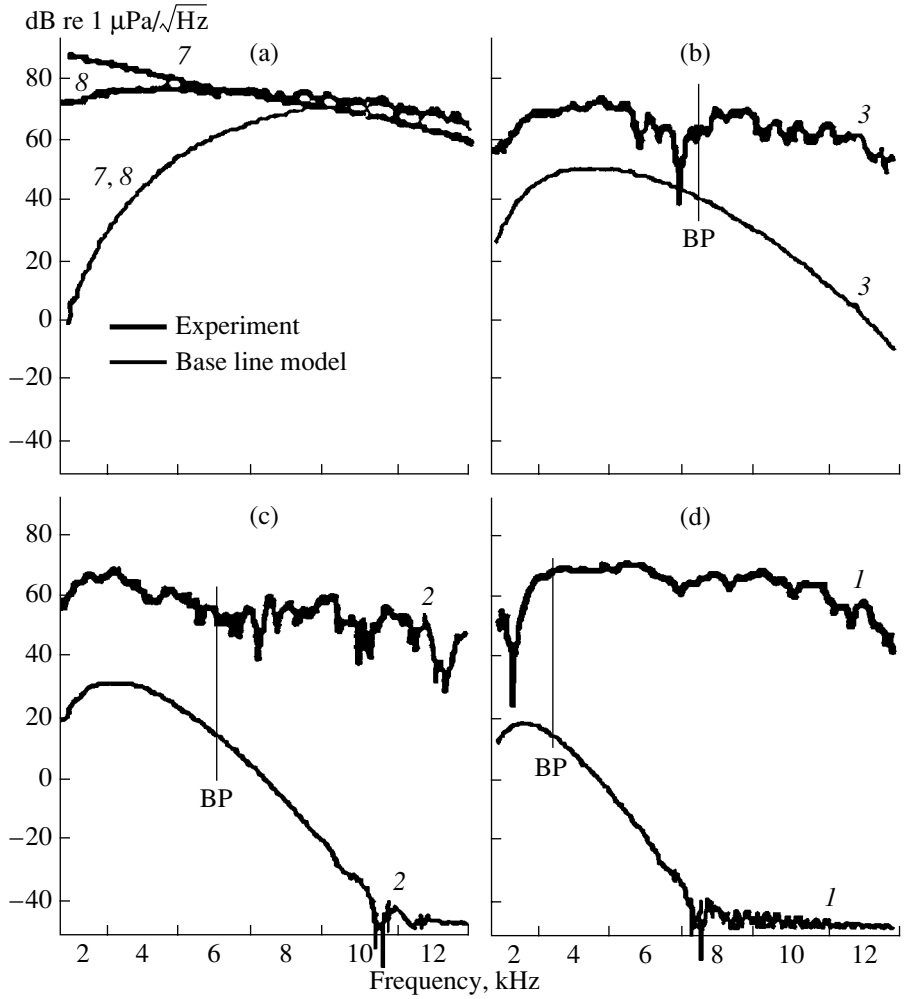

Fig. 5. Power spectral density of the received signals: (a) hydrophones *7* and *8* are at the bottom; (b) hydrophone *3* is at a depth of 1 m in the bottom material; (c) hydrophone *2* is at a depth of 1.8 m in the bottom material; and (d) hydrophone *1* is at a depth of 2.6 m in the bottom material.

SCUUV that moves at a height $h = (10–15)$ m above the bottom, the ultimate range of the SSS is 550–750 m on each side. Such distances correspond to grazing angles that are lower than 1°.

When the grazing angles are that small, the impedance interface behaves as a pressure-release screen, near which, according to the classical description, the level of the sound pressure decreases as the squared distance. Such a spread law should make the SSS nearly inoperative. However, the anomalous results were obtained just with this unusual operational mode of the SSS, which was tested in the Sea of Japan at depths of $H = (2500–3000)$ m. The experimental data obtained in 1998–1999 are presented in Fig. 6.

In the SSS images of the sea bottom, structures can be seen that have a form of alternating dark and bright bands. These structures characterize the interference processes that take place in the near-bottom propagation of the SSS sound signals at low grazing angles. It is natural to assume that, with unchanged conditions of interference, the spatial interference period is constant, because it is governed by nothing but the spatial frequencies of the interfering waves. However, if the bottom relief changes, the SSS images will exhibit only the horizontal projection of the spatial interference period. Therefore, in fact, Fig. 6 represents a topographic map of the sea floor, at which the interference bands play the role of isobaths. Close positions of the bands indicate a sharp rise in the bottom profile, while an increase in the apparent interfering period means smoothing of the bottom.

Another feature of the interference is illustrated in Fig. 7. It can be seen that there is no interference at the flat portions of the bottom, even at overcritical incidence angles and high levels of backscattering. However, if a bottom hole appears, to which a dark spot corresponds in the SSS image, and an extremely low backscattering level occurs, the interference bands do appear at the outer side of the hole, where the hole changes into a bottom rise.

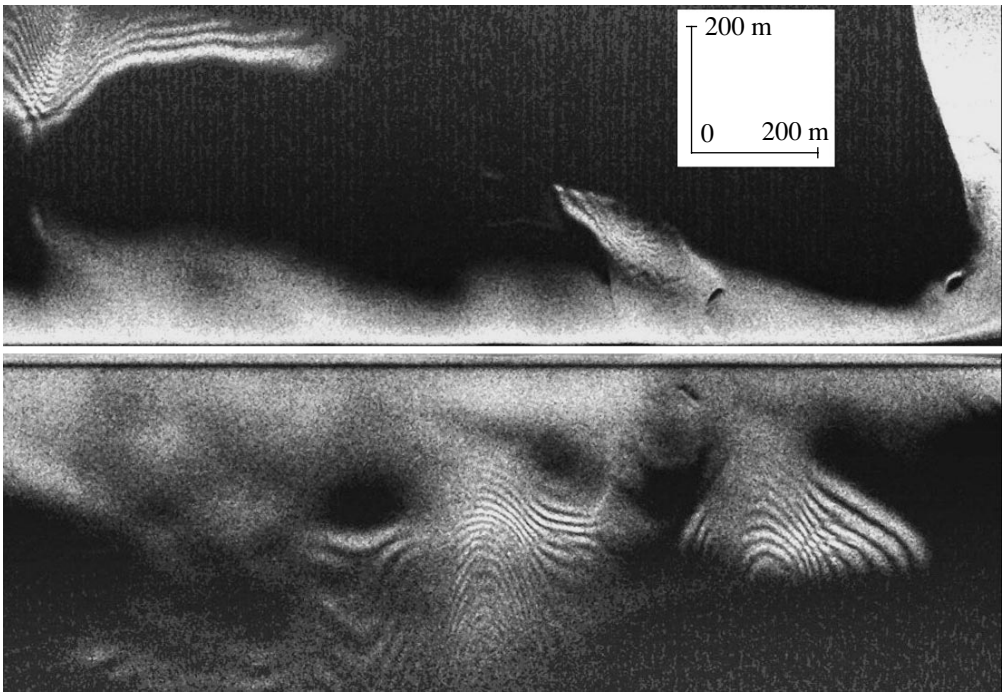

Fig. 6. Bottom image obtained in the Sea of Japan at a depth of 2500 m (the experiment of 1998).

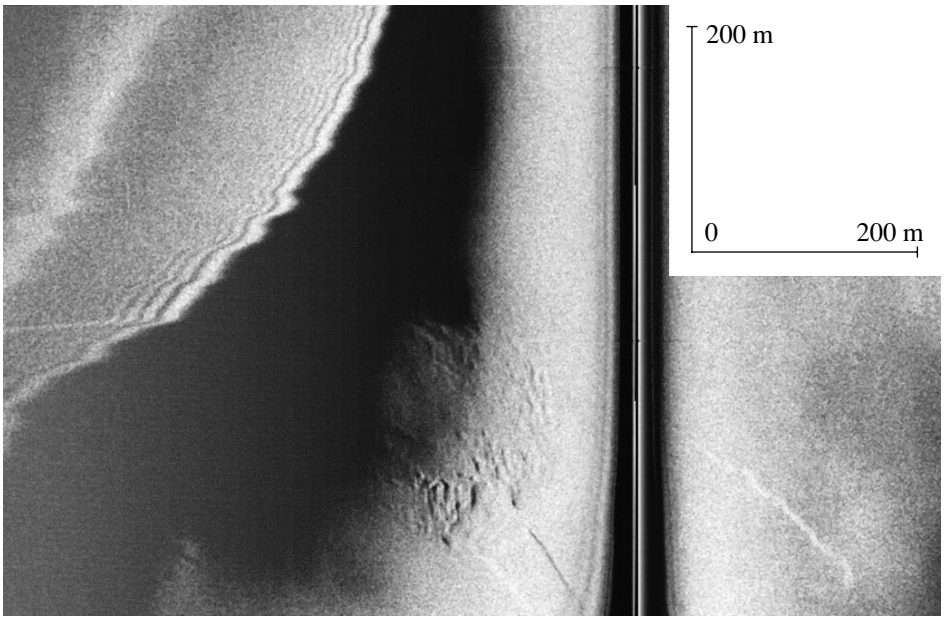

Fig. 7. Bottom image obtained in the Sea of Japan at a depth of about 3000 m (the experiment of 1999).

Figures 8 and 9 show other examples of the SSS images of the bottom, which were obtained in 2001 in the Barents Sea at depths of 150–170 m. The height of the SCUUV above the bottom was as small as 1–2 m, corresponding to the grazing angles 0.2°–1.0°. The rocky sea floor was covered with a layer of sediments. In all images, the interference appears only at the outer sides of the bottom holes, the interference structures themselves being quite stable and regular in their shapes.

Summarizing all experimental data obtained in deep-water regions of the Sea of Japan, shallow-water harbors of the Peter the Great Bay, and the Barents Sea, we can state that the interference structures occur quite

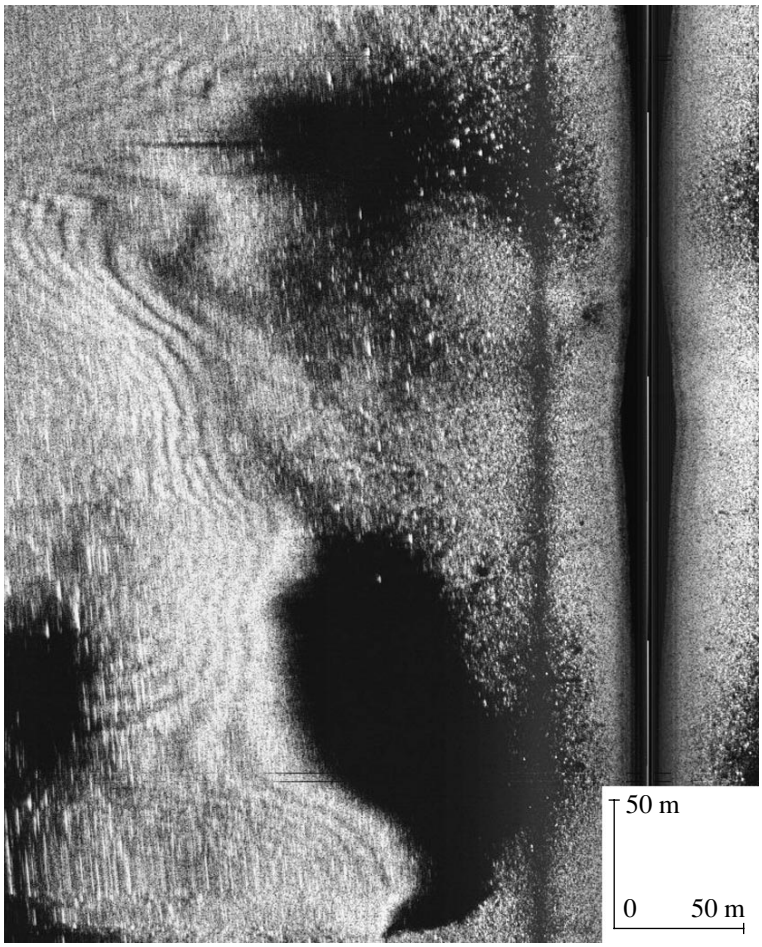

Fig. 8. Bottom image obtained in the Barents Sea at a depth of 150 m (the experiment of 2001).

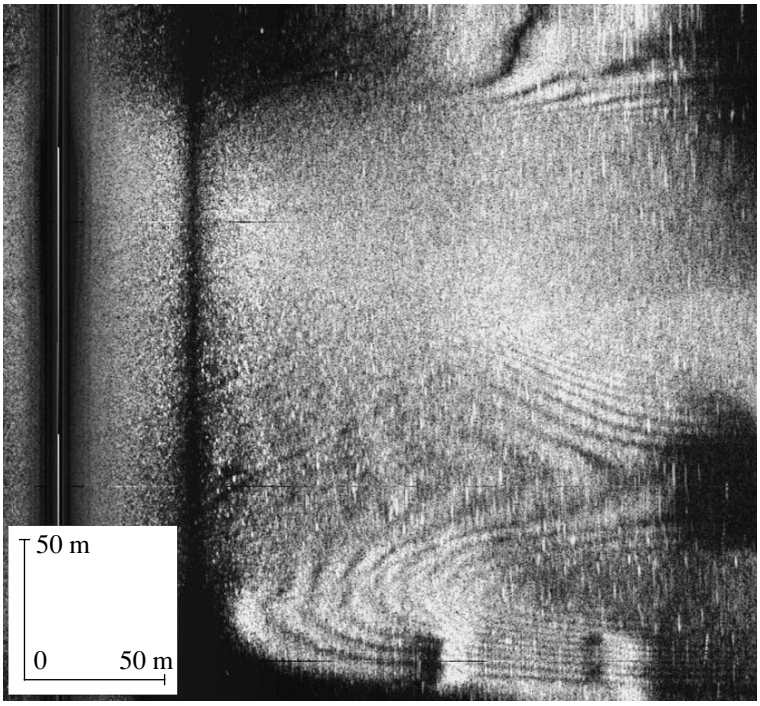

Fig. 9. Bottom image obtained in the Barents Sea at a depth of 170 m (the experiment of 2001).

regularly when the SCUUV is towed at small heights above the bottom. For all interference structures, the following features are characteristic:

—the interference occurs in a zone corresponding to the overcritical grazing angles;

—the interference occurs nowhere but at the outer side of the dark spots corresponding to the holes in the bottom;

—the spatial period of the interference varies from several meters to several tens of meters, depending on the bottom relief.

The anomaly of the data obtained consists in that an interference period as large as that cannot be explained by the classical description, i.e., in terms of the water and bottom-material waves for which the spatial interference period is by two orders of magnitude higher than the observed one. Actually, the spatial interference period of the water and bottom-material waves is governed by the simple relation $L = \lambda\frac{C}{\Delta C}$, where $\lambda \approx 2$ cm is the wavelength at the SSS operational frequencies, $\Delta C = C_2 - C_1$, $C = \frac{1}{2}(C_2 + C_1)$, and C_1 and C_2 are the velocities of the water and bottom-material waves, respectively. By specifying $\Delta C \approx 0.1C$ for soft bottom materials of the sediment type, we obtain the estimate $L \approx 10\lambda$. However, the SSS cannot resolve such a fine spatial structure of the interference. The diffraction scattering of the incident wave by the bottom roughness cannot lead to such highly ordered interference structures as well. It is also evident that the Chotiros–Biot theory fails to explain the observed interference structures due to the slow wave that occurs in a two-phase medium like a sandy bottom.

The analysis of the data obtained in numerous and, sometimes, unique experiments of the last two decades leads to a conclusion that these experiments posed many questions, but the answers given by many researchers can explain only some individual aspects of the problem. The scale of the problem and its importance for applied acoustics allow us to hope that further theoretical attempts will not be restricted by correcting the known physical statements and models.

REFERENCES

1. L. M. Brekhovskikh, *Waves in Layered Media*, 1st ed. (Nauka, Moscow, 1957; Academic, New York, 1960).
2. T. G. Muir, C. W. Horton, and L. A. Thomson, Sound Vibr. **64** (4), 539 (1979).
3. K. L. Williams and L. J. Satkoviak, J. Acoust. Soc. Am. **86**, 311 (1989).
4. N. P. Chotiros, in *Proceedings of Oceans'89* (1989), Vol. 3, p. 1158.
5. R. A. Altenburg, N. P. Chotiros, and C. M. Faulkner, J. Acoust. Soc. Am. **89**, 165 (1991).
6. F. A. Boyle and N. P. Chotiros, J. Acoust. Soc. Am. **91**, 2615 (1992).
7. N. P. Chotiros, in *Proceedings of Oceans'94* (1994), Vol. 2, p. 250.
8. N. P. Chotiros, J. Acoust. Soc. Am. **97**, 199 (1995).
9. M. A. Biot, J. Appl. Phys. **33**, 1482 (1962).
10. S. V. Gol'din, Yu. I. Kolesnikov, and G. V. Polozov, in *Proceedings of X Session of the Russian Acoustic Society* (GEOS, Moscow, 2000), p. 186.
11. N. P. Chotiros, D. E. Smith, J. N. Piper, *et al.*, Acoust. Oceanogr. Proc. Inst. Acoust. **23**, Part 2, 355 (2001).
12. N. P. Chotiros, D. Yelton, and M. Stern, J. Acoust. Soc. Am. **106**, 1681 (1999).
13. N. P. Chotiros, F. M. Mautner, A. Lovir, *et al.*, IEEE J. Ocean Eng. **22** (4), 604 (1997).
14. J. E. Moe and D. R. Jackson, J. Acoust. Soc. Am. **103**, 275 (1998).
15. D. R. Jackson and A. N. Ivakin, J. Acoust. Soc. Am. **103**, 336 (1998).
16. A. N. Ivakin and D. R. Jackson, J. Acoust. Soc. Am. **103**, 346 (1998).
17. E. I. Thorses, D. R. Jackson, and K. L. Williams, J. Acoust. Soc. Am. **107**, 263 (2000).
18. A. Magner, W. L. J. Fox, H. Schmidt, *et al.*, J. Acoust. Soc. Am. **107**, 1215 (2000).
19. H. J. Simpson and B. H. Houston, J. Acoust. Soc. Am. **107**, 2329 (2000).
20. A. Magner, E. Bovio, W. L. J. Fox, and H. Schmidt, J. Acoust. Soc. Am. **108**, 987 (2000).
21. E. I. Thorses, K. L. Williams, D. R. Jackson, *et al.*, Acoust. Oceanogr. Proc. Inst. Acoust. **23**, Part 2, 344 (2001).

Translated by E. Kopyl

Acoustical Physics, Vol. 48, No. 4, 2002, pp. 388–399. Translated from Akusticheskiĭ Zhurnal, Vol. 48, No. 4, 2002, pp. 447–460.

Coding of Amplitude-Modulated Signals in the Cochlear Nucleus of a Grass Frog

N. G. Bibikov

Andreev Acoustics Institute, Russian Academy of Sciences, ul. Shvernika 4, Moscow, 117036 Russia

e-mail: bibikov@akin.ru

Received September 20, 2001

Abstract—To study the mechanisms that govern the coding of temporal features of complex sound signals, responses of single neurons located in the dorsal nucleus of the medulla oblongata (the cochlear nucleus) of a curarized grass frog (*Rana temporaria*) to pure tone bursts and amplitude modulated tone bursts with a modulation frequency of 20 Hz and modulation depths of 10 and 80% were recorded. The carrier frequency was equal to the characteristic frequency of a neuron, the average signal level was 20–30 dB above the threshold, and the signal duration was equal to ten full modulation periods. Of the 133 neurons studied, 129 neurons responded to 80% modulated tone bursts by discharges that were phase-locked with the envelope waveform. At this modulation depth, the best phase locking was observed for neurons with the phasic type of response to tone bursts. For tonic neurons with low characteristic frequencies, along with the reproduction of the modulation, phase locking with the carrier frequency of the signal was observed. At 10% amplitude modulation, phasic neurons usually responded to only the onset of a tone burst. Almost all tonic units showed a tendency to reproduce the envelope, although the efficiency of the reproduction was low, and for half of these neurons, it was below the reliability limit. Some neurons exhibited a more efficient reproduction of the weak modulation. For almost half of the neurons, a reliable improvement was observed in the phase locking of the response during the tone burst presentation (from the first to the tenth modulation period). The cooperative histogram of a set of neurons responding to 10% modulated tone bursts within narrow ranges of frequencies and intensities retains the information on the dynamics of the envelope variation. The data are compared with the results obtained from the study of the responses to similar signals in the acoustic midbrain center of the same object and also with the psychophysical effect of a differential sensitivity increase in the process of adaptation. © *2002 MAIK "Nauka/Interperiodica".*

In the analysis of complex sound signals in auditory systems of humans and animals, the main role is played by the mechanisms that provide the coding of the temporal variations of the signal amplitude in separate frequency channels. To study these mechanisms, it is convenient to use anurans, which, on the one hand, have a relatively simple auditory system and, on the other hand, are capable of performing a detailed analysis of both environmental sounds and communication calls of their own species. Male frogs produce mating vocalizations for one or two weeks after hibernation. These sounds form continuous signals with the dominant frequency within 0.4–0.6 kHz and the modulation frequency within 20–40 Hz [1, 2]. Such signals can be considered as a simplified model of other complex signals, including speech. Hence, the problem of signal encoding in the auditory system of anurans is important for understanding the general mechanisms of the auditory system operation in both animals and humans.

In studying the coding of amplitude-modulated (AM) signals, most researchers use one of the following types of stimuli: AM tone bursts [3–6] or continuous AM signals [7, 8]. This paper studies the response of isolated neurons to AM tone bursts. The majority of publications concerned with this subject deal with the case of 100% modulation depth, and the point of interest was the modulation transfer function, i.e., the dependence of the mean firing rate or the synchronization coefficient of the response on the modulation frequency. It was demonstrated that the majority of peripheral neurons located in the primary auditory center, i.e., the dorsal nucleus of the medulla oblongata (a homologue of the cochlear nucleus of mammals), reproduce the amplitude modulation in the frequency range from several hertz to hundreds of hertz [6, 9, 10].

Studies of the neural response of the dorsal nucleus to stimuli with a small modulation depth are few in number. In one publication, it was shown that, for relatively intense stimuli, a 10% modulation is adequately reproduced at high frequencies of 100–160 Hz but practically not reproduced at a lower frequency of 10 Hz.

In the auditory center of the midbrain of a frog, the character of coding of AM tone bursts noticeably changes. In the case of 100% modulated signals, most neurons were found to exhibit the best phase locking with the envelope waveform at relatively low modulation frequencies (10–40 Hz). This tendency was retained even for the neurons for which the highest firing rate was observed at modulation frequencies within 50–80 Hz [3]. A somewhat broader frequency range of the amplitude modulation reproduction was only

1063-7710/02/4804-0388$22.00 © 2002 MAIK "Nauka/Interperiodica"

observed for some neurons of the torus semicircularis of toads [11].

The neural responses of the midbrain to signals with a modulation frequency of 20 Hz and modulation depths of 80 and 10% and with a carrier intensity level of 20–30 dB above the threshold were studied in detail for the grass frog in [12]. A reliable discrimination of 10% amplitude modulation was observed for 104 of 186 neurons studied, and 66 of these neurons exhibited an improvement of phase locking during the AM tone presentation, from the initial modulation period of the AM stimulus to the terminal one. The comparison of these data with the fragmentary data obtained in similar conditions for the cochlear nuclei of other anuran species suggested that an improvement of the phase locking of the response with weak periodic amplitude variations of relatively low frequency occurs along the auditory pathway. To verify this hypothesis, a study of the response stimulated by signals with a modulation frequency of 20 Hz in the cochlear (dorsal medullary) nucleus of a grass frog (*Rana temporaria*) was carried out, and this study is the subject of this paper. The parameters of the signals were approximately the same as in the study of the midbrain neurons [12].

The preparation of the animals, the acoustic stimulation, and the methods of recording the responses were described in a number of previous publications [8, 12, 13] and will be briefly outlined below.

Frogs collected in autumn were studied in winter and in spring. An operation consisting in the elimination of part of the braincase above the medulla oblongata was performed under hypothermia [14], and the edges of the hole were treated with lidocaine. After the frogs recovered from the anesthesia, they were immobilized by an allopherin injection. The frog under investigation was wrapped in moist gauze to provide cutaneous respiration and placed on a vibration-isolated table in a soundproof chamber. The electrodes were represented by glass pipettes filled with 2M NaCl; the pipette ends were 0.5–3.0 μm in diameter. The electrodes were positioned immediately behind the cerebellum and moved by a step-motor microdrive, which was controlled from outside the chamber. Since the cochlear nucleus is located immediately on the dorsal brain surface, the instant when it was hit by the electrode could be detected by the abrupt appearance of an asynchronous evoked activity in response to the test stimulus (a broadband noise burst).

The neuronal responses were amplified by an MZ-4 Nichon Kohden high-impedance amplifier and a power amplifier with a passband of 0.25–3.0 kHz. The signal was observed by an oscilloscope and listened to through headphones. After detecting a neuron with a spike amplitude that provided its reliable identification and separation from noise, its optimal (characteristic) carrier frequency and the response threshold at this frequency were determined audiovisually. The neuron spikes were transformed by a Schmidt trigger to standard pulses and then entered in a PC for real-time data processing.

The tone signals were obtained from a G3-110 analog generator possessing an input for providing the amplitude modulation. The modulating sinusoid was supplied from a G6-28 signal generator. The tone bursts were formed by an electronic switch controlled by a G5-60 pulse generator, which determined the duration and period of the stimulus presentation. The modulation frequency was synchronized with the stimulus onset in such a way that the modulating function began from the phase corresponding to the beginning of the amplitude decrease from the mean level (a half-period delay of the sinusoid). The rise and fall times of a tone burst were 5 ms. The signal intensity level was varied by an attenuator at a step of 1 dB.

The acoustic signals were delivered to the frog's tympanum via a dynamic telephone through a plastic tube. The signal presentation was ipsilateral to the cerebral hemisphere under study. The calibration of the closed acoustic system was performed for each frog with the use of a half-inch condenser microphone with a thin probe tube. The microphone with the tube was preliminarily calibrated in a soundproof chamber.

The main experiments were performed with 512.5-ms-long tone bursts. The AM signals included a 12.5-ms-long initial part, within which the amplitude increased during the first 5 ms and then decreased, and ten full 20-Hz modulation periods, which were counted starting from the minimal amplitude value. Correspondingly, the maximal amplitudes were observed within 37.5, 87.5, and 127.5 ms after the stimulus onset, etc. The interval between the signal presentations usually was 1.5–2.0 s, and the number of presentations varied from 25 to 100.

In the course of the experiment, the peri-stimulus time histograms (PSTHs) of the response were obtained with a 0.5-ms width of one bin. The histograms were obtained in terms of the instantaneous firing rate (the number of spikes in a reading divided by the number of presentations and the width of the bin). To monitor the stationary character of the response, the time dependence of the mean firing rate was recorded at a step of 2 s. In all cases described in this paper, the response remained stationary.

After the experiment, the neurons were classified according to their responses to tone bursts without amplitude modulation. The classification was performed automatically by a program used earlier in studying the torus semicircularis [12]. Preliminarily, the PSTH of the response was summed over four points, so that its step was equal to 2 ms. The first stage of classification included the determination of the response latency delay by the instant when the instantaneous firing rate reached a given value, which usually was 40 spikes per second. In some cases (for neurons with a very high spontaneous firing or a very weak

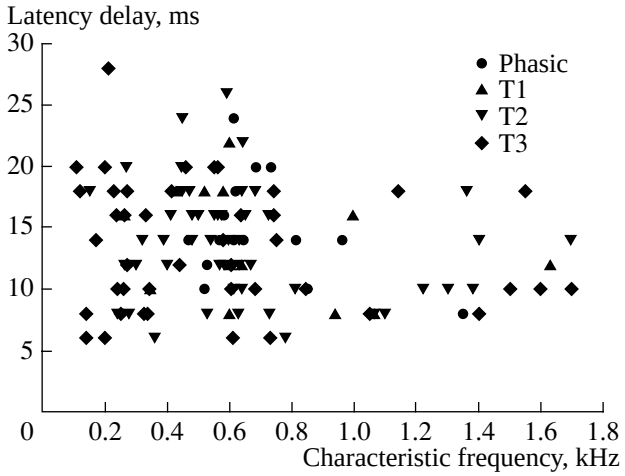

Fig. 1. Relation between the characteristic frequencies and latency delays of the response for 133 neurons of the cochlear nucleus of a grass frog. Different kinds of dots represent different groups of neurons classified according to the shape of the PSTHs.

evoked firing), the threshold value for the latency delay could be varied by the experimenter.

The following steps of the data processing were identical for all neurons. First, the mean spike rate was calculated for the interval 0–12 ms after the latency delay. This value was divided by the mean rate for the interval 0–512 ms after the latency delay. If the resulting ratio was greater than ten, the neuron was classified as a phasic unit. If this ratio was between five and ten, the neuron was ascribed to the T1 group. Neurons characterized by the ratios between two and five were classed as T2 units, and when the ratio was between one and two, as T3 units. In the experiments described in this paper, no neurons with a mean firing rate increasing with time were observed, and, hence, the corresponding group was not considered. This classification ignores some of the possible features of the response development with time (e.g., chopper or pause patterns of the discharge); however, such features were rather uncommon.

The following analysis of the PSTHs of the response consisted in the calculation of the coefficients of the firing synchronization with the sequential modulation periods. The 512-ms-long time interval taken after the latency delay was divided into the initial part (12 ms) and ten 50-ms-long fragments. The distribution of spikes within each of the periods was considered as a circular vector distribution for which the synchronization coefficient (the normalized length of the vector sum) and the phase of the maximum (the direction of the vector sum) could be determined [15]. The values of these parameters were also calculated for the superposition of all ten periods. For the synchronization coefficient obtained for individual periods, we use the term partial synchronization coefficient (PSC), and for the quantity obtained by the superposition, we use the term overall synchronization coefficient (OSC). For both the individual periods and the whole response, the reliability of the phase locking with the envelope waveform was estimated [16].

The results of this study are based on the data obtained from 133 single neurons located in the cochlear nucleus of the grass frog. The characteristic frequencies of neurons were between 130 Hz and 1.7 kHz. In this series of experiments, we observed a relatively small number of neurons optimally responding to frequencies above 1.0 kHz. This result was somewhat different from the data obtained previously [17]. The response thresholds at the characteristic frequencies varied from 20 to 70 dB SPL, which agreed well with the previous data [18].

The latency delays obtained for the neurons of the dorsal nucleus were within 6–28 ms, and only six neurons exhibited latency delays longer than 20 ms. This distribution was much narrower than that observed for the midbrain [19], and the average value of the latency delay was much smaller than in the midbrain. Figure 1 shows the latency delay versus the characteristic frequency of neurons (on a semilogarithmic scale). No reliable correlation between the latency delay and the characteristic frequency could be noticed for the whole set of neurons, as well as for the separate neuron groups that differed in the shape of the PSTHs.

As was mentioned above, the neurons were classified into four groups according to the shape of the PSTHs of the responses to the characteristic-frequency tones, whose intensities were within 20–30 dB above the threshold. Of the 133 neurons studied, 17 neurons belonged to the phasic group, 14 to the T1 group, 53 to the T2 group, and 49 to the T3 group. No significant differences were observed between the characteristic frequency distributions for the phasic, T1, T2, and T3 units. The mean values of the latency delay were 14.9, 13.6, 13.81, and 13.22 ms for the phasic, T1, T2, and T3 neurons, respectively. A two-sample t-test with different variances revealed no reliable difference in the mean values of the latency delay for different neuron groups, although, qualitatively, one could notice that, on the average, the phasic neurons responded with relatively greater delays.

The response to 80% amplitude modulation was studied for 129 neurons. Examples of the PSTH of the response to pure tone bursts and AM tone bursts are shown in Figs. 2 and 3. According to the shape of the PSTH of the response to a tone burst (Fig. 2a), a typical tonic neuron 61427 (a characteristic frequency of 270 Hz) belongs to the T3 group. Like the majority of neurons with low characteristic frequencies, it was capable of reproducing the carrier frequency (Figs. 2d–2f). The response to a signal with 80% modulation depth exhibited a distinct phase locking with the modulation period (Fig. 2b) and, simultaneously, with the period of the carrier frequency (Fig. 2e). Neuron 11207, whose response is shown in Figs. 3a–3c, belongs to the

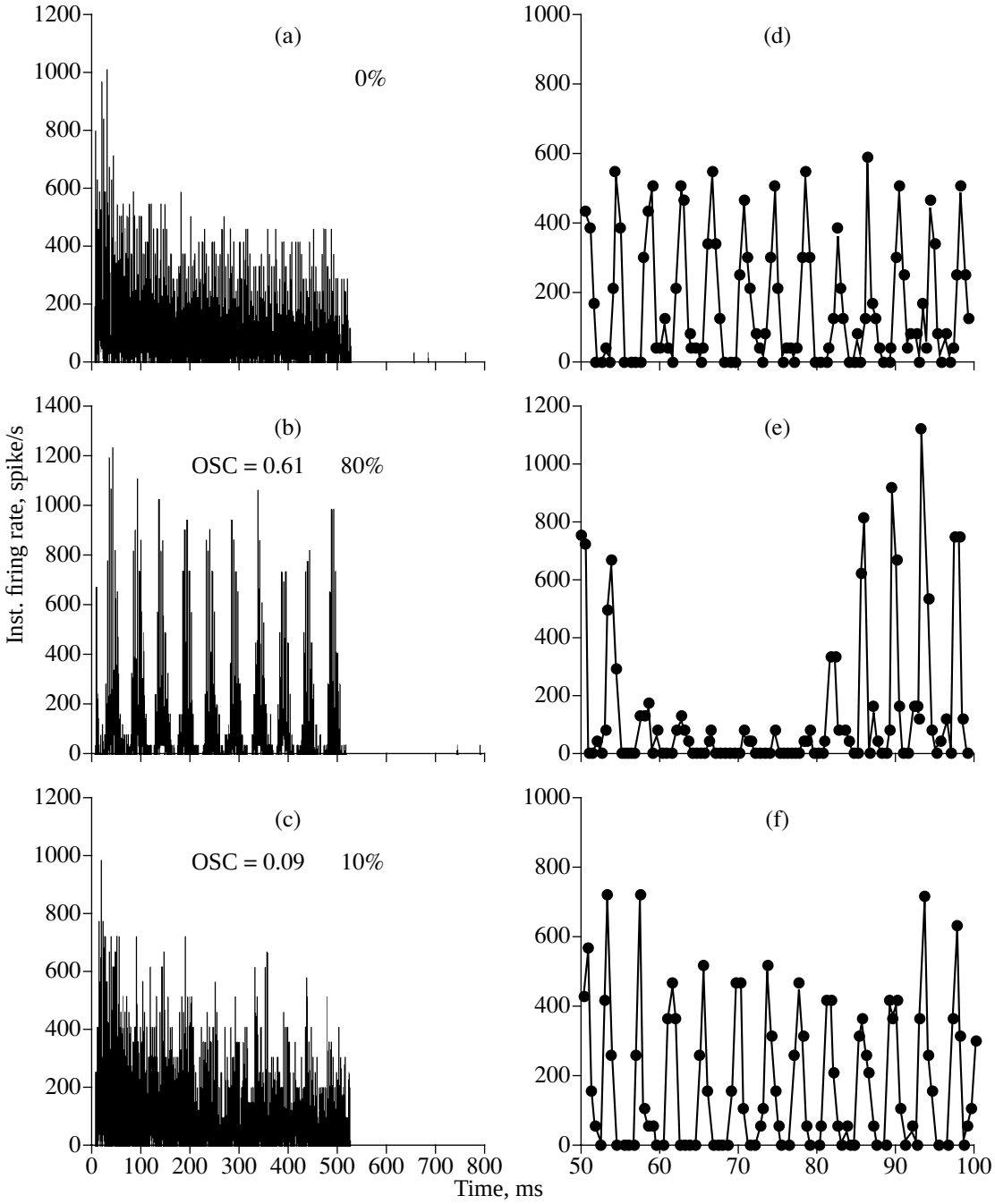

Fig. 2. PSTHs of the response of a typical low-frequency tonic neuron [the 61427 neuron; the T3 group; a signal frequency (SF) of 0.27 kHz; a signal level (SL) of 78 dB SPL] to (a, d) a 0.5-s-long pure tone burst, (b, e) a 80% amplitude modulated tone burst, and (c, f) a 10% modulated tone burst. The abscissa axis represents the time elapsed after the signal onset, and the ordinate axis represents the instantaneous firing rate. (a–c) The plots on the left present the whole histograms, and (d–f) the plots on the right show the region between 50 and 100 ms. (b, c) In two of the plots, the values of the overall synchronization coefficient are indicated.

T1 group, and neuron 10610 (Figs. 3d–3f) exhibited a phasic response to the tone signal. Both these neurons reproduce the 20-Hz modulation of the signal with even better phase locking than that observed for the tonic neuron. The accuracy of the phase locking with the 80% modulated signal is highest for the phasic neuron.

It should be noted that the great majority of the neurons under study adequately reproduced the amplitude modulation with a frequency of 20 Hz and a depth of 80% (Fig. 4, the abscissa axis). However, some difference can be noticed in the efficiency of the reproduction of this modulation for neurons with different types of

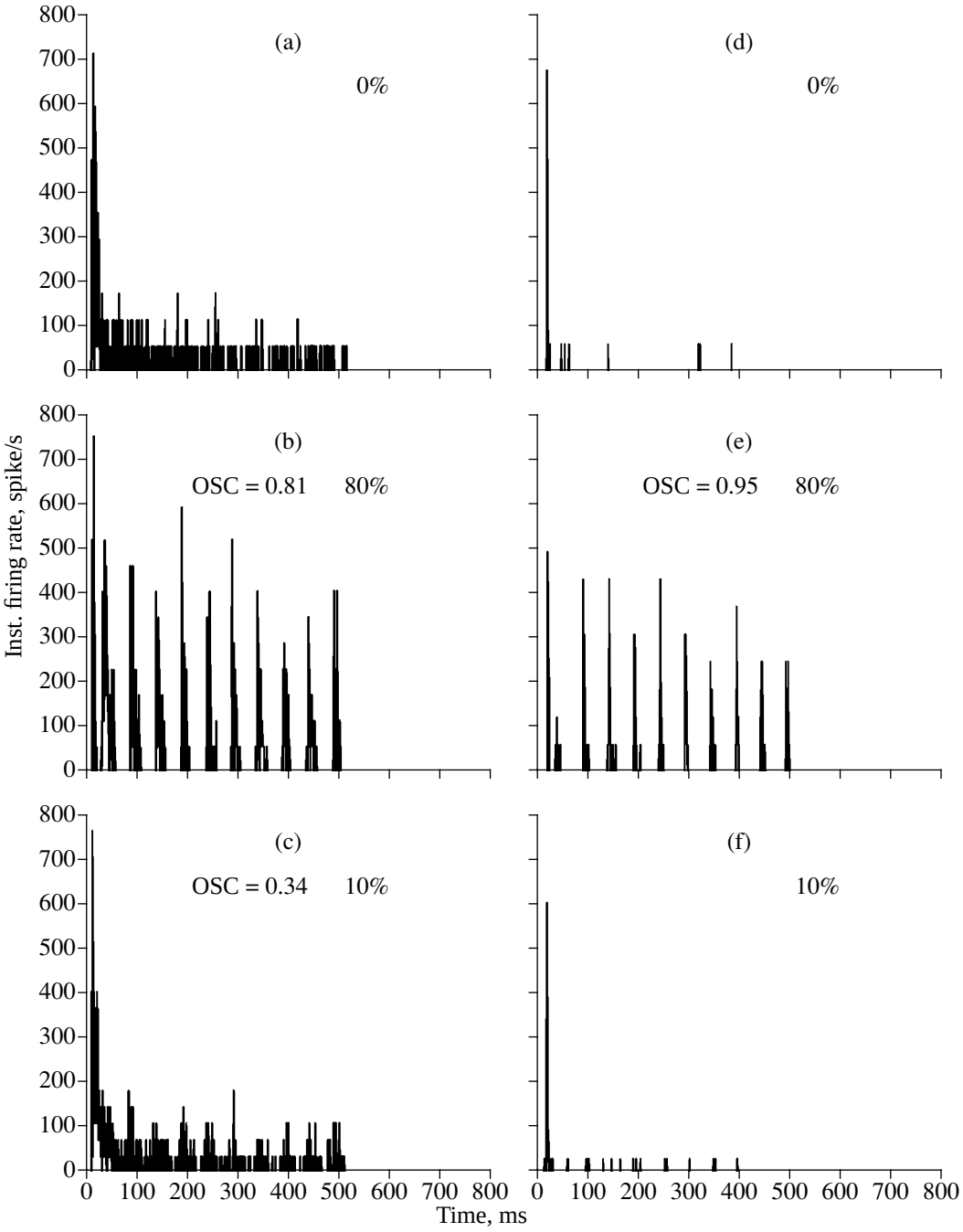

Fig. 3. PSTHs of the response of (a–c) a tonic neuron with a sharp short-term adaptation (11207; T1 group; SF, 0.61 kHz; SL, 74 dB SPL) and (d–f) a phasic neuron (10610; phasic group; SF, 0.62 kHz; SL, 83 dB SPL) to 0.5-s-long (a, d) pure tone bursts, (b, e) 80% amplitude modulated tone bursts, and (c, f) 10% modulated tone bursts. The notations are the same as in Fig. 2.

the PSTH of the response. Of 17 phasic neurons, 13 reproduced the signal with the 80% modulation depth. Four other neurons responded to the signal with 80% modulation depth only at the beginning of the stimulus. For 13 phasic neurons, which reproduced the modulation of sound, the average value of the OSC was equal to 0.921. All 13 neurons of the T1 group reproduced the 80% modulation of the signal with a somewhat smaller value of the OSC: 0.71. The difference between the groups was reliable (the probability of the coincidence of the average values was $P < 0.0002$). The neurons of the T2 group reproduced the 80% modulation with an average OSC of 0.65 (the number of neurons was 46; in comparison with the T1 group, $P = 0.07$, and with the phasic group, $P < 0.0001$). Finally, the neurons of the T3 group reproduced this signal with an average OSC

of 0.50 (N = 43; in comparison with other groups, P < 0.0001). Thus, in response to a signal with a large modulation depth, a phase locking with the signal envelope was observed for almost all neurons (except for several phasic units); however, the phase locking was weaker for neurons with a more tonic type of the response, i.e., with a less pronounced short-term adaptation.

In our experiments, the neural response to AM tone bursts with 10% modulation depth was of most interest. In studying the auditory center of the midbrain [12], we divided all neurons into three groups that differed in the response to this kind of signals. Neurons of one of these groups were incapable of reproducing weak periodic amplitude variations. In the second group of neurons, the modulation was reproduced with a low efficiency for only part of the signal (usually with a low efficiency). The third group of neurons, which was of chief interest, reproduced the modulation with an efficiency that noticeably increased from the first to the last period of the AM tone burst. For the last periods, the efficiency was rather high, being in some cases comparable to the efficiency observed for the 80% modulation depth. For the neurons of the cochlear nucleus, the aforementioned classification proved to be unsuitable. The point is that the majority of neurons of the cochlear nucleus reproduce the 10% modulation with a rather low efficiency. In this case, it is not easy to reveal the very fact of the modulation reproduction, much less the increase in the strength of the phase locking of the response during the stimulus presentation (see Figs. 2c and 3c). Therefore, we consider the quantitative characteristics of neurons without separating them into groups by this feature.

The response to signals with the 10% modulation depth was studied for 104 neurons. None of the 15 phasic neurons studied in this series of the experiment were able to reproduce the 10% modulation of the signal (Fig. 3f). These neurons retained the phasic character of the discharge according to the classification described above (see the description of the experimental technique). In some cases, single pulses were observed within the signal duration. Sometimes, it was possible to qualitatively notice their phase locking with the envelope waveform (Fig. 3f). However, the small number of these pulses (no more than 10–20 per 50 signal presentations; i.e., the average probability of the pulse appearance within one period was less than 0.04) allowed no quantitative analysis.

Figure 4 shows the OSC for the responses to tone bursts with 10% modulation versus the OSC characterizing the responses to 80% modulated signals for 85 tonic neurons studied at two modulation depths. In the case of tone bursts with 10% modulation, the average value of the OSC was equal to 0.25 for the T1 group (N = 9), 0.18 for the T2 group (N = 45), and 0.11 for the T3 group (N = 34). A reliable difference was only observed between the T1 and T3 groups, but the general tendency toward an increase in the OSC with the

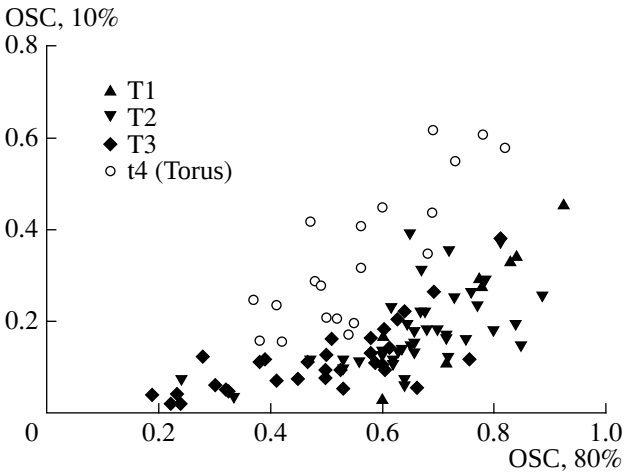

Fig. 4. Relation between the OSCs obtained with 80 and 10% modulated signals for 85 neurons of the cochlear nucleus (the full dots) and 20 neurons of the torus semicircularis (the empty circles). Different kinds of full dots correspond to different groups of the cochlear nucleus neurons classified according to the shape of the PSTHs.

growth of the short-term adaptation manifested itself almost as clearly as in the case of signals with the large modulation depth.

From Fig. 4, one can see the positive correlation between the OSCs obtained for 80 and 10% modulation depths. The correlation coefficient for these values is 0.70 with the following equation of the regression line with zero initial value: OSC(10%) = 0.278 OSC(80%).

On the other hand, the same figure shows that, in the case of the 10% modulation depth, the neurons of the cochlear nucleus exhibit a not too high average strength of the phase locking with the envelope waveform. Of the 89 neurons studied, 66 units had an OSC smaller than 0.2 and 26 units had an OSC smaller than 0.1. Approximately half the neurons (44 of 89) had an unreliable response–envelope phase locking according to the criterion P < 0.001, although, for many of these neurons, the phase locking was reliable according to the criterion P < 0.005.

The phase locking is much weaker than that observed for tonic neurons of the torus semicircularis from the group characterized by a reliable phase locking enhancement from the first to the last modulation period of the tone burst. This is evident from Fig. 4, where the OSC values obtained for 20 typical neurons of the torus that belong to this group are shown by empty circles. In the torus, one also can see a positive correlation between the OSC(80%) and OSC(10%). However, even in the case of equal values of the OSC(80%), the values of the OSC(10%) in the torus are much higher than those in the cochlear nucleus.

For 89 tonic units stimulated by a signal with a small modulation depth, regression lines of the dependence of the PSC on the number of the modulation period were obtained. Figure 5 shows the squared values of the

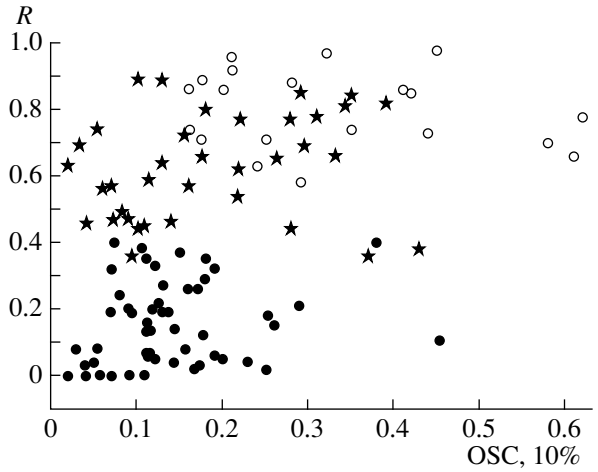

Fig. 5. Relation between the OSCs obtained with 10% modulated signals and the correlation coefficients of the PSCs for 89 neurons of the cochlear nucleus (the full dots) and 20 neurons of the torus semicircularis (the empty circles). The stars show the reliable dependences for the neurons of the cochlear nucleus ($P < 0.001$). All dependences obtained for the neurons of the midbrain are reliable.

correlation coefficients versus the OSC value. The asterisks mark the values (36 of 89) for which the probability of a zero correlation was smaller than 0.005. In all these cases, as well as in all cases when the correlation coefficient exceeded 0.2, the regression line had a positive slope; i.e., the efficiency of the envelope reproduction increased within the stimulus duration. This kind of dependence was observed with almost the same probability for all three groups of tonic neurons. In the neurons of the torus semicircularis, which belonged to the selected group, the correlation was most clearly pronounced (empty circles in Fig. 5).

Unexpectedly, the synchronization enhancement during the signal presentation was observed independently of the value of the OSC. In many cases, this enhancement was reliable even for OSCs smaller than 0.1. Let us consider some specific examples of this kind of neuron behavior. Neuron 11206 stimulated by a tone burst with the 10% modulation depth had an OSC as small as 0.129, although, because of the high mean firing rate and, hence, a large sample volume, this value reliably differed from zero. The significance of individual PSCs, excluding the PSCs obtained for the fifth and tenth periods, was below the chosen criterion. At the same time, the dependence of the PSC on the period number was characterized by a correlation coefficient of 0.64 and was quite reliable (Fig. 6a, diamonds). A similar behavior is characteristic of neuron 10718, for which a reliable phase locking was observed for only the last period.

The fact that the firing of such neurons retains the information on the waveform of the signal envelope is demonstrated by the relative stability of the phases of histograms obtained for sequential modulation periods (Fig. 6b). In the 11206 unit, for all modulation periods starting form the third one, the values of the phase delay were localized within 160°–190°, i.e., close to the phase corresponding to the maximal signal amplitude (remember that the phase was measured beginning from the envelope minimum).

The triangles in Fig. 6a show the results obtained by studying neuron 11207, which had relatively high values of the OSC (0.34) and PSC (see Fig. 6). The response of this neuron, which was ascribed to the T1 group, was illustrated in Fig. 3c. During the signal presentation, the response was relatively weak, so that the PSC, despite its high numerical values, was not reliable because of the small number of pulses in the response to each period. The phase of the response, except for the first period, remained within 120°–165°; i.e., it corresponded to the increase in the signal amplitude from the average value to the maximal one.

Note that, in this neuron, as in some other neurons, the phase delay of the response to the first period was smaller than the phase delays of the responses to other periods. This is caused by the fact that, in the initial part of the response, the effect of the short-term adaptation is strongly pronounced. As a result, the initial part of the period stands out.

Similar data for three other neurons are shown in Figs. 6c (the dependence of the PSC on the period number) and 6d (the dependence of the phase on the period number). Note that, for the 10903, 11209, and 11107 neurons, no reliable dependence of the PSC on the period number was obtained. In addition, almost all values of the PSC statistically did not differ from zero. However, it is evident that the responses of these neurons retain the information on the signal envelope. This is confirmed first of all by the distributions of the values of the phase delay. One can see that most delays are concentrated within the interval 90°–180°; i.e., they again correspond to the phase of the amplitude increase from the average to the maximal value.

For the superior parts of the auditory system to be able to use the information on the temporal envelope of the signal from the firing of the cochlear nucleus neurons, it is necessary to summarize the firing of many neurons. In this case, the phase locking of the responses of different neurons with one signal is necessary. The analysis of the data presented in Fig. 6 shows that the average phase values of the responses of different neurons of the cochlear nucleus are concentrated within 90°–180° with respect to the minimum, i.e., in the interval where the amplitude increases from the average value to the maximal one. However, in determining the phase delay, we performed the subtraction of the latency delays, which could be different for different neurons. Assuming that the travel times of the spikes from the cochlear nucleus neurons under study to the region of the input summation are approximately equal, it is possible to estimate the dynamics of the input effect on the central neuron by the summation of the outputs

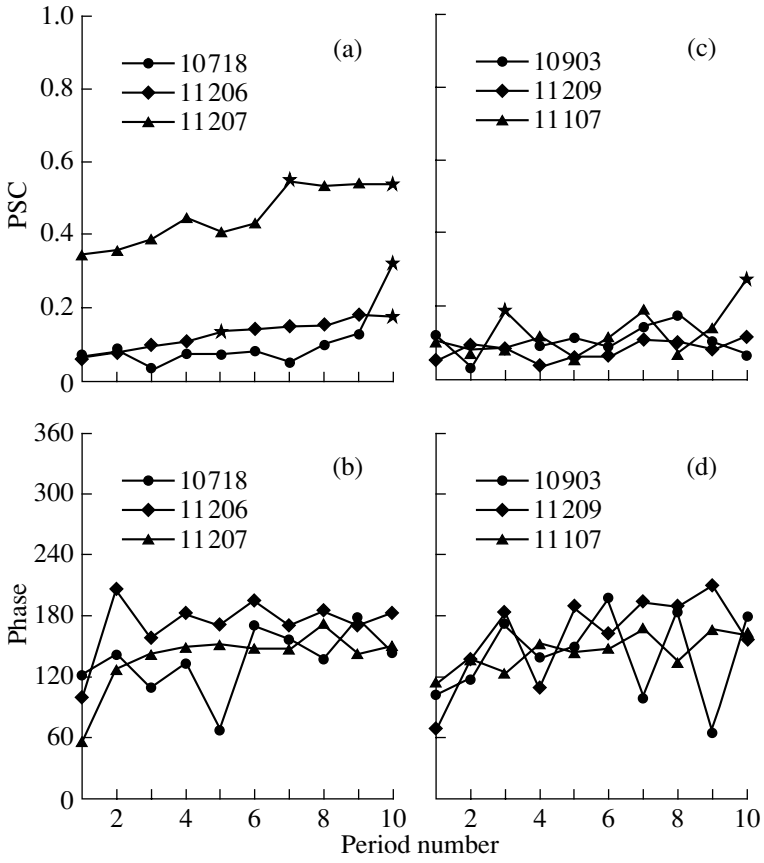

Fig. 6. Dependence of the (a, c) PSC and (b, d) phase of the neural response to individual modulation periods on the number of the modulation period: (a, b) three neurons with a pronounced dependence of the PSC on the period number (10718: T3 group; SF 1.7 kHz; SL 74 dB SPL; 11206: T3 group, SF 0.60 kHz, SL 74 dB SPL; 11207: T1 group, SF 0.61 kHz, SL 74 dB SPL) and (c, d) three neurons with the absence of this dependence (10903: T3 group, SF 1.5 kHz, SL 75 dB SPL; 11209: T2 group, SF 0.58 kHz, SL 56 dB SPL; 11107: T2 group, SF 0.54 kHz, SL 65 dB SPL). The stars show the values of the PSC that reliably differ from zero.

of many cochlear nucleus neurons responding to a single signal. On the basis of the data available, the characterization of the response of the set of the dorsal nucleus neurons to some specific signal is impossible, because, for each neuron, we used a signal with its own optimal frequency. To qualitatively estimate the ability of a set of neurons to reproduce the envelope, the following operation was performed. For 30 neurons that had the characteristic frequencies within 0.55–0.65 kHz, their responses to signals of characteristic frequencies with intensity levels of 65–85 dB were summarized into one PSTH and normalized by dividing the total instantaneous firing rate by the number of neurons.

The results of this summation are shown in Fig. 7a. The resulting PSTH adequately reproduces the signal envelope, although the value of the OSC is as small as 0.108. The dependence of the PSC on the period number has a positive slope and is quite reliable ($P < 0.001$). The phase is retained almost without changes within all nine periods, starting from the second one. The first period is an exception for the reasons indicated above. In the case under consideration, this difference is most pronounced, because the summation also includes the phasic neurons.

On the whole, the resulting distributions of neurons in characteristic frequencies and thresholds agree well with the data obtained for the same anuran species (*Rana temporaria*) from the studies of the auditory nerve fibers [20] and the torus semicircularis [12, 17], as well as the studies of the same brain structure, i.e., the dorsal medullary nucleus [9]. However, in the series of experiments under discussion, we observed a considerable number of neurons tuned to frequencies of 0.5–0.6 kHz and a relatively small number of neurons optimally responding to frequencies above 1.0 kHz. We noticed that, in the experiments carried out in spring, the proportion of neurons tuned to frequencies of 0.5–0.6 kHz was greater than in the experiments carried out in winter. The frequency range 0.5–0.6 kHz corresponds to the main spectral maximum of the mating call of the grass frog. Presumably, our observation relates to the manifestation of the general tendency for the receiving part of the auditory system to adjust to the parameters of the acoustic stimuli that are of vital importance for the animal.

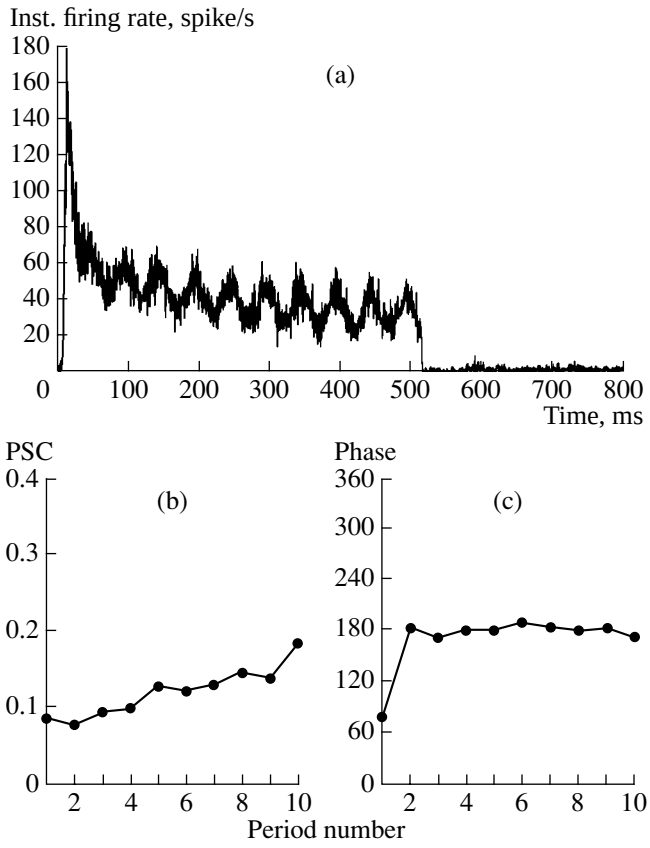

Fig. 7. (a) Normalized PSTH obtained by averaging the responses of 30 neurons to a 10% amplitude modulated signal (the notations are the same as in Fig. 2); (b) dependence of the PSC on the period number for this cooperative histogram; and (c) dependence of the phase of the response on the period number (the notations are the same as in Fig. 6).

The comparison with the data obtained for the cochlear nucleus [18] and torus semicircularis [19] of a lake frog (*Rana ridibunda*) reveals a considerable difference between the species. More than half of the lake frog's neurons had characteristic frequencies higher than 1 kHz, whereas the percentage of such neurons in the grass frog was relatively small.

The distribution of the latency delays of the neural responses of the dorsal nucleus (Fig. 1) agrees well with the data presented for the leopard frog (*Rana pipiens*) [5, 21] and the bullfrog (*Rana catesbeiana*) [22], for which the range of variation of this parameter was 3–25 ms. Some discrepancy is observed for the phasic neuron group, which, according to the data given in [5], is characterized by small latency delays of the response (4–9 ms). However, it should be taken into account that we used tone bursts with a rise time of 5 ms, whereas in the cited experiments [5] the rise time was 1 ms. The delay of the response naturally increases with increasing rise time of the tone burst, and this dependence is most pronounced for the phasic neurons [23]. Moreover, since we calculated the latency delay by adding up the readings of four neighboring histogram segments 0.5 ms wide each, a value of, e.g., 6 ms was ascribed to the responses with the latency delays from 4 to 6 ms.

The classification of the neurons of the cochlear nucleus according to the shape of the PSTHs was performed earlier for the lake frog (*Rana ridibunda*) [18] and the leopard frog (*Rana pipiens*) [5] on the basis of qualitative criteria. In both cases, the principles and the results of the classification approximately agreed with the data reported in this paper. In particular, it was found that, compared to the auditory nerve fiber, the cochlear nucleus produces a new, purely phasic type of response. The lake frog was found to have eight such neurons out of 86 [18], and the leopard frog had 12 out of 98 [5], which agrees well with the results obtained in our experiments (17 out of 133). The relatively small group of neurons with a burst-type discharge observed in the cited experiments did not manifest itself in our experiments with the grass frog. In all species studied, the most typical cells were those with a moderate adaptation feature, which approximately corresponded to the T2 group of our samples.

It is of interest to compare the types of the PSTH obtained for the dorsal nucleus and the auditory nerve. It is well known that, in anurans, even different fibers of the auditory nerve differ in the temporal patterns of their responses to tone bursts [24]. Moreover, in studying the auditory nerve of the leopard frog and the bullfrog [24, 25], 4–5% of neurons were found to exhibit such a strongly pronounced adaptation that, according to our classification scheme, they should be ascribed to the phasic type or the T1 type. However, even in these limiting cases, the responses lasted for no less than 60 ms after the signal onset [25]; i.e., each response presumably consisted of a burst of spikes. In the grass frog, the neurons of this type were characterized by an inhibition of the spontaneous activity [20]. In other experiments [4], no phasic fibers of the auditory nerve were detected. We believe that the purely phasic response, which consists in the generation of one phase-locked spike in response to the tone onset (see Fig. 3d), arises in the auditory system of anurans (as in the auditory systems of other vertebrates) only among the second-order neurons. One can assume that this kind of response occurs in specialized neurons whose function is to determine the instants corresponding to the onset (or an abrupt change in the parameters) of the sound signal [26]. Note that the percentage of phasic units continues to grow in passing to the central parts of the auditory system [19].

The response to signals with a large modulation depth in the neurons of the cochlear nucleus of anurans had been studied earlier by a number of researchers [6, 9, 21, 27]. In these studies, the attention was focused on the derivation of the modulation transfer functions. The analysis of the functions presented in the cited publications shows that almost all tonic neurons efficiently reproduce the 20-Hz modulation frequency [6]. Some neurons with the phasic type of discharge were able to

reproduce high modulation frequencies without responding to signals whose modulation frequencies were 10 or 20 Hz (see Fig. 5a from [6]). This agrees well with the results of our experiments, because among the 133 neurons studied by us, only four units did not reproduce the 80% modulation with a frequency of 20 Hz, and all these units were phasic. As in the auditory system of mammals [28], the low-frequency neurons are able to efficiently reproduce the carrier frequency and the modulation frequency simultaneously (Fig. 2e).

It should be taken into account that, in our experiments, we used only one modulation frequency, so that the phase locking strength can be underestimated with respect to the optimal value. However, note that the frequency 20 Hz is close to the pulse rate of the mating call of the species under study and, for most neurons, it is close to the optimal modulation frequency.

It is possible to perform a direct comparison between the efficiencies of coding in the auditory centers of the medulla oblongata and the midbrain of the grass frog for the envelope of 80% modulated tone bursts with the aforementioned modulation frequency. In response to such tone bursts, 46% of the neurons of the torus semicircularis are characterized by the OSCs greater than 0.5, and 7.5% of neurons, by the OSCs greater than 0.9 [12]. Data close to these were obtained by other authors for the same species [27] and for other anuran species [6].

The results of this study show that, in the case of stimuli with high modulation indices, the average values of the OSC in the medulla oblongata are no smaller (or greater) than in the midbrain, because PSCs exceeding 0.5 were observed for 70% of neurons, and PSCs exceeding 0.9, for 11%. In our opinion, this fact does not testify that the modulation reproduction in the midbrain is inferior to that in the medulla oblongata, but it indicates that new types of neurons specializing in the perception of sound parameters other than amplitude modulation appear in the midbrain. In addition, it should be noted that the total number of neurons in the auditory center of the midbrain is approximately an order of magnitude greater than the number of neurons in the cochlear nucleus. As a result, in the midbrain, the total number of neurons that adequately reproduce the 80% modulation should be greater.

In both peripheral (this study) and central [12] parts of the auditory system of anurans, neurons with OSCs exceeding 0.9 were usually characterized by phasic responses to pure tone bursts. Moreover, a general tendency was observed for an increase in the OSC with increasing short-term adaptation to the tone burst stimulation. For neurons of the cochlear nucleus, this relation seems to be universal, because, in mammals, a high-index modulation is best reproduced by just the phasic neurons of the cochlear nucleus [29].

As for tone bursts with small modulation depths, the coding of their amplitude modulation by the neurons of the cochlear nucleus of anurans is poorly understood. A monotone decrease in the PSC with decreasing modulation index was revealed in [6].

In our experiments, we observed no phasic units reproducing the 10% modulation. Thus, the widely accepted concept that phasic neurons provide a better reproduction of the signal envelope should be reconsidered. In fact, phasic units generate a phase-locked discharge when they are stimulated with signals with a large modulation depth. On the other hand, they are usually incapable of reproducing small amplitude variations, at least at low modulation frequencies. This conclusion generally agrees with the results obtained for the auditory center of the midbrain of the same object [12], although, for several phasic neurons of the midbrain, we observed phase-locked responses for the last modulation periods of a 612.5-ms-long tone burst (see Fig. 5a from [12]). A similar effect was described for the neurons of the midbrain of a bullfrog [30]. We believe that, in our experiments, the absence of such neurons in the medulla oblongata is not determined by the sampling limitation. Presumably, the formation of such specialized responses occurs only in the central structures of the brain.

The main purpose of this study was the investigation of the improvement in the phase locking of the neural response with small variations of the signal amplitude during a tone burst presentation. This effect was described by us in detail for the midbrain neurons, and now it was also observed in the medulla oblongata. Almost half of the neurons exhibited a reliable positive correlation of the PSC with the period number. However, the degree of this correlation was found to be much lower than in the case of the specialized neurons of the midbrain. In addition, the phase locking of the response achieved for the last signal modulation periods in the medulla oblongata was weaker than the corresponding phase locking in the midbrain. Thus, it is evident that the improvement of the discrimination of small amplitude variations in the process of adaptation manifests itself already at the periphery of the auditory system and becomes more pronounced in the specialized neurons of the central parts of the brain. The potential possibility of such an improvement is determined by a synchronous firing of the set of neurons of the medulla oblongata (Fig. 7). It is of interest to perform a similar analysis of the response of a set of neurons to a single signal (or to close signals) for other parts of the auditory system.

In our experiments, many parameters of the input signal were fixed. The carrier frequency was always equal to the characteristic frequency of the neuron, the modulation frequency was 20 Hz, and the mean sound level was about 20–30 dB above the response threshold. Evidently, it is of interest to find out how the OSC value and the effect of phase locking improvement with time depend on these parameters. Preliminary data show that, in both medulla oblongata and midbrain [12], the

aforementioned effect is retained in a wide range of signal levels and for different carrier frequencies.

A question arises as to whether the effect under discussion is universal for the auditory systems of other anuran species and for other vertebrate classes. Despite the fact that no detailed description of such an effect could be found by us in other authors' publications, the analysis of some of the experimental data reported in the literature testifies to the generality of this effect. For example, it is quite noticeable in one of the histograms illustrating the response of the neurons of the cochlear nucleus of a leopard frog to a tone burst with a modulation frequency of 50 Hz and a 10% modulation depth (see Fig. 8d in [6]). There also are some interesting results indicating that the sensitivity to amplitude variations can improve during the stimulus presentation in the auditory system of mammals. The effect is not observed in the PSTHs obtained for the neurons of the auditory nerve fiber of a guinea pig (Fig. 10 from [31]), but it is visible in the PSTHs obtained for the tonic neurons of the cochlear nucleus of a cat (Figs. 22 and 23 from [29]). In the midbrain of rats [32], as well as in the midbrain of anurans [12, 30], extreme manifestations of the effect were observed: the phasic neurons began reproducing the signal modulation some time after the stimulus onset. Finally, an increase with time in the efficiency of the coding of small amplitude variations manifests itself in psychophysical experiments [33–35].

It should be noted that in our experiments we studied only the initial stage of the adaptation process, namely, the first ten modulation periods. At this stage, the maximal values of the PSC were observed for the last periods (Fig. 6a), and the function displayed no saturation. Many indirect data testify that, in the medulla oblongata, as well as in the midbrain [13], the phase locking of the response can continue to improve for many seconds. This is confirmed by the fact that the synchronization coefficients obtained for 10% modulation in the full adaptation conditions [7] were on the average about 0.3–0.6, i.e., considerably greater than the PSCs recorded in our study even for the last periods of a tone burst. It appears that the phase locking enhancement in the course of the long-term adaptation in the medulla oblongata manifests itself as clearly as in the midbrain. It is of interest to perform a quantitative study of the dynamics of the coding of small amplitude variations in the course of the long-term adaptation for the neurons of the medulla oblongata.

The specific mechanism (or mechanisms) responsible for the phase locking improvement during the initial stage (the first second) and the following adaptation process is still poorly understood. Most likely, in the course of the adaptation, the level of the synaptic effect gradually adjusts to the level corresponding to the spike generation threshold. This self-adjustment can be determined by the internal properties of the neuron. A highly probable mechanism responsible for the improvement of the reproduction of small amplitude variations during the stimulus presentation is the calcium-dependent potassium conductance. Such channels were revealed in many elements of the auditory system, from the hair cells of the turtle cochlea [36] to the pyramidal neurons of the human cerebral cortex [37]. Model studies of these channels [38] showed that their functioning leads to an exponential decrease in the instantaneous firing rate with a time constant varying for different neurons as a function of the rate of secondary calcium release from the intracellular sources. However, the most typical values of the time constants are within several tens or hundreds of milliseconds [38], which agrees well with our observations. The calcium-dependent sodium current must lead to a hyperpolarization shift of the membrane potential, i.e., to a displacement of the mean level of the input signal relative to the threshold level of spike generation. As a result, when intense stimuli are presented, the input signal approaches the threshold level and, hence, small variations of the intense signal are more clearly discriminated.

An attractive possibility to explain the slow adjustment of the level of the synaptic effect appears in connection with the plastic rearrangement of synapses, which had been recently observed in neural networks [39]. According to these data, many neurons exhibit a feedback between the efficiency of the synaptic input and the firing activity at the output. With the appearance of the exciting synaptic potential immediately before the pulse generation, the efficiency of the given input increases (this well-known hypothesis was formulated by Hebb [40]), but with the appearance of the input after the output pulse, the efficiency of the input decreases. The effect of the input reduction is somewhat more pronounced than the positive feedback. As a result, in the presence of a strong synaptic effect, its level gradually adjusts to the spike generation threshold, thus providing an efficient reproduction of small variations in the input signal. Other possible mechanisms include the interaction of the exciting synaptic inputs with the delayed inhibitions [41] or a gradual increase in the spike generation threshold.

Thus, we arrive at the following conclusions. The second-order neurons located in the dorsal (cochlear) nucleus of the medulla oblongata of a grass frog distinctly reproduce the 80% amplitude modulation of tone bursts containing ten modulation periods when the modulation frequency is 20 Hz. The reproduction of the 10% modulation is, on the average, rather weak and manifests itself only in the response averaged over tens of presentations. The analysis of such average responses in the form of peri-stimulus time histograms reveals the tendency for an enhancement of the phase locking of the response in the course of the adaptation, from the first modulation period to the last one. Although this effect is reliable, it is less pronounced in the case under study than in the specialized group of neurons occupying a more central position [12].

There are reasons to believe that, in a real situation of a single presentation, the summation over sequential stimulus presentations, which has been artificially used in constructing the PSTHs, can be replaced by the summation over the inputs from many peripheral neurons. This is confirmed by the relative closeness of the phase delays of the responses of different neurons (Fig. 6), as well as by the results of the model summation of neural firing in response to the signals in relatively narrow frequency and intensity ranges (Fig. 7).

ACKNOWLEDGMENTS

All computer programs for recording and processing the experimental data were developed by S.V. Nizamov. The work was supported by the Russian Foundation for Basic Research, project nos. 99-04-49110 and 02-04-48236.

REFERENCES

1. W. Walkowiak and J. Brzoska, Behav. Ecol. Sociobiol. **11**, 247 (1982).
2. B. Diekampf and H. C. Gerhard, J. Comp. Physiol. A **177**, 173 (1995).
3. G. J. Rose and R. R. Capranica, J. Neurophysiol. **53**, 446 (1985).
4. A. S. Feng, J. C. Hall, and S. Siddique, J. Neurophysiol. **65**, 424 (1991).
5. J. C. Hall and A. S. Feng, J. Neurophysiol. **64**, 1460 (1990).
6. A. S. Feng and W. Y. Lin, J. Neurophysiol. **72**, 2209 (1994).
7. O. N. Gorodetskaya and N. G. Bibikov, Neĭrofiziologiya **17**, 390 (1985).
8. N. G. Bibikov, Sens. Sist. **1**, 353 (1987).
9. I. H. M. van Stokkum, Hear. Res. **29**, 223 (1987).
10. W. J. M. Epping, Hear. Res. **45**, 1 (1990).
11. G. J. Rose and R. R. Capranica, J. Comp. Physiol. A **154**, 211 (1984).
12. N. G. Bibikov and S. V. Nizamov, Hear. Res. **101**, 23 (1996).
13. N. G. Bibikov and O. N. Grubnik, Sens. Sist. **10**, 5 (1996).
14. H. M. Kaplan, Fed. Am. Soc. Exp. Biol., Fed. Proc. **28**, 1541 (1969).
15. J. M. Goldberg and P. B. Brown, J. Neurophysiol. **32**, 613 (1969).
16. E. Batschelet, *Circular Statistics in Biology* (Academic, London, 1981).
17. N. G. Bibikov, Zh. Évol. Biokhim. Fiziol. **10**, 40 (1974).
18. N. G. Bibikov and T. V. Kalinkina, Zh. Évol. Biokhim. Fiziol. **18**, 491 (1982).
19. N. G. Bibikov, Akust. Zh. **16**, 199 (1970) [Sov. Phys. Acoust. **16**, 168 (1970)].
20. J. Christensen-Dalsgaard, M. B. Jorgensen, and M. Kannewor, Hear. Res. **119**, 155 (1998).
21. J. C. Hall and A. S. Feng, J. Neurophysiol. **66**, 955 (1991).
22. A. S. Feng and R. R. Capranica, J. Neurophysiol. **39**, 871 (1976).
23. J. C. Hall and A. S. Feng, Hear. Res. **36**, 261 (1988).
24. A. L. Megela, J. Acoust. Soc. Am. **75**, 1155 (1984).
25. A. L. Megela and R. R. Capranica, J. Neurophysiol. **46**, 465 (1981).
26. D. Oertel, Annu. Rev. Physiol. **61**, 497 (1999).
27. W. Walkowiak, J. Comp. Physiol. A **155**, 57 (1984).
28. P. X. Joris and T. C. Yin, J. Acoust. Soc. Am. **91**, 215 (1992).
29. R. D. Frisina, R. L. Smith, and S. C. Chamberlain, Hear. Res. **44**, 99 (1990).
30. T. B. Alder and G. J. Rose, Nat. Neurosci. **1**, 519 (1998).
31. N. P. Cooper, D. Robertson, and G. K. Yates, J. Neurophysiol. **70**, 370 (1993).
32. A. Rees and A. R. Palmer, J. Acoust. Soc. Am. **85**, 1978 (1989).
33. N. F. Viemeister and S. P. Bacon, J. Acoust. Soc. Am. **84**, 172 (1988).
34. N. G. Bibikov and I. P. Makeeva, Akust. Zh. **35**, 1004 (1989) [Sov. Phys. Acoust. **35**, 585 (1989)].
35. G. Canevet, B. Scharf, and L. M. Ward, Acustica **74**, 69 (1991).
36. E. M. Jones, M. Gray-Keller, and R. Fettiplace, J. Physiol. (London) **518**, 653 (1999).
37. D. D. McCormick and A. Williamson, Proc. Natl. Acad. Sci. USA **86**, 8098 (1989).
38. X. J. Wang, J. Neurophysiol. **79**, 1549 (1998).
39. S. J. Martin, R. D. Grimwood, and R. G. Morris, Annu. Rev. Neurosci. **23**, 649 (2000).
40. D. O. Hebb, *The Organization of Behavior. A Neuropsychological Theory* (Wiley, New York, 1949).
41. N. G. Bibikov, J. Phys. (Paris) **4**, 233 (1992).

Translated by E. Golyamina

Acoustical Physics, Vol. 48, No. 4, 2002, pp. 400–405. Translated from Akusticheskiĭ Zhurnal, Vol. 48, No. 4, 2002, pp. 461–466.

Interference Acoustooptic Technique for Sound Velocity Measurements

S. V. Bogdanov

Institute of Semiconductor Physics, Siberian Division, Russian Academy of Sciences, pr. Akademika Lavrent'eva 13, Novosibirsk, 630090 Russia

e-mail: bogd@isp.nsc.ru

Received January 22, 2001

Abstract—The effect of an acoustic link between a buffer and a solid sample on the accuracy of the sound velocity measurements in the sample by interference techniques and, in particular, the interference acoustooptic technique [11] is considered. The phase difference between the waves going out of the sample and reflected from it, which is introduced by the acoustic link, is determined. It is demonstrated that, in the range of link thicknesses $0.1 \le h \le 1.0$ μm, the correction to the sound velocity depends little on the link thickness. A procedure that allows one to determine this correction and the actual sound velocity in each specific case is proposed.

The velocity of sound propagation is important both by itself and as an instrument for investigating various properties of materials, such as elastic properties, piezoelectricity, phase transitions, and many other phenomena [1–5]. Various techniques (including high-precision ones) adapted to different specific conditions had been developed for sound velocity measurements [6–10]. The requirements on the accuracy of its determination are now becoming more stringent. Recently, a new, relatively simple technique was proposed for the sound velocity measurements in solids (both isotropic and anisotropic) [11]. This technique can be readily automated. The technique is based on the observation of interference of two sound waves: the wave reflected from the front face of a sample and the wave transmitted through the sample, reflected from its rear face, and going out of it. The medium where the interfering waves propagate is a solid isotropic buffer made of an optically transparent material. A thin laser beam is transmitted through the buffer across the direction of sound propagation, and its diffraction by the interfering waves is observed. As the frequency of sound varies, the phase shift between these waves also varies, and the interference maxima and minima of the resulting wave are detected by the corresponding maxima and minima of the intensity of diffracted light. Since the intensity of diffracted light is proportional to the square of the amplitude of the resulting sound wave, the observed light maxima turn out to be much sharper than the sound maxima. This noticeably increases the accuracy of the proposed technique.

A measuring cell consists of a transducer, a buffer, a sample, and a common support shaped as a frame. Acoustic links are introduced between the transducer and the buffer and between the buffer and the sample. We ignored the link influence on the phase shift between the waves propagating in the system [11]. The following pulses resulting from successive reflections are observed in the buffer when a single high-frequency pulse is fed to the transducer: the pulse incident from the transducer U_1; the pulse reflected from the front face of the sample U_2; the pulse that entered the sample, was reflected from its rear face, and returned into the buffer U_3; and a series of pulses U_4, U_5, … transmitted through the sample several times due to multiple reflections. The carrier of all these pulses has the same frequency, wavelength, and polarization. The pulses will interfere in the case of overlapping. The interference of the pulses U_2 and U_3 was studied in [11]. It was demonstrated that, when the acoustic link is ignored, the formula for the determination of the sound velocity is very simple:

$$V = \frac{2L\Delta f}{N}, \tag{1}$$

where V is the sound velocity, L is the sample length, Δf is the frequency interval within which the interference maxima (or minima) are observed, and N is their number.

In our previous paper [11], we did not analyze what thickness of the acoustic link h should be considered as small and what is the error introduced by it, although it is clear that such an error must exist, because the pulses U_2 and U_3 travel different distances in the acoustic link. Naturally, it is necessary to take the acoustic link into account in the case of high-precision measurements.

In this paper, we take into account the presence of an acoustic link between the buffer and the sample. However, we still assume it to be sufficiently thin (the corresponding criterion is given below). There is no need to take into account the presence of an acoustic link

1063-7710/02/4804-0400$22.00

between the transducer and the buffer, because it affects only the parameters of the radiated pulse and does not affect the process of further reasoning.

Let us consider the interference of the high-frequency carrier of the pulses U_2 and U_3 by assuming that they propagate perpendicularly to the interfaces. We assign the following indices to the quantities belonging to the adjacent media: index 1 to the buffer, index 2 to the acoustic link, and index 3 to the sample. Let us introduce the notations: V_1 is the sound velocity in the buffer, $k_1 = \omega/V_1$ is the wave number, l is the buffer length, V_2 is the sound velocity in the acoustic link, $k_2 = \omega/V_2$ is the wave number, h is the thickness of the acoustic link, V_3 is the sound velocity in the sample, $k_3 = \omega/V_3$ is the wave number, and L is the sample length.

Let us denote the phase shift of the high-frequency carrier of the pulse U_3 relative to U_2 by $\Delta\Phi_{32}$. It is the sum of the phase shift produced by the sample, $2k_3L$, and the phase produced by the presence of the acoustic link, $\alpha = \alpha(f, h)$. Thus, at a constant link thickness, we have $\Delta\Phi_{32} = 2k_3L + \alpha(f)$.

As the frequency varies, $\Delta\Phi_{32}$ sequentially takes on the values $\Delta\Phi_{32} = 2n\pi$ and $(2n + 1)\pi$; i.e., U_2 and U_3 are either in phase or in antiphase, and therefore, a beating of the summary signal amplitude A is observed. Correspondingly, the intensity beating of diffracted light is observed as well.

Let the nth maximum of the diffracted light intensity be observed at the frequency f_1 at the preset link thickness h, i.e.,

$$2\pi f_1\left(\frac{2L}{V_3}\right) + \alpha(f_1) = 2\pi n,$$

and a certain mth maximum, where $m = (n + N)$, at the frequency f_2:

$$2\pi f_2\left(\frac{2L}{V_3}\right) + \alpha(f_2) = 2\pi(n + N).$$

Thus, $N = m - n$ maxima are observed as the frequency varies within $\Delta f = f_2 - f_1$. We obtain

$$2\pi N = 2\pi\left(\frac{2L}{V_3}\right)\Delta f + \Delta\alpha,$$

where $\Delta\alpha = \alpha(f_2) - \alpha(f_1)$.

This yields the expressions

$$V_3 = \frac{2L\Delta f}{N - \dfrac{\Delta\alpha}{2\pi}} \quad (2a)$$

or

$$V_3 = \frac{2L\Delta f}{N}\left(1 + \frac{\Delta\alpha}{2\pi N}\right). \quad (2b)$$

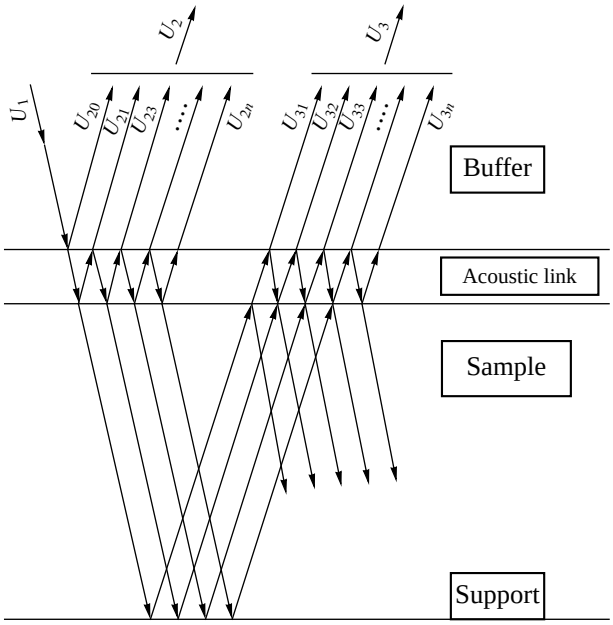

Fig. 1. Schematic diagram of the set of waves propagating in the buffer–acoustic link–sample–support system: U_1, U_2, and U_3 are the incident, reflected, and outcoming waves, respectively.

The relative error is equal to $\Delta V_3/V_3 = \Delta\alpha/(2\pi N + \Delta\alpha)$.

If $\Delta\alpha > 0$, the presence of an acoustic link leads to an underestimated value of V_3 calculated by Eq. (1) in comparison with the true value. To determine V_3 in the presence of an acoustic link, it is necessary to know $\Delta\alpha \equiv \Delta\alpha(f_1, f_2, h)$.

To determine α and, then, $\Delta\alpha$ as functions of frequency, thickness h, and properties of the acoustic link itself, one has to solve the problem by taking into account an additional layer (with the thickness h) between the buffer and the sample. The pattern of the waves propagating in the system is given schematically in Fig. 1, where the incidence angle is taken as nonzero and the refraction at passage from one medium to another is ignored for the sake of illustration. The lines with arrows in Fig. 1 show the waves propagating in the system that are produced by a single incident wave U_1 as a result of multiple reflections. The waves U_2 and U_3, which we are interested in, result from the summation of the corresponding partial waves. Below, we will assume that the problem under consideration is stationary. This allows us to ignore the time problem. The last is possible if the incident pulse is longer than the setting time of the stationary state τ_s, which can be represented in the form $\tau_s = m2h/V_2$. Here, m is the numerical factor about 20–30. If, in addition, the double time of wave propagation along the sample (forward and backward) $\tau_o = 2L/V_3$ is greater than τ_s, the problem can be divided into two independent ones: (a) the wave transmission from the buffer through the link into the sample (see Fig. 2a) and (b) the wave transmission from the sample

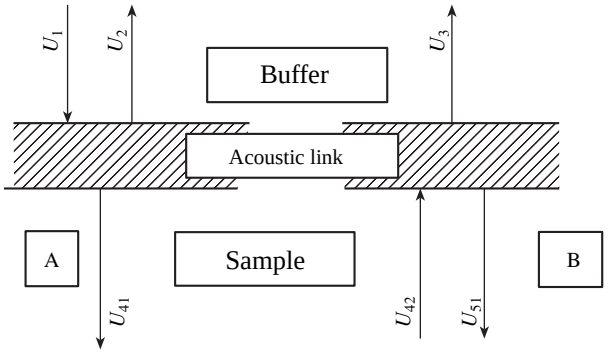

Fig. 2. Schematic diagram of stationary waves propagating in the system: part A is for the buffer–acoustic link–sample direction and part B is for the sample–acoustic link–buffer direction; U_1, U_2, and U_3 are the incident, reflected, and outcoming waves, respectively.

through the link into the buffer (see Fig. 2b). This provides an opportunity not to solve the problem of wave transmission in the buffer–link–sample–link–buffer system and use a known solution for the wave transmission through a layer (see, e.g., [12]). The latter condition ($\tau_o \gg \tau_s$) imposes a limitation on the admissible thickness of the link: $h \ll LV_2/mV_3$. The waves in the buffer U_1, U_2, U_3, … are denoted by single indices in compliance with the notation introduced in [11]. The waves in the sample have double indices: U_{41}, U_{42}, U_{51}, …, which can be understood from Fig. 2. The waves shown in Fig. 2 are the sum of the corresponding partial waves.

Further, we will need the following:

—the amplitude coefficient of reflection from the interface of the media "*i*" and "*k*" (in the case of a normal incidence) $R_{ik} = \dfrac{Z_i - Z_k}{Z_i + Z_k}$—a wave is incident from the medium "*i*" and reflected back to the medium "*i*";

—the amplitude coefficient of transmission through the interface of the media "*i*" and "*k*" (in the case of a normal incidence) $T_{ik} = \dfrac{2Z_i}{Z_i + Z_k}$—a wave is incident from the medium "*i*" and transmitted to the medium "*k*."

Here, $Z_i = \rho_i V_i$ is the acoustic impedance of the medium "*i*," ρ_i is the density, and V_i is the sound velocity in the medium "*i*."

For the case given in Fig. 2a, the coefficients of reflection from a layer R and transmission T_{13} have the form

$$R = \frac{R_{12} + R_{23}\exp(-j2k_2h)}{1 + R_{12}R_{23}\exp(-j2k_2h)};$$

$$T_{13} = \frac{T_{12}T_{23}\exp(-jk_2h)}{1 + R_{12}R_{23}\exp(-j2k_2h)}.$$

Thus, $U_2 = RU_1$ and $U_{41} = T_{13}U_1$. In the case shown in Fig. 2b, we consider only the outgoing wave U_3. To determine this wave, we take into account the fact that the wave U_{41} is transmitted through the sample, reflected from the rear face of the sample, transmitted through the sample again, and arrives at the acoustic link with the phase shift $2Lk_3$. Thus, we have $U_{42} = R_{34}U_{41}\exp(-2k_3L)$ or $U_{42} = R_{34}T_{13}U_1\exp(-2k_3L)$. Here, R_{34} is the coefficient of reflection from the support. In our case, $R_{34} = 1$ (reflection from an air gap) and $U_{42} = T_{13}U_1\exp(-2k_3L)$. It is easy to show that the coefficient of transmission through the layer in the direction from the sample is $T_{31} = T_{13}(Z_3/Z_1)$. Taking this into account, we have for the outgoing wave U_3

$$U_3 = (Z_3/Z_1)T_{13}^2U_1\exp(-2k_3L).$$

We introduce the notations $2k_2h \equiv x$, $2k_3L \equiv y$, and $T \equiv (Z_3/Z_1)T_{13}^2\exp(-y)$. In this case, $U_3 = TU_1$.

Let us reduce R and T to the forms

$R = \mathrm{Re}(R) - j\,\mathrm{Im}(R)$ and $T = \mathrm{Re}(T) - j\,\mathrm{Im}(T)$, where

$$\mathrm{Re}(R) = \frac{R_{12}(1 + R_{23}^2) + R_{23}(1 + R_{12}^2)\cos(x)}{1 + R_{12}^2R_{23}^2 + 2R_{12}R_{23}\cos(x)}, \tag{3a}$$

$$\mathrm{Im}(R) = \frac{R_{23}(1 - R_{12}^2)\sin(x)}{1 + R_{12}^2R_{23}^2 + 2R_{12}R_{23}\cos(x)}, \tag{3b}$$

$$\mathrm{Re}(T) = \frac{Z_3T_{12}^2T_{23}^2[2R_{12}R_{23}\cos(y) + \cos(y + x) + R_{12}^2R_{23}^2\cos(y - x)]}{Z_1[1 + R_{12}^2R_{23}^2 + 2R_{12}R_{23}\cos(x)]^2}, \tag{3c}$$

$$\mathrm{Im}(T) = \frac{Z_3T_{12}^2T_{23}^2[2R_{12}R_{23}\sin(y) + \sin(y + x) + R_{12}^2R_{23}^2\sin(y - x)]}{Z_1[1 + R_{12}^2R_{23}^2 + 2R_{12}R_{23}\cos(x)]^2}. \tag{3d}$$

In the case of an overlapping of the pulses $U_2 = RU_1$ and $U_3 = TU_1$, the latter interfere, forming the summary wave U_{23}. Its amplitude A is equal to

$$A = A_1\sqrt{|R|^2 + |T|^2 + 2[\mathrm{Re}(R)\mathrm{Re}(T) + \mathrm{Im}(R)\mathrm{Im}(T)]}. \quad (4)$$

Here, A_1 is the amplitude of the incident wave U_1, which we take equal to unity, and $|\ldots|$ are the absolute values of R and T.

We note that

$$\left[\frac{\mathrm{Re}(R)\mathrm{Re}(T) + \mathrm{Im}(R)\mathrm{Im}(T)}{|R||T|}\right] = \cos(\phi_T - \phi_R) = \cos(\Delta\Phi_{32}).$$

Recall that the phase difference $\Delta\Phi_{32}$ (i.e., the phase difference between the outgoing and reflected waves, U_3 and U_2) is caused by the presence of the sample ($2Lk_3$) and the presence of the acoustic link [$\alpha(f, h)$]. Thus, we have

$$\Delta\Phi_{32} = 2Lk_3 + \alpha(f, h) = \arccos\left[\frac{\mathrm{Re}(R)\mathrm{Re}(T) + \mathrm{Im}(R)\mathrm{Im}(T)}{|R||T|}\right].$$

To determine $\alpha(f, h)$, it is necessary to take $L = 0$. In this case, we obtain

$$\alpha(f, h) = \arccos\left[\frac{\mathrm{Re}(R)\mathrm{Re}(T) + \mathrm{Im}(R)\mathrm{Im}(T)}{|R||T|}\right]_{L=0}. \quad (5)$$

Essentially, Eq. (5) is the solution to the problem under consideration: at the preset parameters of the system, it is necessary to calculate α at two limiting frequencies f_1 and f_2 of the frequency range in use, to determine $\Delta\alpha = \alpha(f_2) - \alpha(f_1)$, and, then, to determine the exact value of the velocity in the sample according to Eq. (2).

Regretfully, there are two difficulties with this algorithm: first, the exact value of the sound velocity in the sample is unknown and, second, the thickness of the acoustic link h is unknown. However, both these difficulties can be avoided if we use the method of successive approximations and approximate the value of the link thickness obtained either from the interference colors of a thin film or from the experimental dependence $R = R(f)$. The value of h can be determined from the comparison of the measured curve $R = R(f)$ with the calculated curve $R = R(f, h)$, where h plays the role of a parameter (see Fig. 3).

The procedure of calculation is best understood from a specific example. Let us consider the determination of the sound velocity in a typical situation of longitudinal waves and a liquid link.

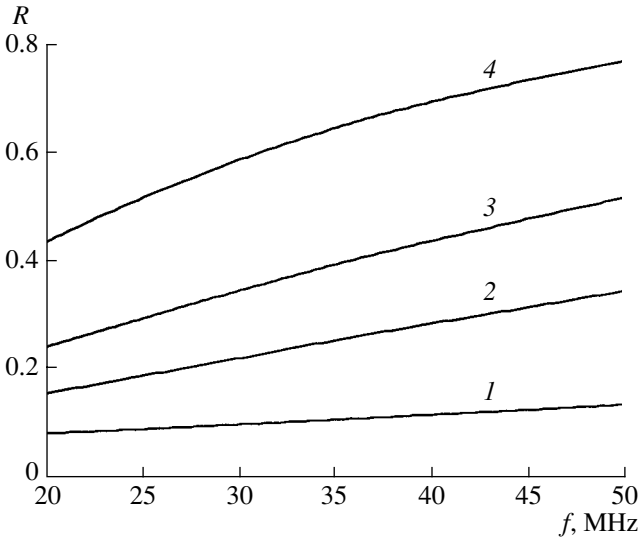

Fig. 3. Dependence of the absolute value of the reflection coefficient R on frequency for the link thickness h = (*1*) 0.1, (*2*) 0.3, (*3*) 0.5, and (*4*) 1.0 μm.

The following parameters of the system are preset:

(1) the buffer (F-4 optical glass): $\rho_1 = 3.67 \times 10^3$ kg/m^3 and $V_1 = 4.1 \times 10^3$ m/s;

(2) the acoustic link (transformer oil): $\rho_2 = 0.897 \times 10^3$ kg/m^3, $V_2 = 1.425 \times 10^3$ m/s, and $h = 0.2 \times 10^{-6}$ m;

(3) the sample (fused quartz): $\rho_3 = 2.2 \times 10^3$ kg/m^3, $V_3 = 5.960 \times 10^3$ m/s, and $L = 10^{-2}$ m.

The following parameters are determined experimentally: $f_1 = 20.214 \times 10^6$ Hz, $f_2 = 49.991 \times 10^6$ Hz, the beating number $N = 100$, and the approximate value of the link thickness $h \simeq 0.3 \times 10^{-6}$ m.

In the computer simulation, we assume that the range of possible link thickness values is $h = (0.05–1.0) \times 10^{-6}$ m, which certainly overlaps its possible value, and consider the frequency range from $f_{10} = 20 \times 10^6$ Hz to $f_{20} = 50 \times 10^6$ Hz, which slightly exceeds the one used in reality.

Let us evaluate the applicability conditions of the stationary wave approximation by taking $m = 30$. This condition is valid when the film thickness is $h \ll V_2L/V_3m \simeq 80$ μm. Thus, even the thickest acoustic link with $h = 1$ μm satisfies the stationary condition to a high accuracy. As a result, the following procedure for calculating the sound velocity is established:

(1) The determination of the velocity $V_3 = V_3(0)$ in the zero approximation. Here and further, the number in parentheses denotes the order of approximation. We calculate the sound velocity $V_3 = V_3(0)$ according to Eq. (1). In our case, $V_3(0) = 5955$ m/s. (The velocity is rounded off to the integral value corresponding to the real accuracy of measurements.)

(2) The determination of the velocity $V_3(1)$ in the first approximation. Taking $Z_3 = \rho_3 V_3(0) = Z_3(0)$ and the link thickness $h = h(1) = 0.3 \times 10^{-6}$ m, we calculate

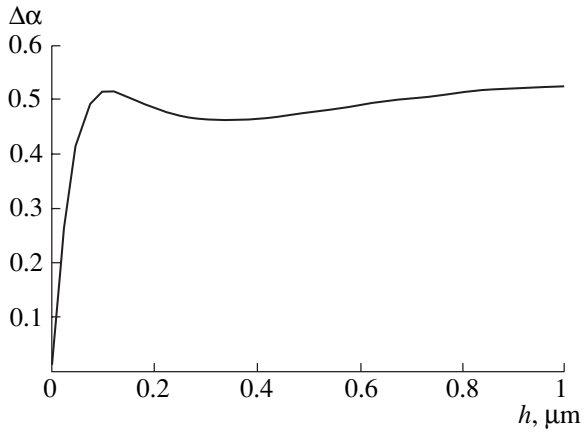

Fig. 4. Dependence of the difference $\Delta\alpha(f_1, f_2, h)$ on the thickness of the acoustic link for V_3 = 5960 m/s, f_{10} = 20 MHz, and f_{20} = 50 MHz.

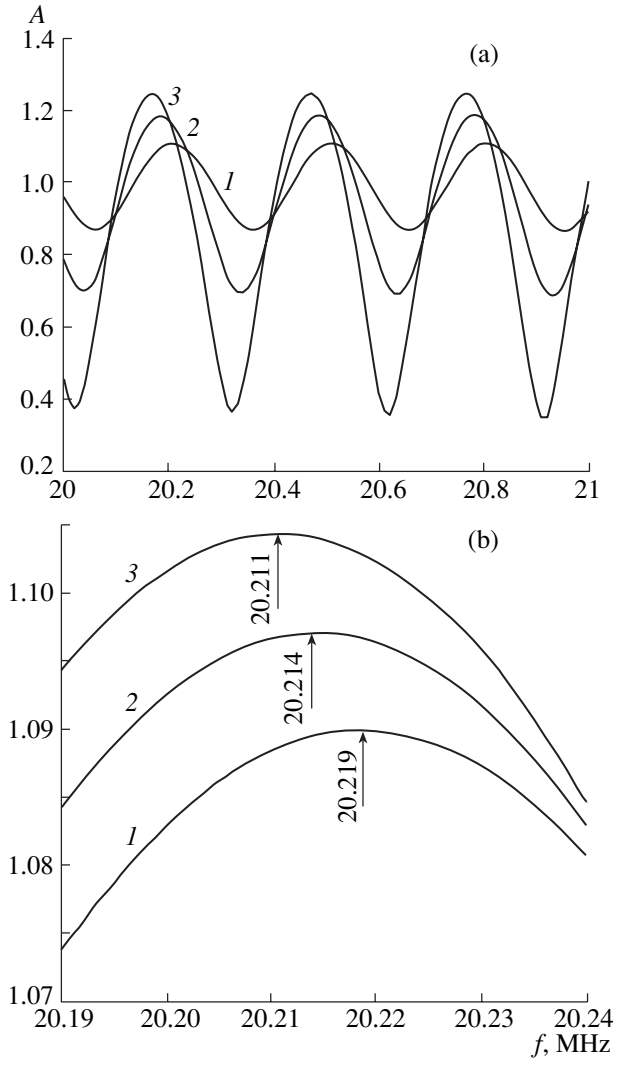

Fig. 5. Dependence of the amplitude A of the summary wave U_{23} on frequency for the velocity V_3 = (a) 5960 and (b) 5959 m/s and for the following values of the thickness of the acoustic link: (a) h = (*1*) 0.1, (*2*) 0.5, and (*3*) 1.0 μm; (b) h = (*1*) 0.15, (*2*) 0.175, and (*3*) 0.2 μm.

$\alpha_1(1)$ and $\alpha_2(1)$ according to Eq. (5) for the frequencies f_1 and f_2 and determine $\Delta\alpha(1)$. Then, we calculate the value of $V_3(1)$ according to Eq. (2). In our case, we obtain $\Delta\alpha(1) = 0.458$ and $V_3(1) = 5959$ m/s. As one can see, $V_3(1)$ differs little from the preset V_3. This can be explained by the weak dependence of $\Delta\alpha$ on the link thickness in the thickness range in use (see Fig. 4). If there is no need for higher accuracy, the calculation may be limited to the determination of $V_3(1)$.

(3) The refinement of the link thickness. For this purpose, we use the dependence $A = A(f, h)$ calculated by Eq. (4). The general form of this dependence for our system in the frequency range with f_{10} = 20 MHz and f_{20} = 21 MHz is presented in Fig. 5a for three values of h. The beating in the system is clearly pronounced. The beating amplitude strongly depends on the link thickness. The frequency at which the maximal amplitude A is observed also depends on the link thickness, and, the greater the link thickness, the lower the frequency corresponding to the maximum. At the same time, the distance between the neighboring maxima almost does not depend on the link thickness. The high accuracy in the determination of the frequencies f_1 and f_2 provides a good resolution of $A = A(f, h)$ with respect to the link thickness. Hence, this dependence can be used to refine the value of h.

For this purpose, at $V_3 = V_3(1)$, we determine a series of functions $A = A(f, h)$ in the vicinity of the frequency f_1 (the first maximum) according to Eq. (4). We select $h = h(2)$, at which the frequency of the maximal amplitude A coincides with the experimentally determined f_1 (see Fig. 5b). In our case, $h(2) = 0.175 \times 10^{-6}$ m.

(4) The determination of $V_3(2)$.

We repeat step 2 described above by using $V_3 = V_3(1)$ and $h = h(2)$. In our case, we obtain $\Delta\alpha = 0.516$ and $V_3(2) \cong 5960$ m/s.

(5) The determination of $h = h(3)$.

We repeat step 3 using $V_3 = V_3(2)$. In our case, this yields $h(3) = 0.2 \times 10^{-6}$ m^3.

(6) The determination of $V_3(3)$.

We repeat step 2 using $V_3 = V_3(2)$ and $h = h(3)$. In this case, we have $\Delta\alpha = 0.518$ and $V_3(3) = 5960$ m/s.

As one can see, $V_3(2)$ and $V_3(3)$ almost coincide. Therefore, the calculations can be terminated at the third approximation.

The following conclusions can be made:

The presence of an acoustic link of any thickness ($h \neq 0$) leads to an error in the determination of the sound velocity by interference methods. This concerns not only the technique considered in this paper, but also any other method using the phase difference between the reflected and outcoming waves (see, e.g., [13, 14]).

The error in the determination of the sound velocity without considering the acoustic link is very small ($\Delta V/V \simeq 7 \times 10^{-4}$). Therefore, the presence of the link should be taken into account only in the case of high-precision measurements.

In high-precision measurements of the sound velocity, it is necessary to perform computer simulation of the system using Eqs. (3)–(5).

REFERENCES

1. Li Baosheng, R. C. Leibermann, and D. J. Weidner, Science **281**, 5377 (1998).
2. Ori Veheskel and Ofer Tevet, J. Am. Ceram. Soc. **82** (1), 136 (1999).
3. S. V. Bogdanov, Akust. Zh. **46**, 609 (2000) [Acoust. Phys. **46**, 530 (2000)].
4. G. Floudas, W. Steffen, and N. Hadjichristides, Europhys. Lett. **44** (1), 37 (1998).
5. D. Mandrus, V. Keppens, and J. L. Sales, Phys. Rev. B **58**, 3712 (1998).
6. R. G. Maev, G. Roman, and V. M. Levin, IEEE Trans. Ultrason. Ferroelectr. Freq. Control **44** (6), 1224 (1997).
7. K. Balakrishnan, K. M. Manmeet, N. L. Ghodke, *et al.*, Rev. Sci. Instrum. **68** (9), 3436 (1997).
8. Kamioka Hiroaki, Jpn. J. Appl. Phys., Part 1 **36** (5A), 2896 (1997).
9. J. Maia Alues and A. M. Vallera, Rev. Sci. Instrum. **69** (1), 130 (1998).
10. Y. Matsuda, H. Nakano, and S. Nagai, Jpn. J. Appl. Phys., Part 2 **39** (1A/B), L59 (2000).
11. S. V. Bogdanov, I. I. Zubrinov, E. V. Pestryakov, and V. K. Sapozhnikov, Akust. Zh. **46**, 35 (2000) [Acoust. Phys. **46**, 27 (2000)].
12. L. M. Brekhovskikh, *Waves in Layered Media*, 1st ed. (Nauka, Moscow, 1957; Academic, New York, 1960).
13. H. J. Mc. Skimin, J. Acoust. Soc. Am. **22**, 413 (1950).
14. H. J. Mc. Skimin, J. Acoust. Soc. Am. **34**, 404 (1962).

Translated by M. Lyamshev

Acoustical Physics, Vol. 48, No. 4, 2002, pp. 406–411. Translated from Akusticheskiĭ Zhurnal, Vol. 48, No. 4, 2002, pp. 467–473.

Evaluation of the Spatial Resolution of Passive Acoustic Thermal Tomography

K. M. Bograchev and V. I. Passechnik†

ELDIS Research Center, Institute of Radio Engineering and Electronics, Russian Academy of Sciences, Starosadskiĭ per. 8, Moscow, 101000 Russia

e-mail: passechn@orc.ru

Received November 27, 2000

Abstract—Possible spatial resolution of a passive acoustic thermal tomograph is evaluated in numerical experiments. A criterion for the evaluation of this parameter is proposed. The criterion is based on the formation of a dip between two reconstructed temperature peaks with increasing distance between the thermal sources in the region under investigation. The spatial resolution depends on the positions of a pair of temperature peaks relative to the body surface and on the algorithm used for the reconstruction of the temperature distribution. An algorithm version providing an adequate reconstruction of the heights of the distribution peaks is suggested. It takes into account *a priori* information on the ultrasonic absorption coefficient and also the characteristics of the heat-transfer processes and the presence of blood circulation in a human body. In the case of lateral positions of the pair of temperature peaks relative to the surface, the spatial resolution is ≈1.7 cm. The prospects for the improvement of the spatial resolution of a passive acoustic thermal tomographs are discussed. © *2002 MAIK "Nauka/Interperiodica".*

Temperature within a biological object is one of its most important characteristics. This characteristic is widely used in medicine, in particular, for monitoring the process of hyperthermia procedures in oncology.

In measuring the temperature inside a human body, the data on the temperature not only at single points of the body but also on the 3D temperature distribution $T(x, y, z)$ within it are especially important. The information carried by thermal acoustic radiation in the megahertz frequency range can be used to measure the temperature within a human body. The fundamentals and prospects of the utilization of thermal acoustic radiation parameters are considered in our previous paper [1].

This radiation emerges from a depth of 2–10 cm from the body surface, depending on the frequency of the received signal. It is detected by piezoelectric transducers. The radiation intensity is the measure of the temperature in the medium, and it is characterized by an effective parameter called the acoustic brightness temperature T_A. The quantity T_A is the temperature of an acoustic blackbody producing the same radiation flux as the body under investigation. In the simplest case of an infinite medium homogeneous in its acoustic properties and ultrasonic absorption, the value of T_A measured by piezoelectric transducers is determined by the formula

$$T_A = \gamma \int_0^\infty T(l) \exp(-\gamma l)\, dl, \qquad (1)$$

where l is the coordinate along the acoustic axis of a piezoelectric transducer (the point $l = 0$ coincides with the transducer position), $T(l)$ is the temperature distribution within the object under study, and γ is the energy coefficient of ultrasonic absorption in the medium.

To obtain the spatial temperature distribution, it is necessary to carry out a series of measurements of thermal acoustic radiation by a set of piezoelectric transducers positioned on the body's surface and scanning the region under investigation in different directions and at different angles. Using the data of these measurements, it is possible to solve the inverse problem, i.e., to reconstruct the initial temperature distribution, which is the objective of tomography. Thus, we deal with a technique for the determination of the spatial distribution of the internal temperature in a human body, i.e., with passive acoustic thermal tomography [1–5]. Up to now, the feasibility of the technique was proved both experimentally (see [1]) and by numerical simulation [1–5]. The possibility of reconstructing both 2D and 3D distributions was demonstrated in [3]. Below, we present a theoretical analysis of the prospects for this technique with respect to spatial resolution.

The procedure of passive acoustic thermal tomography, which is based on the utilization of the acoustic thermal radiation of an object, includes several stages: the data acquisition (using special signal detectors and scanning schemes), the signal processing, and the solution of the inverse problem. At the last stage, one of the most important problems is the high-precision reconstruction of the peak heights in the temperature distributions. Evaluation of the possible spatial resolution of the technique is one of the most difficult problems, because

† Deceased.

a combined high-precision reconstruction of several peaks is needed. The first estimates of the spatial resolution (about 1 cm [2]) were made on the basis of the reconstruction of single-mode (one peak) distributions of temperature. The basic method of investigation was numerical simulation. First, we simulated the solution of the direct problem, i.e., the acquisition of measurement data on the intensity of thermal acoustic radiation. Then, the solution of the inverse problem was simulated, i.e., the reconstruction of the temperature distribution from the measurements. The temperature distributions considered in [2] contained small numbers of pixels (16–25), and, therefore, the resolution estimates could not be reliably substantiated. Values of about 1 mm were presented in [6, 7], where only theoretical physical estimates were used. These estimates were also of purely qualitative character. A suggestion was made that a high spatial resolution could be obtained using a correlation reception with the use of no less than five sensors simultaneously [8]. These results were obtained only in model experiments in the audio frequency range. Verification of this hypothesis is a task for the future.

We propose using the method of a numerical experiment and studying the reconstruction of bimodal temperature distributions in order to analyze the spatial resolution of a passive acoustic thermal tomograph [3]. Ways of estimating the quality of such a reconstruction are discussed in [4].

This paper is devoted to the estimation of a possible spatial resolution of the technique with the use of different algorithms for solving the inverse problem.

We restricted ourselves to the reconstruction of 2D temperature distributions $T(x, y)$. The numerical simulation was performed in several stages. At first, we selected a certain scanning scheme; then, we solved the direct problem—i.e., we calculated the temperature distribution in the presence of preset thermal sources and determined the set of the corresponding acoustic brightness temperatures; and, finally, we solved the inverse problem—i.e., we reconstructed the initial distribution.

The following model of a passive acoustic thermal tomograph was used in the computer simulation. The temperature distribution was reconstructed in a square area with the dimensions 10×10 cm^2. A matrix of piezoelectric transducers was positioned at the surface, i.e., at one side of this area (Fig. 1). We assumed that the central reception frequency was 1 MHz. We also assumed that the directivity pattern of piezoelectric transducers had the form of a beam, which was an approximation of a real directivity pattern of a focused piezoelectric transducer. The lines originating from the transducer points show the directions of scanning at different rotation angles φ of the acoustic axis of the corresponding sensor.

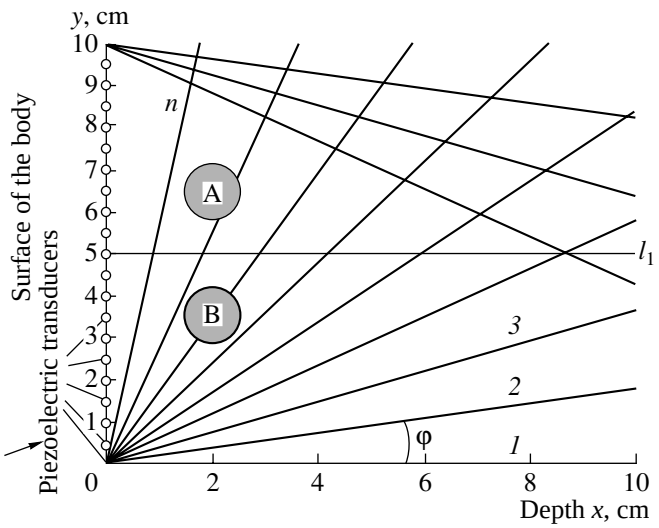

Fig. 1. Scheme of scanning of the area under study with the dimensions 10×10 cm^2 in the xy plane. The x coordinate is directed into the body (the point $x = 0$ is the body surface), and the y coordinate is oriented along the body surface. Temperature readings were made at the nodes of the grid, shown by dashed lines (the number of reading points is $N_H = 225$). The semicircles denote the piezoelectric transducers. The numbers *1*, *2*, *3*, …, *n* are the numbers of the scanning angles of piezoelectric transducers, which are measured with respect to the x axis. At $0 \le y < 5$ cm, the rotation angle is $\varphi = 0°–\varphi_{MAX}$; at $5 < y \le 10$ cm, $\varphi = -\varphi_{MAX}–0°$; and at $y = 5$ cm, $-\varphi_{MAX} \le \varphi \le \varphi_{MAX}$; here, $\varphi_{MAX} \approx 80°$. The heated areas A and B are positioned laterally with respect to the surface. The arrow indicates the observation angle for the temperature distributions given in Fig. 2.

In solving the direct problem, we set as initial the temperature distributions formed in an object in the presence of two point sources of temperature described as

$$q_i(x, y) = q_0 \exp(-((x - x_i)^2 + (y - y_i)^2)/d^2), \quad (2)$$

where the characteristic width of a source is $d = 0.4$ cm, x_i and y_i are the source coordinates ($i = 1, 2$), and q_0 is the normalizing factor. In this case, we took into account the fact that the corresponding temperature distribution in a human body must satisfy the heat equation allowing for the convective heat transfer due to the blood circulation [3–5]. In the simplest case of a medium homogeneous in its thermal-physical characteristics, the stationary equation of thermal diffusivity has the form

$$T(x, y) - x_D^2 \Delta T(x, y) = q(x, y), \quad (3)$$

where Δ is the Laplacian, $q(x, y)$ is the spatial density of temperature sources, and $x_D = \sqrt{D/\lambda}$ is the characteristic length determined by the thermal diffusivity D and the volume blood circulation λ (the amount of liters of blood flowing through 1 kg of a tissue per 1 s); in different tissues, the values of x_D range within $x_D \approx 0.3–1.6$ cm. The acoustic brightness temperatures were calculated by Eq. (1), and the value of the energy coef-

ficient of absorption γ was assumed to be constant and equal to 0.2 cm^{-1}. A Gaussian random error with an rms value of $dT_A = 0.1$ K was imposed on the values of T_A calculated in such a way.

The Tikhonov regularization method was used in solving the inverse problem. In this case, we compared the reconstruction quality for two different algorithms of Tikhonov's regularization: global and local. The latter algorithm was suggested by us for increasing the quality of the reconstruction of the distribution peak heights [3]. It takes into account *a priori* information on the physical features of the temperature distribution within a human body that are determined by the heat transfer processes and the presence of blood circulation, which are described by Eq. (3). The quality criterion for the reconstruction of the temperature distribution was the rms reconstruction error averaged over the whole area:

$$dT_R = \sqrt{\sum_{i=0}^{N_x-1}\sum_{j=0}^{N_y-1}(T(x_i, y_j) - Tr(x_i, y_j))^2/N_H}, \quad (4)$$

where $Tr(x, y)$ is the reconstructed temperature distribution, $N_x = 15$, $N_y = 15$, and $N_H = N_x^* N_y$.

Two algorithms tested up to now (global and local) yield the following results in the case of reconstruction of single-mode temperature distributions [5].

The error of the temperature reconstruction dT_R depends on the position the temperature source in depth. For a source depth of 2.5 cm with an rms error of a single measurement of the acoustic brightness temperature $dT_A = 0.1$ K, the reconstruction error is $dT_R \approx 0.3$ K (reconstruction by the method of global regularization). The local regularization provides an opportunity to reduce dT_R approximately by 10–15% in many cases. As the distance from the temperature source to the surface grows, dT_R increases. In the case of the local regularization, dT_R increases noticeably slower with increasing depth of the temperature source. The value of the error is $dT_R \approx 0.45$ K when the distance from the source to the surface is $H = 8$ cm in the case of the local algorithm, while $dT_R \approx 0.7$ K for the global algorithm. It is necessary to note that, in the case of utilization of both algorithms, the peaks reconstructed at large distances from the surface are noticeably spread.

The method of the local regularization is more stable in the case of reconstructing small temperature increments, which is its essential advantage. For example, according to the data of our calculations, in the reconstruction of distributions with small temperature increments ($T_{MAX} = 3$ K), the global regularization technique does not yield any solution, whereas the local regularization technique provides an opportunity to reconstruct such temperature distributions.

The resolution of the passive thermal tomography was evaluated by the quality of the reconstruction of a temperature distribution in the form of two peaks, which was produced by two temperature sources in the area under investigation [1, 3]. The reconstruction was performed for various distances from these peaks to the surface and various positions of these peaks with respect to the surface, i.e., a lateral position (the line connecting the centers of temperature sources is parallel to the surface of the body), a transverse position (this line is perpendicular to the surface of the body), and a diagonal position (the centers of the temperature sources lie on the diagonal of the area under study). In this connection, we selected for evaluation a pair of peaks with a large temperature increment of 5 K in the maxima.

Figure 2 shows examples of the reconstruction of temperature distributions produced by two thermal sources, which create a bimodal temperature distribution with the maximal values $T_{MAX} = 5$ K in a medium with the value of the characteristic length $x_D = 1.6$ cm, in the case of increasing distance between them (the two sources move apart). The sources are positioned laterally, at a distance of $H = 2$ cm from the surface, and move away from each other symmetrically with respect to the line l_1 (Fig. 1). Four successive stages of the separation of two sources (lines *a*–*d*) are demonstrated. The observation angle for the temperature distributions in the studied area is indicated in Fig. 1 by an arrow.

The initial temperature distributions in the form of two peaks are shown in the first column of Fig. 2. The second and third columns, respectively, show the distributions reconstructed using the algorithms of global and local regularization. Each example of a reconstructed distribution is obtained at a single realization of noise in the studied set of acoustic brightness temperatures $\mathbf{T}_A$. Two peaks were clearly resolvable in each of the cases, *a*–*d*. Evidently, as the distance between the peaks increases, their separation becomes even clearer. One can see that, at this distance ($H = 2$ cm) from the sources to the surface, in the case of global regularization, the resolution of peaks in the reconstructed distribution is distinctly visible at all distances *d* between the sources. At the same time, in the case of the local technique, the two peaks in the reconstructed distribution merge into one broad peak at the minimal studied distance between the sources (line *a*). The greater the distance between the sources, the better the peaks in the reconstructed distributions are separated. One can also see from Fig. 2 that the reconstructed temperature peaks differ to a certain extent from the initial ones in their width and shape.

Several different criteria of resolution of two sources are used in acoustics. In the Rayleigh criterion, it is assumed that two point sources are resolved if the maximal response to one of the sources coincides with the first zero of the response to the other source. This criterion is used mainly with respect to the sources of monochromatic radiation. In the case of formation of an incoherent image, this criterion is often formulated as follows: two points can be resolved if there is a

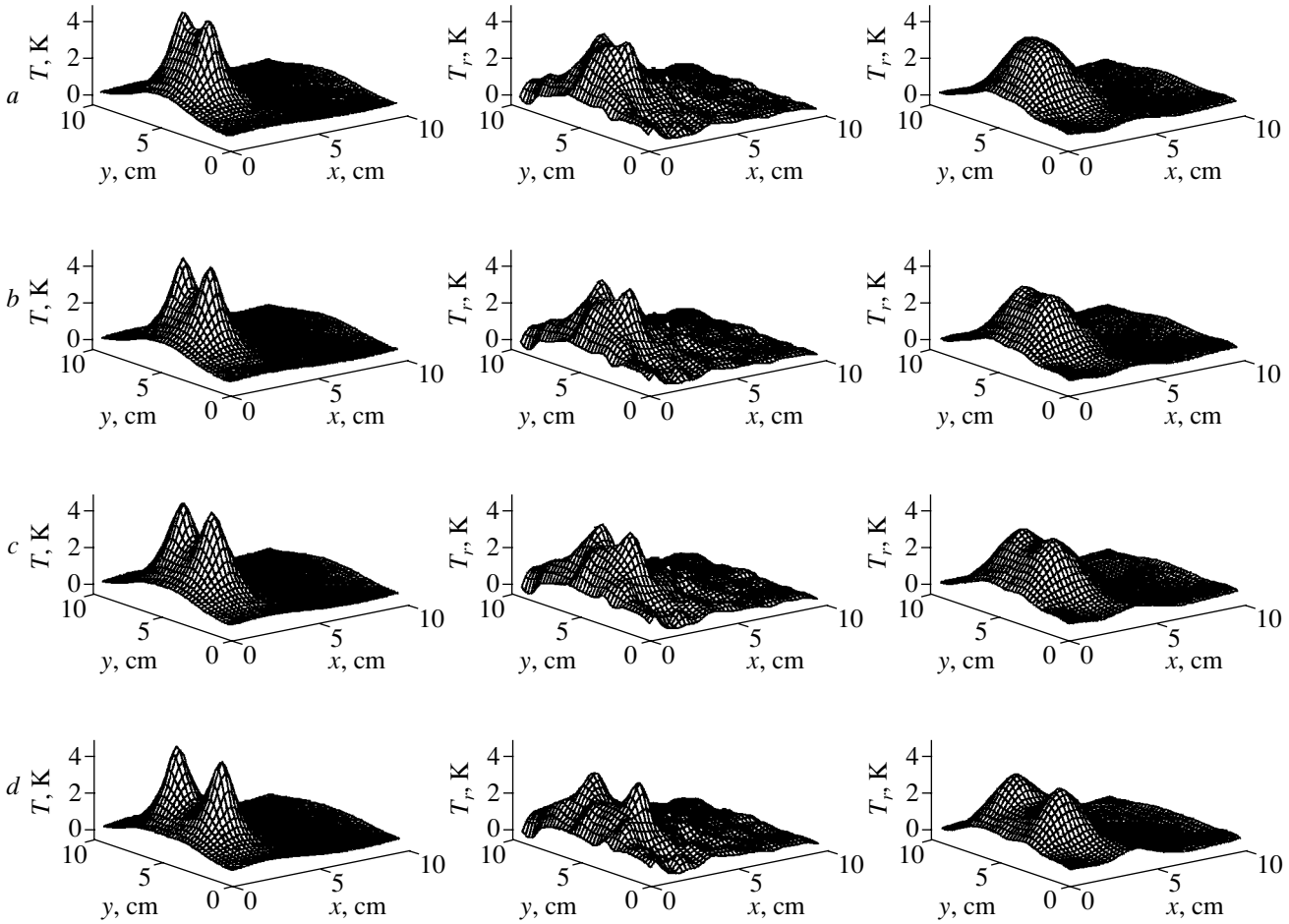

Fig. 2. Examples of the reconstructed temperature distributions in the case of increasing distance d between two thermal sources (lines *a*, *b*, *c*, and *d* correspond to $d \approx 1.7$, 2.1, 2.5, and 3 cm, respectively). The sources are positioned laterally, at a distance of $H =$ 2 cm from the surface. The first column shows the initial temperature distributions, and the second and third columns, the temperature distributions reconstructed by the techniques of global and local regularizations, respectively. The observation angles for the temperature distributions in the area are indicated by an arrow in Fig. 1. The maximal value of the temperature (in the peaks) is equal to $T_{MAX} = 5$ K, and the characteristic length is $x_D = 1.6$ cm.

26.5% dip in the middle point between them in the distribution pattern.

The Sparrow criterion of resolution is more general, because it is applied equally to the formation of coherent images and, e.g., to a Gaussian beam, which has no distinct spatial zero in the response to a point source. According to the Sparrow criterion, two point sources are resolved if the intensity in the middle between two points is equal to the total intensity at one point.

The case under study differs from those described above by the fact that the reconstructed temperature distribution fluctuates quite strongly depending on the reconstruction realization, i.e., on the initial distribution of noise. This means that the pair of temperature peaks to be resolved also fluctuates. Thus, the problem of resolution of a pair of peaks is of a statistical character in our case. Therefore, to evaluate the limit of resolution, i.e., the minimal distance d between the temperature sources at which two temperature peaks exist in the reconstructed distribution, we used a criterion of peak resolution different from those described above, this criterion being of a statistical character. The criterion of resolution of two temperature peaks was assumed to be the presence of a dip between them in the reconstructed distribution.

We presumed that the value of the dip h_r in the reconstructed distribution was a normally distributed random quantity with the average value $\overline{h_r}$. We assumed that the peaks were located at a distance equal to the limit of resolution when the value of $\overline{h_r}$ was equal to the doubled rms dispersion σ of the value of the reconstructed temperature on the average over the studied area:

$$\overline{h_r} = 2\sigma. \tag{5}$$

It can be readily demonstrated that, for the case when the probability of a random event is evaluated

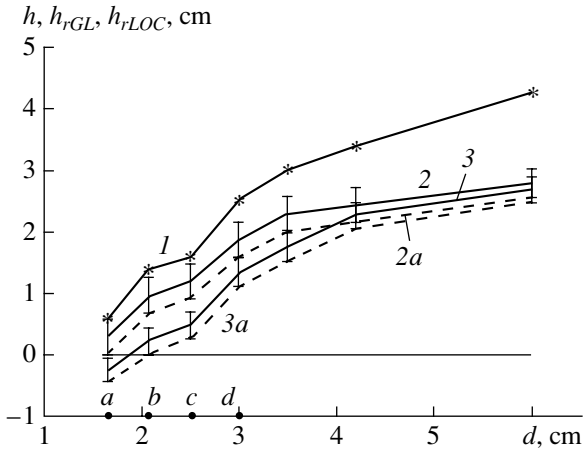

Fig. 3. Evaluation of the spatial resolution in the case of the lateral positions of the sources. The dependence of the depth of the dip between two peaks, i.e., the parameters h, $\overline{h_{rGL}}$, and $\overline{h_{rLOC}}$, on the distance d between the peaks. Curve *1* corresponds to the dip depth h in the initial distribution, and curves *2* and *3*, to the average dip depths in the distributions reconstructed by the global ($\overline{h_{rGL}}$) and local ($\overline{h_{rLOC}}$) regularization techniques, respectively. Points *a*, *b*, *c*, and *d* correspond to the temperature distributions shown in Fig. 2 in lines *a*, *b*, *c*, and *d*. The parameters are the same as in Fig. 2. The vertical segments on curves *2* and *3* indicate the doubled values of the rms dispersion ($\pm 2\sigma$) for T_{rGL} and T_{rLOC}, respectively. The dashed lines correspond to the quantities $\overline{h_{rGL}} - 2\sigma$ and $\overline{h_{rLOC}} - 2\sigma$ for curves *2* and *3* (curves *2a* and *3a*, respectively). The resolution limit for curve *2* corresponds to the point *a* ($d0_{GL} \approx 1.7$ cm), and for curve *3*, to the point *b* ($d0_{LOC} \approx 2.1$ cm).

over nine realizations, this criterion means that the initial pair of temperature peaks is considered as resolvable when the dip in the reconstruction occurs with a probability of $P \geq 0.95$.

The application of the criterion to a series of separations of the peaks located laterally with respect to the surface (Fig. 2) is shown in Fig. 3. The values of the parameters T_{MAX}, x_D, and H are the same as in Fig. 2. Figure 3 presents the dependence of the depth of a dip between the initial peaks, i.e., the parameter h, on the distance d between the peaks (curve *1*). Additionally, this figure shows similar dependences for the average dip depths $\overline{h_{rGL}}$ and $\overline{h_{rLOC}}$ for the distributions reconstructed using the global (curve *2*) and local (curve *3*) regularizations, respectively. The vertical segments on curves *2* and *3* indicate the doubled values of the rms dispersion ($\pm 2\sigma$) for T_{rGL} and T_{rLOC}, respectively. The points *a*, *b*, *c*, and *d* in Fig. 3 correspond to the distributions given in Fig. 2 in lines *a*, *b*, *c*, and *d*.

As the distance d between the peaks increases, the depth of the dip between them grows in the initial distribution (curve *1*) and in the distributions reconstructed using both global and local techniques (curves *2* and *3*, respectively). Curves *2* and *3* lie below curve *1*, because, in the process of the reconstruction, the temperature peaks flatten to a certain extent (which is a consequence of the systematic error introduced by the reconstruction algorithm), and the depth of the dip between the peaks decreases in comparison with the initial one.

Curve *3* in Fig. 3 goes into the negative region ($\overline{h_{rLOC}} < 0$) at small values of d. As one can see from Fig. 2 (line *a*, third column), this means that in the case of the reconstruction of temperature peaks very close to each other by the technique of local regularization, the distribution form is distorted to such a great extent that a peak appears instead of a dip in the reconstructed distribution.

The dashed lines indicate the values $\overline{h_{rGL}} - 2\sigma$ and $\overline{h_{rLOC}} - 2\sigma$ for curves *2* and *3* (curves *2a* and *3a*, respectively). According to the criterion described above, the value of d, at which a dashed line intersects the line $h = 0$, is considered to be the limit of the spatial resolution $d0$. This means that, at $d = d0$, Eq. (5) is valid. As one can see from Fig. 3, this happens approximately at the point *a* ($d0_{GL} \approx 1.7$ cm) for curve *2* and at the point *b* ($d0_{LOC} \approx 2.1$ cm) for curve *3*, where $d0_{GL}$ and $d0_{LOC}$ are the limits of spatial resolution in the cases of reconstruction using global and local regularizations, respectively.

Thus, in the case of the global regularization, the limit of resolution in space is $d0_{GL} \approx 1.7$ cm for the given values of the parameters. In the case of the local regularization, for the same values of the parameters, the limit of resolution in space is $d0_{LOC} \approx 2.1$ cm. These estimates are obtained for the lateral positions of the peaks. The proposed criterion was also applied to other cases of peak positions with respect to the surface. From the results of computer simulation, it follows that, in the presence of two temperature sources, the initial temperature distribution is best reconstructed in the case of the lateral positions of the sources, and the worst reconstruction is in the case of the transverse positions; the case of the diagonal positions is intermediate. The resolutions for the lateral and diagonal positions of the sources are almost the same. The resolution in the case of the transverse position of the sources is worse by approximately a factor of 1.5 as compared to the case of two other positions of the peaks, because, in the case of the transverse position, the far peak is screened by the near one. Thus, the estimates given above are the best.

It is necessary to note that the better spatial resolution in the case of the reconstruction using global regularization in comparison with that using local regularization manifests itself only for certain types of reconstructed distributions, e.g., in the case of small distances from the peaks to the surface (≈2–3 cm for the closest peak) and high values of the temperature T_{MAX}. It may happen that, at large distances from the surface

and low T_{MAX}, global regularization will be unable to provide the temperature reconstruction and the question about its spatial resolution will become meaningless. At the same time, local regularization provides reconstruction with a sufficiently high spatial resolution. It is necessary to note that these estimates are made in the framework of the selected model of a thermal tomograph. In particular, the position of the matrix of piezoelectric transducers on the object's surface is an approximation. In the case of a real tomograph, the matrix of piezoelectric transducers can be separated from the surface by the thickness of an immersion layer. We believe that a change in the tomograph scheme will not substantially affect the result of our consideration.

Two kinds of application of thermal tomographs are possible in the future: for obtaining qualitative information about the temperature distribution in a human body and for measuring the spatial temperature distribution with preset accuracy and spatial resolution (e.g., for the problem of hyperthermia, the measurement accuracy must be no worse than 0.5 K and the spatial resolution, about ≈0.3–0.5 cm). The first of these applications can be realized with the equipment available today, by using the algorithms described above. The second application requires an improvement of the parameters of passive acoustic thermal tomographs. Since the spatial resolution is determined by the quality of the reconstruction of the distribution peaks, we expect that the basic prospects for improving the reconstruction quality for temperature distributions, including the spatial resolution, are connected with the improvement of algorithms for solving the inverse problem, in particular, with the development of algorithms that allow one to reduce the systematic error in the reconstruction of the heights of temperature peaks. We note that acoustic thermal tomographs can be used not only in medicine, but also in other fields, e.g., in the food industry [9]. The estimates obtained above suggest that acoustic thermal tomography can find its place among other modern techniques of medical thermal imaging [10, 11].

ACKNOWLEDGMENTS

This work was supported by the Russian Foundation for Basic Research, project no. 00-01-00361.

REFERENCES

1. V. I. Passechnik, A. A. Anosov, and K. M. Bograchev, Biomed. Radioélektron., No. 2, 3 (1999).
2. A. A. Anosov, M. G. Isrefilov, and V. I. Pasechnik, Radiotekhnika (Moscow), No. 9, 65 (1995).
3. Yu. V. Gulyaev, K. M. Bograchev, I. P. Borovikov, *et al.*, Radiotekh. Élektron. (Moscow) **43** (9), 140 (1998).
4. V. I. Passechnik, A. A. Anosov, and M. G. Isrefilov, Int. J. Hyperthermia **15** (2), 123 (1999).
5. K. M. Bograchev and V. I. Pasechnik, Akust. Zh. **45**, 742 (1999) [Acoust. Phys. **45**, 667 (1999)].
6. V. A. Burov and E. E. Kasatkina, Akust. Zh. **43**, 162 (1997) [Acoust. Phys. **43**, 135 (1997)].
7. E. E. Kasatkina, Candidate's Dissertation in Physics and Mathematics (Moscow State University, Moscow, 2000).
8. V. V. Gerasimov, Yu. V. Gulyaev, A. V. Mirgorodskiĭ, *et al.*, Akust. Zh. **45**, 487 (1999) [Acoust. Phys. **45**, 433 (1999)].
9. J. G. Ibarra, Y. Tao, J. Walker, and C. Griffis, Trans. ASAE **42**, 1383 (1999).
10. A. Gorbach, S. Sato, J. Heiss, *et al.*, Epilepsia **40**, 51 (1999).
11. R. A. Kruger, H. E. Reynolds, W. Kiser, *et al.*, Radiology **210** (2), K06H (1999).

Translated by M. Lyamshev

Acoustical Physics, Vol. 48, No. 4, 2002, pp. 412–422. Translated from Akusticheskiĭ Zhurnal, Vol. 48, No. 4, 2002, pp. 474–484.

Active–Passive Thermoacoustic Tomography

V. A. Burov, P. I. Darialashvili, and O. D. Rumyantseva

Physical Faculty, Moscow State University, Vorob'evy gory, Moscow, 119899 Russia

e-mail: burov@phys.msu.su

Received October 10, 2001

Abstract—A scheme of acoustic correlation thermotomography is considered for a medium that is inhomogeneous in temperature, absorption coefficient, and phase velocity of ultrasound. It is demonstrated that, with the use of an external "illuminating" field (of thermal origin or generated artificially), it is possible to separately reconstruct the distributions of all aforementioned parameters. © *2002 MAIK "Nauka/Interperiodica".*

The great number of papers devoted to acoustic thermometry and the variety of schemes of passive thermoacoustic tomography considered there are evidence of a serious interest taken in this problem both by acoustical designers of such schemes and by researchers, as well as by the potential users of the corresponding systems.

The properties of the fields of thermoacoustic radiation are almost exactly described by the model of a normally distributed random field. The verification of any statistical hypotheses concerning the properties of such a field is reduced to the formation and processing of a sample space–time correlation matrix of signals received by an antenna array. This is the reason why we concentrate on the correlation systems of thermal tomography [1, 2]. The schemes of ray intensimetry from this point of view are a simplified particular case of these systems. In this connection, in this paper, we consider the process of correlation measurement that serves as the basis for thermoacoustic devices. We also discuss the new possibilities arising when additional sources of thermal fields or specially generated random fields, whose radiation intensities are comparable with the intensities of thermoacoustic fields present in the medium under investigation, are introduced into the system. This method of tomograph operation can be called active–passive, because it uses both types of fields in the system by varying their mutual relationships.

The basic relationship determining the mean-square value of acoustic pressure $\langle p^2 \rangle$ in the simplest case of propagation of a quasi-plane wave along a ray in a medium nonuniformly heated and nonuniformly absorbing, but homogeneous with respect to the phase velocity of sound, has the form [3]

$$\langle p^2(x_0) \rangle \sim \int_{-\infty}^{x_0} \alpha(x) T(x) \exp\left[-\int_{x}^{x_0} \alpha(\xi) d\xi \right] dx. \qquad (1)$$

Here, x_0 is the receiver coordinate, α is the absorption coefficient (in power), and T is the absolute temperature. An important property (quite natural from the point of view of thermodynamics) is the fact that any distribution of absorption in the isothermal conditions does not lead to a change in the value of $\langle p^2 \rangle$, and the informative quantity is the product of the temperature deviation (in comparison with the average background) and the local value of the absorption coefficient. This follows from the fact that, at $T \equiv$ const, the value of the integral in Eq. (1) is identically equal to T, independently of the form of $\alpha(x)$. Such a property is also inherent in correlation systems. However, it has a more complex character, which can be used for the enhancement of the tomograph informative capability, as is shown below (and described briefly in our previous paper [4]). At the same time, the character of the formation of a thermoacoustic signal and its correlation properties impose certain restrictions of both fundamental and purely technological (precision) nature. These problems are also treated below.

CORRELATION PROPERTIES OF THERMOACOUSTIC RADIATION OF A THIN ABSORBING LAYER

Let us consider a model that provides an opportunity to obtain in a sufficiently simple way the results important for the following consideration. The choice of a model is not fundamentally important and is determined only by convenience.

Let two identical plane receivers (hydrophones *1* and *2* in Fig. 1) and a thin (much thinner than the average wavelength λ) absorbing layer be located in a volume filled with a weakly absorbing liquid medium and bounded by walls. We assume that the receivers have small internal losses and their material and thickness cause small distortions of the field. Such receivers, from the diffuse noise field inside a dish, separate the components in the form of random plane waves propagating in opposite directions that are perpendicular to the plane of the receivers. In the case of small internal losses, the signal from these hydrophones is determined basically by their radiation resistance; i.e., it results

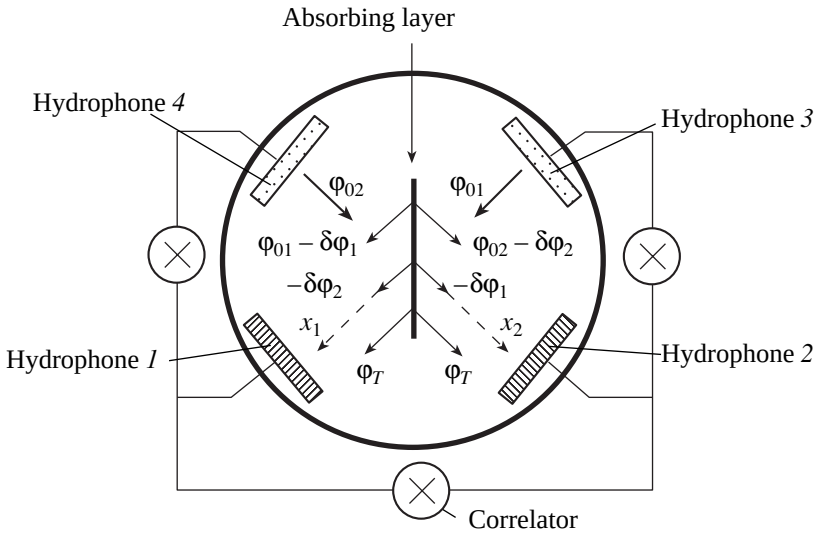

Fig. 1. Thin absorbing layer in an isothermal medium.

from the fluctuation effect of the medium. Despite the fact that practical manufacture of such receivers is rather difficult, it is fundamentally possible, and the above assumptions simplify further consideration. We assume also for the sake of simplicity that the far fields of the receivers reach the bounding walls and the absorbing layer extends along the diagonal of the intersection zone of the far fields of receivers *1* and *2*. The distances (along the axes of the corresponding far fields) between the absorbing layer and the receivers can be different. The absorbing layer is assumed to be liquid and to have the same initial value of the real part of the phase velocity c_0 as the surrounding liquid. From the thermal radiation of the absorbing layer, the hydrophones also separate random plane waves with the fronts parallel to the plane of the hydrophones.

All aforementioned elements of the model have the same temperature. Therefore, the intensity emitted by the layer is such that it compensates for the corresponding absorbed part of the thermoacoustic field (radiated by the walls and filling the volume) and restores in this way the thermodynamic equilibrium in the volume.

Let us take the plane wave φ_0 radiated by the part of the wall that lies in the "frontal" sensitivity zone of one of the hydrophones (e.g., hydrophone *1*). The wave equation for the potential of the particle velocity φ in a medium inhomogeneous in viscosity and with a constant density ρ_0 has the form

$$\frac{\partial^2\varphi}{\partial t^2} - c_0^2\Delta\varphi - \frac{b(\mathbf{r})}{\rho_0}\frac{\partial}{\partial t}(\Delta\varphi) = f_0(\mathbf{r}, t), \qquad (2)$$

where $b = (4/3)\eta + \xi$; η and ξ are the coefficients of shear and bulk viscosity; and f_0 are the external sources produced by fluctuation processes in the walls of the volume. In the quasi-monochromatic approximation, Eq. (2) transforms to a reduced wave equation (a time dependence of the form $\sim\exp(-i\omega t)$):

$$\Delta\varphi + \frac{\omega^2}{c_0^2}\varphi = \frac{ib\omega}{\rho_0 c_0^2}\Delta\varphi + F_0. \qquad (3)$$

Further, we examine the near wave field of the hydrophones. Let the x_1 axis coincide with the axis of the near wave field of hydrophone *1* and the 1D problem along this axis be considered. In this case, taking into account the fact that the Green function for such a problem has the form $G(x, x') = -(i/2k_0)\exp(ik_0|x - x'|)$, the Lippmann–Schwinger equation for Eq. (3) is $\varphi(x_1) = \varphi_0(x_1) + \int\frac{b(x')}{2\rho_0 c_0}\exp(ik_0|x_1 - x'|)\frac{\partial^2\varphi(x')}{(\partial x')^2}dx'$. Here, φ_0 is the unperturbed field of the sources F_0. In the first Born approximation, the solution has the form

$$\varphi(x_1) \approx \varphi_0(x_1) - \frac{k_0^2}{2\rho_0 c_0}\int b(x')\varphi_0(x') \times \exp(ik_0|x_1 - x'|)dx' \equiv \varphi_0(x_1) - \delta\varphi(x_1), \qquad (4)$$

the validity of this approximation requiring that the condition $|\varphi_0(x_1)| \gg |\delta\varphi(x_1)|$ be satisfied at all x_1. The minus sign before $\delta\varphi$ corresponds to the attenuation of the primary wave, which is small within the domain of applicability of this approximation.

MECHANISM OF COMPENSATION OF THE THERMAL RADIATION OF AN ABSORBING LAYER

In the description of the correlation properties of the signals u_1 and u_2 received by the first and second hydrophones, it is convenient to use the complex function of mutual coherence: $\Gamma_{12}(\tau) = \overline{u_1(t)u_2^*(t+\tau)}$, where the

overbar means time averaging (it is assumed that the processes are ergodic and the initial signals u_1 and u_2 are represented in a complex form, e.g., an analytical form). The imaginary part of the function $\Gamma_{12}(\tau)$ is the Hilbert transform of its real part (in the case of narrow-band signals, it is precisely the transition from $\cos\omega\tau$ to $\sin\omega\tau$).

If external radiation from the walls is incident on the layer, the secondary sources producing the field with the phase opposite to the initial field are generated in the layer. In this case, the emission of such layer-scattered waves occurs both in the direction of the x_1 axis and in the symmetric (with respect to the layer plane) direction of the x_2 axis, which is determined in the geometry of the adopted model as the direction to hydrophone *2*. It is necessary to consider possible changes that occur in the correlation properties of the signals received by hydrophones *1* and *2* because of the presence of the absorbing layer. The primary waves φ_{01} and φ_{02} from the corresponding regions of the absorbing walls arrive at the intersection region of the far fields of the hydrophones. They are not cross-correlated. The primary waves $(\varphi_{01} - \delta\varphi_1)$ and $(\varphi_{02} - \delta\varphi_2)$ attenuated by the layer go out of the intersection region, as well as the waves $(-\delta\varphi_1)$ and $(-\delta\varphi_2)$ propagating in directions symmetrical with respect to the layer. Furthermore, the signals of the thermal self-radiation of the absorbing layer φ_T arrive at both hydrophones. In the case of the considered relative positions of the layer and hydrophones *1* and *2*, these are the correlated signals separated by the hydrophones from the total radiation of the layer. They are totally correlated when the layer thickness tends to zero. Thus, the function of mutual coherence of signals is

$$\Gamma_{12}(\tau) = \langle(\varphi_{01} - \delta\varphi_1 - \delta\varphi_2 + \varphi_T)|_t \times (\varphi_{02} - \delta\varphi_2 - \delta\varphi_1 + \varphi_T)^*|_{t+\tau}\rangle$$

(here and below, the functions without the sign of complex conjugation are received by hydrophone *1* at the time moment *t*, and those with the conjugation sign (*), by hydrophone *2* at the time moment $t + \tau$). From the signal independence, it follows that

$$\langle\varphi_{01}\varphi_{02}^*\rangle = \langle\varphi_{01}\delta\varphi_2^*\rangle = \langle\varphi_{01}\varphi_T^*\rangle = \langle\delta\varphi_1\varphi_{02}^*\rangle = \langle\delta\varphi_1\delta\varphi_2^*\rangle = \langle\delta\varphi_1\varphi_T^*\rangle = \langle\delta\varphi_2\delta\varphi_1^*\rangle = \langle\delta\varphi_2\varphi_T^*\rangle = \langle\varphi_T\varphi_{02}^*\rangle = \langle\varphi_T\delta\varphi_2^*\rangle = \langle\varphi_T\delta\varphi_1^*\rangle = 0 \quad \forall\tau.$$

Then, we have

$$\Gamma_{12}(\tau) = \langle\delta\varphi_1\delta\varphi_1^*\rangle + \langle\delta\varphi_2\delta\varphi_2^*\rangle - \langle\varphi_{01}\delta\varphi_1^*\rangle - \langle\delta\varphi_2\varphi_{02}^*\rangle + \langle\varphi_T\varphi_T^*\rangle. \quad (5)$$

In the case of the considered geometry of a thin absorbing layer and hydrophones, the function $\mathrm{Re}\Gamma_{12}(\tau)$ is symmetrical and the function $\mathrm{Im}\Gamma_{12}(\tau)$ is antisymmetrical with respect to the delay time $\tau = \bar{\tau}_{12}$ that is equal to the difference in the times of propagation from the layer to hydrophones *2* and *1* (for the axial symmetry of the pattern with respect to the layer plane shown in Fig. 1, $\bar{\tau}_{12} = 0$). At such a delay, which means "phasing" with the layer, we have

$$\Gamma_{12}(\tau = \bar{\tau}_{12}) = \langle|\delta\varphi_1|^2\rangle + \langle|\delta\varphi_2|^2\rangle - \langle\varphi_{01}\delta\varphi_1^*\rangle - \langle\delta\varphi_2\varphi_{02}^*\rangle + \langle|\varphi_T|^2\rangle = 2\langle|\delta\varphi_1|^2\rangle - 2\mathrm{Re}\langle\varphi_{01}\delta\varphi_1^*\rangle + \langle|\varphi_T|^2\rangle, \quad (6)$$

since, by virtue of the isothermal walls,

$$\langle|\varphi_{01}|^2\rangle = \langle|\varphi_{02}|^2\rangle, \quad \langle|\delta\varphi_1|^2\rangle = \langle|\delta\varphi_2|^2\rangle, \quad \text{and at} \quad \tau = \bar{\tau}_{12} \quad \langle\varphi_{01}\delta\varphi_1^*\rangle = (\langle\delta\varphi_2\varphi_{02}^*\rangle)^*. \quad (7)$$

Since the appearance of additional absorbing regions in the path of the fluctuation signal formation does not change the power of the received signal in the isothermal case, for the autocorrelation function of signals from hydrophone *1*, the above result means that

$$\Gamma_{11}(\tau) = \langle(\varphi_{01} - \delta\varphi_1 - \delta\varphi_2 + \varphi_T)|_t \times (\varphi_{01} - \delta\varphi_1 - \delta\varphi_2 + \varphi_T)^*|_{t+\tau}\rangle = \langle\varphi_{01}|_t \times \varphi_{01}^*|_{t+\tau}\rangle \quad \forall\tau.$$

From the comparison of this expression with Eq. (5) with allowance for the equality $\langle\delta\varphi_1\varphi_{01}^*\rangle = \langle\delta\varphi_2\varphi_{02}^*\rangle\,\forall\tau$, it follows that

$$\Gamma_{12}(\tau) = 0 \quad \forall\tau.$$

Therefore, the correlation property of the thermal self-radiation of the layer is exactly compensated by the anticorrelation property of the background thermal radiation scattered by this layer. Thus, the isothermal with the background distribution of the absorption coefficient of the medium does not affect the correlation properties of thermal radiation in the case of thermal tomography at difference delays.

CORRELATION MEASUREMENTS IN A NONISOTHERMAL (NONEQUILIBRIUM) CASE

The situation changes drastically in the nonequilibrium case, when the temperature of the background radiation $T_{bg}(\mathbf{r})$ differs from the intrinsic temperature $T(\mathbf{r})$ of some absorbing region of the medium. In this case, the effect of total compensation fails and a "nonequilibrium" distributed source of intrinsic and scattered thermal noise arises with the spatial density of power distribution $I_T(\mathbf{r})$ determined by the local relationship

$$I_T(\mathbf{r}) \sim \alpha(\mathbf{r})[T(\mathbf{r}) - T_{bg}(\mathbf{r})]; \quad \alpha(\mathbf{r}) = b(\mathbf{r})\omega^2/(\rho_0 c_0^3). \quad (8)$$

Since two quantities $\alpha(\mathbf{r})$ and $T(\mathbf{r})$, which are usually unknown simultaneously, are present in Eq. (8), it is necessary to perform two measurements at different values of the background temperature $T_{bg} = T_1$ and $T_{bg} = T_2$. This gives two expressions:

$$\begin{cases} \alpha(\mathbf{r})[T(\mathbf{r}) - T_1(\mathbf{r})] = \Theta_1(\mathbf{r}) \\ \alpha(\mathbf{r})[T(\mathbf{r}) - T_2(\mathbf{r})] = \Theta_2(\mathbf{r}), \end{cases} \tag{9}$$

where $\Theta_1(\mathbf{r})$ and $\Theta_2(\mathbf{r})$ are the estimated values of $I_T(\mathbf{r})$, which is the power distribution density of nonequilibrium sources of self- and scattered radiation, at T_1 and T_2, respectively. The values of Θ_1 and Θ_2 can be reconstructed by one of the methods producing an unbiased estimate on the basis of the data measured in a correlation system in the case of phasing according to difference delays [5, 6]. The following estimates are obtained from Eq. (9):

$$\hat{T} = \frac{\Theta_1 T_2 - \Theta_2 T_1}{\Theta_1 - \Theta_2}, \quad \hat{\alpha} = \alpha_0 \frac{\Theta_2 - \Theta_1}{T_1 - T_2}, \tag{10}$$

where α_0 is the dimensional coefficient. If the studied object corresponds to the considered model and is a thin absorbing layer in a weakly absorbing medium, Eqs. (10) solve the problem of combined estimation of the absorption coefficient and the temperature of the layer.

Here, we should note the possibility of a negative value of $I_T(\mathbf{r})$ in the case of $T_{bg}(\mathbf{r}) > T(\mathbf{r})$. The negative value can appear in estimating the radiation power of the absorbing layer with the help of a correlation system and is caused by the anticorrelation property of the field scattered by the layer and the incident primary background radiation. The sign of the radiation power estimated by a correlation system reflects the energy balance in a nonequilibrium situation. The negative sign is the evidence of dominance of the external field absorption over the thermal self-radiation.

EFFECT OF THE INHOMOGENEITY OF THE PHASE VELOCITY IN THE MEDIUM

The situation becomes noticeably more complex if the medium is also inhomogeneous in phase velocity together with the inhomogeneity of the absorption coefficient and heating temperature. Just this situation takes place usually in reality, because the change of the absorption coefficient is usually accompanied by changes in the elastic and density characteristics of the medium.

It is also convenient to monitor the effect of the change of the phase velocity by using a thin layer as an example. Now, we assume that, apart from the absorption, the phase velocity in the layer is different from the velocity in the surrounding medium. Equation (3) now takes the form

$$\Delta\varphi + \frac{\omega^2}{c_0^2}\varphi = \frac{ib\omega}{\rho_0 c_0^2}\Delta\varphi + \nu\varphi + F_0, \quad \text{where} \quad \nu(\mathbf{r}) = \left(\frac{\omega^2}{c_0^2} - \frac{\omega^2}{c^2(\mathbf{r})}\right). \tag{11}$$

The term $\nu\varphi$ on the right-hand side of Eq. (11) describes the secondary sources caused by the difference of the local value of phase velocity $c(\mathbf{r})$ from the background value c_0. In the first Born approximation, an equation analogous to Eq. (4) acquires an additional term

$$\begin{aligned} \varphi(x_1) &\approx \varphi_0(x_1) \\ &- \frac{k_0^2}{2\rho_0 c_0}\int b(x')\varphi_0(x')\exp(ik_0|x_1 - x'|)dx' \\ &- \frac{i}{2k_0}\int \nu(x')\varphi_0(x')\exp(ik_0|x_1 - x'|)dx' \\ &\equiv \varphi_0(x_1) - \delta\varphi_b(x_1) - i\delta\varphi_\nu(x_1). \end{aligned} \tag{12}$$

The imaginary unit before the second integral term in Eq. (12) is evidence of a phase shift by $\pm\pi/2$ in the wave scattered from the inhomogeneity of $\nu(\mathbf{r})$ with respect to the primary wave; i.e., it determines the advance or delay of the total transmitted wave. Since the inhomogeneity in velocity does not produce thermal self-radiation, no energy compensation occurs for the wave scattered by this inhomogeneity. Its power is proportional to the power of the primary wave, i.e., to the temperature $T_{bg}(\mathbf{r})$ of the background thermoacoustic field.

Now, if we abandon the requirement of sufficiency of the first Born approximation and proceed to the iterative expansion of the Lippmann–Schwinger equation into a series, then taking into account of terms with the order of smallness no higher than the second in $\Gamma_{12}(\tau)$ turns out to be sufficient for further consideration, because the layer is thin (and in the general case, because the linear dimensions of the resolution element of a correlation system are sufficiently small, about $\lambda/4$). In this approximation, the expression for $\Gamma_{12}(\tau)$ is analogous to Eqs. (5) and (6) with allowance for Eq. (7), but the expansion terms corresponding to scattering by the inhomogeneities $b(\mathbf{r})$ and $\nu(\mathbf{r})$ are taken into account in the correction $\delta\varphi$ up to the second order of smallness. In this case, the basic conclusions are as follows:

(i) The real part of the coherence function "phased" with the layer (i.e., when $\tau = \bar{\tau}_{12}$) consists of a term proportional to the absorption coefficient and the temperature difference $(T - T_{bg})$, and also to a term proportional to the square of ν and the absolute temperature T_{bg}:

$$\mathrm{Re}\,\Gamma_{12}(\tau = \bar{\tau}_{12}) \sim A(b)(T - T_{bg}) + B^-(\nu^2)T_{bg}. \tag{13}$$

(ii) The imaginary part of the "phased" function $\Gamma_{12}(\tau = \tau_{12}^-)$ vanishes,

$$\mathrm{Im}\,\Gamma_{12}(\tau = \tau_{12}^-) = 0,$$

because $\mathrm{Im}\langle \varphi_{01}\delta\varphi_1^*\rangle = -\mathrm{Im}\langle \delta\varphi_2\varphi_{02}^*\rangle$ at $\tau = \tau_{12}^-$ (see Eqs. (6) and (7)). In this case, in the first Born approximation, the terms of the form $\langle\varphi_{01}(i\delta\varphi_{v1})^*\rangle$ and $\langle(i\delta\varphi_{v2})\varphi_{02}^*\rangle$ compensate each other at $\tau = \tau_{12}^-$.

Nevertheless, the terms of the type $\langle\varphi_0\delta\varphi^*\rangle$ can be reconstructed in a somewhat different experiment. For this purpose, in the same experimental scheme given in Fig. 1, it is necessary to introduce additional hydrophones *3* and *4* positioned on the other side of the layer, opposite hydrophones *1* and *2*, respectively. It is also assumed that all hydrophones are essentially transparent to thermoacoustic radiation and possess a double-sided sensitivity to radiation. The inclusion of some details of the thermodynamics of measurements using such hydrophones and the possibility of their additional radiation due to their coupling with the input stages of amplifiers can make the consideration somewhat more complicated but in essence changes nothing; i.e., the presence of hydrophones *3* and *4* does not affect the previous conclusions. The function of mutual coherence $\Gamma_{32}(\tau)$ for the hydrophone pair *3–2* has two peaks at the delays $\tau = \pm\tau_{32}^+$. The value of τ_{32}^+ is equal to the total propagation time of the signal φ_{01} from hydrophone *3* to the scattering layer and further to hydrophone *2* in the form of the waves $\delta\varphi$ scattered by the components b and ν of the layer inhomogeneity ($\delta\varphi \approx \delta\varphi_b + i\delta\varphi_\nu$ in the first Born approximation):

$$\begin{aligned}\Gamma_{32}(\tau = \tau_{32}^+) &= \langle \varphi_{01}|_t \times (\varphi_{02} - \delta\varphi_2 - \delta\varphi_1 + \varphi_T)^*|_{t+\tau_{32}^+}\rangle \\ &= -\langle \varphi_{01}|_t \times \delta\varphi_1^*|_{t+\tau_{32}^+}\rangle.\end{aligned}$$

The peak $\Gamma_{32}(\tau = -\tau_{32}^+)$ of the same function $\Gamma_{32}(\tau)$ for the delay $\tau = -\tau_{32}^+$ is provided by the signal propagating from hydrophone *2* to the layer and further to hydrophone *3*. An analogous situation takes place for the function $\Gamma_{41}(\tau)$ for the hydrophone pair *4–1*.

In the case of total delays, the thermal self-radiation of the layer φ_T is uncorrelated at the receiving hydrophones and does not contribute to the coherence function. In this case, the real part $\mathrm{Re}\,\Gamma_{32}(\tau = \pm\tau_{32}^+)$ is determined by the terms proportional to bT_{bg} and $\nu^2 T_{bg}$, and the imaginary part, by the term of the form νT_{bg}:

$$\mathrm{Re}\,\Gamma_{32}(\tau = \pm\tau_{32}^+) \sim -\frac{1}{2}A(b)T_{bg} + \frac{1}{2}B^+(\nu^2)T_{bg}, \quad (B^+(\nu^2) \approx B^-(\nu^2)), \tag{14}$$

$$\mathrm{Im}\,\Gamma_{32}(\tau = \pm\tau_{32}^+) \sim C(\nu)T_{bg}. \tag{15}$$

It follows from Eqs. (13) and (14) that the difference

$$\begin{aligned}&\mathrm{Re}\,\Gamma_{12}(\tau = \tau_{12}^-) - 2\mathrm{Re}\,\Gamma_{32}(\tau = \tau_{32}^+) \\ &= \mathrm{Re}\,\Gamma_{12}(\tau_{12}^-) - [\mathrm{Re}\,\Gamma_{32}(\tau_{32}^+) + \mathrm{Re}\,\Gamma_{32}(-\tau_{32}^+)] \sim \alpha T\end{aligned} \tag{16}$$

makes it possible to estimate the value of the product of the absorption coefficient and the local value of temperature somewhat more precisely than directly from the value of $\mathrm{Re}\,\Gamma_{32}(\tau = \pm\tau_{32}^+)$ at close values of T and T_{bg}. In fact, the measurement of $\Gamma_{32}(\tau)$ at total delays represents an active location of inhomogeneity, when the background thermoacoustic field plays the role of the probing radiation.

The principal terms are reduced in Eqs. (13)–(15). Thus, the behavior of the real components of the coherence functions, $\mathrm{Re}\,\Gamma_{12}(\tau = \tau_{12}^-)$ and $\mathrm{Re}\,\Gamma_{32}(\tau = \pm\tau_{32}^+)$, and the imaginary component, $\mathrm{Im}\,\Gamma_{32}(\tau = \pm\tau_{32}^+)$, is different. It depends on both the change in the temperature of the background thermoacoustic field and the type of inhomogeneities.

CORRELATION PROPERTIES OF THE THERMOACOUSTIC RADIATION OF AN INHOMOGENEOUS MEDIUM

The simplest model of a thin layer provided an opportunity to fully clarify the behavior of the correlation properties of the fields of local sources of the self- and scattered thermoacoustic radiation.

In the general case, the analysis of the situation is somewhat more complex, being the same in essence. For example, in a 2D case, the consideration of the correlation properties of the field of a refractive-absorbing inhomogeneity with small wave dimensions, which is located in a volume with absorbing walls, produces the results analogous to those given above. They can be obtained by considering a contour Σ (for example, a circle) containing the studied region V. It is assumed that receivers with small wave dimensions and also small angular (with respect to the points of the studied region) dimensions are positioned along this contour (Fig. 2). For further analysis, it is necessary to examine the secondary source producing a scattered signal that is correlated with the background field received by a fixed pair of hydrophones P_i and P_k. For this purpose, it is necessary to reconstruct the field within the region of the inhomogeneity's location by using the Kirchhoff

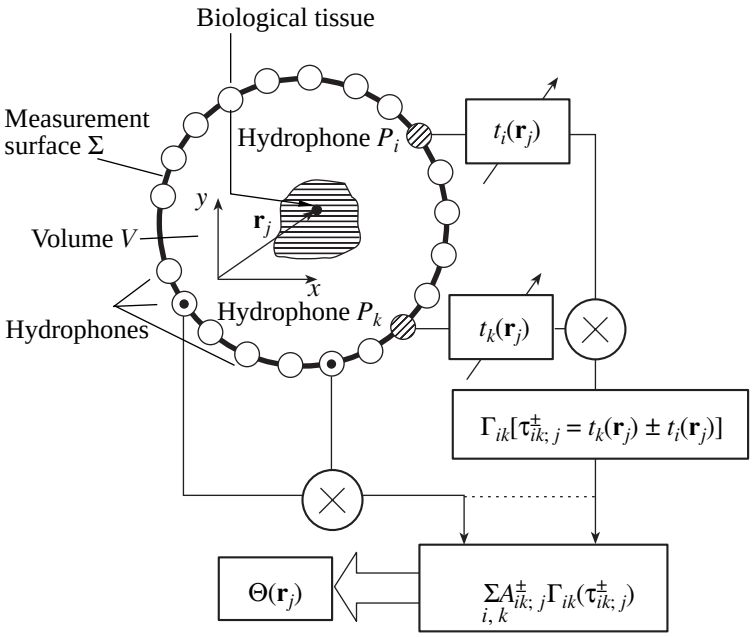

Fig. 2. Correlation system with a circular array.

equation written in two alternative forms: for the advanced and retarded Green functions G^- and G^+,

$$\int_{\Sigma}\left[\varphi(\mathbf{r}')\frac{\partial G^{\pm}(\mathbf{r}-\mathbf{r}')}{\partial \mathbf{n}'} - G^{\pm}(\mathbf{r}-\mathbf{r}')\frac{\partial \varphi(\mathbf{r}')}{\partial \mathbf{n}'}\right]d\sigma' = \varphi(\mathbf{r}), \quad \mathbf{r}\in V. \tag{17}$$

Here, $\mathbf{n}'$ is the outer normal to the contour Σ and the functions $G^{\pm}(\mathbf{r}-\mathbf{r}')$ satisfy the equation $\nabla^2 G^{\pm} + k_0^2 G^{\pm} = \delta(\mathbf{r}-\mathbf{r}')$.

In this case, at the site of the inhomogeneity, the field component exciting the scatterer and correlated with the signals received at the points P_i and P_k is determined by Eq. (17) with $G^-(\mathbf{r})$ and by the regions of integration in the vicinities of these points. This equation provides an opportunity to describe the correlation properties of the field resulting from the scattering of the background field by an elementary inhomogeneity and received by the receivers P_i and P_k and to combine its correlation function with an analogous correlation function of thermal self-radiation of the absorbing component of the same inhomogeneity, i.e., to construct a quantity $\Gamma_{ik}(\tau)$ analogous to $\Gamma_{12}(\tau)$ for a thin layer. The correlation of the scattered signals received by the receivers P_i and P_k reaches its maximum in this case at a relative time delay of $\tau = \tau^-_{ik}$, compensating the difference in the propagation times of a signal from an elementary inhomogeneity to the observation points.

An alternative form of Eq. (17) uses the retarded Green function $G^+(\mathbf{r})$; i.e. it describes the field in the region within Σ, which is produced by external sources, using the field entering the region (as having differed from Eq. (17) for G^-, which provides the same description using the field leaving the region). This equation for G^+ provides an opportunity to describe the correlation properties of the same function $\Gamma_{ik}(\tau)$, which is analogous to the quantity $\Gamma_{32}(\tau)$ for a thin layer, between the background field entering the region and the field scattered by the inhomogeneity within Σ, i.e. to describe again a peculiar location mode. This means that the background field from the walls, which is detected by one of the receivers (e.g., P_i), reaches the elementary scattering inhomogeneity under investigation and the field scattered by it then reaches the second receiver P_k within a total time of τ^+_{ik}. An analogous situation takes place in the case of the opposite time shift ($-\tau^+_{ik}$) on account of the propagation of the background field from the second receiver P_k to the inhomogeneity and further, to the first receiver P_i. This means that $\Gamma_{ik}(\tau)$ has two more peaks at the values $\tau = \tau^-_{ik}$ (apart from the peak at $\tau = \pm\tau^+_{ik}$).

The examination of the correlation properties coincides in many respects with that in the case of the analysis of the thin-layer model. It leads to analogous results: the real part of the mutual coherence function of the field $\mathrm{Re}\Gamma_{ik}(\tau = \tau^-_{ik})$ "phased" with the region of inhomogeneity by a compensation of the difference in the times of propagation to P_k and P_i is determined by the contribution of the sum of the terms of the type $\sim b^{m+1}\nu^{2n}$ ($m, n = \overline{0, \infty}$) proportional to $(T - T_{bg})$ and all degrees of b, and also by the sum of the terms with even

degrees of ν proportional to the temperature of the background radiation T_{bg}. The real part of the coherence function $\mathrm{Re}\Gamma_{ik}(\tau = \pm\tau_{ik}^{+})$ phased by the compensation of the sum of the propagation times is determined by the sum of the terms of the type $\sim b^{m+1}\nu^{2n}$ (m, $n = \overline{0, \infty}$) proportional to the inverted absolute background temperature, i.e., $(-T_{bg})$, and by the sum of the terms containing even degrees of ν and also proportional to T_{bg}. The difference between the real parts of the coherence functions $\mathrm{Re}\Gamma_{ik}(\tau_{ik}^{-}) - 2\mathrm{Re}\Gamma_{ik}(\tau_{ik}^{+})$ in the case of the compensation of the corresponding difference and summary delay times provides an opportunity to determine the form of the distribution $\alpha(\mathbf{r})T(\mathbf{r})$, analogously to Eq. (16). Primarily, this is the spatial distribution of the absorption coefficient, which is an important factor for diagnostics, since it provides an opportunity to judge, e.g., the blood saturation of a tissue [7, 8].

The imaginary part of the coherence function, $\mathrm{Im}\Gamma_{ik}(\tau = \pm\tau_{ik}^{+})$, in the case of the compensation of the total delay time is determined by the terms containing all degrees of b and uneven degrees of ν and also proportional to the temperature T_{bg}; i.e., these are the terms of the type $\sim b^{m}\nu^{2n+1}T_{bg}$ (m, $n = \overline{0, \infty}$), the lowest of which is the term $\sim\nu T_{bg}$. Since the dimensions of a resolution element for a multi-input correlation system are sufficiently small ($\leq\lambda/2$), then, as before, it is sufficient to take into account only the term linear in b (and in the case of a more precise examination, also the term quadratic in b) and the term quadratic in ν in the real parts $\mathrm{Re}\Gamma_{ik}(\tau = \tau_{ik}^{-})$ and $\mathrm{Re}\Gamma_{ik}(\tau = \pm\tau_{ik}^{+})$, and in the imaginary part $\mathrm{Im}\Gamma_{ik}(\tau = \pm\tau_{ik}^{+})$, the term linear in ν and T_{bg}. The expressions are similar to Eqs. (13)–(15) at the delay times $\tau_{ik}^{\pm}$ corresponding to the required phasing.

These properties are sufficient for an almost complete estimation of the acoustic parameters of a tissue and the temperature conditions in its volume.

SCHEME OF ACTIVE–PASSIVE THERMOACOUSTIC TOMOGRAPHY OF A NONUNIFORMLY HEATED INHOMOGENEOUS MEDIUM

A system of correlation thermotomography can be realized in various ways [1, 2]. A correlation scheme (Fig. 2) consisting of a circular receiving array is selected for further analysis. Each pair of the receiving elements of the system array (i, k) is used to estimate the time dependence of the corresponding functional unit of the coherence matrix: $\Gamma_{ik}(\tau) = \overline{u_i(t)u_k^{*}(t+\tau)}$. In the case of processing, the values of the measured coherence functions $\Gamma_{ik}(\tau)$ are summarized with the weights compensating the total or difference time delay and signal attenuation in the course of the propagation from a separated local source at the point $\mathbf{r}$ to the observation points and also taking into account the data redundancy depending on the array geometry. The analysis of the formation methods for the matrix of weighting coefficients and the whole algorithm goes beyond the framework of this paper and will be presented in a separate publication. The only point important for further consideration is the fact that the estimates for the spatial distribution of the power density components of the sources of the corresponding type are formed as a result of such a processing. Each resolution element of the region under investigation has unknown local values of the absorption coefficient, ultrasonic phase velocity, intrinsic temperature, and temperature of the background field. Nevertheless, it is possible to suggest a scheme of measurements that provides an opportunity to evaluate all these quantities.

Let us consider the temperature dependence of the background field formed by the local power density of the effective primary sources of thermal field and the secondary sources of the scattered field, as estimated in the process of the space–time accumulation of the real and imaginary parts of the functions $\Gamma_{ik}(\tau^{\pm})$. At the first stage, it is assumed that the operations of measurement and formation of the estimate of the power density are performed without errors; i.e., the propagation time is compensated exactly.

The real part of the accumulated sum is $\mathrm{Re}\Gamma_{\Sigma}^{-} \equiv \mathrm{Re}\sum_{i,k} A_{ik;j}^{-}\Gamma_{ik}(\tau_{ik;j}^{-})$, where $A_{ik;j}^{-}$ are the weighting coefficients and $\tau_{ik;j}^{-} = t_k(\mathbf{r}_j) - t_i(\mathbf{r}_j)$ are the relative (i.e., difference) time delays for the ith and kth receivers and the jth spatial element of the region under investigation. This real part gives the total estimate of the power of thermoacoustic sources, which consists of terms of the type $\sim b^{m+1}\nu^{2n}(T - T_{bg})$ (m, $n = \overline{0, \infty}$) proportional to the product of the viscous loss coefficient and the temperature difference $(T - T_{bg})$ and also of the contribution of the terms with even degrees of ν (foremost, this is the term of the second order in ν), this contribution being proportional to the absolute temperature of background radiation. The imaginary part of the accumulated coherence function has the form $\mathrm{Im}\Gamma_{\Sigma}^{+} \equiv \mathrm{Im}\sum_{i,k} A_{ik;j}^{+}\Gamma_{ik}(\tau_{ik;j}^{+})$, where $\tau_{ik;j}^{+}$ is the total delay time, and it yields the estimate of the local power distribution of the sources of the background field scattered by the velocity inhomogeneities; this estimate is determined by the terms of the type $\sim b^{m}\nu^{2n+1}T_{bg}$ (m, $n = \overline{0, \infty}$), i.e., primarily by the linear term $\sim\nu T_{bg}$. The dependence of the accumulated total values of $\mathrm{Re}\Gamma_{\Sigma}^{-}$ and $\mathrm{Im}\Gamma_{\Sigma}^{+}$ on the temperature factors (in the case of an exact compensation of all time delays, i.e., in the case

of focusing at the region of interest) is analogous to the dependence considered earlier for a single value of $\mathrm{Re}\Gamma_{ik}(\tau = \tau_{ik}^-)$ or $\mathrm{Im}\Gamma_{ik}(\tau = \tau_{ik}^+)$, respectively. In fact, the formation of distributions, i.e., patterns, on the basis of $\mathrm{Re}\Gamma_\Sigma^-$ and $\mathrm{Im}\Gamma_\Sigma^+$ represents a tomography by hyperbolic ($\tau^- = \text{const}$) and elliptic ($\tau^+ = \text{const}$) sections.

In the case of an exact compensation, in phasing to a definite element of inhomogeneity, the characters of the real and imaginary parts of the total coherence functions $\Gamma_\Sigma^\pm$ are different and clearly defined, and the mutual influence of Γ_Σ^- and Γ_Σ^+ at the point of phasing is virtually absent in the case of a sufficiently wide band of utilized frequencies Δf: $\tau_{ik;\,j}^+ - \left|\tau_{ik;\,j}^-\right| \gg 1/\Delta f\ \forall i, k, j$.

Moreover, in the process of scanning, in the case of phasing to a certain spatial point different from the position of a solitary inhomogeneity, it is important that no mutual influence of the real and imaginary parts of the function Γ_Σ^+ be present. This means that the instrument functions constructed on the basis of $\mathrm{Re}\Gamma_\Sigma^+$ and $\mathrm{Im}\Gamma_\Sigma^+$ must not affect each other. To prove this requirement, instrument functions of a correlation system were calculated for the case of exact phasing of the coherence function $\Gamma_{ik}(\tau = \tau_{ik;\,j}^+)$ of a point source field. It was found that, even in the case of a narrowband signal, the influence of the imaginary components $\mathrm{Im}\Gamma_{ik}(\tau_{ik;\,j}^+)$ on the real part of the instrument function is negligibly small. The influence of the components $\mathrm{Re}\Gamma_{ik}(\tau_{ik;\,j}^+)$ on the imaginary part of the instrument function is also small. This means that a "quasi-point" inhomogeneity of absorption produces a response of the correlation system only in the form of the real component of the instrument function and the imaginary component of the response to the same inhomogeneity of phase velocity is determined by the value of ν (in this case, the real part of the instrument function is the quantity of the second degree of smallness with respect to ν).

As a result of the "focusing" of the matrix elements $\Gamma_{ik}(\tau)$, two "images" are obtained: $\mathrm{Re}\Gamma_\Sigma^-(\mathbf{r}) \equiv \Theta_1(\mathbf{r})$ and $\mathrm{Im}\Gamma_\Sigma^+(\mathbf{r}) \equiv \Theta_3(\mathbf{r})$. These images determine the power distribution of effective sources in the medium at certain distributions of the medium temperature $T(\mathbf{r})$ and the local temperature of the background radiation $T_{bg}(\mathbf{r}) = T_1(\mathbf{r})$, which can be described by the expressions generalizing the first expression in Eqs. (9):

$$\beta(\mathbf{r})[T(\mathbf{r}) - T_1(\mathbf{r})] + \gamma(\mathbf{r})T_1(\mathbf{r}) = \Theta_1(\mathbf{r}), \quad (18)$$

$$\zeta(\mathbf{r})T_1(\mathbf{r}) = \Theta_3(\mathbf{r}), \quad (19)$$

where, in the approximation of lower degrees, $\beta(\mathbf{r})$ is the term linear in the coefficient $b(\mathbf{r})$, $\gamma(\mathbf{r})$ is the term quadratic in $\nu(\mathbf{r})$, and $\zeta(\mathbf{r})$ is the term linear in $\nu(\mathbf{r})$, the latter being determined by single scattering of the field of background radiation from the velocity inhomogeneities $\nu(\mathbf{r})$. Taking only these principal terms into account is sufficient, because signals from various spatial regions with dimensions of the order of magnitude of the resolution element contribute independently to the estimates of $\Gamma_\Sigma^\pm$, and, as has been mentioned, the dimensions of the resolution element do not exceed $\lambda/2$.

It is impossible to determine all unknown parameters of the medium from Eqs. (18) and (19). Therefore, it is necessary to perform additional measurements at the second background temperature $T_{bg}(\mathbf{r}) = T_2(\mathbf{r})$. A direct change of this temperature by heating the absorbing walls is difficult, because it requires a long time for heating, and it is inconvenient from all points of view. Therefore, we suggest introducing additional active sources of the noise field into the tomography scheme so that this noise field is added to the thermoacoustic field present in the region under investigation. These sources excited by generators of random or pseudorandom signals must produce a field similar (in its space–time correlation properties) to the natural thermal noise field. The methods of formation of such a field need additional discussion that goes beyond the limits of this paper. It may be just noted that there are several technologically sensible methods of its generation.

In this case, two analogous equations for the second value of the background temperature are added to Eqs. (18) and (19):

$$\beta(\mathbf{r})[T(\mathbf{r}) - T_2(\mathbf{r})] + \gamma(\mathbf{r})T_2(\mathbf{r}) = \Theta_2(\mathbf{r}), \quad (20)$$

$$\zeta(\mathbf{r})T_2(\mathbf{r}) = \Theta_4(\mathbf{r}). \quad (21)$$

We assume for simplicity that the dimensional proportionality factors necessary in Eqs. (18)–(21) are taken into account in the values of Θ_1–Θ_4. An additional difficulty is the fact that the temperature of background radiation T_2 created in an active way is produced totally by external sources. In this case, the degree of penetration of external radiation into the absorbing medium is *a priori* unknown. However, the local value of the temperature $T_2(\mathbf{r})$ can be estimated using the fact that the suggested technique is intended for medical applications.

If the temperature of all elements of the correlation tomography system is close to the temperature of the tissue under investigation, i.e., about 310 K, the background temperature $T_1(\mathbf{r})$ is close to this value with a relative accuracy of $\sim 10^{-2}$. A better coincidence with the average tissue temperature can be realized by setting the system temperature equal to the temperature of a specific patient. However, as we will see below, this is not necessary. Therefore, the value of $T_1(\mathbf{r})$ in Eqs. (18)–(21) may be considered to be approximately

constant and known. In this case, the estimates $\zeta(\mathbf{r})$ and $T_2(\mathbf{r})$ follow from Eqs. (19) and (21):

$$\zeta(\mathbf{r}) = \frac{\Theta_3(\mathbf{r})}{T_1}; \quad T_2(\mathbf{r}) = \frac{\Theta_4(\mathbf{r})}{\Theta_3(\mathbf{r})}T_1. \tag{22}$$

Deducting Eq. (20) from Eq. (18), it is easy to obtain an estimate

$$b(\mathbf{r}) \sim \beta(\mathbf{r}) = \frac{\Theta_1(\mathbf{r}) - \Theta_2(\mathbf{r})}{T_2(\mathbf{r}) - T_1(\mathbf{r})} + \gamma(\mathbf{r}). \tag{23}$$

The value of $\gamma(\mathbf{r})$ can be obtained from the already estimated values of $\zeta(\mathbf{r}) \sim \nu(\mathbf{r})$, because $\gamma(\mathbf{r}) \sim \nu^2(\mathbf{r})$, however this is not exactly needed. This follows from the fact that the variations of sound velocity and absorption typical of biological tissues lead to comparable distortions of the field. For example, the relative distortions of the megahertz-range field in the course of the transmission through a medium with a velocity that differs from the background velocity by 10 m/s or has an excessive absorption of 2 dB/cm are close, and the relative distortion of the field within the length of the resolution element ~1 mm does not exceed 10^{-2}. Therefore, the term of the second order of smallness $\gamma(\mathbf{r})$ is many tens of times smaller than the first order term $\beta(\mathbf{r})$ and can be ignored in the estimate given by Eq. (23):

$$\beta(\mathbf{r}) \approx \frac{\Theta_1(\mathbf{r}) - \Theta_2(\mathbf{r})}{T_2(\mathbf{r}) - T_1(\mathbf{r})}. \tag{24}$$

The deviation of the local temperature from the background value of $T_1(\mathbf{r})$ is estimated with the same relative accuracy $\sim 10^{-2}$ by the expression following from Eqs. (18) and (24):

$$\Delta T(\mathbf{r}) \equiv T(\mathbf{r}) - T_1(\mathbf{r}) \approx \frac{\Theta_1(\mathbf{r})[T_2(\mathbf{r}) - T_1(\mathbf{r})]}{\Theta_1(\mathbf{r}) - \Theta_2(\mathbf{r})}. \tag{25}$$

It is necessary to stress that, in the case $T_2(\mathbf{r}) = (2\text{–}3)T_1(\mathbf{r})$, we have $|\Theta_2(\mathbf{r})| \gg |\Theta_1(\mathbf{r})|$. In this case,

$$\Delta T(\mathbf{r}) \approx -\frac{\Theta_1(\mathbf{r})}{\Theta_2(\mathbf{r})}[T_2(\mathbf{r}) - T_1(\mathbf{r})]. \tag{26}$$

The resulting estimate $\Delta T(\mathbf{r})$ presumes the constancy of the temperature of the background radiation $T_1(\mathbf{r})$ at the first step. It is easy to perform further iterative refinement of all estimates. Indeed, knowledge of the first step estimates $\Delta T(\mathbf{r})$ and the distribution of the absorption coefficient $b(\mathbf{r})$ from Eq. (24) provides an opportunity to refine the distribution of $T_1(\mathbf{r})$, and, using it, also the distribution of $T_2(\mathbf{r})$. In this way, one can refine the estimate $\Delta T(\mathbf{r})$. The iterative procedure can be continued further if needed. However, the expediency of such a continuation requires a very high accuracy of the initial data.

INFLUENCE OF THE MEASUREMENT ERRORS AND OF THE PRECISION OF THE ALGORITHM OPERATIONS

It is natural that the question of the required precision of the implementation of all algorithm stages is of major importance for the evaluation of the practical feasibility and capabilities of the system solving the problems of such complexity. In fact, there are several relevant questions, and they are of both fundamental and technological nature, remaining nevertheless very important. The question of the first kind is about the evaluation of the required accumulation factor in a multielement correlation system that is necessary for the precision of the estimate of the basic statistical parameter, i.e., temperature, to make the estimate informative. Indeed, in the case of thermal tomography measurements, the values of $T(\mathbf{r})$, $T_1(\mathbf{r})$, and $T_2(\mathbf{r})$ are reflected in the intensities of random waves, which are estimated by correlative accumulation. To provide the physical meaning of the intermediate and final estimates with the precision $\sim \delta T$, it is necessary for the accumulation factor F to be sufficiently large,

$$F \geq (T_{1,2}/\delta T)^2, \tag{27}$$

since, in the opposite case, the fact of temperature variation by the value δT makes it impossible to evaluate it statistically using the considered techniques.

The accumulation factor in a correlation system is determined by the number of correlative pairs in use, the band of the received frequencies Δf, and the averaging time t_0:

$$F \sim M(M-1)\Delta f t_0.$$

Here, M is the number of hydrophones in the array. At $T_{1,2} \sim 300$°K and $\delta T \sim 0.1$°K, the accumulation factor $F > (10^7\text{–}10^8)$ is necessary. This can be realized readily at $M \geq 10^2$ and $\Delta f t_0 \sim 10^5$, i.e., in the case of utilization of an extended array. On the contrary, in an array with a small number of elements like the one given in Fig. 1, the indicated precision can be attained only by using a considerably longer accumulation time. In the process of accumulation, it is necessary also to take into account the fact that a noticeable part of the received signal is not produced by the thermal noise of the medium but represents noise of different origins (losses in a transducer, input stage noise, etc.). As a result, a several times greater accumulation factor may be required. The value of the accumulation parameter obtained above and satisfying the condition given by Eq. (27) represents a lower estimate corresponding to the observation of a solitary heated object with the dimensions of the order of magnitude of the resolution element. In the case of processing the data from a large heated region, a signal from an elementary volume w is masked by the noise radiation from other elements of the medium with the effective volume $V' \sim 1/\alpha^3$, and to

estimate the temperature T of the volume w with the precision δT, it is necessary for the ratio of the response of the correlation system to fluctuations at the same output (i.e., the signal-to-noise ratio) to exceed unity: $\left(\frac{S}{N}\right)_{\text{out}} \cong F\left(\frac{w}{V'}\frac{\delta T}{T}\right)^2 > 1$. At $w \approx (0.5\ \text{cm})^3 \approx 10^{-1}\ \text{cm}^3$, $V' \approx (10 \times 10 \times 1\ \text{cm}) = 10^2\ \text{cm}^3$, $\delta T \approx 0.5$°K, and $T \approx 300$°K, an estimate $F \geq 5 \times 10^{11}$ is obtained. This estimate noticeably exceeds the previous estimate and requires an increase in the parameter of time accumulation up to values of $\Delta f t_0 \sim 5 \times 10^6$ at $M^2 \sim 10^5$.

A provision made for the required accumulation factor is necessary first of all for the reconstruction of the distribution $\Theta_1(\mathbf{r})$ with the sufficient precision, since just this precision determines the validity of the estimate $\Delta T(\mathbf{r})$. Errors in estimating other quantities involved in Eq. (26) play a less important role. An increase in the resolution requirements leads to a sharp growth of the accumulation parameter up to values that are unreal in practice. The value of w used above far exceeds the volume of the resolution element. Therefore, the secondary averaging of the estimates $\Theta_1(\mathbf{r}) \div \Theta_4(\mathbf{r})$ over the corresponding region w can be used, which, naturally, smoothes the fluctuations of these estimates.

The second important point determining the precision of the estimate of the distribution $\Theta_1(\mathbf{r})$ is the errors in the compensation of the propagation delay times in the process of the reconstruction of the distributions $\mathrm{Re}\Gamma_\Sigma^-(\mathbf{r})$ and $\mathrm{Im}\Gamma_\Sigma^+(\mathbf{r})$. The sources of such errors can be of two types. First, these are the inaccuracies in hydrophone positioning in the array and the deviations in the acoustic parameters of hydrophones. These technical errors are reduced as the equipment is modified. The second type is the distortions introduced by the inhomogeneities of ultrasonic velocity in the medium under investigation. These inhomogeneities can be estimated beforehand in the mode of active tomography in the same system, using techniques analogous to the ones considered by Parkhomenko *et al.* [9]. They can be evaluated also directly from the data on the focusing of $\mathrm{Im}\Gamma_\Sigma^+(\mathbf{r})$, since this distribution is determined by terms of the form νT_{bg} (see Eq. (22)), and the parameter $\nu(\mathbf{r}) = \frac{\omega^2}{c_0^2} - \frac{\omega^2}{c^2(\mathbf{r})}$ depends on the distribution of the phase velocity. An iterative technique can be used for the refinement of the estimate of the velocity $c(\mathbf{r})$, which leads to a considerable reduction of errors. Another factor making the situation simpler is the fact that the errors in focusing, i.e., in the values of $A_{ik;\,j}^{\pm}$ and $\tau_{ik;\,j}^{\pm}$, are averaged over a large number of components ($\sim M^2$) and, hence, are reduced by a factor of M (in the case of a symmetrical distribution of phasing errors, or at least in the case of a zero median of their distribution). The number of receivers in a complete correlation system lies within 10^2–10^3. As a result, the influence of the fluctuation errors of focusing can be reduced to the level of the corrections of the second order of smallness. Nevertheless, possible systematic errors can be the main origin of the errors in the estimation of the temperature $\Delta T(\mathbf{r})$ (but not the parameters $\nu(\mathbf{r})$ and $b(\mathbf{r})$, which are influenced by these errors to a lesser extent).

CONCLUSION

The proposed scheme of thermal tomography is not the only one possible technologically. However, it provides an opportunity to evaluate all parameters of a tissue and analyze the reasons and factors determining the capabilities and limitations inherent in thermal tomography. The proposed scheme takes into account the basic features of the formation of a thermoacoustic field of a complex object. The space–time correlation properties of such a field (Gaussian!) are the comprehensive initial data (the so-called sufficient statistics). Therefore, the estimates obtained above for the attainable sensitivity of a thermal system are universal to a certain extent.

The main factor providing for the success or failure in designing highly informative systems of thermal tomography is precision. Primarily, this is the precision of taking into account the influence of refraction and propagation time in a biological tissue.

A difficult technological problem is the large amount of calculations, which was evaluated in [2]. An important difficult problem is also the design of an array (uniformly dense or sparse [9]) with transducers of high degree of similarity and small internal losses. The problem of the introduction of additional calibrated quasi-thermal radiation is also complicated, and the requirements for the characteristics of the latter need additional study.

The proposed active–passive combined method offers some new opportunities that were not considered in this paper, e.g., the formation of a nonstationary or anisotropic pseudorandom field providing additional information on the object.

ACKNOWLEDGMENTS

We are grateful to V.I. Mirgorodskiĭ for a brief discussion, which stimulated us for conducting this study.

The work is supported by the Russian Foundation for Basic Research, project nos. 01-02-16282 and 00-15-96530.

REFERENCES

1. R. A. Hessemer, Jr., US Patent No. 4416552 (22 November 1983).

2. V. A. Burov and E. E. Kasatkina, Akust. Zh. **43**, 162 (1997) [Acoust. Phys. **43**, 135 (1997)].
3. V. I. Babiĭ, Morsk. Gidrofiz. Issled., No. 2 (65), 189 (1974).
4. V. A. Burov and P. I. Darialashvili, in *Proceedings of XI Session of the Russian Acoustical Society* (GEOS, Moscow, 2001), Vol. 2, pp. 34–38.
5. V. A. Burov, E. E. Kasatkina, O. D. Rumyantseva, and S. A. Filimonov, in *Proceedings of XI Session of the Russian Acoustical Society* (GEOS, Moscow, 2001), Vol. 2, pp. 30–34.
6. V. A. Burov, E. E. Kasatkina, O. D. Rumyantseva, and S. A. Filimonov, Acoust. Imaging **26** (2002) (in press).
7. J. Folkman, J. Natl. Cancer Inst. **82**, 4 (1990).
8. S. B. Fox, K. S. Gatter, and A. L. Harris, J. Pathol. **179**, 232 (1996).
9. P. P. Parkhomenko, M. F. Karavaĭ, E. G. Sukhov, *et al.*, Patent of the Russian Federation No. 2145797 C1 (23 June 1999).

Translated by M. Lyamshev

Acoustical Physics, Vol. 48, No. 4, 2002, pp. 423–429. Translated from Akusticheskiĭ Zhurnal, Vol. 48, No. 4, 2002, pp. 485–492.

Year-to-Year Variability of the Long-Range Propagation Conditions in the Norwegian Sea

R. A. Vadov

Andreev Acoustics Institute, Russian Academy of Sciences, ul. Shvernika 4, Moscow, 117036 Russia

e-mail: vadov@akin.ru

Received May 16, 2001

Abstract—On the basis of the experimental data on the sound field formation in the Norwegian Sea, the year-to-year variability of the propagation conditions is estimated. A comparative analysis is performed for the data obtained from two long-range-propagation experiments with explosion-generated signals. The experiments were carried out in summertime (August) on a path crossing the central deep-water part of the Norwegian Sea and were separated in time by a period of four years. Noticeable changes are found to occur in the sound speed fields between the two experiments. These changes are related to a change in the distance between the cores of cold waters (observed in the region of the Norwegian Basin) and warm waters (observed in the region of the Lofoten Basin). According to calculations, the observed changes in the sound speed structure can lead to considerable changes in the propagation anomaly and in the range dependence of the sound field decay. In spite of the noticeable difference in the propagation conditions, the experimental coefficients of low-frequency attenuation differ little for the two experiments. *© 2002 MAIK "Nauka/Interperiodica".*

The Acoustics Institute carried out repeated experiments to study the attenuation, the space–time characteristics, and the energy structure of the sound field in the underwater sound channel (USC) of the Norwegian Sea. In the previous publication [1], these experimental data were used to analyze the spatial variability of the propagation conditions in the Norwegian Sea. A number of experiments carried out with cw sound sources in the Norwegian and Lofoten basins were considered. In two studies of long-range sound propagation, explosion-generated sound signals were used. One of these studies was performed in summertime (August), the second (similar) was carried out four years later. In both experiments, the same propagation paths that crossed the central deep-water part of the Norwegian Sea were used. It is advantageous to compare the data of these two studies to estimate the year-to-year variability of the propagation conditions in the Norwegian Sea.

The hydrological environment of the Norwegian Sea is governed by the currents existing there [2, 3]. Through the Faeroe–Shetland Trench, warm salt waters of the Atlantic Ocean pass into the Norwegian Sea (a branch of the Gulf Stream called the Norwegian Current). From the north and northwest, cold Arctic waters intrude (the Eastern Greenland Current). As the Norwegian Current travels north, streams separate from it and produce large cycles that are directed counterclockwise. The directions of local currents and the depth to which they penetrate are mainly governed by the general relief of the seafloor, which is rather rough in the Norwegian Sea. The central part of the sea is occupied by two basins, the Norwegian and Lofoten, with sea depths up to 3000–3600 m.

The USC axis is shallower in the Norwegian Basin than in the Lofoten. From south to north, the depth of the USC axis changes from 500–600 to 1000–1100 m on the propagation path. This change is accompanied by the formation of the second, weakly pronounced minimum in the sound speed, at the depths ~150–300 m. In the course of the experiments, the sound speeds near the surface and at the depth of the main USC differed by 18–24 m/s. Near the bottom (with a sea depth of 3300 m), the sound speed was by 32–40 m/s higher than that near the surface. Because of the summer warming of the near-surface water layers, a temperature-discontinuity layer occurred at depths of 25–40 m, in which the negative gradient of the sound speed reached –0.7 to –1.3 1/s.

Figure 1 shows the structure of the sound speed field, which was obtained by hydrologically surveying the path during the first and second experiments on long-range propagation of the explosion-generated signals. In surveying, 7–10 sets of hydrological measurements were performed at different distances along the path. In Fig. 1, the neighboring isospeed curves differ by 1 m/s. The sound speed field is related to the bottom relief measured in the first experiment. Although each experiment was accompanied by echo-sounding, the measured profiles were somewhat different, because the transmitting vessel slightly deviated from the path on different tacks. On the other hand, the locations of the most significant bottom rises were nearly the same in all measured bottom profiles.

Two sound speed fields shown in Fig. 1 are noticeably different: mainly in the steepness of the depth

1063-7710/02/4804-0423$22.00

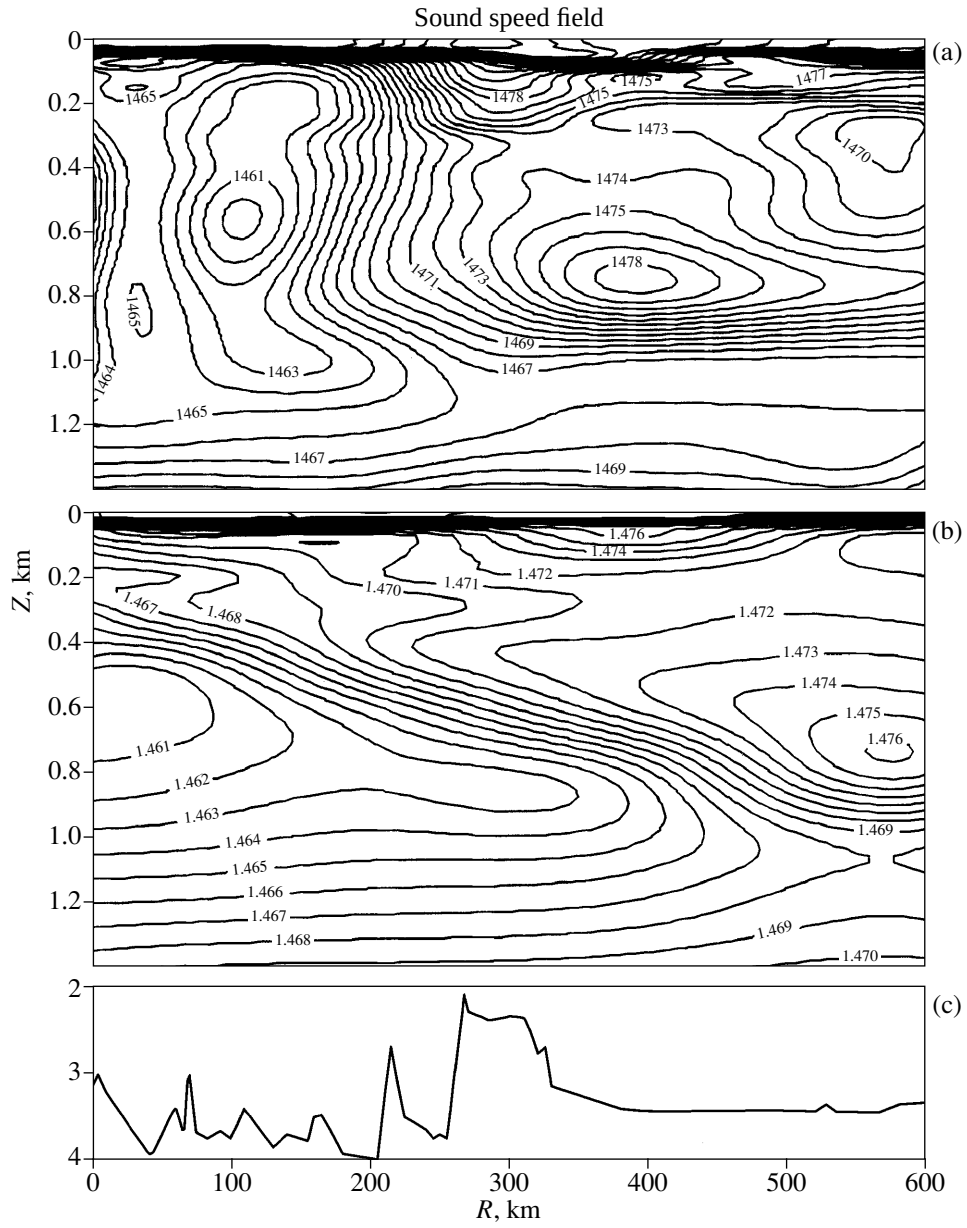

Fig. 1. Sound speed field and the bottom relief measured on the path of long-range propagation of explosion-generated signals in two experiments separated by four years in time. The numbers near isolines indicate the sound speeds (in m/s). (a) The sound speed field in the first experiment; (b) the sound speed field in the second experiment; and (c) the bottom relief along the path (according to echo-sounding survey that accompanied the first experiment).

increase observed for the isospeed curves along the path. The characteristic feature of the sound speed fields is the existence of a core of cold waters in the Norwegian Basin (with a sound speed of about 1460 m/s at depths of ~600–650 m). In the Lofoten Basin, a core of warm waters exists (with sound speeds of ~1476–1478 m/s). For the two experiments, the distance between the cores (as measured along the path) differs by a factor of about two. When this distance was 250–300 km (in the first experiment), the isospeed curves became deeper rather sharply in the region between the Norwegian and Lofoten basins. When the cores were separated by 550–600 km (in the second experiment), the depth of isospeed curves changed smoothly. The cold and warm cores observed in the experiments can be undoubtedly related to the cold Arctic and warm Atlantic waters that are brought into the Norwegian Sea by the East-Island Current and the branch of the Gulf Stream.

The cold core of the Norwegian Basin can be also detected from the Naval Oceanographic Office Data Warehouse [4]. However, the more mobile core of warm waters, which we observed in the Lofoten Basin, does not manifest itself in this database.

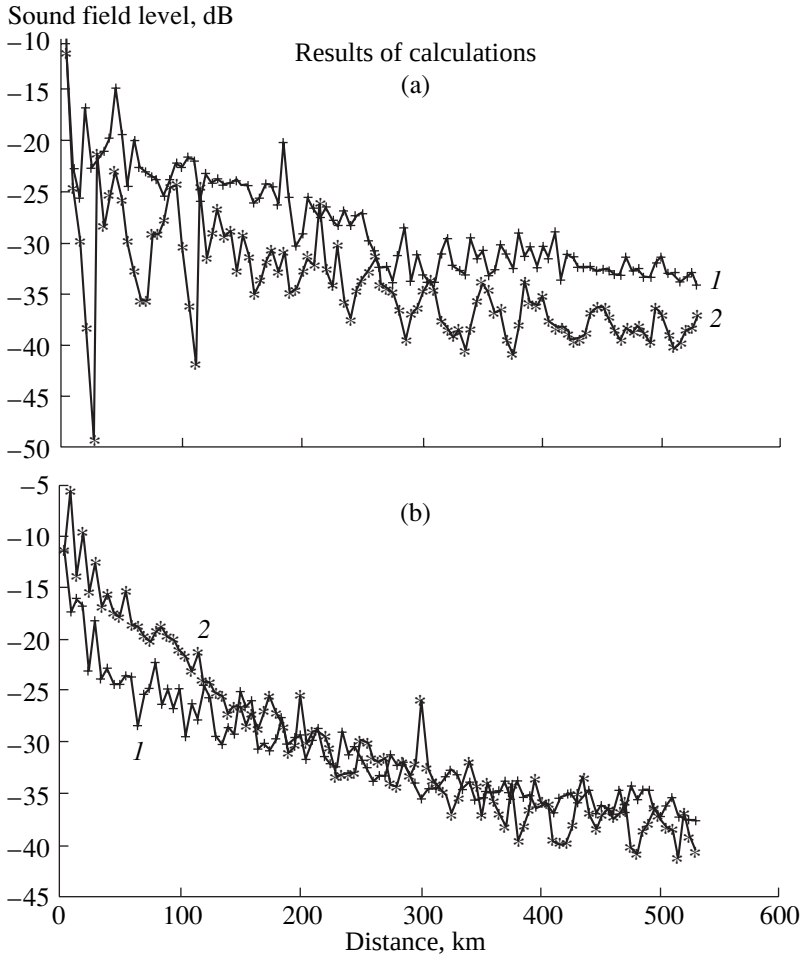

Fig. 2. Calculated sound fields for the (*1*) first and (*2*) second experiments separated by four years. The source and receiver depths are (a) both 300 m and (b) 300 and 600 m, respectively.

It is worth considering the effects of sound speed variability caused by the aforementioned changes in the location of the warm water core. Unfortunately, the experimental layouts (namely, the source and receiver positions) are noticeably different for the two sets of measurements, and comparative analysis of the effect of environmental changes on the sound field is difficult. To perform such an analysis, we calculated the sound field decay on the path for both combinations of the source and receiver positions. In the calculations, the computer code by Vagin [5] was used for a plane sea surface and an absorbing bottom. A number of transmission and reception horizons were specified, including those that corresponded to the experiments. Figure 2 shows the decays of the sound field level, which were calculated for the hydrological situations of the first and second experiments. The sound sources that moved along the path were at depths of 300 and 600 m, the receiver was at the 600-m horizon, at the southern end point of the path. The difference in the decay laws are quite noticeable. In the first case, the levels of the sound field change by 5–7 dB (on the average) along nearly the entire path. In the second case, a considerable change in the steepness of the decay is observed (up to 10–15 dB at 1000 km).

In the second experiment with the explosion-generated sound sources, the receiving vessel was at the southernmost point of the path. The transmitting vessel traveled at a speed of 11 knots away from the receiving one and dropped small explosive charges equipped with pressure-sensitive detonators. The dropping intervals were 7–8 min for the first and second convergence zones and 20 min for the rest of the path. The charges exploded at a depth of 150 m. At the moments of dropping, the distance between the vessels was determined from the travel time of the sound signal. Periodically, the distance was corrected by means of the satellite navigation systems of both vessels. In total, 100 charges were exploded. The explosion-generated signals were received by omnidirectional systems at the horizons 100 (above the USC axis) and 1200 m (below the USC axis). The wind speed changed from 8 to 10 m/s during experimentation, and the wind directions were 40° to 50° relative to the path.

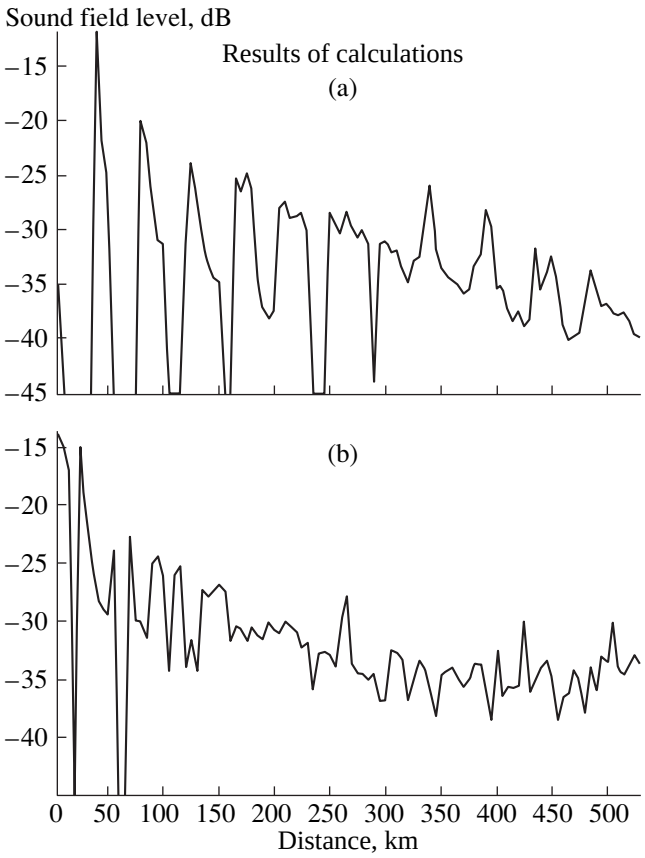

Fig. 3. Calculated sound field for the second experiment. The source and receiver depths are (a) 150 and 100 m and (b) 150 and 1200 m, respectively.

The sound speed at the 150-m depth (the horizon of explosions) differed by 7–9 m/s from that at the USC axis. The charges were exploded above the USC axis. However, the USC captured the rays that left the source at angles within ±8° relative to the horizon. At the chosen reception depths, the zonal structure of the sound field was formed. At a reception depth of 1200 m, the sound speed was by 5–6 m/s lower than at the transmission depth. The sound speed at the reception depth 100 m was as little as 1–2 m/s higher than at the transmission depth.

Figure 3 illustrates the sound field calculated with Vagin's ray-approximation computer code for the actual bottom relief and sound speed profiles changing along the path. In the calculations, the reception depths were 100 and 1200 m and the source moved at the 150-m depth, in accordance with the experimental layout. The sea floor was supposed to be ideally absorptive. The objective of the calculations was to consider the zonal structure of the sound field, along with its changes caused by the movement of the source. At a reception depth of 100 m, up to six to seven convergence zones are formed, the last one corresponding to a distance of about 300 km. At a reception depth of 1200 m, the zonal structure can be observed at ranges shorter than 60–70 km.

In the vicinity of the boundary between the Norwegian and Lofoten Basins, the bottom significantly rises (to a depth of 2100 m, where the sound speed becomes equal to that at the surface). So, at distances longer than 200–250 km, the signals reflected solely by the surface are screened by the bottom rise and do not reach the receivers. At the receivers, signals arrive that are either "water" signals or those reflected from both bottom and surface, the latter signals being strongly attenuated by the bottom.

Thus, to estimate the attenuation coefficient (to exclude the effects of the wavy surface) in this experiment, one should analyze the decay of the sound field received at a depth of 1200 m for the path fraction ranging from 250 to 650 km, where a stable pattern of total insonification exists (according to the calculations, the last shadow zone corresponds to the distances 60.5–67 km at this horizon).

Such estimates of the attenuation coefficient were obtained for the frequency band from 160 to 800 Hz. To exclude the known law of geometric spread, we used the "differential" method, which has been repeatedly used to interpret experimental data obtained in intricate environments. This method is based on two assumptions. The first one consists in the concept that the geometric spread is not known but the same for the whole frequency band at hand. The second assumption is that the frequency dependence of the attenuation coefficient has a power-law form with no constant component. According to the differential method, one normalizes the sound field levels at individual frequencies to the level at a frequency that is treated as the reference one. By doing so, one totally excludes the unknown law of geometric spread. From the normalized decays, the differential attenuation coefficient is determined at each frequency, which can be shown to be the difference between the total attenuation coefficients at two frequencies: the frequency to be analyzed and the reference one. By approximating the frequency dependence of the differential attenuation coefficient by a power-law function and omitting the free term, we obtain the following expression for the total attenuation coefficient:

$$\beta = af^n. \quad (1)$$

As a sound field characteristic that is equivalent to the power of the explosion-generated signal within the frequency band Δf, we use the quantity

$$E_f = \int_0^T p_f^2(t)\,dt,$$

where T is the signal duration and $p_f(t)$ is the pressure in the explosion-generated signal, which is normalized to the frequency band Δf. The power-spectral analysis of the explosion-generated signals and the subsequent

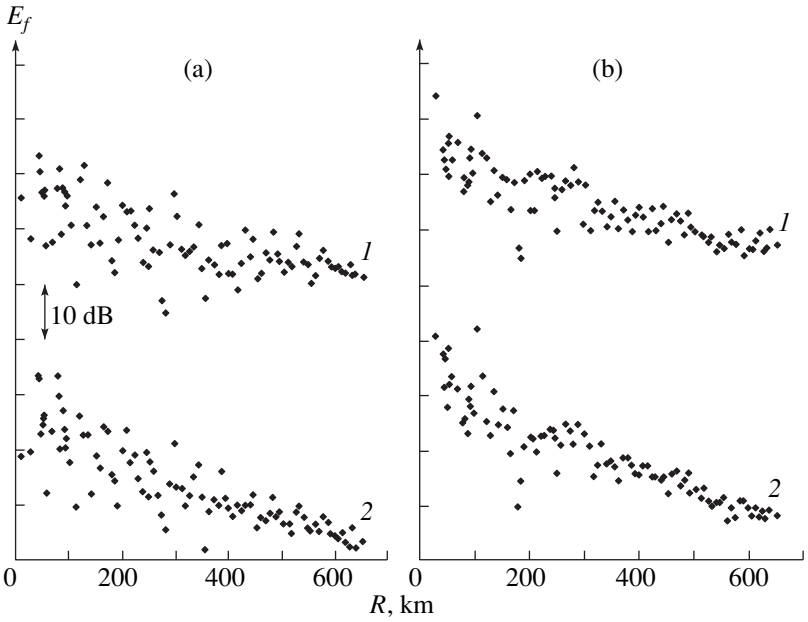

Fig. 4. Experimental sound field decays for the second experiment at the frequencies (*1*) 200 and (*2*) 400 Hz. The source and receiver depths are (a) 150 and 100 m and (b) 150 and 1200 m, respectively.

processing of the experimental data were performed with the use of a computer.

As a result, the decay curves were obtained for the sound field level. These curves can serve as the starting data for estimating the frequency dependence of the attenuation coefficient. Figure 4 shows the experimental decay curves at the frequencies 200 and 400 Hz, for reception depths of 100 and 1200 m. One can notice rather sharp changes in the decays that occur in the vicinity of the boundary between the Norwegian and Lofoten Basins. It is difficult to detect the zonal structure of the sound field from the experimental decays. This difficulty seems to be caused by the too large separations (~7–8 km) of adjacent explosions. However, the spread in the experimental levels of the sound field received at a depth of 1200 m becomes significantly lower starting from distances of 200–250 km, while, at a reception depth of 100 m, the spread smoothly decreases at distances from 250 to 500 km.

To describe the attenuation at the 1200-m reception depth by Eq. (1) (with frequency in kHz and attenuation in dB/km), we obtained the following values of the parameters: $a = 0.07$ and $n = 1.2$. Remember that, for describing the frequency dependence of sound attenuation by Eq. (1), in the first experiment we obtained the parameters: $a = 0.044$–0.052 and $n = 0.99$–0.925.

The attenuation coefficients determined from the experiment at hand are summarized in the table. For comparison, the next to last column of the table shows the absorption coefficients calculated according to formulas given in [6]. These absorption coefficients depend on the temperature (T), salinity (S), and hydrogen exponent (pH). To calculate the absorption in the Norwegian Sea, we specified the following parameters of the sea medium: $T = 272.5$°K, $S = 35.2$‰, and pH = 8.15–8.2.

The expressions determined from the first and second experiments lead to similar values of the attenuation coefficient. These values calculated according to Eq. (1) with the aforementioned parameters agree well with each other for the whole frequency band (63–800 Hz): the spread is no higher than ±20%. At lower (<200 Hz) frequencies, this spread is within the estimated measuring accuracy: ±0.001–0.002 dB/km. However, the power-law exponents differs by a factor of 1.2–1.3 for the two experiments.

The decays of the sound field received at the 100-m depth were also used to estimate the attenuation (although there was a zonal structure of the field up to a distance of 300 km). In doing so, we faced certain difficulties. In the power-law approximation of the frequency dependence of the differential attenuation coefficients, a very high (undoubtedly overestimated) constant component arose. To obtain a more realistic estimate for this reception horizon, we used an attenuation value of 0.0173 dB/km, which corresponds to the 1200-m reception depth at a reference frequency of 315 Hz. The results of analyzing the explosion-generated signals received at a depth of 100 m are presented in the table (see the last column). Earlier, we never estimated the attenuation coefficient for the case of the transition from zonal to full-insonification structures of the sound field.

All attenuation coefficients obtained in both the first and second experiments (except for those presented in the last column of the table) are shown in Fig. 5. One

Attenuation coefficients obtained by the differential method for the path fraction bounded by the distances 250 and 650 km from the reception point

Frequency, Hz	Attenuation coefficient, dB/km at a reception depth of 1200 m		Absorption coefficient, dB/km	Attenuation coefficient, dB/km at a reception depth of 100 m
	experiment	calculation according to Eq. (1)	calculation according to [5]	experiment
160	0.008	0.0076	0.0015–0.0016	0.004
200	0.012	0.0100	0.0023–0.0025	0.007
250	0.012	0.0131	0.0035–0.0038	0.009
315	0.015	0.0173	0.0054–0.0058	0.017
400	0.025	0.0231	0.0084–0.0089	0.025
500	0.033	0.0303	0.0122–0.0130	0.034
630	0.038	0.0400	0.0175–0.0190	0.043
800	0.054	0.0534	0.0250–0.0264	0.050

Note: At the frequencies 630–800 Hz, the attenuation was determined for distances shorter than 550 km.

can conclude that, in spite of considerable changes in the propagation conditions, the experimental attenuation coefficients obtained in the two experiments differ little from each other. Comparative analysis of the data leads to the conclusion that the summertime frequency dependence of attenuation in the Norwegian Sea can be described by the following expression: $\beta = \{0.06\, f_{\mathrm{kHz}}^{1.1}\}$ dB/km.

At the same time, the attenuation can be only partially attributed to sound absorption in the seawater;

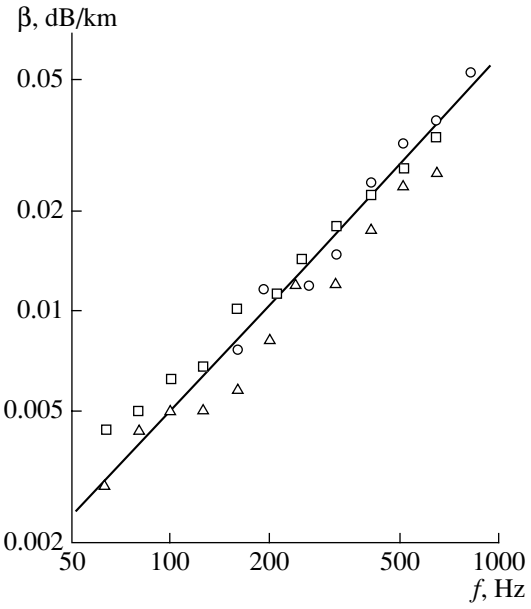

Fig. 5. Experimental attenuation coefficients obtained by the differential method from the data of the (△, □) first and (○) second experiments. The line shows the frequency dependence of the attenuation, as described by the expression $\beta = \{0.06\, f_{\mathrm{kHz}}^{1.1}\}$ dB/km.

i.e., an additional attenuation mechanism is required. As we [1] have mentioned above, the most probable cause of such high attenuation coefficients in the Norwegian Sea is the sound scattering by thermal inhomogeneities, such as fine-structural ones whose horizontal size is by 1–2 orders of magnitude higher than the vertical size. The following considerations confirm this concept.

(i) The Norwegian Sea is strongly influenced by currents (cold East-Island and warm North-Atlantic ones). According to a large body of experimental data [7], a justified conclusion can be drawn that fine-structural inhomogeneities are generated in ocean regions that are influenced by strong currents (like the Kamchatka one). For such inhomogeneities, the following values of the rms fluctuation of the acoustic refraction index are characteristic: $\mu^2 \cong 10^{-5}$–10^{-7}.

(ii) In accordance with the results obtained in [8], the attenuation coefficients obtained in our experiment at frequencies of ~400–500 Hz can be explained by the sound scattering from the fine-structural inhomogeneities if $\mu^2 \cong 1.4 \times 10^{-7}$.

(iii) If the fine-layered ocean inhomogeneities are supposed to be of fractal nature, the low-frequency attenuation exhibits a power-law frequency dependence [9] which, with certain parameters of the fractal, has an exponent that agrees with our experimental data.

Finally, let us formulate the conclusions that can be drawn from the above analysis of the experimental data on the year-to-year variability of the conditions of the sound field formation in the underwater sound channel of the Norwegian Sea.

On the propagation path that crosses the central deep-water region of the Norwegian Sea from southwest to northeast, the depth of the USC axis changes from 600 to 1000–1100 m. In different years, the

steepness of this change is different, depending on the relative positions of the cold and warm water cores that are always present in the Norwegian and Lofoten basins, respectively, at a depth of about 600 m. In our experiments, separated by four years in time, the distances between these cores changed by a factor of more than two.

For a certain steepness of the change in the depth of the channel axis, the calculations lead to the 5- to 7-dB change in the propagation anomaly for some depths of the source and the receiver. At other source and receiver depths, a noticeably different steepness of the sound field decay can be observed.

In spite of the considerable change in the sound speed profiles measured in the two experiments with the explosion-generated sound signals, the low-frequency attenuation coefficient determined by the differential method changes insignificantly.

ACKNOWLEDGMENTS

This work was supported by Russian Foundation for Basic Research, project nos. 01-02-16636 and 01-05-64711.

REFERENCES

1. R. A. Vadov, Akust. Zh. **48**, 28 (2002).
2. V. F. Sukhoveĭ, *Seas of the World Ocean* (Gidrometeoizdat, Leningrad, 1986).
3. B. S. Zalogin and A. N. Kosarev, *Seas* (Mysl', Moscow, 1999), p. 400.
4. Address of Database on the Internet: http://128.160.23.42/.
5. A. V. Vagin, *A Report of Institute of Acoustics* (Acad. Nauk SSSR, Moscow, 1974).
6. R. A. Vadov, Akust. Zh. **46**, 624 (2000) [Acoust. Phys. **46**, 544 (2000)].
7. I. D. Rostov, Candidate's Dissertation in Geography (Vladivostok, 1985).
8. Yu. P. Lysanov and I. A. Sazonov, Akust. Zh. **39**, 697 (1993) [Acoust. Phys. **39**, 366 (1993)].
9. Yu. P. Lysanov and L. M. Lyamshev, in *Proceedings of the Fourth European Conference on Underwater Acoustics* (Rome, 1998), p. 801.

Translated by E. Kopyl

Acoustical Physics, Vol. 48, No. 4, 2002, pp. 430–435. Translated from Akusticheskiĭ Zhurnal, Vol. 48, No. 4, 2002, pp. 493–498.

Calculation of the Nonlinearity Parameter for Some Types of Gaseous and Liquid Mixtures

D. A. Denisov

Mendeleev Chemical Technology University of Russia, Miusskaya pl. 9, Moscow, 125047 Russia

e-mail: smi@logic.ru

Received March 25, 1997; in final form, November 28, 2001

Abstract—Relations that allow one to calculate the nonlinearity parameters for some types of multicomponent systems from the parameters involved in the equations of state are presented. Relations for estimating the derivatives of the speed of sound with respect to temperature and pressure in a two-component mixture from the data on the properties of pure components are obtained. The calculated values of the aforementioned derivatives agree well with the values obtained from the experimental dependences of the speed of sound on temperature and pressure in a two-component mixture. © *2002 MAIK "Nauka/Interperiodica".*

According to [1, 2], the nonlinearity parameter B/A plays an important role in nonlinear acoustics and is of interest for many fields of science, such as underwater acoustics and medicine.

Quite often, the nonlinearity parameter for mixtures, $(B/A)_{mix}$, is calculated as a sum of nonlinearity parameters $(B/A)_i$ for the components multiplied by their respective molar fractions in the mixture [1].

To calculate $(B/A)_{mix}$ by the thermodynamic method according to the equation [3],

$$\frac{B}{A} = \rho_0\left(\frac{\partial u^2}{\partial P}\right)_{T,\rho_0} + \alpha\frac{T}{C_P}\left(\frac{\partial u^2}{\partial T}\right)_{P,\rho_0} M, \qquad (1)$$

where u is speed of sound, T is the temperature (K), P is the pressure, ρ_0 is the density of the unperturbed system, C_P is the isobaric molar heat capacity of a component or the average isobaric molar heat capacity of the mixture, and M is the molar mass of a component or the average molar mass of the mixture, it is necessary to know the dependence of the speed of sound on P and T for the pure components.

This paper presents the equations for calculating $(B/A)_{mix}$ from the properties of pure components for some types of gas mixtures without knowing the dependence of the speed of sound in pure components on P and T. In addition, equations for calculating $(B/A)_{mix}$ on the basis of Eq. (1) are obtained for mixtures whose formation from pure components at T = const and P = const satisfies the following conditions: (i) the change in volume at mixing, V^M, is zero, and (ii) the change in the enthalpy at mixing, H^M, does not depend on T.

To obtain the relations for calculating $(B/A)_{mix}$ for some types of mixtures, we start from the formula defining the quantity B/A [4]:

$$\left(\frac{B}{A}\right)_{mix} = \frac{\rho_{mix}}{u_{mix}^2}\left(\frac{\partial^2 P}{\partial \rho_{mix}^2}\right)_{S,\rho_{mix0}}, \qquad (2)$$

where ρ_{mix} is the mixture density, ρ_{mix0} is the unperturbed mixture density, u_{mix} is the speed of sound in the mixture, and S is the entropy. The derivative on the right-hand side can be represented in the form

$$\left(\frac{\partial^2 P}{\partial \rho_{mix}^2}\right) = \frac{V_{mix}}{\rho_{mix}^2}\left[2\left(\frac{\partial P}{\partial V_{mix}}\right)_S + V_{mix}\left(\frac{\partial^2 P}{\partial V_{mix}^2}\right)_S\right], \qquad (3)$$

where V_{mix} is the mixture volume.

Since the mixture entropy differs from the entropies of pure components, the derivatives for the mixture in the last two relations can hardly be expressed in terms of similar derivatives for the mixture components. We apply the last relation to the calculation of $(B/A)_{mix}$ for a mixture of ideal gases with constant isochoric heat capacities. To find the derivatives $(\partial P/\partial V_{mix})_S$ and $(\partial^2 P/\partial V_{mix}^2)_S$, one should consider two forms of the adiabatic equation [5]:

$$dU_{mix} + PdV_{mix} = 0, \qquad (4)$$

$$dH_{mix} - V_{mix}dP = 0, \qquad (5)$$

where U_{mix} and H_{mix} are the internal energy and the enthalpy, respectively. The last two equations can be presented in another form:

$$\sum_{i=1}^{r} C_{Vi}n_i dT - P\sum_{t=1}^{r} n_t d\nu_t = 0, \qquad (6)$$

$$\sum_{i=1}^{r} C_{Pi}n_i dT - \sum_{l=1}^{r} \nu_l n_l dP = 0, \qquad (7)$$

where C_{Pi} and C_{Vi} are the isobaric and isochoric molar heat capacities of the ith component of the mixture, n_i is the number of moles of the ith component in the mixture, ν_l is the molar volume of lth component, and r is

the number of components in the mixture. Now, we can easily obtain the adiabatic equation:

$$PV_{\text{mix}}^{K_{\text{mix}}} = \text{const}, \tag{8}$$

where K_{mix} is the adiabatic index of the mixture:

$$K_{\text{mix}} = \left(\sum_{i=1}^{r} C_{Pi}\right)\left(\sum_{j=1}^{r} C_{Vj}\right)^{-1}. \tag{9}$$

One can easily find the expression for the derivative $(\partial P/\partial V_{\text{mix}})_S$,

$$\left(\frac{\partial P}{\partial V_{\text{mix}}}\right)_S = -K_{\text{mix}}\frac{V_{\text{mix}}}{P}, \tag{10}$$

which can be rewritten in the form

$$\left(\frac{\partial P}{\partial V_{\text{mix}}}\right)_S = -\frac{K_{\text{mix}}}{V_{\text{mix}}^2}nRT. \tag{11}$$

Here, R is the universal gas constant and n is the total number of moles of all components in the mixture.

One can easily find the formula for the second derivative $(\partial^2 P/\partial V_{\text{mix}}^2)_S$:

$$\left(\frac{\partial^2 P}{\partial V_{\text{mix}}^2}\right)_S = \frac{K_{\text{mix}}}{V_{\text{mix}}^3}(K_{\text{mix}}+1)nRT. \tag{12}$$

Taking into account the formula for the mixture density ρ_{mix},

$$\rho_{\text{mix}} = \frac{1}{V_{\text{mix}}}\sum_{l=1}^{r} n_l M_l, \tag{13}$$

where M_l is molar mass of the lth component, we find, according to [4], the relation for u_{mix},

$$u_{\text{mix}}^2 = \left(\frac{\partial P}{\partial \rho_{\text{mix}}}\right)_{S,\,\rho_{\text{mix}0}}, \tag{14}$$

or, according to another formula following from Eq. (14),

$$u_{\text{mix}}^2 = -\frac{V_{\text{mix}}}{\rho_{\text{mix}}}\left(\frac{\partial P}{\partial V_{\text{mix}}}\right)_{S,\,\rho_{\text{mix}0}}. \tag{15}$$

For a mixture of ideal gases, we obtain

$$u_{\text{mix}}^2 = \left(\sum_{j=1}^{r} n_j M_j\right)^{-1} nRTK_{\text{mix}}. \tag{16}$$

If all components of the mixture have the same adiabatic index, the relation for u_{mix} has a form similar to that of the sound speed in a single-component ideal gas, the only difference being that the average molar mass of the mixture appears in place of the molar mass of the component. Taking Eq. (3) into account, one can easily obtain the expression for the second derivative

$$\left(\frac{\partial^2 P}{\partial \rho_{\text{mix}}^2}\right)_S = \frac{V_{\text{mix}}^3}{\sum_{l=1}^{r} n_l M_l}\left[\frac{nV_{\text{mix}}K_{\text{mix}}(K_{\text{mix}}+1)RT}{V_{\text{mix}}^3} - \frac{2K_{\text{mix}}}{V_{\text{mix}}^2}nRT\right], \tag{17}$$

which can be easily reduced to the form

$$\left(\frac{\partial^2 P}{\partial \rho_{\text{mix}}^2}\right)_S = \frac{K_{\text{mix}}(K_{\text{mix}}-1)}{\left(\sum_{l=1}^{r} n_l M_l\right)^2}V_{\text{mix}}nRT. \tag{18}$$

From the last relation and Eq. (2), we derive the expression

$$\left(\frac{B}{A}\right)_{\text{mix}} = K_{\text{mix}} - 1, \tag{19}$$

which is similar to the expression for a single-component ideal gas.

Now, we obtain the formula for calculating the nonlinearity parameter of the gas mixture described by the Shishkov–Noble–Abel equation [6], which can be presented in the form

$$P(V_{\text{mix}} - nb_{\text{mix}}) = nRT, \tag{20}$$

where b_{mix} is defined as [5]

$$b_{\text{mix}} = \frac{1}{n}\sum_{i=1}^{r} n_i b_i. \tag{21}$$

The parameter b_{mix} is used for calculating $(B/A)_{\text{mix}}$, for example, in the theory by Flory [1]. From Eq. (20), according to [7], the adiabatic equation is obtained in the form

$$T(V_{\text{mix}} - nb_{\text{mix}})^{R/C_{V\text{mix}}} = \text{const}, \tag{22}$$

where the average isochoric molar heat capacity $C_{V\text{mix}}$ is defined by the expression

$$C_{V\text{mix}} = \frac{1}{n}\sum_{j=1}^{r} n_j C_{Vj}. \tag{23}$$

Taking into account the expression

$$C_P = C_V - (\partial P/\partial T)_{V_{\text{mix}}}^2(\partial V_{\text{mix}}/\partial P)_T \tag{24}$$

relating C_P and C_V [7], and also the formulas for the derivatives $(\partial P/\partial T)_{V_{\text{mix}}}$ and $(\partial P/\partial V_{\text{mix}})_T$,

$$\left(\frac{\partial P}{\partial T}\right)_{V_{\text{mix}}} = \frac{nR}{V_{\text{mix}} - nb_{\text{mix}}}, \tag{25}$$

$$\left(\frac{\partial P}{\partial V_{\text{mix}}}\right)_T = -\frac{nRT}{(V_{\text{mix}} - nb_{\text{mix}})^2}, \tag{26}$$

which follow from Eq. (20), one can easily show that the difference between the values of C_P and C_V for a gas described by the Shishkov–Noble–Abel equation is equal to R, as in the case of ideal gases. Therefore, the adiabatic equation can be written in the form

$$P(V_{\text{mix}} - nb_{\text{mix}})^{K_{\text{mix}}} = \text{const}. \tag{27}$$

The last formula yields the expressions for the derivatives,

$$\left(\frac{\partial P}{\partial V_{\text{mix}}}\right)_S = -\frac{K_{\text{mix}}}{V_{\text{mix}} - nb_{\text{mix}}}P, \tag{28}$$

$$\left(\frac{\partial^2 P}{\partial V_{\text{mix}}^2}\right)_S = \frac{K_{\text{mix}}}{(V_{\text{mix}} - nb_{\text{mix}})^2}(K_{\text{mix}} + 1)P, \tag{29}$$

and for the sound speed u_{mix},

$$u_{\text{mix}}^2 = K_{\text{mix}}RTM_{\text{mix}}^{-1}, \tag{30}$$

where M_{mix} is the average molar mass of the mixture.

Using Eq. (2), one can easily obtain the relation

$$\left(\frac{\partial^2 P}{\partial \rho_{\text{mix}}^2}\right)_S = \frac{nK_{\text{mix}}V_{\text{mix}}RT}{\rho_{\text{mix}}^2(V_{\text{mix}} - nb_{\text{mix}})^3}[V_{\text{mix}}(K_{\text{mix}} - 1) + 2nb_{\text{mix}}], \tag{31}$$

which leads to the equation for the nonlinearity parameter [8]:

$$\left(\frac{B}{A}\right)_{\text{mix}} = \frac{V_{\text{mix}}(K_{\text{mix}} - 1) + 2nb_{\text{mix}}}{V_{\text{mix}} - nb_{\text{mix}}}. \tag{32}$$

At $b_{\text{mix}} = 0$, the last relation yields Eq. (19).

For a gas mixture described by the van der Waals equation [5], we have

$$\left(P + \frac{n^2 a_{\text{mix}}}{V_{\text{mix}}^2}\right)(V_{\text{mix}} - nb_{\text{mix}}) = nRT, \tag{33}$$

where the mixture parameter a_{mix} is related to similar parameters a_i of the components [5]:

$$a_{\text{mix}} = \frac{1}{n^2}\left(\sum_{j=1}^{r} na_j^{1/2}\right)^2. \tag{34}$$

As shown in [7], the adiabatic equation can be written in the form of Eq. (22). One can easily write the adiabatic equation in another form:

$$\left(P + \frac{n^2}{V_{\text{mix}}^2}a_{\text{mix}}\right)(V_{\text{mix}} - nb_{\text{mix}})^{1 + R/C_{V\text{mix}}} = \text{const}. \tag{35}$$

For the derivative $(\partial P/\partial V_{\text{mix}})_S$, we obtain

$$\left(\frac{\partial P}{\partial V_{\text{mix}}}\right)_S = -\left(1 + \frac{R}{C_{V\text{mix}}}\right)\frac{nRT}{(V_{\text{mix}} - nb_{\text{mix}})^2} - \frac{2n^2}{V_{\text{mix}}^3}a_{\text{mix}}, \tag{36}$$

which leads to the following relation for u_{mix}:

$$u_{\text{mix}}^2 = \frac{V_{\text{mix}}}{\sum_{j=1}^{r} n_j M_j} \times \left[\frac{nRT}{V_{\text{mix}}}\left(1 + \frac{R}{C_{V\text{mix}}}\right)\frac{V_{\text{mix}}^2}{(V_{\text{mix}} - nb_{\text{mix}})^2} - \frac{2n^2}{V_{\text{mix}}^2}a_{\text{mix}}\right]. \tag{37}$$

Formula (36) leads to the expression for $(\partial^2 P/\partial V_{\text{mix}}^2)_S$:

$$\left(\frac{\partial^2 P}{\partial V_{\text{mix}}^2}\right)_S = \left(1 + \frac{R}{C_{V\text{mix}}}\right)\left(2 + \frac{R}{C_{V\text{mix}}}\right) \times \left(P + \frac{n^2}{V_{\text{mix}}^2}a_{\text{mix}}\right)\frac{1}{(V_{\text{mix}} - nb_{\text{mix}})^2} - \frac{6n^2}{V_{\text{mix}}^4}a_{\text{mix}}, \tag{38}$$

which can be represented as

$$\left(\frac{\partial^2 P}{\partial V_{\text{mix}}^2}\right)_S = \left(1 + \frac{R}{C_{V\text{mix}}}\right)\left(2 + \frac{R}{C_{V\text{mix}}}\right) \times \frac{nRT}{(V_{\text{mix}} - nb_{\text{mix}})^3} - \frac{6n^2}{V_{\text{mix}}^4}a_{\text{mix}}. \tag{39}$$

It can be easily seen that, at $a_{\text{mix}} = 0$, Eq. (38) coincides with Eq. (29), and Eq. (36) coincides with Eq. (28).

Now, taking into account Eq. (3), we find the expression for the derivative,

$$\left(\frac{\partial^2 P}{\partial \rho_{\text{mix}}^2}\right)_S = \frac{V_{\text{mix}}nRT}{(V_{\text{mix}} - nb_{\text{mix}})^3}\left(1 + \frac{R}{C_{V\text{mix}}}\right) \times \left(\frac{R}{C_{V\text{mix}}}V_{\text{mix}} + 2nb_{\text{mix}}\right) - \frac{8n^2 a_{\text{mix}}}{V_{\text{mix}}^2\rho_{\text{mix}}^2}, \tag{40}$$

which at $a_{\text{mix}} = 0$ coincides with Eq. (31).

From Eq. (40), we obtain

$$\left(\frac{B}{A}\right)_{\text{mix}} = \frac{\dfrac{V_{\text{mix}}nRT}{(V_{\text{mix}}-nb_{\text{mix}})^3}\left(1+\dfrac{R}{C_{V\text{mix}}}\right)\left(\dfrac{R}{C_{V\text{mix}}}V_{\text{mix}}+2nb_{\text{mix}}\right)-\dfrac{8n^2a_{\text{mix}}}{V_{\text{mix}}^2}}{\dfrac{nRTV_{\text{mix}}}{\rho_{\text{mix}}(V_{\text{mix}}-nb_{\text{mix}})^2}\left(1+\dfrac{R}{C_{V\text{mix}}}\right)-\dfrac{2n^2a_{\text{mix}}}{V_{\text{mix}}^2}}, \tag{41}$$

which at $a_{\text{mix}} = 0$ coincides with Eq. (32) for a gas mixture described by the Shishkov–Noble–Abel equation.

In most cases, one fails to obtain the formulas for calculating $(B/A)_{\text{mix}}$ from the parameters of the components and has to use Eq. (1), which requires information on the pressure and temperature dependences of the sound speed. When using the dependences of the sound velocities in the components, u_i, on P and T, one need not compare the experimental and calculated values of $(B/A)_{\text{mix}}$. The validity of equations used in this case can be assessed on the basis of the comparison between the calculated values of the derivatives $(\partial u_{\text{mix}}/\partial T)_P$ and $(\partial u_{\text{mix}}/\partial P)_T$ and the values of the same derivatives obtained from the experimental dependence of the sound speed on P and T. It is precisely the values of the derivatives $(\partial u_{\text{mix}}/\partial T)_P$ and $(\partial u_{\text{mix}}/\partial P)_T$ found from the experimental dependences of the sound speed on P and T that allow one to determine the experimental values of $(B/A)_{\text{mix}}$ [10]. Now, we consider the expression for the adiabatic compressibility of a mixture consisting of two components $\beta_{S\text{mix}}$ [11]:

$$\beta_{S\text{mix}} = \left\{\frac{1}{v_{\text{mix}}}\left[\frac{x_1v_1^2}{u_1^2M_1}+\frac{(1-x_1)v_2^2}{u_2^2M_2}\right] + \frac{Tx_1(1-x_z)}{C_{P\text{mix}}v_{\text{mix}}}C_{P1}C_{P2}Y^2\right\}, \tag{42}$$

where v_i is the molar volume of the ith component; C_{Pi} is the isobaric molar heat capacity of the ith component, v_{mix} is the molar volume of the mixture; α_i is the expansion coefficient of the ith component ($i = 1, 2$);

$$v_{\text{mix}} = x_1v_1 - (1-x_1)v_2; \tag{43}$$

$C_{P\text{mix}}$ is the isobaric molar heat capacity of the mixture,

$$C_{P\text{mix}} = x_1C_{P1} + (1-x_1)C_{P2}; \tag{44}$$

and

$$Y = \frac{\alpha_1}{C_{P1}}v_1 - \frac{\alpha_2}{C_{P2}}v_2. \tag{45}$$

According to [12], Eq. (42) is valid when the isobaric and isothermal mixing of pure components satisfies two conditions: (i) the change in the total volume of the system is zero, and (ii) the change in the enthalpy at mixing does not depend on T. Many mixtures that are formed of pure components at P = const and T = const in compliance with these conditions include not only ideal mixtures, but also, in particular, many regular mixtures [5].

As follows from the well-known equality [4]

$$u^{-2} = \rho\beta_S, \tag{46}$$

where β_S is the adiabatic compressibility and ρ is the density, the derivative $(\partial u_{\text{mix}}^{-2}/\partial T)_P$ can be found from the formula

$$\left(\frac{\partial u_{\text{mix}}^{-2}}{\partial T}\right) = \rho_{\text{mix}}\left(\frac{\partial\beta_{\text{mix}}}{\partial T}\right) + \beta_{\text{mix}}\left(\frac{\partial\rho_{\text{mix}}}{\partial T}\right), \tag{47}$$

where ρ_{mix} is the mixture density and M_{mix} is the average molar mass of the mixture:

$$S_{\text{mix}} = M_{\text{mix}}v_{\text{mix}}^{-1}, \tag{48}$$

$$M_{\text{mix}} = x_1M_1 + (1-x_1)M_2. \tag{49}$$

From Eq. (42), we obtain the expression for the derivative $(\partial\beta_{S\text{mix}}/\partial T)_P$:

$$\begin{aligned}\left(\frac{\partial\beta_{S\text{mix}}}{\partial T}\right)_P &= \frac{x_1v_1[x_1v_1+2(1-x_1)v_2]M_1^{-1}u_1^{-2}-x_1(1-x_1)v_1^2M_2u_2^{-2}}{v_{\text{mix}}^2}\left(\frac{\partial v_1}{\partial T}\right)_P \\ &+ \frac{(1-x_1)v_2[(1-x_1)v_2+2x_1v_1]M_2^{-1}u_2^{-2}-x_1(1-x_1)v_2^2M_1^{-1}u_1^{-2}}{v_{\text{mix}}^2}\left(\frac{\partial v_2}{\partial T}\right)_P \\ &+ \frac{x_1(1-x_1)}{v_{\text{mix}}C_{P\text{mix}}}C_{P1}C_{P2}\rho_{\text{mix}}Y^2 + \frac{\rho_{\text{mix}}}{v_{\text{mix}}}\left[\frac{x_1v_1^2}{M_1}\left(\frac{\partial u_1^{-2}}{\partial T}\right)_P + \frac{(1-x_1)v_2^2}{M_2}\left(\frac{\partial u_2^{-2}}{\partial T}\right)_P\right] \\ &+ \frac{x_1(1-x_1)}{v_{\text{mix}}C_{P\text{mix}}}\rho_{\text{mix}}Y^2\left[C_{P1}\left(\frac{\partial C_{P2}}{\partial T}\right)_P + C_{P2}\left(\frac{\partial C_{P1}}{\partial T}\right)_P\right]\end{aligned} \tag{50}$$

$$-\frac{x_1(1-x_1)C_{P1}C_{P2}Y^2}{v_{\text{mix}}C_{P\text{mix}}^2}\left[x_1\left(\frac{\partial C_{P1}}{\partial T}\right)_P+(1-x_1)\left(\frac{\partial C_{P2}}{\partial T}\right)_P\right]-\frac{x_1(1-x_1)C_{P1}C_{P2}Y^2}{v_{\text{mix}}^2C_{P\text{mix}}}\left[x_1\left(\frac{\partial v_1}{\partial T}\right)_P+(1-x_1)\left(\frac{\partial v_2}{\partial T}\right)_P\right]$$

$$+\frac{2x_1(1-x_1)C_{P1}C_{P2}Y}{v_{\text{mix}}C_{P\text{mix}}}\left[\frac{1}{C_{P1}}\left(\frac{\partial^2 v_1}{\partial T^2}\right)_P-\frac{1}{C_{P2}}\left(\frac{\partial^2 v_2}{\partial T^2}\right)_P\right]-\frac{2x_1(1-x_1)C_{P1}C_{P2}Y}{v_{\text{mix}}C_{P\text{mix}}}\left[\frac{\alpha_1}{C_{P1}^2}v_1\left(\frac{\partial C_{P1}}{\partial T}\right)_P-\frac{\alpha_2 v_2}{C_{P2}}\left(\frac{\partial C_{P2}}{\partial T}\right)_P\right].$$

Formulas (47) and (50) were used to calculate the derivative $(\partial u_{\text{mix}}/\partial T)_P$ for a mixture of liquids: carbon tetrachloride and methanol. The experimental dependence of u_{mix} on T for this mixture and the value of the derivative $(\partial u_{\text{mix}}/\partial T)_P$ calculated on its basis are presented in [10]. In the calculations, the following data on the properties of liquid CCl_4 and CH_3OH at 30°C were used: $\rho_1 = 1569.7$ kg m^{-3}, $\rho_2 = 781.7$ kg m^{-3}, $u_1 = 903.9$ m s^{-1}, $u_2 = 1084.8$ m s^{-1}, $(\partial u_1/\partial T)_P = -3.17$ m s^{-1} K^{-1}, $(\partial u_2/\partial T)_P = -3.22$ m s^{-1} K^{-1} [10] (the subscript 1 refers to the properties of CCl_4 and the subscript 2, to the properties of CH_3OH), $C_{P1} = 131.7$ J mol^{-1} K^{-1}, $C_{P2} = 81.6$ J mol^{-1} K^{-1} [13], the dependences of C_{P1} and C_{P2} on T from [14], and the dependences of ρ_1 and ρ_2 on T from [15].

The fulfillment of the first of the two conditions is confirmed by the small difference obtained at $x_1 = 0.3$ between the calculated value $\rho_{\text{mix}} = 1180.5$ kg m^{-3} and the experimental one $\rho_{\text{mix}}^{\text{exp}} = 1184.0$ kg m^{-3}. The value of the derivative $(\partial\beta_{S\text{mix}}/\partial T)_P$ is 7.123×10^{-12} Pa^{-1} K^{-1}, while the sum of the first and the second terms that occupy the two first lines on the right-hand side of Eq. (50) along with the term containing the derivatives $(\partial u_1^{-2}/\partial T)_P$ and $(\partial u_2^{-2}/\partial T)_P$ is equal to 7.065 Pa^{-1} K^{-1}.

The value of $(\partial u_{\text{mix}}/\partial T)_P$ calculated for $x_1 = 0.3$ equals –2.759 m s^{-1} K^{-1}, and its value obtained from the experimental dependence of u_{mix} [10] is –2.96 m s^{-1} K^{-1} [10].

To calculate the derivative $(\partial u_{\text{mix}}^{-2}/\partial T)_P$, we use a formula similar to Eq. (47), which also follows from Eq. (46):

$$\left(\frac{\partial u_{\text{mix}}^{-2}}{\partial P}\right)_T = \rho_{\text{mix}}\left(\frac{\partial\beta_{S\text{mix}}}{\partial P}\right)_T+\beta_{S\text{mix}}\left(\frac{\partial\rho_{\text{mix}}}{\partial P}\right)_T. \qquad (51)$$

The formula for the derivative $(\partial\beta_{S\text{mix}}/\partial P)_T$ is similar to expression (50), differing only in that the derivatives with respect to P for pure components appear in place of the similar derivatives with respect to T, and the term similar to the third term on the right-hand side of Eq. (50), i.e., the term of the form $\frac{x_1(1-x_1)}{v_{\text{mix}}C_{P\text{mix}}}C_{P1}C_{P2}Y^2$, is absent. The derivatives in the expression for $(\partial\beta_{S\text{mix}}/\partial P)_T$ were calculated using the data on the isothermal compressibility of the components [13]. In the course of the calculations, we neglected the terms involving the derivatives of isobaric molar heat capacity with respect to P. The calculations showed that all terms involved in the expression for the derivative $(\partial\beta_{S\text{mix}}/\partial P)_T$, except for the term with the derivatives of the sound speed with respect to P for pure components, make no contribution to the value of the derivative $(\partial\beta_{S\text{mix}}/\partial P)_T$, which equals 1.04792 Pa^{-2}. The first term on the right-hand side of Eq. (51) is several orders of magnitude greater than the second term. The value of the derivative $(\partial u_{\text{mix}}/\partial P)_T$ calculated using the data for pure components is –0.528 m s^{-1} Pa^{-1}. The value found from the experimental dependence of u_{mix} on P is –0.531 m s^{-1} Pa^{-1} [10]. The cited paper [10] presents only the values of the derivatives $(\partial u_{\text{mix}}/\partial T)_P$ and $(\partial u_{\text{mix}}/\partial P)_T$ found from the experimental dependences of u_{mix} on P and T. In [2], the values of the nonlinearity parameter are calculated for more complex systems with the use of several models without comparing the results with the experiment.

Thus, relations are obtained that allow one to calculate the parameter of nonlinearity for some types of gas mixtures from the values of their component parameters involved in the equation of state. On the basis of the relation for the speed of sound in a two-component mixture, whose isobaric-isothermal formation is not accompanied by changes in volume, under the condition that the enthalpy change at mixing does not depend on T, the formulas are obtained for calculating the derivatives $(\partial u_{\text{mix}}/\partial T)_P$ and $(\partial u_{\text{mix}}/\partial P)_T$ from the data on the properties of the pure components. The calculation by these formulas for a mixture of CCl_4 and CH_3OH gives the values that are close to those obtained from the experimental dependences of the speed of sound on T and P.

ACKNOWLEDGMENTS

I am grateful to Senior Researcher E.S. Balankina for providing the information on the experimental temperature and pressure dependences of the speed of sound in mixtures.

REFERENCES

1. J. Jugan, R. Abracham, and M. Abdulkhadar, Pramana J. Phys. **45** (3), 221 (1995).
2. R. Abraham, M. A. Khadar, and J. Jugan, J. Acoust. Soc. Am. **106**, 1284 (1999).

3. R. T. Bayer and S. P. Leteher, *Ultrasonics* (Academic, New York, 1969).
4. V. A. Krasil'nikov and V. V. Krylov, *Introduction to Physical Acoustics* (Nauka, Moscow, 1984).
5. I. Prigogine and R. Defay, *Chemical Thermodynamics* (Longmans Green, London, 1954; Nauka, Novosibirsk, 1966).
6. V. F. Baĭbuz, V. Yu. Zitserman, L. M. Golubushkina, and Yu. G. Chernov, *Chemical Equilibrium in Nonideal Systems* (Inst. Vys. Temp. Akad. Nauk SSSR, Moscow, 1986).
7. L. D. Landau and E. M. Lifshits, *Statistical Physics*, 2nd ed. (Nauka, Moscow, 1964; Pergamon, Oxford, 1980).
8. D. Denisov, in *29th Winter School on Molecular and Quantum Acoustics* (Upper Silesian Div. Polish Acoust. Soc., Gliwice, 2000), p. 29.
9. D. A. Denisov, in *Physical Acoustics. Wave Propagation and Diffraction: Proceedings of XI Session of the Russian Acoustical Society* (GEOS, Moscow, 2001), p. 64.
10. Hiroyasu Nomura, Tsunetaka Banba, and Yutaka Miyahara, J. Acoust. Soc. Jpn. **30** (4), 228 (1974).
11. I. G. Mikhaĭlenko, Yu. P. Blagov, and A. S. Butko, Fiz. Zhidk. Sostoyaniya, No. 2, 3 (1974).
12. D. Denisov, Meteorol. Z., N.F. **7**, 226 (1998).
13. *Physical Quantities. Handbook*, Ed. by I. S. Grigor'ev and E. Z. Meĭlikhov (Énergoatomizdat, Moscow, 1991).
14. N. B. Vargaftik, *Handbook of the Thermophysical Properties of Gases and Liquids* (Fizmatgiz, Moscow, 1963).
15. G. F. Krestov, V. N. Afanas'ev, and L. S. Efremova, *Physico-Chemical Properties of Binary Solvents: A Handbook* (Nauka, Moscow, 1988).

Translated by A. Kruglov

Acoustical Physics, Vol. 48, No. 4, 2002, pp. 436–440. Translated from Akusticheskiĭ Zhurnal, Vol. 48, No. 4, 2002, pp. 499–503.

Acoustic Study of Adsorbed Liquid Layers

G. B. Dorjin and I. G. Simakov

Department of Physical Problems, Buryat Scientific Center, Siberian Division, Russian Academy of Sciences, ul. Sakh'yanovoĭ 6, Ulan Ude, 670047 Russia

e-mail: lmf@pres.bsc.buryatia.ru

Received November 27, 2000

Abstract—Interference measurements of small variations in the velocity and attenuation of surface acoustic waves (SAWs) are used to investigate water layers up to 15 nm thick adsorbed on the surface of a lithium niobate crystal. The frequency dependence of the relative variation of the SAW velocity with the adsorption of water vapor is measured in the range from 40 to 400 MHz. Acoustic techniques are used to experimentally estimate the frequency dependence of the dielectric constant of adsorbed water and its dipole relaxation frequency along with the dependence of the adsorption layer thickness on the water vapor pressure in the surrounding medium. A simple expression is proposed for calculating the dispersion of the SAW velocity in a solid loaded with a thin liquid layer. © *2002 MAIK "Nauka/Interperiodica".*

In a liquid spread over the surface of a solid, a thin layer is formed under the effect of surface forces, and this layer differs in its structure and properties from the bulk liquid phase [1–4]. Examples of such layers with a modified structure are thin liquid interlayers and wetting and adsorbed liquid films [3]. The structuring effect of the field of surface forces is most pronounced when the lyophilic solid surfaces interact with polar liquids [2, 3].

In a wet medium, a layer of adsorbed water is formed on the surface of a solid, its thickness depending on the humidity of the medium and the surface properties. The structural modification of the adsorbed water layer is related to the rearrangement of hydrogen bonds and to the formation of an ordered orientation structure, which is different near the hydrophilic and hydrophobic surfaces. The structural transformation manifests itself in the changes that occur in the number and energy of hydrogen bonds between molecules, in the rotational and translational mobility, and in the viscosity and density of water [1]. Close to a hydrophilic surface, the water density is usually higher, the molecular dipoles of water are mostly perpendicular to the surface, and the mobility of molecules is lower than in the bulk of water. The structure-sensitive physical properties of the adsorbed water depend on the layer thickness and differ from those of the water bulk [1–3]. The purpose of this work is to acoustically investigate the water adsorbed on the surface of a lithium niobate crystal and to demonstrate the possibility of investigating the properties of liquid layers on the basis of the analysis of perturbations of surface waves.

To analyze the interaction of surface acoustic waves (SAWs) with liquid in a layered system, one should solve a system of equations including the equations of motion and the electrostatic equations along with the equations for piezoelectric media and the boundary conditions. The analysis of the numerically calculated dispersion curve of the SAW velocity showed [5] that, at small values of the layer thickness, the velocity variation is linear and can be approximated by the dependence $\Delta V/V \approx 0.4h/\lambda$. We assume that, when a SAW propagates in the system formed by a liquid layer and a solid halfspace and when the layer thickness is small ($h \ll \lambda$), the effect of the liquid layer on the relative variation of the SAW velocity is reduced to perturbations in the mechanical and electric boundary conditions:

$$-\frac{\Delta V}{V} = (A + B)\frac{h}{\lambda}, \tag{1}$$

where $\Delta V = V - V_0$; V_0 and V are the SAW velocities on the free and the layer-loaded surfaces; h is the liquid layer thickness; and λ is the SAW wavelength.

The factor A corresponds to the SAW velocity variation that results from the mechanical effect of the liquid layer. It is obtained from the dispersion equation for the system formed by the isotropic solid halfspace and the liquid layer [6] and relates the SAW parameters to the acoustic impedances of both the solid and the liquid:

$$A = \frac{\rho_f V_f}{\rho_s V_s}\tan Q, \tag{2}$$

where ρ_f and ρ_s are the densities of the liquid and the solid, respectively; $Q = \arccos(V_f/V_s)$ is the angle of the acoustic waves' propagation in the liquid [7]; V_f is sound velocity in the liquid; and V_s is SAW velocity.

The factor B is obtained by the impedance method [8] from the equality condition for the effective dielectric constants of the liquid layer and the piezoelectric at

the boundary. It relates the electromechanical coupling coefficient k of the piezoelectric and the dielectric characteristics of the medium, the liquid layer, and the piezoelectric to the SAW velocity:

$$B = \frac{\pi k^2 \varepsilon_p}{(\varepsilon_p + \varepsilon_0)^2} \frac{\varepsilon_f^2 - \varepsilon_0^2}{\varepsilon_f}, \quad (3)$$

where ε_p, ε_f, and ε_0 are the relative dielectric constants of the piezoelectric, the liquid, and the air (vacuum), respectively. The dielectric constant of air is $\varepsilon_0 \approx 1$, and the dielectric constant of water is $\varepsilon_f \gg \varepsilon_0$. Then, expression (3) can be written in a simpler form [5]:

$$B = \frac{\pi k^2 \varepsilon_P \varepsilon_f}{(\varepsilon_p + 1)^2}. \quad (4)$$

The difference between the exact value of the SAW velocity variation with the normalized layer thickness h/λ, which is numerically determined from the solution of the system of equations for the layered structure (water–lithium niobate), and the approximate value calculated by Eq. (1) does not exceed 0.01% at $h/\lambda \le 0.02$. The adsorbed water layer thickness is usually less than 35 nm [3], and, at SAW frequencies below 1 GHz, h/λ is still less than 0.01. Therefore, Eq. (1) can be used for analyzing both thin layers of water with bulk properties and adsorbed water layers.The effect of the field of surface forces on the adsorbed water is similar to the pressure effect on the bulk water: it also increases the density and the bulk modulus. At the same time, the surface force field leads, by redistributing the free and structured water, to a decrease in both the water density and the mobility of water molecules. Thus, the effect of surface forces differs from that of pressure, which destroys the structure of bulk water [9], makes it denser, and increases the translational and orientational mobility of molecules. The process of ordering (and, hence, loosening) of the bordering water is accompanied by a general decrease in intermolecular distances. Apparently, that is why the change in density of thin water interlayers between the hydrophilic (5–30 nm thick) and hydrophobic (4–5 nm thick) surfaces of mica could not be experimentally determined [1]. According to the estimates given in [3], the density of water in the adsorbed layer differs from that in the bulk by less than 1%, the value of A being almost independent of the sound velocity in water. Therefore, the tabular values of water density in the bulk and of the corresponding sound velocity were used in the calculations (at 20°C and p = 1 atm, ρ_f = 998.2 kg/m^3 and V_f = 1483 m/s).

As a result of using the tabular values of water parameters instead of the values modified under the effect of the surface force field, which is similar to the effect of pressure, the factor $(A + B)$ is determined with an error of $\delta = (A - A_0)/(A + B)$. This error can be estimated using the pressure dependence of the water density $\rho_f(p)$, its bulk modulus $K(p)$, and the sound velocity in water $V_f(p)$. The numerical calculations showed (see table) that, if the water density increases by 0–2% under the effect of pressure, the bulk modulus and the sound velocity increase by 0–12.8 and 0–6.05%, respectively. The error in the determination of the factor $(A + B)$ increases monotonically from zero to 0.28%. This demonstrates the small effect of changes in the acoustic parameters of water on the value of the factor A. In the table, $\Delta p = (p - 1)$ atm and $\Delta i = i(p) - i_0$, where i represents ρ_f, K, or V_f. At 20°C and atmospheric pressure, A = 0.19468 and B = 0.21684.

Table

Δp, atm	$\Delta\rho/\rho_f$, %	$\Delta K/K$, %	$\Delta V/V_f$, %	δ, %
112	0.5	3.14	1.35	0.09
232	1.0	6.43	2.87	0.16
360	1.5	9.55	4.36	0.23
497	2.0	12.8	6.05	0.28

It should be noted that the factor A increases with water density and sound velocity, while the factor B decreases when the dielectric loading varies, because the dielectric constant of the bordering water, when measured at the same frequency in the range 0.1–10 MHz, is usually less than that of the water bulk [3]. The decrease in the factor A without a change in the density ρ_f is possible only in the case of a considerable increase in the sound velocity in water, i.e., at high frequencies, when the acoustic relaxation properties of water manifest themselves [10].

To investigate the anomalous properties of thin layers, it is necessary to use highly sensitive methods for measuring the acoustic parameters of liquids [11, 12]. In the experiment, we used a modification of the method for measuring small variations of the SAW velocity and attenuation [12]. The method is based on the interference of counterphase surface waves generated in the pulse mode by two transducers. The signal of the balance disturbance for phases or amplitudes (as a result of adsorption, for instance) is recorded by the third transducer. When measuring the relative variations of the SAW velocity, the sensitivity of the method is 10^{-7}–10^{-8}, and, in the case of amplitude variations, it is 10^{-3}–10^{-4} dB.

A lithium niobate crystal with an optically polished YZ-cut working surface was preliminarily cleaned in a glow discharge and placed over the surface of twice-distilled water in a closed thermostatically controlled chamber. The necessary pressure of the water vapor was predetermined and controlled with an accuracy of 0.1%. The vapor was adsorbed by the working surface of the crystal. The frequency range of the SAW was 40–400 MHz.

In the case of a normal dispersion, Eq. (1) leads to a linear dependence of the relative variation of the SAW velocity on the thickness of the liquid layer. It is well known that the thickness of a water layer adsorbed on

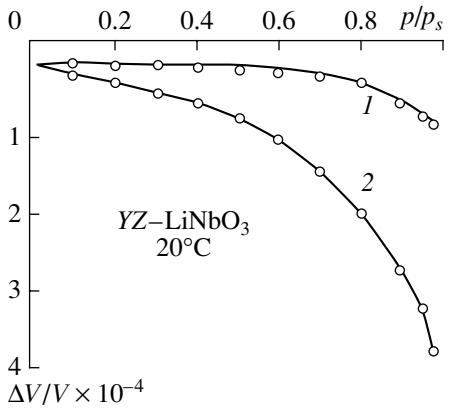

Fig. 1 Dependence of the relative variation of the SAW velocity on the relative water vapors pressure for the SAW frequencies (*1*) 43 and (*2*) 388 MHz.

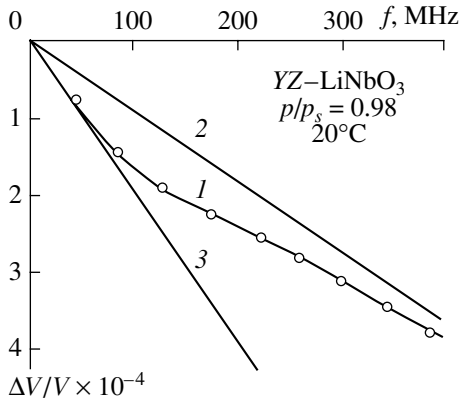

Fig. 2 Frequency dependence of the variation of the SAW velocity at a fixed vapor pressure: (*1*) the experimental curve and the dependences calculated by Eq. (1) for ε_f = (*2*) 5.2 and (*3*) 80.

the surface of a solid depends, at a constant temperature, on the vapor pressure in the surrounding medium. Figure 1 demonstrates the experimental dependences of the relative variation of the SAW velocity on the relative vapor pressure (p/p_s varies from zero to unity). At a saturated vapor pressure ($p = p_s$), the experimental results are badly reproduced because of the intense formation of droplets. It can be seen that the SAW velocity decreases in the wet medium. The variation of the SAW velocity with pressure is nonlinear and grows with frequency.

The curves demonstrate a nonlinear dependence of the adsorbed layer thickness and a possible dependence of the factor ($A + B$) on the vapor pressure, and also a possible dependence of the parameters of adsorbed water, ρ_f, V_f, and ε_f, on the layer thickness. It should be noted that curve *2* (Fig. 1, $f_2 > f_1$) cannot be obtained by a simple scaling of curve *1* by the factor f_2/f_1, which points to a possible frequency dependence of the SAW parameters and, consequently, of the factor ($A + B$) in Eq. (1).

At the fixed thickness of the absorbed layer, which is determined by the constant vapor pressure and temperature, in the case of a normal dispersion, Eq. (1) also leads to the linear frequency dependence of the relative variation of SAW velocity. Figure 2 demonstrates an experimental frequency dependence of the relative variation of SAW velocity in the water layer adsorbed on the lithium niobate surface at the constant vapor pressure $p/p_s = 0.98$ (curve *1*). The nonlinear character of the experimental curve *1*, unlike the calculated curves *2* and *3*, also testifies to a frequency dependence of the factor ($A + B$). Curve *2* corresponds to the dependence given by Eq. (1) at $\varepsilon_f = \varepsilon_\infty$, and curve *3*, to the same dependence at $\varepsilon_f = \varepsilon_s$, where ε_s and ε_∞ are the static and the high-frequency dielectric constants of the liquid. For water at 20°C, we take $\varepsilon_s = 80$ and $\varepsilon_\infty = 5.2$. Hence, in the adsorbed liquid layer with a modified structure different from that of the bulk liquid, a violation of the linear dispersion law of the SAW velocity is observed.

Such a violation of the linear dispersion law is possible when the parameters of the liquid that enter into factors A and B are frequency-dependent. At a fixed layer thickness, a frequency-dependent parameter can be the sound velocity in liquid. This assumption is valid in the frequency range corresponding to the viscoelastic relaxation. At the same time, in the dipole-relaxation frequency range, a frequency-dependent parameter of the liquid can be its dielectric constant. The processes of the dielectric and viscoelastic relaxations are interrelated to the extent that the analogy between the rotational and translational motion is acceptable. They are characterized by the corresponding relaxation times (in low-viscosity liquids, they are about 10^{-10} s). In the adsorbed layer, the decrease in the rotational and translational mobility can lead to a considerable increase in the dielectric and viscoelastic relaxation times [1]. However, according to [10], the process of the structural relaxation in the structured liquids is an intermediate stage of the dielectric relaxation process; this stage defines the dielectric relaxation rate. Therefore, the dielectric relaxation time is much longer than the relaxation time of the bulk modulus of the liquid, and, hence, is also much longer than the relaxation time of its rate. Hence, the frequency region of the dipole relaxation is below that of the viscoelastic relaxation, and the most probable frequency-dependent parameter at a fixed layer thickness is the dielectric constant of the liquid.

It should be noted that the viscoelastic parameters of a thin water layer can be estimated from the acoustic measurements with the help of the technique developed in [4, 13]. For this purpose, the measurements of $\Delta V/V$ should be performed for different directions of SAW propagation in the same plane of the substrate and with the same adsorption layer in the path of wave propagation. Knowing the characteristics of a SAW in every

direction of propagation and measuring the corresponding values of $\Delta V/V$, we obtain a system of linear equations with an unambiguous solution.

The frequency dependence of the dielectric constant of the adsorbed water is shown in Fig. 3. The curve indicates a relaxation process with the relaxation time $\tau \sim 10^{-8}$ s. The relaxation process in the water bulk with the closest value of the relaxation time (10^{-10} s) is the dielectric dipole relaxation (Debye relaxation). The dispersion of dielectric constant in the case of the dipole relaxation is determined by the well-known expression

$$\varepsilon_f - \varepsilon_\infty = \frac{\varepsilon_s - \varepsilon_\infty}{1 + \omega^2\tau^2}, \quad (5)$$

where ω is the angular frequency. The curve in Fig. 3 is calculated by Eq. (5) at $\tau \approx 2 \times 10^{-8}$ s, $\varepsilon_s = 80$, and $\varepsilon_\infty = 5.2$. The dots mark the values of the dielectric constant calculated by Eqs. (1)–(4) from the experimental data dor $\Delta V/V$ at frequencies in the range 40–400 MHz.

Taking into account the anomalous dispersion of a SAW, a curve for the dependence of the adsorption layer thickness on humidity was plotted with the help of Eq. (1) (Fig. 4). It can be seen that the layer thickness grows nonlinearly with increasing humidity of the environment. When the vapor pressure reaches p_s, the dependence $h = f(p/p_s)$ should asymptotically approach the saturation axis ($p = p_s$); i.e., the adsorption layer thickness should increase without limit. However, as one can see from Fig. 4, the thickness of the water layer adsorbed on the lithium niobate surface has a finite value at a humidity of 100%: $h_0 \cong 17$ nm. A probable reason is the modified water structure formed in the layer under the effect of the surface force field, which manifests itself in the difference between the saturated vapor pressure over the adsorbed water surface and that over the bulk water surface.

It should be noted that the decrease in both layer thickness and temperature results in changes in the viscoelastic and dielectric properties of the adsorbed water. For example, the change of the dielectric constant manifests itself in an increase in the dipole relaxation time.

Thus, the investigation of the dispersion of the SAW velocity in thin water layers demonstrated that the dispersion dependence in the adsorbed water is nonlinear and determined by the dependence of the layer thickness on humidity. The frequency measurements at a constant thickness revealed the dispersion of the dielectric constant due to the dipole relaxation. The considerable increase of the dipole relaxation time is caused by the change in the structure of water in the layer under the effect of the surface force field of the crystal. The simple expression proposed in this paper for calculating the SAW velocity in solids loaded with a thin layer of liquid, as well as the method of measuring small variations of the velocity and attenuation, allow one to estimate the changes in the acoustic and dielectric parameters of liquids. This proposed technique opens up new possibilities for investigating the relaxation processes in thin water layers and the bulk properties of liquids in layered structures. It can be used for studying thin layers of other liquids. In addition, the dispersion features of the SAW velocity should be taken into account in designing SAW devices intended for operation in humid conditions at frequencies that fall within the dielectric relaxation range.

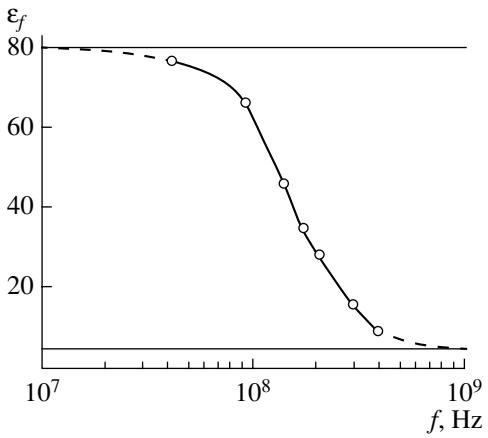

Fig. 3 Dielectric constant of adsorbed water as a function of the SAW frequency. The dashed lines show the regions of the calculated curve outside the SAW frequency range.

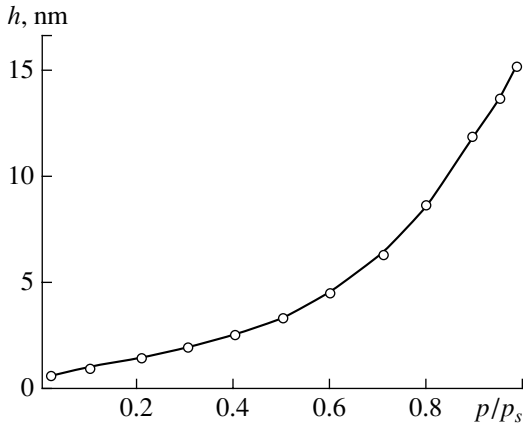

Fig. 4 Thickness of the adsorbed water layer as a function of the relative pressure of water vapor.

REFERENCES

1. N. V. Churaev, Kolloidn. Zh. **58** (6), 725 (1996).
2. N. V. Churaev, Kolloidn. Zh. **62** (5), 581 (2000).
3. B. V. Deryagin, N. V. Churaev, and V. M. Muller, *Surface Forces* (Nauka, Moscow, 1985).
4. V. I. Anisimkin, S. A. Maksimov, Ch. Kaliendo, and É. Verona, Poverkhnost, No. 3, 73 (1998).
5. I. G. Simakov and G. B. Dorjin, in *Dynamics of Continuum: Acoustics of Inhomogeneous Media* (Inst. Gidrodin.

Sib. Otd. Ross. Akad. Nauk, Novosibirsk, 1999), No. 115, pp. 132–135.

6. I. A. Viktorov, *Surface Acoustic Waves in Solids* (Nauka, Moscow, 1981).
7. A. V. Arapov, V. S. Goncharov, Yu. M. Fridman, and I. B. Yakovkin, Akust. Zh. **31**, 145 (1985) [Sov. Phys. Acoust. **31**, 85 (1985)].
8. S. V. Biryukov, Yu. V. Gulyaev, V. V. Krylov, and V. P. Plesskiĭ, *Surface Acoustic Waves in Inhomogeneous Media* (Nauka, Moscow, 1991).
9. G. N. Zatsepina, *Physical Properties and Structure of Water* (Mosk. Gos. Univ., Moscow, 1998).
10. T. Litovitz and C. Davies, in *Physical Acoustics: Principles and Methods*, Ed. by W. P. Mason (Academic, New York, 1965; Mir, Moscow, 1968), Vol. 2, Part A.
11. K. Lautscham, F. Wente, Schrader, and U. Kaatze, Meas. Sci. Technol. **10**, 1432 (2000).
12. G. B. Dorjin, I. G. Simakov, and V. D. Bazarov, in *The ISSWAS Proceedings* (Novosibirsk, 1986), Vol. 2, p. 335.
13. V. I. Anisimkin, Yu. V. Gulyaev, and I. V. Anisimkin, Poverkhnost, No. 8, 3 (2000).

Translated by A. Kruglov

Acoustical Physics, Vol. 48, No. 4, 2002, pp. 441–447. Translated from Akusticheskiĭ Zhurnal, Vol. 48, No. 4, 2002, pp. 504–511.

Audibility Thresholds for a Pure Tone in the Presence of a Pulse Jam in the Bottlenose Dolphin

N. A. Dubrovsky and M. N. Sukhoruchenko

Andreev Acoustics Institute, Russian Academy of Sciences, ul. Shvernika 4, Moscow, 117036 Russia

e-mail: dubrov@akin.ru

Received July 16, 2001

Abstract—The effect of a pulse jam on the audibility of pure tones in the bottlenose dolphin (*Tursiops truncatus*) is investigated. The pulse jam consists of a sequence of pairs of identical short pulses with a pulse spacing of 50 μs in each pair and with a pair repetition rate of 300 s^{-1}. The test signal is represented by pure tones in the frequency range 20–100 kHz. The audibility thresholds for the test signals are measured at 10-kHz steps, both in the presence of the pulse jam and in its absence, on the basis of the conditioned-reflex method with food reinforcement. The resulting dependence of the threshold shifts (TS) due to the pulse jam on the frequency of the test signal has a complex form. This dependence can be separated into three components: (1) the oscillations of the TS curve that correlate with the extrema of the spectral density of the jam, so that the peaks and dips of the TS curve correspond to the maxima and minima of the spectral density, respectively; (2) the component monotonically decreasing as the frequency grows up to 80 kHz, which distinguishes the TS curve under consideration from the rising curve obtained for masking by random noise; and (3) the frequency-independent component of the TS curve. The following auditory features are associated with these components: component 1 determines the timbre of the pulse jam; component 2 is presumably related to the pitch corresponding to the frequency $1/\tau$; and component 3 exhibits a rather strong auditory feature of random noise due to the random neural activity caused by the pulse jam in the whole auditory filter band. © *2002 MAIK "Nauka/Interperiodica".*

When a sounding pulse produced by a dolphin hits an underwater target, the echo from the latter often has the form of a sequence of several pulses (the so-called primary and secondary echoes) spaced at different intervals [1, 2]. Studies of the behavior of bottlenose dolphins showed that these animals are quite sensitive to the difference in the intervals between the pulses when these intervals are much smaller than 200–300 μs [1, 3]. However, according to the data of electrophysiological studies of the bottlenose dolphin brainstem [4], the evoked neural response to the second pulse of a pair of equal-amplitude pulses is barely detectable for pulse spacings about 200–300 μs and grows as these intervals increase above 200–300 μs. The fact that the behavior studies demonstrated a high sensitivity of dolphins to the difference in pulse spacings as small as that recommends one to look for its explanation in the mechanism of spectral auditory analysis, which has been much studied for other animals, as well as for humans.

The spectral density of the paired pulse amplitudes is a periodic function with maxima at n/τ, where $n = 0, 1, 2, 3, \ldots$ and τ is the time delay between single pulses in each pair; i.e., the paired pulses have an oscillating spectrum with a period along the frequency axis ($f = 1/\tau$). The distribution of the excitation level over the set of auditory filters can be considered as the "auditory" or "internal" spectrum of a physical stimulus. The internal spectrum can be obtained experimentally by measuring the audibility thresholds for pure tones under the action of another stimulus, whose internal spectrum is to be determined. In the literature, the method of studying the masking thresholds when pure tones are masked with complex stimuli is referred to as the "profile analysis" [5, 6]. This method is used, e.g., for studying speech sounds [7].

This paper reports on the study of the internal spectrum of paired pulses, which form the clicks imitating the echolocation signals of a bottlenose dolphin, with a very small pulse spacing. Such signals are very important stimuli for an echolocating animal in the biological sense. The experiment consisted in measuring the detection thresholds for pure tones in the presence of a pulse jam and in its absence.

The experimental setup is sketched in Fig. 1. The measurements were performed in a concrete tank. A two-meter-long separating net was fixed with one end to a plank (*P*). The animal under test occupied the starting position at the other end of the net, away from the plank. At a 1-m distance from the plank, acoustic sources (S) were suspended at a depth of approximately 1.5 m on both sides of the net. The sources simultaneously produced the same pulse jam. A test signal (a pure tone) could appear at any source at random. With the appearance of the test signal, the dolphin was expected to leave its starting position and approach the source from which the signal was sent. When the dol-

1063-7710/02/4804-0441$22.00 © 2002 MAIK "Nauka/Interperiodica"

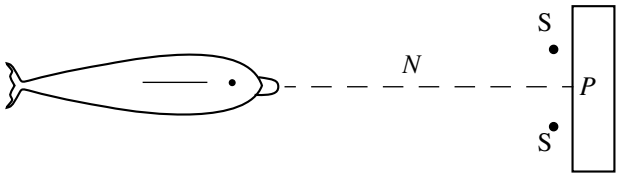

Fig. 1. Schematic diagram of the experiment: the dolphin occupying the starting position, (*N*) a separating net, (S) two acoustic sources, and (*P*) the plank from which the test signal was controlled and the animal was rewarded with food.

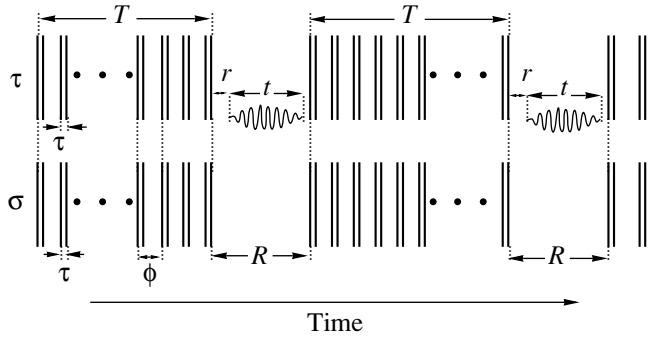

Fig. 2. Time diagram of acoustic stimulation: *T* is the period of the pulse jam generation, τ is the delay between single pulses within pairs forming the pulse jam, 1/ϕ is the pair repetition rate, *t* is the duration of the pure tone serving as the test signal and supplied at random to one of the two channels (left or right) in pauses of length *R*, and *r* is the tone delay with respect to the beginning of the pause. The pause repetition rate and the rate of the test signal presentation coincide and are equal to $1/(T + R) = 1\ s^{-1}$. The diagram scale is arbitrary.

phin made a correct choice, it was encouraged with fish. At the moment when the dolphin approached the source, the test signal was turned off. The food given to the dolphin in the case of the right choice, or the absence of food in the case of the wrong choice, served as a signal for the dolphin to return to the starting position. The measurements were performed with an animal that was adjusted to life in artificial pools for years and was used earlier in various studies of audibility thresholds, including those with pulsed signals. In our experiments, no preliminary training was necessary for the dolphin to detect the tone signal in the presence of the pulse jam (or in its absence). With the very first presentations of the test signal, whose level exceeded any expected audibility thresholds, the dolphin correctly accomplished the task.

Figure 2 shows the time diagram of the acoustic stimulation. The stimulation paradigm is described in detail in [8]. The paired pulses that represented the jam had a fixed spacing of 50 μs and a repetition rate of $300\ s^{-1}$. The pulse jam was interrupted once in a second for a 7-ms-long pause *R*; i.e., the operation period of the pulse jam *T* was less than 1 s by the pause length *R*. Within the pause, a test signal appeared at one of the sources: a 6-ms-long piece of a sinusoid, including the leading and trailing edges 1-ms-long each. The acoustic pulses were obtained as a result of the shock excitation of piezoceramic spheres by short videopulses. The spheres were 10 mm in diameter. The duration of a single acoustic pulse in water did not exceed 30 μs. The oscillograms of the pulses from different sources for the same electric pulse were recorded at the rostrum of the animal in its starting position (the oscillograms can also be found in [8]). The peak value of the pulses was constant and corresponded to approximately 60 dB over the audibility threshold for a single pulse.

The frequency values for the test tone were selected at random, with a step of 10 kHz equal to the half-period of the spectral density oscillations of the paired pulses, and in such a way that these frequencies corresponded to the extrema of the spectrum of the paired pulses. In the absence of a jam, the test tones were also presented with a repetition rate once per second.

A specific feature of the threshold determination with the use of a separating net is the possibility of a binaural localization of the source of the test signal by the analysis of interaural differences when the signal amplitude exceeds the threshold level. However, the source localization at threshold levels is likely to occur in a monaural way.

The thresholds were determined by the staircase method, which allows one to automatically maintain the signal level in the threshold region. The signal amplitude was gradually reduced from the level that was preliminarily known to be above the threshold to the level at which the dolphin made the first mistake. After this, the amplitude was increased until the dolphin gave a correct response. Then, the amplitude was decreased to the value at which the dolphin again was mistaken, and so on. Up to ten such reversals were used when the threshold was determined in the presence of the pulse jam, and five to six reversals, when the jam was absent. The signal amplitude in the threshold region was varied at a constant step of 5 dB, and the total number of the test stimulus presentations in the threshold region was 20–30 at every test frequency. The threshold value in a given series was obtained by averaging the intermediate signal levels between the correct and incorrect responses at the points of reversal. The number of repeated sessions at every frequency was four to five in the presence of the pulse jam and two to three in its absence. The repeated threshold values were also averaged. The thresholds were calculated in decibels relative to an arbitrarily chosen amplitude of the test signal at the source input.

The results of measurements are presented in Fig. 3. The lower curve shows the frequency dependence of the test tone detection thresholds in the absence of the pulse jam, and the upper curve shows the corresponding dependence in the presence of the pulse jam. According to Fig. 3, in the absence of jam, the thresh-

olds only slightly decrease with growing frequency, which agrees well with the threshold data reported in [9] (for frequencies of 20–100 kHz). In the presence of the pulse jam, a rather strong frequency dependence is observed in the frequency range 20–70 kHz, within which the thresholds decrease by about 30 dB.

The effect of the pulse jam on the detection thresholds observed in our experiments can be caused by different physiological factors, namely, nonsimultaneous masking and adaptation (and/or fatigue). To determine the individual contributions of these two factors to the threshold changes, special measurements are necessary, which are beyond the scope of this study. Therefore, below, we will use the term "threshold shift" (TS) to denote the difference between the thresholds in the presence and absence of the pulse jam with the understanding that it includes the total result of masking and adaptation (and/or fatigue). By definition, the TS does not depend on the auditory acuity in the absence of jam.

Figure 4a presents the frequency dependence of the TS. The vertical line segments show the estimated standard errors for the difference between the average values of the TS obtained in the presence and absence of jam. This estimate (S_{x-y}) can be obtained from the formula [10] $S^2_{x-y} = s^2\{x\}/n_x + s^2\{y\}/n_y$, where $s^2\{x\}$ and $s^2\{y\}$ are the estimates of the threshold variance near different average values and n_x and n_y are the numbers of the threshold values obtained in the presence of the pulse jam and in its absence, respectively.

The frequency dependence of the TS has a complex form. To make the analysis more convenient, this dependence can be represented as a superposition of several curves. First of all, one can notice the oscillations of the TS curve. The arrows above the curve indicate the positions that correspond to the maxima and minima of the spectral density of the pulse jam used in the experiment. The arrows directed upwards refer to the maxima, and the arrows directed downwards, to the minima. One can see that the oscillations of the TS curve correlate well with those of the spectral density of the pulse jam up to a frequency of 80 kHz. The peaks of the TS curve exactly coincide with the maxima of the spectral density of the jam, and the dips in this curve correspond to the minima. Since the correlation between the oscillations of the TS curve and the extrema of the pulse jam spectrum was observed for the entire curve up to 80 kHz, we considered it possible to combine and average the threshold data for two adjacent peak values. The comparison of the new mean values (with the new estimates of the standard error in the difference between the means) and the mean value of the TS at an intermediate frequency corresponding to the position of the TS minimum revealed a rather high level of statistical significance of the TS difference for almost all extrema of the pulse jam spectrum: 99% according to Student (and only in one case, 95%).

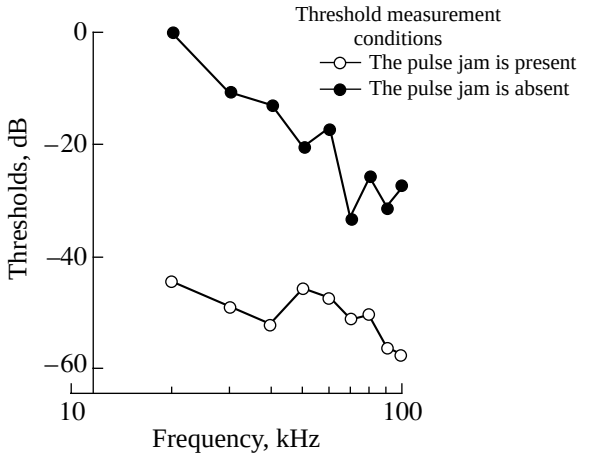

Fig. 3. Dependence of the audibility thresholds for pure tones on the tone frequency in the presence of the pulse jam and in its absence. The thresholds are given in decibels relative to an arbitrarily chosen amplitude of the test tone at the source output. The pulse jam consists of paired pulses with a pulse spacing of 50 μs and with a pair repetition rate of 300 s^{-1}.

Figure 4a also shows the general decrease in the TS curve with the increase in the test signal frequency up to 70 kHz. Connecting all peak values of the TS curve in Fig. 4a, we obtain a broken line, which illustrates the monotone decrease in the TS with different rates in regions *1* and *2* and a slight increase in region *3* (at frequencies above 70 kHz). Figure 4b presents the acoustic spectra of single pulses obtained from different sources in response to the same electric pulse and also the average acoustic spectrum, which was calculated by the Fourier transformation of the single pulse oscillograms. The spectrogram of a single pulse can be considered as an envelope of the spectral density oscillations of the paired pulses. The frequency dependence of the spectral density represented by the single-pulse spectrogram and the broken line in Fig. 4a exhibit opposite behavior. As the frequency grows, the spectral density of a single pulse increases, whereas the TS represented by the broken line decreases. This situation takes place for all frequencies up to 70 kHz, and only above 70 kHz do both the TS and the spectral density of a single pulse increase with increasing frequency.

Let us draw a straight line parallel to the abscissa axis through the lowest point of the TS curve. This line shows that the level to which the TS decreases is still rather high (it exceeds by 20 dB the audibility threshold for a 70-kHz tone in the absence of pulse jam). We assume that this line represents the frequency-independent component of the total effect produced by the pulse jam.

Consider the three aforementioned components of the TS curve from the physiological point of view. The correlation of the peaks of the TS curve with those of the spectrum of paired pulses is no surprise. Psychoacoustic studies of masking pure tones by stimuli with

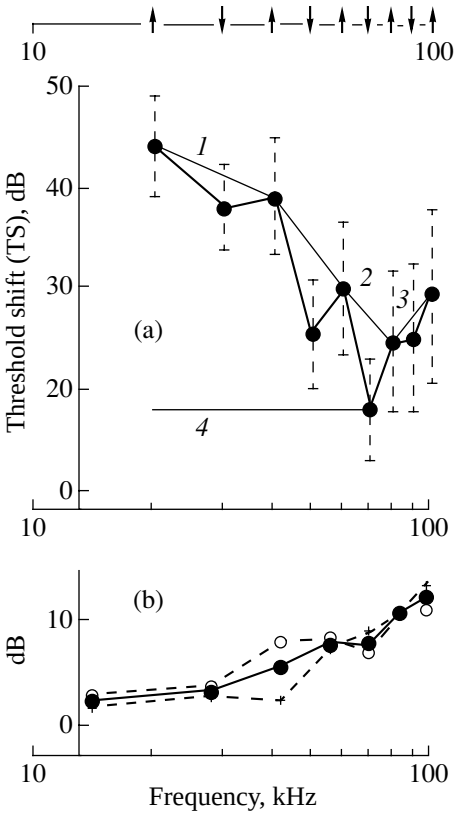

Fig. 4. (a) Dependence of the TS on the test tone frequency (the thick line). The arrows above the curve indicate the positions of the maxima (upward arrows) and minima (downward arrows) of the spectral density of the paired pulses forming the pulse jam. The dashed vertical line segments show the estimates of the standard error for the difference between the average thresholds obtained in the presence and absence of pulse jam. The upper points of the TS curve form a broken line (the thin line) whose different parts are marked by numbers *1–3*. The meaning of lines *1–4* is explained in the main body of the paper. (b) Spectrograms of single acoustic pulses recorded in water from different sources in response to the same electric pulse (the dashed lines) and the average spectrogram for the two sources (the thick line).

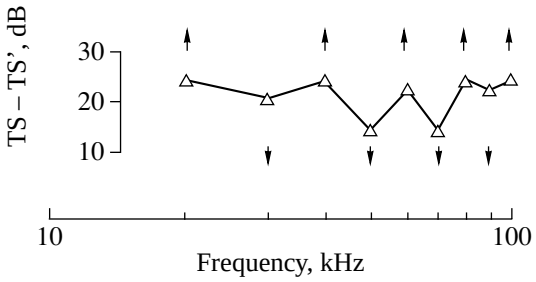

Fig. 5. Curve constructed with the aim to eliminate the effect of the slope of components *1* and *2* (see Fig. 4a). TS' denotes the ordinate values of the broken line relative to line *4* (see Fig. 4a). The upward and downward arrows indicate the positions of the maxima and minima, respectively, of the spectral density of the paired pulses (the pulse jam).

different kinds of complex spectra, e.g., by noise with rippled or oscillating spectrum [11] or by speech sounds [7], reveal a similar phenomenon. One can assume that the peaks of the TS curve represent the "hearing spectrum" of the paired pulses. Although no correlation is observed at frequencies above 80 kHz, its absence can be explained by the superimposition of the ascending part of the broken line (component *3* in Fig. 4a). Eliminating the value of the TS (the broken line in Fig. 4a) taken with respect to the straight line that is drawn through the inflection point of the TS curve in the direction parallel to the abscissa axis (Fig. 4a), we obtain a correlation between the peaks of the TS curve and the maxima of the spectral density of the pulse jam within the whole frequency band under study (Fig. 5), although for frequencies of 80–100 kHz, the peak amplitude is much smaller. It should be noted that the discrimination between the bandpass noise with rippled and constant spectral densities by dolphins [12] is possible for the central frequencies no higher than 100 kHz. This result agrees with our data on the reduced response of auditory filters with a tuning frequency of 90–100 kHz to a complex stimulus (Fig. 5).

The correlation between the spectral density oscillations of the pulse jam and the peaks of the TS curve is possible at frequencies no higher than the frequencies at which the difference in the output signals of the adjacent auditory filters begins to manifest itself. Since, at frequencies of 90–100 kHz, the amplitude of the peaks of the curve shown in Fig. 5 strongly decreases, one can expect that the ability to resolve the spectral density oscillations by the critical band mechanism is limited by frequencies somewhat above 100 kHz. On the basis of the data obtained in this study, we can roughly estimate the width of the critical bands. The half-period of the spectral density oscillations of the pulse jam under consideration is equal to 10 kHz, and the adjacent peaks and dips of the spectral density of the jam must somehow be resolved by the adjacent auditory filters with a tuning frequency near 100 kHz. Therefore, as the estimate of the critical bandwidth for a frequency of 100 kHz, we can accept a value somewhat lower than 10%. This estimate is close to that obtained for dolphins by the method of masking one pure tone by another for a frequency of 50 kHz [13].

However, it should be noted that, according to the estimate given in [14], for dolphins, the width of an idealized auditory filter at a frequency of 100 kHz has a much smaller value: about 2.5 kHz. In the experiments [14], the bottlenose dolphin exhibited reversals of the spectral density ripples of bandpass noise with different central frequencies. The number of the spectral density peaks was fixed, but the bandwidth decreased with increasing central frequency. The detection of the reversals of a rippled spectral density of noise is possible using different mechanisms: the resolution of the peaks by different critical bands and also within a single critical band. In the latter case, to detect the reversals of the noise ripples, it is sufficient that the half-

period of the spectral density oscillations be no smaller than the differential threshold in frequency. In the cited publication [14], the resolution of the peaks in frequency was characterized by the threshold value of the density of peaks in the spectral density of noise, or the number of peaks per conditional frequency band. For a frequency of 100 kHz, the relative density of peaks (the ratio of the central frequency to the distance between the peaks on the frequency scale) at the reversal detection threshold was equal to 40 [14]; i.e., the frequency interval between the peaks, or the period of the spectral density oscillations, was 2.5 kHz. Hence, the whole bandwidth for the number of the spectral density peaks in use (four) was near 10 kHz. This value coincides with the aforementioned estimate of the critical band (10%). In addition, the half-period of the spectral density for the threshold value presented above is equal to 1.25 kHz, which is of the same order of magnitude as the differential threshold in frequency. Therefore, we assume that, in the cited experiments [14], the dolphin was likely to exhibit a reversal of the spectral density ripples within a single critical band.

The correlation of the jam spectrum oscillations with the peaks of the TS curve is possible up to the frequency near which the adjacent auditory filters still resolve the adjacent peaks and dips of the spectral density period. The frequency characteristics of the high-frequency filters strongly overlap [15], and the difference between the output signals of the filters tuned to the adjacent peak and dip decreases with increasing frequency until it reaches the threshold level. Thus, the condition for the threshold resolution of the peaks and dips in the spectral density is $\Delta f_t > 1/2\Delta f$, where Δf_t is the threshold difference between the frequencies of the adjacent extrema of the spectrum and Δf is the period of the spectral density oscillations of the noise. For the pulse jam used in our studies, $\Delta f = 20$ kHz, and this condition is satisfied near 100 kHz; i.e., the ratio $\Delta f_t/\Delta f$ is approximately equal to 10%. According to [13], the tuning parameter of the auditory filter, Q_{10} (the ratio of the central frequency to the bandwidth of an equivalent rectangular filter at a level of 10 dB below the maximum of the frequency characteristic), is estimated as 6 kHz for a frequency of 108 kHz (about 6%). Thus, the estimate obtained by us for Δf_t is close to the value of the tuning parameter Q_{10} of the auditory filter, although we did not obtain a zero amplitude of the threshold peak (Fig. 5).

Finally, we note that the amplitude of the peaks of the TS curve (Fig. 5) decreases at low frequencies (20–40 kHz) as well. This result can be explained by the fact that the level of the spectral components of a single pulse decreases with decreasing frequency (Fig. 4b).

Thus, the results of the profile analysis allow us to explain the oscillations of the TS curve. An unexpected phenomenon is the monotonic decrease in the TS value with increasing frequency (components *1* and *2* of the broken line in Fig. 4a; the inflection at 40 kHz is ignored). First, (as was mentioned above) the monotone component of the TS and the spectrogram of a single acoustic pulse depend on frequency in opposite ways (Figs. 4a and 4b). Second, an important difference is observed between the frequency dependence of the TS curve at frequencies of 20–70 kHz (components *1* and *2* of the broken line) and the curve corresponding to the masking of pure tones by random noise. It is well known [16] that, for humans, the white-noise masking at frequencies above 500 Hz grows at a rate of 10 dB per decade. This growth is explained by the broadening of the critical bands with increasing frequency. A similar frequency dependence of the random-noise masking was obtained for dolphins [17]. The broken line shown in Fig. 4a exhibits a decrease in the TS by almost 20 dB as the frequency of the test signal increases from 20 to 70 kHz. This behavior of the TS curve cannot be explained by conventional spectral mechanisms. Only at frequencies of 70–100 kHz is a slight increase in the TS with frequency observed (component *3* of the broken line in Fig. 4a), as in the case of masking by random noise (and also according to the form of the spectral density curve for a single pulse, Fig. 4b).

Figure 4a shows that the most substantial TS corresponds to the test signal frequency equal to 20 kHz, i.e., to the frequency $f_0 = 1/\tau$ ($\tau = 50$ μs). This suggests that the unusual behavior of the TS curve with frequency is a result of a sort of masking of a simple tone by a complex tone. In contrast to a simple tone, a complex tone is represented by a periodic (a set of harmonics) and an aperiodic signal with an oscillating spectral density. For a complex tone, it is possible to find with fair accuracy a pure tone whose pitch corresponds to the fundamental frequency of the periodic signal or to the frequency $f_0 = 1/\tau$ for either paired pulses or ripple noise. This kind of noise is obtained by combining a segment of white noise with its delayed replica. The frequency $f_0 = 1/\tau$ is often called the fundamental frequency of an aperiodic broadband signal.

The perception of the pitch of paired pulses by humans even in the absence of the frequency $f_0 = 1/\tau$ in the spectrum was first demonstrated in [18]. The pitch of complex tones is sometimes called virtual, even when the fundamental frequency is present in the spectrum [12].

The ability to respond to the fundamental frequency of complex periodic sounds in which the fundamental frequency is absent was revealed in all vertebrates ever studied: fish, frogs, birds, cats, and monkeys (see the review in [19]). The ability of dolphins to discriminate between the noise types with rippled and constant spectral densities was studied in [12]. The widespread ability of vertebrates to detect the spectral-time periodicity of a complex stimulus testifies to the importance of the auditory feature related to this kind of periodicity. This feature can be nothing but pitch. There is no reason to believe that dolphins are incapable of pitch perception for complex stimuli with periodic spectra. The possibil-

ity of explaining the unique echolocation abilities of dolphins by the pitch extraction from a complex stimulus consisting of a sequence of identical pulses has been much discussed in the literature (see the review in [20]).

In our experiments, the dolphin seems most likely to respond to the pitch of the pulse jam. Since the spectrogram of a single acoustic pulse forming the pair exhibits a rather steep decrease as the frequency approaches 20 kHz (Fig. 4b), the 20-dB increase in the threshold for the 20-kHz test signal (Fig. 4a) cannot be explained by masking of a pure tone by another tone at the same frequency. The interval $f_0 = 1/\tau$ between the peaks of the spectrum of the pulse jam used in the experiment was also equal to 20 kHz. Therefore, such a large TS at the frequency 20 kHz can be attributed to only the considerable pitch strength in the perception of the complex tone (the pulse jam). The term "pitch strength" of a complex sound is common in psychoacoustics (see the review in [21]) and is an important characteristic of the perception of complex tones [22].

The decrease in the TS with increasing frequency (Fig. 4a) is more difficult to explain. Let us assume that the pitch strength in the perception of a complex tone is determined by the number of spectral peaks resolved by the critical bands, as well as by the accuracy of the analysis of the spectral density period on the scale of "auditory frequencies." In our experiments, the number of the spectral peaks of the pulse jam was fixed (in all experiments, the delay between the paired pulses was the same: 50 μs). Therefore, it is reasonable to expect that the behavior of the broken line in Fig. 4a is determined by the accuracy of the analysis of the spectral density period of the paired pulses. The period of the spectral density was reproduced in the auditory system owing to the change in the signal level at the outputs of the adjacent critical bands. As a consequence of the critical band broadening, every next, higher frequency, period of the spectrum covers a smaller number of critical bands. Hence, the estimate of the spectral density period becomes less accurate. The roughest estimate should be obtained in the frequency region where the adjacent auditory filters resolve only the adjacent extrema of the pulse jam spectrum. With further broadening of the critical band, even the peaks of the spectral density cannot be resolved. We assume that, for our pulse jam, the spectrum period with the spectral density maximum at a frequency of 20 kHz covers approximately ten critical bands (if the critical band width is about 10%).

If the accuracy of the analysis of the spectral density period determines the pitch strength in the perception, then, owing to this mechanism, different spectral regions play different roles in the formation of the pitch of the complex stimulus. As the tuning frequency of the auditory filter grows, the role of the high-frequency regions in the formation of the strength of the pitch perception decreases, and, hence, the corresponding masking effect of the complex tone (the pulse jam) is reduced. Therefore, the increase in the test tone frequency in our experiment was accompanied by the drop in the masking effect of the pulse jam pitch and, hence, by the descent of the TS curve. At frequencies near 100 kHz, different cases are possible, depending on the way the critical bands are organized. (It is known that critical bands can be arranged by the auditory system with reference to different frequencies [16].) If the frequency corresponding to the maximum of the spectrum period and the tuning frequency of the auditory filter coincide at a frequency of 100 kHz, the spectrum period covers one full critical band and the lateral critical bands symmetric about the central one. Between the lateral critical bands, the remainder of the spectrum period is distributed. In this case, the difference in the signals at the outputs of the adjacent critical bands is present, and, hence, some information on the form of the spectrum period is retained in the auditory system. Another possible case of the critical band arrangement is as follows: two approximately identical critical bands are symmetric about the frequency corresponding to the spectral maximum and cover the whole spectrum period. In this case, the difference between the signals at the outputs of the adjacent critical bands will be absent; i.e., no information on the form of the spectrum period will be enter the auditory system. As one can see from Fig. 5, a small peak at 100 kHz is still observed in the TS curve. Therefore, in our experiments, we most probably dealt with the first of the two cases described above.

Thus, a monotonic decrease in the TS with increasing frequency of the test tone can be explained by the decrease in the accuracy of the analysis of the spectral density periodicity of the pulse jam in the region near the test tone and by the related decrease in the contribution of the local piece of the spectrum to the formation of the pitch strength. The fact that different spectral regions play different roles in the perception of the pitch of a complex stimulus was demonstrated in the psychoacoustic experiments with ripple noise [23, 24].

The ability of cats to discriminate between sets of harmonics by the fundamental frequency (300–400 Hz) absent in the spectrum of a given set, i.e., by the pitch of a set, was demonstrated in behavioral studies [25]. The quantitative characteristic used in these studies for the characterization of the sensitivity of a cat to the difference in the fundamental frequencies of the sets of harmonics testified to a monotonic decrease in the sensitivity with increasing central frequency of the sets. The authors of the cited publication [25] explain this dependence by the decrease in the pitch strength of a set of harmonics with growing frequency.

Now, we have to discuss the third TS component that is shown separately in Fig. 4a as a straight line parallel to the abscissa axis. According to the data of psychoacoustic studies, when a human listens to noise with a rippled spectral density, he perceives two different features of the stimulus: the noise feature and the tone

feature [26]. The frequency-independent component of the TS curve (Fig. 4a) represents the high level (about 20 dB) of the noise feature in the perception of the pulse jam, this feature being unrelated to the periodicity of the spectral density of the paired pulses.

Thus, the TS curve obtained in our experiments can be considered as a superposition of three components. First, we obtained an exact correlation between the oscillations of the TS curve and the positions of the extrema of the pulse jam spectrum on the frequency axis: the peaks and dips of the TS curve correspond to the maxima and minima of the spectral density of the jam, respectively. We believe that this correlation reflects the internal spectrum of the jam. In our opinion, the internal (auditory) spectrum of paired pulses provides the timbre feature of the pulse jam.

In contrast to masking by random noise, in the case of the pulse jam, the TS monotonically decreases with increasing frequency of the test tone. The maximum of the monotonic component of the TS curve corresponds to the test frequency $1/\tau = 20$ kHz. We attribute the monotone component of the TS curve to the pitch of the pairs in the pulse jam. We explain the decrease in the TS with increasing frequency of the test tone by the decrease in the accuracy of the analysis of the period of the spectral density oscillations in the region near the test frequency and by the corresponding decrease in the contribution of the local spectrum segment to the total strength of the pitch perception.

We can surmise that the dolphin is able to manipulate the pitch strength of a sequence of clicks with a small pulse spacing by raising the lower frequency limit of the sounding pulse spectrum. This frequency increase may result in the suppression of the lower frequencies of the echo signal spectrum and a corresponding reduction of the masking effect governed by the pitch of the complex tone. In some situations, depending on the acoustic properties of the water area and on the echolocation task, such a manipulation can increase the noise immunity of the echo signal. Data testifying that the sounding pulses of a dolphin can have different lower frequency limits are presented in the review [27].

The frequency-independent component (Fig. 4a) exhibits a rather strong noise feature, which provides the masking effect due to the random neural activity caused by the pulse jam within the whole auditory filter band.

ACKNOWLEDGMENTS

This work was supported by the Russian Foundation for Basic Research, project no. 00-04-49311.

We are grateful to N.G. Bibikov for carefully reading the manuscript and for valuable comments.

REFERENCES

1. V. M. Bel'kovich and N. A. Dubrovsky, *Sensory Basis of Orientation in Cetaceans* (Nauka, Leningrad, 1976).
2. W. W. L. Au, in *The Sonar of Dolphins* (Springer, New York, 1993).
3. V. A. Vel'min and N. A. Dubrovsky, Dokl. Akad. Nauk SSSR **225**, 470 (1975).
4. V. V. Popov and A. Ya. Supin, *Electrophysiology of Marine Mammal Sensory Systems* (Nauka, Moscow, 1986), pp. 85–106.
5. D. Green and G. Kidd, J. Acoust. Soc. Am. **73**, 1260 (1983).
6. D. Green, Z. Onsan, and T. Forrest, J. Acoust. Soc. Am. **81**, 692 (1987).
7. M. F. Spiegel, J. Acoust. Soc. Am. **84**, 2033 (1988).
8. M. N. Sukhoruchenko, in *Marine Mammal Sensory Systems*, Ed. by J. A. Thomas, R. A. Kastelein, and A. Ya. Supin (Plenum, New York, 1992), pp. 277–286.
9. C. S. Johnson, in *Marine Bioacoustics* (Oxford, 1967), Vol. 2, pp. 247–260.
10. V. Yu. Urbakh, *Biometric Methods* (Nauka, Moscow, 1965).
11. W. A. Yost, J. Acoust. Soc. Am. **66**, 400 (1979).
12. W. W. L. Au and J. L. Pawloski, J. Acoust. Soc. Am. **86**, 591 (1989).
13. C. S. Johnson, J. Acoust. Soc. Am. **49**, 1317 (1971).
14. A. Ya. Supin, M. G. Pletenko, and M. B. Tarakanov, in *Marine Mammal Sensory Systems*, Ed. by J. A. Thomas, R. A. Kastelein, and A. Ya. Supin (Plenum, New York, 1992), pp. 277–286.
15. V. V. Popov, A. Ya. Supin, and V. O. Klishin, J. Acoust. Soc. Am. **102**, 3795 (1997).
16. E. Zwicker and R. Feldtkeller, *The Ear as a Communication Receiver* (Acoust. Soc. Am., New York, 1999; Svyaz', Moscow, 1971).
17. C. S. Johnson, J. Acoust. Soc. Am. **44**, 965 (1968).
18. W. R. Thurlow and F. M. Small, Jr., J. Acoust. Soc. Am. **27**, 132 (1955).
19. R. R. Henry, J. Comp. Physiol. A **181**, 239 (1997).
20. P. W. B. Moore, R. W. Hall, W. A. Friedl, and P. E. Nachtigal, J. Acoust. Soc. Am. **76**, 314 (1984).
21. F. L. Wightman, J. Acoust. Soc. Am. **54**, 407 (1973).
22. L. Wiegrebe, J. Acoust. Soc. Am. **109**, 1082 (2001).
23. R. M. Warren and J. A. Bashford, Jr., J. Acoust. Soc. Am. **84**, 2058 (1988).
24. W. A. Yost and R. Hill, J. Acoust. Soc. Am. **64**, 485 (1978).
25. H. Heffner and I. C. Whitfield, J. Acoust. Soc. Am. **59**, 915 (1976).
26. R. D. Patterson, S. Handel, W. A. Yost, and A. J. Datta, J. Acoust. Soc. Am. **100**, 3286 (1996).
27. N. A. Dubrovsky, *Echolocation by Dolphins* (TsNII Rumb, Leningrad, 1975).

Translated by E. Golyamina

Acoustical Physics, Vol. 48, No. 4, 2002, pp. 448–452. Translated from Akusticheskiĭ Zhurnal, Vol. 48, No. 4, 2002, pp. 512–516.

Estimation of the Relaxation Parameters of a Cholesteric Liquid by the Parameters of Acoustic Streaming

O. A. Kapustina, N. A. Kolesnikova, and O. V. Romanova

Andreev Acoustics Institute, ul. Shvernika 4, Moscow, 117036 Russia

e-mail: bvp@akin.ru

Received June 20, 2001

Abstract—The possibility of determining the relaxation time of cholesteric liquid crystals with a large helix pitch from the parameters of acoustic streaming is demonstrated experimentally. © *2002 MAIK "Nauka/Interperiodica".*

It is known that acoustic relaxation is a manifestation of internal nonequilibrium processes in a medium. These processes are connected with the restoration of its thermodynamic equilibrium that is disturbed by fluctuations of pressure and temperature in a sound wave. Like any nonequilibrium phenomenon, relaxation is determined not only by the thermodynamic characteristics of the medium but depends essentially on its macroscopic parameters. Starting from the time when Mandel'shtam and Leontovich developed the relaxation theory of liquids [1], this problem has attracted the attention of many researchers for several decades. It was found that acoustic relaxation leads to deviations of the frequency dependences of sound velocity and absorption coefficient from the form of these dependences predicted by classical hydrodynamics [2, 3]. As for liquid crystals, a rather large number of papers have been devoted to the investigation of this problem.The basic results of these studies are generalized in the monographs [4–6]. The latest publications [6, 8] demonstrate that relaxation processes make a decisive contribution to the mechanism of macrostructural variations of a liquid crystal layer under the effect of ultrasound. For example, according to [7], an adequate description of the mechanism of destabilization of the planar texture of a nematic liquid crystal layer in an ultrasonic field is possible only in the framework of nonequilibrium hydrodynamics. According to preliminary data, the same approach to the analysis of the orientation behavior of cholesteric liquid crystals leads to the conclusion that the scaling relationships determining the threshold characteristics of the two-dimensional domains induced in a planar layer by ultrasound depend on the relationship between the ultrasonic frequency $\omega/2\pi$ and the relaxation frequency [8]. For example, the spatial period Λ of domains in the high-frequency range, where $\omega\tau \gg 1$, does not depend on the ultrasonic frequency and is proportional to $(P_0 d\tau)^{1/2}$, whereas, at low frequencies when $\omega\tau \ll 1$, this period is $\Lambda \sim (P_0 d\omega)^{1/2}$. Here, d is the thickness of the liquid crystal layer, P_0 is the equilibrium value of the cholesteric helix pitch, and τ is the relaxation time of the order parameter. It is essential that the analysis of this effect in the framework of the classical Leslie–Ericksen hydrodynamics common in physics of liquid crystals [9] leads to the relationship $\Lambda \sim (P_0 d)^{1/2}$ within the whole considered frequency range [6]. In view of the above, it seems evident that an experimental verification of these scaling relationships, which are characteristic of the relaxation process related to the relaxation of the order parameter of a liquid crystal and leading to an anisotropy of the dynamic elasticity $\Delta E(\omega, \tau)$, provides an opportunity to determine the applicability of the new approach to cholesteric liquid crystals and to evaluate the admissibility of some assumptions introduced in the model [8]. It is common to treat the experimentally observed acoustic anisotropy of liquid crystals [10] as the contribution of the sum of two independent relaxation processes, one of which is connected with the relaxation of the order parameter and the other, with the relaxation of the end groups of molecules. The model [8] takes into account only one of them. The relaxation time of the order parameter is one of the key factors determining the orientation behavior of a liquid crystal system, and it is necessary for a quantitative comparison of the theoretical predictions and experimental data. Thus, the problem of the determination of the relaxation time in cholesteric liquid crystals seems very important. A conventional technique for investigating the relaxing media is ultrasonic spectroscopy [5], which allows one to determine the relaxation times of various relaxation processes from the experimentally determined frequency dependences of the acoustic parameters of a liquid crystal. However, such a technique needs complex and cumbersome equipment that provides an opportunity to conduct high-precision measurements of the absolute values of ultrasonic velocity or absorption in a wide frequency range.

This paper discusses the possibility of measuring the relaxation time in a cholesteric liquid crystal with a

1063-7710/02/4804-0448$22.00

weakly distorted structure (with a helix pitch of $P \lesssim 10^{-4}$ cm, which is much greater than the light wavelength) by the parameters of acoustic streaming.[1] This simple method was suggested and successfully tested in [12] for Newtonian liquids.

Let us consider the acoustic streaming of a cholesteric liquid, which accompanies the propagation of a damped plane wave in the direction of the x axis from a radiator of radius R (Fig. 1a). The radiator is positioned in the plane corresponding to the coordinate $x = 0$. An ultrasonically nonreflecting boundary lies at the distance $l \gg R, \lambda$ from the radiator. The fundamental set of equations describing the acoustic streaming in a Newtonian liquid has the form [13]

$$\begin{aligned}(U\nabla)U &= -\nabla P/\rho_0 + \alpha n\delta^2 W/\rho_0 \\ &+ \eta\nabla^2 U/\rho_0 + [1/3\eta(0) + \mu(0)]\nabla\nabla U/\rho, \\ \nabla(U + V\rho/\rho_0) &= 0.\end{aligned} \tag{1}$$

Here, U is the velocity of acoustic streaming, P and V are the sound pressure and the particle velocity in an ultrasonic wave, W is the energy density in the wave, $\delta = 1 - Un/C_0$, C_0 is the ultrasonic velocity in the medium, n is the unit vector in the direction of the wave vector, ρ and ρ_0 are the densities of the medium in the unperturbed and perturbed states, and $\eta(0)$ and $\mu(0)$ are the shear and bulk viscosities. The coefficient α in the set of equations (1) stands for the ultrasonic absorption coefficient in the Newtonian liquid and is connected with its parameters by the expression

$$\alpha = \omega^2[4/3\eta(\omega) + \mu(\omega)]/2\rho_0 C^3(\omega), \tag{2}$$

where

$$\begin{aligned}\eta(\omega) &= G_\infty\tau/(1 + \omega^2\tau^2), \\ \mu(\omega) &= \rho_0\tau(C_\infty^2 - C_0^2)/(1 + \omega^2\tau^2), \\ C(\omega) &= (C_0^2 + C_\infty^2\omega^2\tau^2)^{1/2}/(1 + \omega^2\tau^2)^{1/2}.\end{aligned} \tag{3}$$

Here, C_0 and C_∞ are the ultrasonic velocities at $\omega \longrightarrow 0$ and $\omega \longrightarrow \infty$, respectively; G_∞ is the shear modulus at $\omega \longrightarrow \infty$. Taking into account Eqs. (3), we can represent Eq. (2) in the form

$$\begin{aligned}\alpha = \omega^2\tau(C_\infty^2 - C_0^2)(1 + \omega^2\tau^2)^{1/2}/2C_0^3(1 \\ + \omega^2\tau^2 C_\infty^2/C_0^2)^{3/2}.\end{aligned} \tag{4}$$

If we restrict the level of action and the velocity of acoustic streaming by the conditions $V/C_0 < 1$, $U/C_0 < 1$, and $\mathrm{Re} = UR/\gamma < 1$ (γ is the kinematical viscosity), the set of Eqs. (1) can be reduced to a form similar to that

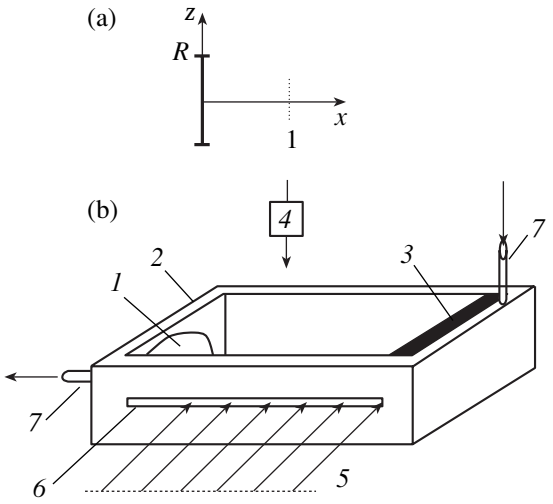

Fig. 1. Measuring technique: (a) the geometry of the problem and (b) the schematic diagram of the experiment. (*1*) An ultrasonic radiator; (*2*) a dish filled with a liquid crystal; (*3*) a sound-absorbing layer; (*4*) a binocular magnifier in the observation system; (*5*) a light beam; (*6*) a slot; and (*7*) elements of a system of thermal stabilization.

of the equations for acoustic streaming of a Newtonian liquid [12]:

$$\begin{aligned}-\nabla P + \alpha W &= \eta\nabla^2 U, \\ \nabla U &= 0.\end{aligned} \tag{5}$$

This means that some conclusions derived from the solutions of equations for streaming in a Newtonian liquid can be extended to non-Newtonian liquids. Since the configurations of these streamings coincide, the distribution of the streaming velocity of a non-Newtonian liquid along the axis of a sound beam ($y = 0$) obeys the law established for Newtonian liquids [12], namely,

$$U_x = U_0(x/\mathrm{R})\exp(-2\alpha x), \tag{6}$$

where $U_0 = V_0^2\,\mathrm{R}^2\alpha/2\gamma$. It follows from here that, on the axis of the sound beam, there is a point with the coordinate

$$x_{\max} = (1/2)\alpha \tag{7}$$

at which the velocity of acoustic streaming takes the maximal value. Thus, determining the value of $x_{\max}$ experimentally, it is possible to determine the absorption coefficient and then calculate the relaxation time τ by Eq. (4).

The experiments were conducted using a mixture of cholesteric and nematic liquid crystals (20% cholesteryl chloride (CC) and 80% methoxybenzylidene-p-n-butylanilin (MBBA) and ethoxybenzylidene-p-n-butylanilin (EBBA)) with the help of the setup schematically represented in Fig. 1b. An ultrasonic source (*1*) (an *X*-cut quartz transducer) was positioned at one end of a dish (*2*) filled with the mixture under investigation. The

[1] It is known that the optical properties of cholesteric liquid crystals change drastically when the light wavelength is comparable with the helix pitch [11].

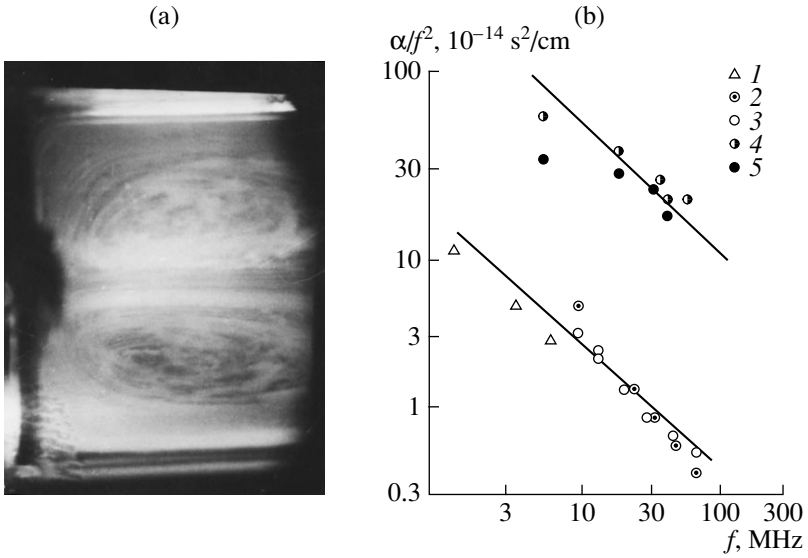

Fig. 2. Summary of basic experimental data: (a) a pattern of a fully developed acoustic streaming of a cholesteric liquid at a frequency of 6.3 MHz and (b) the frequency dependence of ultrasonic absorption (*1*) in the CC/MBBA/EBBA mixture at a temperature of 40°C, (*2*, *3*) in MBBA at the temperatures 30 and 40°C, and (*4*, *5*) in cholesteryl linoleate at the temperatures 32 and 44°C.

other end of the dish was covered with a sound-absorbing layer (*3*) to provide the traveling wave mode. A system of thermal stabilization of the setup allowed one to control the liquid temperature within the interval 20–60°C and maintain it constant within ±0.5°C. The geometry of the experiments was as follows: the observation of the field of streaming was conducted from above through a binocular magnifier (*4*); the illumination was through a slot in a side wall of the dish by a light beam (*5*) in the direction perpendicular to the axis of the sound beam. The level of action was monitored by the voltage across the transducer (*1*). The frequency was varied in the interval 2–10 MHz.

The essence of the experiments conducted is as follows. The level of action is set so as to correspond to the ultrasonic intensity ~1 W/cm^2. For this purpose, the radiators used in the experiments are calibrated preliminarily by the acoustic radiometer technique and the system of thermal stabilization is tuned in such way that the temperature within the liquid crystal is maintained constant. In the course of the setup operation, the thin layer of the liquid crystal that is immediately adjacent to the radiator surface is heated due to the ultrasonic absorption and passes into an isotropic state. Since, in this state, the liquid crystal becomes transparent to a light beam and, in the cholesteric phase, it scatters light, the interface between the two phases is easily identified. The acoustic streaming arising in the liquid crystal that retains the anisotropic mesomorphic state entrains the isotropic liquid crystal in its motion, and the isotropic liquid moves in the anisotropic light-scattering medium in the form of a thin transparent stream "drawing" the streaming lines through the whole volume of the dish. The typical pattern of a fully developed acoustic streaming of a cholesteric liquid is given in Fig. 2a (top view, a frequency of 6.3 MHz). The light lines observed against the dark background in this picture are identified as the streaming lines, and they are produced by the movement of the isotropic phase transparent to light. Analyzing the relative positions of these lines, it is possible from their density to determine the interval of the values of x within which the maximum of the acoustic streaming velocity on the sound beam axis takes place and to calculate the values of α and τ. The experimental results are given in Fig. 2b in the form of the frequency dependence of the absorption coefficient, α/f^2, of the investigated mixture at the temperature 40°C (dots *1*).The same figure shows the values of α/f^2 given in the literature [4, 5] for comparison. In the frequency range where the coefficients of shear and bulk viscosity do not depend on frequency, it is common to characterize the sound absorption by the value α/f^2, which, in this case, also does not depend on frequency and is a parameter characterizing the properties of the medium. The results were obtained using the conventional ultrasonic spectroscopy technique for a nematic liquid crystal (MBBA at temperatures of 30 and 40°C, dots *2* and *3*) and a cholesteric liquid crystal (cholesteryl linoleate at temperatures of 32 and 44°C, dots *4* and *5*). One can see that the experimental values of α/f^2 for the investigated mixture, which were obtained at frequencies of 2.1, 6.3, and 10.5 MHz, almost do not differ from the absorption observed in this frequency range for MBBA, whereas a considerable quantitative difference exists with respect to cholesteryl linoleate. Such an ambiguity seems quite natural if we take into account the ratio of the nematic and cholesteric components in the investigated mixture. The results presented here allow us to make a conclusion that, when applied to cholesteric liquid crystals with a large helix pitch, the

Data obtained for the relaxation time in the CC/MBBA/EBBA mixture, in p-azoxyanizol (PAA), in heptyl oxybenzoic acid (HOBA), and in the CC/CM mixture by different methods

	CC/MBBA/EBBA			HOBA	PAA	CC/CM
$\Delta t = t - t_c$, °C	14			14	14	
f, MHz	2.1	6.3	10.5	3–50	3–60.5	12
$\tau \times 10^9$, s	2.6	1.1	1	5*	2.5* / 4.4**	50[14]
Measuring technique	By the parameters of acoustic streaming			By the ultrasonic spectroscopy		

* According to the data on the ultrasonic absorption.
** According to the data on the dispersion of the ultrasonic velocity.

method suggested in [12] for measuring the absorption coefficient α in Newtonian liquids by the configuration of acoustic streaming gives a correct qualitative frequency dependence $\alpha(f)$ and a good qualitative coincidence of the absolute values of α with the experimental data provided by conventional acoustic spectroscopy measurements for liquid crystals of close compositions.

The next step of the study is the calculation of the relaxation time τ of the mixture from the experimental values of α by using Eq. (2). It follows from the data given in the table that there is a certain difference in the values of τ obtained for the CC/MBBA/EBBA mixture at different frequencies. Apparently, this can be connected with the fulfilment of the condition $\alpha l \geq 1$, which reflects the influence of the dish wall on the streaming configuration, at different frequencies. This condition is assumed to be valid in the framework of the theoretical ideas adopted by us for the distribution of acoustic streaming velocities in a Newtonian liquid. The table also gives the values of the relaxation time τ obtained using the conventional ultrasonic spectroscopy techniques for the following liquid crystal compounds: p-azoxyanisol (PAA), heptyloxybenzoic acid (HOBA), and a mixture of cholesteryl chloride and cholesteryl myristate (CC/CM). These data are given for comparison. All values given in the table correspond to the same difference in temperatures of liquid crystals $\Delta t = t - t_c = 14$°C, where t_c is the temperature of the liquid crystal transition to the isotropic state and t is the current temperature. One can see that the relaxation times obtained in the experiments with acoustic streaming in the CC/MBBA/EBBA mixture with the cholesteric structure correlate in the order of magnitude with the values of τ for nematic liquid crystals (PAA and HOBA), which is caused by the high content of the nematic component in the mixture.

The results presented above allow us to conclude that the method of evaluating the relaxation time by the configuration of acoustic streaming provides an opportunity to estimate rather fast and accurate the order of magnitude of this quantity. The advantage of the method is its simple realization without any special complex equipment. It is also essential that there is no need to measure the absolute values of acoustic streaming velocities in the medium to obtain the necessary information. To evaluate the relaxation time, it is enough just to determine the positions of the streaming lines. Proceeding from the fact of correlation between the values of the relaxation time obtained by this technique and by the conventional methods of ultrasonic spectroscopy, it is possible to make certain conclusions not only on the potentialities of the suggested technique in application to cholesteric liquid crystals with a large helix pitch but also on the validity of the theoretical model of the medium that is based on the linear rheological equation [13] for this type of mesophase in the considered frequency range. It is also possible to consider as justified the assumptions introduced in the process of analysis, which gave rise to Eq. (6).

It is necessary to note that the accuracy of the proposed method can be considerably increased by measuring, if necessary, the distribution of the absolute values of velocity at the axis of the sound beam by the known techniques proven before [15–17].

ACKNOWLEDGMENTS

The work is supported by the Russian Foundation for Basic Research, project no. 00-02-17732.

REFERENCES

1. L. I. Mandel'shtam and M. A. Leontovich, Zh. Éksp. Teor. Fiz. **7** (3), 438 (1937).
2. *Physical Acoustics: Principles and Methods*, Ed. by W. P. Mason (Academic, New York, 1965; Mir, Moscow, 1968), Vol. 2.
3. I. G. Mikhaĭlov, V. A. Solov'ev, and Yu. P. Syrnikov, *Fundamentals of Molecular Acoustics* (Nauka, Moscow, 1964).
4. *Advances in Liquid Crystals*, Ed. by G. H. Brown (Academic, New York, 1978), Vol. 3, pp. 168–235.
5. A. P. Kapustin, *Experimental Study of Liquid Crystals* (Nauka, Moscow, 1978).
6. *Handbook of Liquid Crystal*, Ed. by D. Demus, J. Goodby, G. W. Gray, H. W. Spiess, and V. Vill (Wiley–VCH, 1998), Chap. 7, pp. 549–568.

7. D. I. Anikeev, O. A. Kapustina, and V. N. Lupanov, Zh. Éksp. Teor. Fiz. **100**, 197 (1991) [Sov. Phys. JETP **73**, 109 (1991)].
8. E. N. Kozhevnikov, Akust. Zh. **47**, 501 (2001) [Acoust. Phys. **47**, 430 (2001)].
9. P. De Gennes, *The Physics of Liquid Crystals* (Clarendon, Oxford, 1974; Mir, Moscow, 1977).
10. M. A. Osipov and E. M. Terent'ev, Preprint No. 5, IKAN (Shubnikov Inst. of Crystallography, USSR Academy of Sciences, 1988).
11. V. A. Belyakov and A. S. Sonin, *Optics of Cholesteric Liquid Crystals* (Nauka, Moscow, 1982), p. 360.
12. N. G. Semenova and Yu. G. Statnikov, Akust. Zh. **19**, 105 (1973) [Sov. Phys. Acoust. **19** (1973)].
13. A. I. Ivanovskiĭ, *Theoretical and Experimental Study of Flows Induced by Sound* (Gidrometeoizdat, Moscow, 1959).
14. K. Miyano and J. B. Ketterson, Phys. Rev. A **12** (2), 615 (1975).
15. A. M. Gabrial and E. G. Richardson, Acustica **5** (1), 28 (1955).
16. E. V. Romanenko, Akust. Zh. **6**, 92 (1960) [Sov. Phys. Acoust. **6**, 96 (1960)].
17. *Physics and Technique of High-Intensity Ultrasound*, Ed. by L. D. Rozenberg (Nauka, Moscow, 1968), Vol. 2, pp. 89–128.

Translated by M. Lyamshev

Acoustical Physics, Vol. 48, No. 4, 2002, pp. 453–457. Translated from Akusticheskiĭ Zhurnal, Vol. 48, No. 4, 2002, pp. 517–522.

Sound Scattering by Random Fractal Inhomogeneities in the Ocean

E. A. Kopyl, Yu. P. Lysanov, and L. M. Lyamshev†

Andreev Acoustics Institute, Russian Academy of Sciences, ul. Shvernika 4, Moscow, 117036 Russia

e-mail: bvp@akin.ru

Received December 14, 2001

Abstract—Sound scattering by random volume inhomogeneities (fluctuations of the refraction index in a medium) with an arbitrary anisotropy is considered using the small perturbation method (Born's approximation). Surfaces (boundaries) of the inhomogeneities are deemed to be fractal ones: the energy spectra of the refraction index fluctuations follow the power law with a nonintegral exponent. Formulas are obtained for the volume scattering coefficient. Frequency and angular dependences of the scattering coefficient and their relations to the fractal dimension of inhomogeneities with different kinds of anisotropy and different sizes (on the sound wavelength scale) are presented. The fractal dimension of the inhomogeneities is estimated. © *2002 MAIK "Nauka/Interperiodica".*

The scattering of acoustic waves by volume inhomogeneities in the ocean is of interest from many points of view. Due to the scattering, the sound field acquires an additional multipath character, space–time fluctuations of the sound field appear, and the coherence of multimode signals decreases, which lowers the efficiency of operation of various kinds of hydroacoustic systems. When propagating in the underwater sound channel, part of the waves leaks out of the channel because of the scattering, which increases the attenuation of the propagating acoustic waves. In the last few years, propagation and scattering of sound in the ocean has been considered using the concept of fractals and ray chaos [1–7].

Previous studies [3] showed that random inhomogeneities possessing fractal properties on a certain scale interval play a key role in the scattering of low-frequency sound in the ocean. The cited paper [3] considered sound scattering by random volume oceanic inhomogeneities (fluctuations of the refraction index) whose typical horizontal dimensions far exceed the vertical ones. In the framework of the first approximation of the small perturbation method used in [3], the volume scattering coefficient of sound is determined by the expression

$$m_v = 2\pi k^4 G(\mathbf{q}), \tag{1}$$

where $\mathbf{q} = \mathbf{k}_s - \mathbf{k}$ is the wave vector of the resonance harmonics in the spatial energy spectrum G of the inhomogeneities and $\mathbf{k}_s$ and $\mathbf{k}$ are the wave vectors of the scattered and incident acoustic radiation, respectively. The correlation function of the spatially homogeneous fluctuations of the refraction index can be presented in the factored form

$$B(\rho) = \langle \mu^2 \rangle N_1(\xi) N_2(\eta), \tag{2}$$

where $\langle \mu^2 \rangle$ is the mean-square fluctuation and N_1 and N_2 are the correlation coefficients in the horizontal plane and in depth. The inhomogeneities are deemed to be isotropic in the horizontal plane, so that the vector argument of the correlation function $\boldsymbol{\rho} = \{\xi, \eta\}$ has two scalar components. The horizontal correlation coefficient is expressed as [8]

$$N_1(X) = \frac{1}{2^{\nu-1}\Gamma(\nu)} X^\nu K_\nu(X). \tag{3}$$

Here, $K_\nu(X)$ is the McDonald function of order ν; $\Gamma(\nu)$ is the gamma-function; $X = \xi/\xi_0$, where ξ is the space separation of observation points; and ξ_0 is the horizontal correlation radius. The corresponding spatial energy spectrum given by the Fourier–Bessel transformation of Eq. (3) has the form

$$G_1(q_\perp) = \frac{\nu \xi_0^2}{\pi (1 + \xi_0^2 q_\perp^2)^{\nu+1}}, \tag{4}$$

where $q_\perp = |\mathbf{q}_\perp|$, $\mathbf{q}_\perp$ is the horizontal component of the vector $\mathbf{q} = \{\mathbf{q}_\perp, q_z\}$. In the vertical direction, the inhomogeneities were deemed small-scale: $\eta_0 q_z \ll 1$, where η_0 is the vertical correlation radius of fluctuations. In this case, the form of the vertical correlation coefficient is inessential, since the vertical spectral density does not depend on q_z,

$$G_2(q_z) \approx \frac{\eta_0}{\pi}, \tag{5}$$

and the total energy spectrum of the refraction index fluctuations is given by the expression

$$G(\mathbf{q}) = \langle \mu^2 \rangle G_1(q_\perp) G_2(q_z). \tag{6}$$

† Deceased.

1063-7710/02/4804-0453$22.00 © 2002 MAIK "Nauka/Interperiodica"

Now, according to Eq. (1), the volume scattering coefficient takes the form

$$m_\nu = \frac{2\nu}{\pi}\langle\mu^2\rangle\frac{\xi_0^2\eta_0 k^4}{(1+\xi_0^2 q_\perp^2)^{\nu+1}}. \quad (7)$$

When inhomogeneities are large-scale in the horizontal plane ($\xi_0 q_\perp \gg 1$), we have

$$m_\nu \approx \frac{2}{\pi}\langle\mu^2\rangle\nu k^4\xi_0^2\eta_0(\xi_0 q_\perp)^{-2(\nu+1)}. \quad (8)$$

All these results of the cited paper [3] are generalized below to the case of anisotropic volume inhomogeneities of a medium.

The first generalization consists in giving up the assumption about the isotropy of the inhomogeneities in the horizontal plane. The refraction index fluctuations are characterized by two horizontal correlation radii ξ_{ox} and ξ_{oy}. The corresponding spectral density can be represented as

$$G_1(\mathbf{q}_\perp) = \frac{\nu\xi_{ox}\xi_{oy}}{\pi(1+\xi_{ox}^2 q_x^2+\xi_{oy}^2 q_y^2)^{\nu+1}}, \quad (9)$$

where $\mathbf{q}_\perp = \{q_x, q_y\}$. Note that an energy spectrum of a similar form was used in [7] in considering horizontally anisotropic inhomogeneities of the sea bottom. The horizontal correlation coefficient corresponding to spectrum (9) is given by the Fourier transformation, whose calculation is presented in Appendix I. The correlation coefficient obtained has the same form as Eq. (3), in which, however, $X = [(\xi_x/\xi_{ox})^2 + (\xi_y/\xi_{oy})^2]^{1/2}$ and ξ_x and ξ_y are the spatial separations along the X and Y axes, respectively. If, as previously, the vertical dimensions of inhomogeneities are large compared to the sound wavelength, the spectrum of the small-scale vertical inhomogeneities of the refraction index has the form of Eq. (5) and the scattering coefficient is given by the formula

$$m_\nu = \frac{2\nu}{\pi}\langle\mu^2\rangle\frac{\xi_{ox}\xi_{oy}\eta_0 k^4}{(1+\xi_{ox}^2 q_x^2+\xi_{oy}^2 q_y^2)^{\nu+1}} \quad (10)$$

with the high-frequency asymptotics (corresponding to the case $(\xi_{oi}q_i)^2 \gg 1$, $i = x, y$) of the form

$$m_\nu \approx \frac{2\nu}{\pi}\langle\mu^2\rangle\xi_{ox}\xi_{oy}\eta_0 k^4(\xi_{ox}^2 q_x^2+\xi_{oy}^2 q_y^2)^{-(\nu+1)}. \quad (11)$$

The following generalization of the model of inhomogeneities under consideration can be obtained when the refraction index fluctuations are three-dimensionally anisotropic. Without resorting to the factorization of the three-dimensional correlation coefficient $N(\xi_x, \xi_y, \eta)$, we can again use the right-hand side of Eq. (3), where now $X = [(\xi_x/\xi_{ox})^2 + (\xi_y/\xi_{oy})^2 + (\eta/\eta_o)^2]^{1/2}$. The three-dimensional Fourier transformation of the correlation coefficient constructed in such a manner (see Appendix II) leads to the following form of the energy spectrum of fluctuations:

$$G(\mathbf{q}) = \frac{\Gamma(\nu+3/2)}{\pi^{3/2}\Gamma(\nu)}\langle\mu^2\rangle \times\frac{\xi_{ox}\xi_{oy}\eta_o}{(1+\xi_{ox}^2 q_x^2+\xi_{oy}^2 q_y^2+\eta_o^2 q_z^2)^{\nu+3/2}}. \quad (12)$$

Note that the formula for the spectrum of three-dimensional isotropic inhomogeneities ($\xi_{ox} = \xi_{oy} = \eta_o \equiv \xi_o$)

$$G(q) = \frac{\Gamma(\nu+3/2)}{\pi^{3/2}\Gamma(\nu)}\langle\mu^2\rangle\frac{\xi_o^3}{(1+\xi_o^2 q^2)^{\nu+3/2}}, \quad (13)$$

where $q^2 = q_x^2 + q_y^2 + q_z^2$, can be found in [8].

The sound-scattering coefficient for the scattering from three-dimensional anisotropic inhomogeneities with spectrum (12) is given by the expression

$$m_\nu = \frac{2\Gamma(\nu+3/2)}{\sqrt{\pi}\Gamma(\nu)}\langle\mu^2\rangle \times\frac{\xi_{ox}\xi_{oy}\eta_o k^4}{(1+\xi_{ox}^2 q_x^2+\xi_{oy}^2 q_y^2+\eta_o^2 q_z^2)^{\nu+3/2}}. \quad (14)$$

For $(\xi_{oi}q_i)^2 \gg 1$, $i = x, y$, and $(\eta_o q_z)^2 \gg 1$, we have

$$m_\nu \approx \frac{2\Gamma(\nu+3/2)}{\sqrt{\pi}\Gamma(\nu)}\langle\mu^2\rangle \times\xi_{ox}\xi_{oy}\eta_o k^4(\xi_{ox}^2 q_x^2+\xi_{oy}^2 q_y^2+\eta_o^2 q_z^2)^{-(\nu+3/2)}. \quad (15)$$

It is of interest to compare the "vertical" spectrum corresponding to Eq. (12) for the small-scale fluctuations of the refraction index in depth with Eq. (5) obtained in [3] under the assumption about the factorization of correlation function (2). The double integration of Eq. (12) leads to the following result:

$$G_z(q_z) = \int_{-\infty}^{\infty}\int_{-\infty}^{\infty}\frac{G(\mathbf{q})}{\langle\mu^2\rangle}dq_x dq_y = \frac{\Gamma(\nu+1/2)}{\sqrt{\pi}\Gamma(\nu)}\frac{\eta_0}{(1+\eta_0^2 q_z^2)^{\nu+1/2}}. \quad (16)$$

If the fluctuations are small-scale in depth ($(\eta_o q_z)^2 \ll 1$), then Eq. (16), as Eq. (5), is approximately independent of q_z, but its dependence on the parameter ν persists:

$$G_z(q_z) \approx \frac{\Gamma(\nu+1/2)}{\sqrt{\pi}\Gamma(\nu)}\eta_0. \quad (17)$$

It is easily seen that, accurate to a constant factor, Eqs. (17) and (5) coincide, and at $\nu = 1/2$, they are equal.

Consider now the frequency dependence of the volume scattering coefficient. We restrict our consideration to the cases when frequency and angular variables

are separated in the expressions for the scattering coefficient. This is true only for the inhomogeneities whose horizontal dimensions are large compared to the acoustic wavelength: $(\xi_{oi}q_i)^2 \gg 1$, $i = x, y$. If, in addition, $(\eta_o q_z)^2 \gg 1$, the short-wave asymptotics of the scattering coefficient m_ν of the three-dimensional fluctuations of the refraction index is determined from Eq. (15). In this case, it has the form

$$m_\nu \sim k^{-2\nu+1}, \tag{18}$$

where k is the sound wave number. Note that Eq. (18) is valid independently of whether the three-dimensional inhomogeneities are isotropic or anisotropic ones.

When the correlation function (and the energy spectrum) allows factorization, the frequency dependence of the scattering coefficient depends on the form of the vertical spectrum. If, as in [3], the vertical fluctuations of the refraction index are small-scale ones $((\eta_o q_z)^2 \ll 1)$, the frequency dependence of the scattering coefficient is determined only by the horizontal spectrum (the inhomogeneities are "two-dimensional"), and we have

$$m_\nu \sim k^{-2\nu+2} \tag{19}$$

independently of whether inhomogeneities are anisotropic or isotropic in the horizontal plane.

Now we consider the angular dependence of the scattering coefficient when the frequency and angular variables are separated in the expression for the scattering coefficient m_ν. The first of such cases was analyzed in [3]. It refers to the refraction index fluctuations that are large-scale and isotropic in the horizontal plane but small-scale along the vertical. In this situation, the frequency dependence, as was noted above, has the form of Eq. (19), and the angular dependence, according to Eq. (8), is given by the expression

$$m_\nu \sim (q_\perp/k)^{-2(\nu+1)}, \tag{20}$$

where $q_\perp = k[\cos^2\chi + \cos^2\chi_s - 2\cos\chi\cos\chi_s\cos(\varphi_s - \varphi)]^{1/2}$.

Here, the grazing angles χ, χ_s and the azimuth angles φ, φ_s characterize the directions of the incidence and scattering of acoustic waves, respectively. In the plane of incidence ($\varphi_s = \varphi$), angular dependence (20) of the scattering coefficient has two maxima corresponding to the condition $q_\perp = 0$. The first maximum is in the direction of the acoustic wave incidence ($\chi_s = \chi$), and the second maximum is in the direction of the specular reflection with respect to the horizontal plane ($\chi_s = -\chi$) (a similar conclusion was obtained in [9] in analyzing the sound scattering by fine-structure oceanic inhomogeneities). The effective halfwidth of these maxima, which is determined by the decrease in the scattering coefficient by a factor two, is equal to $\Delta\chi = \chi\varepsilon^{1/2}/(k\xi_o\sin\chi)$ for $k\xi_o\sin\chi \gg 1$ and $\Delta\chi = (4\varepsilon)^{1/2}(k\xi_o)^{-1/2}$ for $\chi = 0$. Here, $\xi_o = \xi_{ox} = \xi_{oy}$ (isotropic inhomogeneities in the horizontal plane) and $\varepsilon = 2^{1/(\nu+1)}$.

This case is of special interest for the following reason. If the frequency and angular variables are separated in the expression for the scattering coefficient, then the frequency dependence of the attenuation coefficient β in the underwater sound channel due to the sound scattering by the "horizontal" (i.e., strongly elongated in the horizontal plane) inhomogeneities and the frequency dependence of the scattering coefficient are identical [3].

Consider the relation between the frequency dependence of the scattering coefficient by inhomogeneities and their fractal dimension in more detail. The volume inhomogeneities can naturally be considered as surface fractals. For volume inhomogeneities with a fractal surface (i.e., with statistically rough surfaces characterized by the power law $G(q) \sim q^{-\gamma}$ with a nonintegral exponent γ), the following relationship between the parameter γ and the fractal dimension D is valid [1]:

$$\gamma = 2d - D, \tag{21}$$

where d is the dimension of the embedding space. For "two-dimensional" ("horizontal") volume inhomogeneities, $d = 2$, and for three-dimensional inhomogeneities, $d = 3$ and, therefore, the fractal dimension of the boundary and surface is $1 < D < 2$ and $2 < D < 3$, respectively, [1].

For two-dimensional inhomogeneities, we assume $D = 1.4$–1.5. Such a choice is not random. From the theory of the fractal dimension of cloud boundaries in the atmosphere, it follows that $1.37 < D < 1.41$, while observations yield the value $D \approx 1.35$ [10]. On the basis of Eqs. (4), (8), (9), (11), (12), (19), and (21), we obtain for large-scale horizontal inhomogeneities the following values: $\nu = 0.3$–0.25 and $m_\nu \sim k^{1.4-1.5}$. Since, in this case, the angular and frequency variables are separated in the expression for the scattering coefficient, the sound attenuation coefficient due to the scattering in the underwater sound channel has the same frequency dependence. Thus, we arrive at the well-known 3/2-power law. It can be seen that this law does not depend on the anisotropy of fractal two-dimensional inhomogeneities. It is only important that their dimensions are large compared with the sound wavelength.

For three-dimensional large-scale inhomogeneities, we can assume $D = 2.4$–2.8. As was noted above, observations in the atmosphere show that cloud boundaries have the fractal dimension $D \approx 1.35$. One can expect that the fractal dimension of the two-dimensional surface of clouds will be $D \approx 2.7$. Therefore, under the assumption that the fractal dimension of the surface of three-dimensional volume fluctuations of the refraction index in the ocean is in the interval $2.4 < D < 2.8$, we obtain for the frequency dependence of the scattering coefficient: $m_\nu \sim k^{0.6-0.7}$.

Now we assume that three-dimensional inhomogeneities have a "smooth" surface. This corresponds to the fractal dimension $D = 2$. From Eqs. (21) and (12), we obtain $\nu = 0.5$, and from Eq. (18), we have $m_\nu \sim k^0$. In other words, the sound scattering coefficient for the scattering by volume fluctuations of the refraction

index does not depend on frequency. This result was, apparently, first obtained in [11] and discussed in detail in [8]. For $\nu = 0.5$, energy spectrum (13), to within a constant factor, coincides with the spectrum corresponding to the correlation function $\exp[-|\xi|/\xi_o]$ used in [11]. The absence of the frequency dependence of the scattering coefficient was also revealed for the sound scattering by random volume inhomogeneities of the bottom of a shallow sea [12].

If we set $\nu = 0.3$, the spectrum of three-dimensional isotropic volume inhomogeneities given by Eq. (13) coincides with the spectrum of local isotropic turbulence, and for the scattering coefficient, as expected, we obtain $m_\nu \sim k^{0.4}$ [8].

Finally, from the formulas presented above, it follows that, in the low-frequency approximation, the Rayleigh scattering occurs and long acoustic waves "overlook" the roughness of the fractal surface of inhomogeneities.

In conclusion, we note that some problems of the scattering and radiation of waves by fractal inhomogeneities in an elastic medium were discussed in [13].

The above-mentioned formulas for the scattering coefficients characterizing the scattering by volume inhomogeneities of various types can, apparently, be useful for the interpretation of experimental data on sound propagation and scattering in the ocean. On the basis of comparison of the computational results and experimental data, it would be possible to determine which of the oceanic inhomogeneities have the greatest effect on the acoustic field in one or another situation and to make some conclusions about the nature of these inhomogeneities.

APPENDIX I

To calculate the correlation coefficient of horizontally anisotropic inhomogeneities that corresponds to spectral form (9), one has to perform a Fourier transformation, i.e., to calculate the double integral

$$N_1(\xi_x, \xi_y) = \int_{-\infty}^{\infty}\int_{-\infty}^{\infty} G_1(q_x, q_y) e^{-i(\xi_x q_x + \xi_y q_y)} dq_x dq_y$$
$$= \frac{\nu \xi_{ox} \xi_{oy}}{\pi} \int_{-\infty}^{\infty}\int_{-\infty}^{\infty} \frac{e^{-i(\xi_x q_x + \xi_y q_y)}}{[1 + \xi_{ox}^2 q_x^2 + \xi_{oy}^2 q_y^2]^{\nu+1}} dq_x dq_y. \quad \text{(I.1)}$$

Note that the factor $(2\pi)^{-1}$, as in [3], refers to a transformation that is the inverse of Eq. (I.1) and determines the energy spectrum from the correlation function.

By applying the change of variables $x = \xi_{ox} q_x$ and $y = \xi_{oy} q_y$, Eq. (I.1) is reduced to the form

$$N_1(a_x, a_y) = \frac{\nu}{\pi} \int_{-\infty}^{\infty}\int_{-\infty}^{\infty} \frac{e^{-i(a_x x + a_y y)}}{[1 + x^2 + y^2]^{\nu+1}} dx dy, \quad \text{(I.2)}$$

where $a_x \equiv \xi_x/\xi_{ox}$ and $a_y \equiv \xi_y/\xi_{oy}$. Changing the variables (x, y) in (I.2) to the polar variables (r, ψ), we obtain

$$N_1(a_x, a_y) = \frac{\nu}{\pi} \int_0^\infty \int_{-\pi}^{\pi} \frac{e^{-ir(a_x \cos\psi + a_y \sin\psi)}}{[1 + r^2]^{\nu+1}} r dr d\psi. \quad \text{(I.3)}$$

For integrating with respect to the polar angle ψ, we use the change of variables $a_x \cos\psi + a_y \sin\psi = b\cos(\psi + \delta)$, where $b = (a_x^2 + a_y^2)^{1/2}$ and $\tan\delta = a_y/a_x$. Then, with allowance for the known expression for the Bessel function $J_0(Z)$ of zero order, we can write

$$\int_{-\pi}^{\pi} e^{-ibr\cos(\psi+\delta)} d\psi = 2\int_0^{\pi} e^{-ibr\cos\psi} d\psi = 2\pi J_0(br),$$

and the calculation of the correlation coefficient is reduced to taking the ordinary integral

$$N_1(b) = 2\nu \int_0^\infty \frac{J_0(br) r dr}{(1 + r^2)^{\nu+1}}. \quad \text{(I.4)}$$

The integral in Eq. (I.4) is a particular case of the table integral (see [14], formula 6.565.4) that leads to the McDonald function $K_{-\nu}(Z)$. Taking into account the properties of the function $K_{-\nu}(Z) = K_\nu(Z)$ [14], we obtain the required correlation coefficient for the fluctuations of the refraction index in the form of Eq. (3) at $X = b \equiv [(\xi_x/\xi_{ox})^2 + (\xi_y/\xi_{oy})^2]^{1/2}$.

APPENDIX II

To determine the spectral density of the three-dimensional anisotropic inhomogeneities that are characterized by the correlation coefficient $N(\xi_x, \xi_y, \eta)$ in the form of Eq. (3) at $X = [(\xi_x/\xi_{ox})^2 + (\xi_y/\xi_{oy})^2 + (\eta/\eta_o)^2]^{1/2}$, one has to perform a three-dimensional Fourier transformation:

$$G(q_x, q_y, q_z)$$
$$= \frac{1}{(2\pi)^3} \int_{-\infty}^{\infty}\int_{-\infty}^{\infty}\int_{-\infty}^{\infty} N(\xi_x, \xi_y, \eta) e^{i(q_x \xi_x + q_y \xi_y + q_z \eta)} d\xi_x d\xi_y d\eta. \quad \text{(II.1)}$$

Introducing the notations $x = \xi_x/\xi_{ox}$, $y = \xi_y/\xi_{oy}$, and $z = \eta/\eta_o$ in the integrand, we reduce Eq. (II.1) to the form

$$G(q_x, q_y, q_z) = \frac{\xi_{ox}\xi_{oy}\eta_0}{2^{\nu-1}\Gamma(\nu)(2\pi)^3}$$
$$\times \int_{-\infty}^{\infty}\int_{-\infty}^{\infty}\int_{-\infty}^{\infty} (x^2 + y^2 + z^2)^{\nu/2} K_\nu(\sqrt{x^2 + y^2 + z^2}) \quad \text{(II.2)}$$
$$\times e^{i(q_x \xi_x x + q_y \xi_y y + q_z \eta z)} dx dy dz.$$

Changing from the variables (x, y, z) to the spherical coordinates (r, θ, ψ) so that $x = r\sin\theta\cos\psi$, $y = r\sin\theta\cos\psi$, $z = r\cos\theta$, and $dxdydz = r^2\sin\theta dr d\theta d\psi$, we obtain

$$G(q_x, q_y, q_z) = \frac{\xi_{ox}\xi_{oy}\eta_0}{2^{\nu-1}\Gamma(\nu)(2\pi)^3}\int_0^\infty\int_{-\pi}^{\pi}\int_0^{\pi} r^{\nu+2}K_\nu(r) \times e^{ir(q_x\xi_{ox}\sin\theta\cos\psi + q_y\xi_{oy}\sin\theta\sin\psi + q_z\eta_o\cos\theta)}\sin\theta dr d\psi d\theta. \quad \text{(II.3)}$$

Taking the integral with respect to ψ, we obtain the Bessel function of zero order (see Appendix I):

$$\int_{-\pi}^{\pi} e^{ir\sin\theta(q_x\xi_{ox}\cos\psi + q_y\xi_{oy}\sin\psi)}d\psi = 2\pi J_0(ar\sin\theta), \quad \text{(II.4)}$$

where

$$a \equiv \sqrt{(\xi_{ox}q_x)^2 + (\xi_{oy}q_y)^2}.$$

In the remaining expression

$$G(q_x, q_y, q_z) = \frac{\xi_{ox}\xi_{oy}\eta_0}{2^{\nu-1}\Gamma(\nu)(2\pi)^2} \times \int_0^\infty\int_0^{\pi} r^{\nu+2}K_\nu(r)J_0(ar\sin\theta)e^{irq_z\eta_o\cos\theta}\sin\theta dr d\theta, \quad \text{(II.5)}$$

the integral with respect to θ

$$I_\theta \equiv \int_0^{\pi} J_0(ar\sin\theta)e^{irq_z\eta_o\cos\theta}\sin\theta d\theta \quad \text{(II.6)}$$

with the use of the substitution $t = \cos\theta$ is reduced to the table integral ([14], formula 6.677.6)

$$I_\theta \equiv \int_{-1}^{1} J_0(ar\sqrt{1-t^2})e^{irq_z\eta_0 t}dt = 2\int_0^1 J_0(ar\sqrt{1-t^2})\cos(rq_z\eta_o t)dt = 2\frac{\sin(br)}{br}, \quad \text{(II.7)}$$

where

$$b \equiv \sqrt{(\xi_{ox}q_x)^2 + (\xi_{oy}q_y)^2 + (\eta_o q_z)^2}.$$

Now, the spectrum of three-dimensional anisotropic inhomogeneities is given by the ordinary integral

$$G(q_x, q_y, q_z) = \frac{\xi_{ox}\xi_{oy}\eta_0}{2^{\nu-2}b\Gamma(\nu)(2\pi)^2}\int_0^\infty r^{\nu+1}K_\nu(r)\sin(br)dr, \quad \text{(II.8)}$$

which is also a tabular one ([14], formula 6.699.3) and is expressed through a hypergeometric function F. The latter, at a given combination of its four arguments, is reduced to an elementary function ([14], formula 9.121.1):

$$F(\nu + 3/2; 3/2; 3/2; -b^2) = (1 + b^2)^{-(\nu+3/2)}, \quad \text{(II.9)}$$

which eventually leads to the required form of Eq. (12) for the energy spectrum of three-dimensional anisotropic fluctuations of the refraction index.

ACKNOWLEDGMENTS

This work was supported by the Russian Foundation for Basic Research, project no. 01-05-64711.

REFERENCES

1. B. B. Mandelbrot, *The Fractal Geometry of Nature* (Freeman, New York, 1983), p. 468.
2. L. M. Lyamshev, in *Proceedings of International Symposium on Hydroacoustics and Ultrasonics* (1997), p. 251.
3. Yu. P. Lysanov and L. L. Lyamshev, Dokl. Akad. Nauk **366**, 36 (1999) [Dokl. Phys. **44**, 264 (1999)].
4. L. M. Lyamshev, in *Proceedings of 7th International Congress on Acoustics and Vibration* (2000), Vol. 3, p. 1503.
5. L. M. Lyamshev, Dokl. Akad. Nauk **378**, 610 (2001) [Dokl. Phys. **46**, 393 (2001)].
6. L. M. Lyamshev and A. Stepnovski, Hydroacoustics **4**, 143 (2001).
7. D. Li, G. V. Frisk, and D. Tang, J. Acoust. Soc. Am. **109**, 1384 (2001).
8. V. I. Tatarskiĭ, *Wave Propagation in a Turbulent Atmosphere* (Nauka, Moscow, 1967).
9. V. S. Gostev and R. F. Shvachko, Akust. Zh. **47**, 623 (2001) [Acoust. Phys. **47**, 540 (2001)].
10. J. Feder, *Fractals* (Plenum, New York, 1988; Mir, Moscow, 1991).
11. H. Booker and W. Gordon, Proc. IRE **38** (4), 401 (1950).
12. Yu. P. Lysanov, Dokl. Akad. Nauk SSSR **251**, 714 (1980).
13. S. A. Shapiro, Geophys. J. Int. **119**, 591 (1992).
14. I. S. Gradshteĭn and I. M. Ryzhik, *Table of Integrals, Series, and Products* (Fizmatgiz, Moscow, 1962; Academic, New York, 1980).

Translated by Yu. Lysanov

Acoustical Physics, Vol. 48, No. 4, 2002, pp. 458–466. Translated from Akusticheskiĭ Zhurnal, Vol. 48, No. 4, 2002, pp. 523–532.

Optimization of the Parameters of Sound-Absorbing Materials Made on the Basis of Rubberlike Media with Heavy Inclusions

S. V. Krynkin and V. V. Tyutekin

Andreev Acoustics Institute, Russian Academy of Sciences, ul. Shvernika 4, Moscow, 117036 Russia

e-mail: Tyutekin@akin.ru

Received June 20, 2001

Abstract—A computer simulation of an acoustic medium characterized by a complex density and synthesized on the basis of a rubberlike material with massive spherical inclusions is performed. The properties of such media are studied for continuous and discrete distributions of the inclusions in size (the resonance frequencies), and the parameters of the medium are optimized to obtain the given properties, in particular, to provide efficient sound absorption over a wide frequency range. Numerical results are presented. © *2002 MAIK "Nauka/Interperiodica".*

The problem of designing composite materials is of interest from the viewpoint of both theory [1–9] and applications [10, 11]. One of the types of such materials are the so-called cavityless materials [1, 5–7, 12, 13] in the form of a rubberlike medium containing massive inclusions of various shapes and dimensions. For analyzing harmonic oscillations and sound absorption in these media, it is convenient to use the notion of complex density [14].

A list of both basic physical assumptions concerning such media and theoretical results obtained from them can be found in [15]. The same publication provides the experimental acoustic parameters of these media and demonstrates their good agreement with the theoretical values; it also presents tentative results on sound-absorbing materials designed on their basis, the performance of such absorbers being almost independent of hydrostatic pressure.

In this paper, we describe the computer simulation of the synthesis of sound-absorbing materials on the basis of a rubberlike medium with spherical inclusions. The effective complex density of such a medium can be written as [1, 5]

$$\frac{\bar{\rho}}{\rho_1} = \rho' + i\rho'' = 1 + \frac{\varepsilon(\rho_2/\rho_1 - 1)}{1 - (ka)^2/(ka)_p^2 + i[(ka/(ka)_p)^2\eta' + ka]}. \quad (1)$$

Here, ρ_1 and ρ_2 are the densities of rubber and inclusions, respectively; a is the radius of an inclusion; $\varepsilon = Nv/V$ is the volume concentration factor (N is the number of inclusions, v is the volume of the inclusion, and V is the total volume); $(ka)_p = \Psi(ka)_0$; $\eta' = \Psi\eta$, where η is the shear loss factor and $\Psi = 1 + \frac{\eta}{2}(ka)_0$; and $(ka)_0 = \sqrt{\frac{9\rho_1}{2\rho_2 + \rho_1}}$ is the dimensionless resonance frequency without regard to the shear loss. As follows from these expressions, $(ka)_p$ is primarily determined by the inclusion-to-rubber density ratio ρ_2/ρ_1. The greater this ratio, the smaller $(ka)_p$ is. Other physical properties described by Eq. (1) are detailed in [15].

We will further describe the medium under study in terms of two parameters: the real part of the dimensionless density, $\rho_0 = \mathrm{Re}(\bar{\rho}/\rho_1)$, and the loss factor divided by $\theta = \mathrm{Im}(\bar{\rho}/\rho_1)/\mathrm{Re}(\bar{\rho}/\rho_1)$.

Note that, to achieve the maximal effect, lead inclusions ($\rho_2 = 11000$ kg/m^3) were used in [15]. In this paper, to synthesize a lighter material, we use inclusions with $\rho_1 = 5500$ kg/m^3, e.g., pebbles. The density of the host medium (rubber) is $\rho_1 = 1130$ kg/m^3.

Figure 1 shows ρ_0 and θ as functions of the dimensionless frequency ka calculated for spherical inclusions of this material with the volume concentration from 0.05 to 0.2 (0.2 is the maximal admissible concentration for these media) taken as a parameter and with the shear loss factor of rubber equal to 0.3.

As can be seen from the figure, at small ka, ρ_0 tends to the constant static value

$$\rho_0 = 1 + \varepsilon(\rho_2/\rho_1 - 1). \quad (2)$$

With increasing ka, ρ_0 rapidly decreases below unity, because the type of the response changes from inertial to elastic, the effective loss θ exhibiting a typically resonance behavior. At the resonance frequency, $\rho_0 = 1$ and θ is close to its maximal value. It can also be noted

1063-7710/02/4804-0458$22.00

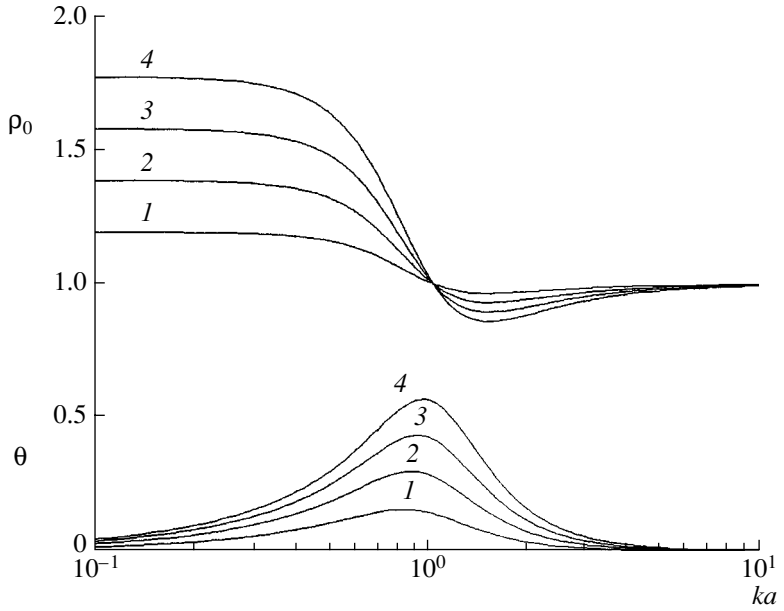

Fig. 1. Real part ρ_0 of the dimensionless complex density of the composite material and loss factor θ as functions of the dimensionless frequency for different concentrations of spherical inclusions with a density of $\rho_2 = 5500$ kg/m^3: $\varepsilon_0 =$ (*1*) 0.05, (*2*) 0.10, (*3*) 0.15, and (*4*) 0.20 kg/m^3.

that ρ_0 and θ rather weakly depend on the shear loss factor η.

Figure 1 reveals that the medium exhibits absorbing properties in a relatively narrow frequency range (about 0.5–0.6 wide). Therefore, to provide the sound absorption over a wide frequency range (e.g., about a decade band or wider), it is necessary to use a variety of inclusions with different resonance frequencies. The values of these frequencies and the corresponding concentrations must be chosen or determined from certain additional assumptions.

To make original expression (1) more convenient for further analysis of the medium under investigation and for the synthesis of sound-absorbing materials, we represent it in a different form. Since we have

$$ka = \omega a/c, \quad (ka)_p = \omega_0 a/c = \chi,$$

where ω is the circular frequency of sound, ω_0 is the circular resonance frequency of the inclusion, c is the velocity of shear waves in rubber, and χ is a constant, expression (1) can be written as

$$\frac{\bar{\rho}}{\rho_1} = \rho_0(1 + i\theta) = 1 + \left(\frac{\rho_2}{\rho_1} - 1\right)R(\omega, \omega_0), \qquad (3)$$

where

$$R(\omega, \omega_0) = \frac{\varepsilon\omega_0^2}{\omega_0^2 - \omega^2(1 - i\eta') + i\chi\omega\omega_0}. \qquad (4)$$

Consider new dimensionless variables

$$\Omega = \frac{\omega}{\omega_{01}}, \quad \Omega_0 = \frac{\omega_0}{\omega_{01}},$$

where $\omega_{01} = \chi c/a_1$ is the lowest resonance frequency indicated by number 1 and a_1 is the radius of the corresponding inclusion.

With these notations, Eq. (4) can be rewritten as

$$R(\Omega, \Omega_0) = \frac{\varepsilon\Omega_0^2}{\Omega_0^2 - (1 - i\eta')\Omega^2 + i\chi\Omega\Omega_0}. \qquad (5)$$

Formulas (3) and (5) can be used to calculate the complex density of the medium with inclusions and, in particular, for the synthesis of such a medium with the prescribed properties. In the following, we consider several such problems, which will help us to achieve our goal, i.e., to develop a sound-absorbing material for hydroacoustic purposes.

As can be seen from Eqs. (3) and (5), the complex density strongly depends on the concentration ε of the inclusions with the resonance frequency Ω_0, so that we can write $\varepsilon = \varepsilon(\Omega_0)$.

At first, we consider (as in [6]) the case of a continuous spectrum of resonance frequencies and, therefore, a continuous spectrum of inclusion sizes. Assume that inclusions of each radius are uniformly distributed over each part of the space with linear dimensions smaller than the acoustic wavelength. Let the continuous function $\varepsilon(\Omega_0)$ be given on the interval $1 \le \Omega_0 \le \Delta$, where unity corresponds to the lowest resonance frequency

and $\Delta = \frac{\omega_{0N}}{\omega_{01}}$ with ω_{0N} being the highest resonance frequency.

In this case, Eqs. (3) and (5) can be written as

$$\frac{\bar{\rho}}{\rho_1} = \rho_0(1 + i\theta) = 1 + \left(\frac{\rho_2}{\rho_1} - 1\right)R(\Omega), \quad (6)$$

where

$$R(\Omega) = \int_1^\Delta \frac{\varepsilon(\Omega_0)\Omega_0^2 d\Omega_0}{\Omega_0^2 - (1 - i\eta')\Omega^2 + i\chi\Omega\Omega_0}. \quad (7)$$

Let us write the denominator in Eq. (5) as

$$\Delta(\Omega_0, \Omega) = \Omega_0^2 - (a_1 + a_2)\Omega\Omega_0 + a_1 a_2 \Omega^2, \quad (8)$$

where a_1 and a_2 are the roots of the equation $\Delta(\Omega_0, 1) = 0$:

$$a_{1,2} = \frac{i\chi}{2} \pm \sqrt{1 - \frac{\chi^2}{4} + i\eta'}.$$

It is significant that any continuous function $\varepsilon(\Omega_0)$ must satisfy the condition

$$\int_1^\Delta \varepsilon(\Omega_0) d\Omega_0 \le \varepsilon_0, \quad (9)$$

where ε_0 is the maximal total concentration, assumed to be equal to 0.2.

Below, we consider several examples with simple functions $\varepsilon(\Omega_0)$, which allow one to obtain analytical solutions for the complex density of the medium.

(1) $\varepsilon(\Omega_0) = \frac{\varepsilon_1}{\Omega_0^2}$.

By virtue of Eq. (9), the normalization factor ε_1 can be expressed here as $\varepsilon_1 = \frac{\varepsilon_0\Delta}{\Delta - 1}$. With allowance for Eq. (8), the integration in Eq. (7) yields

$$R(\Omega) = \frac{\varepsilon_0\Delta}{\Delta - 1}(\Omega)^{-1}[F_2(\Omega) - F_1(\Omega)]. \quad (10)$$

Here, $F_i = (a_2 - a_1)^{-1} \ln\frac{\Delta - a_i\Omega}{1 - a_i\Omega}$, $i = 1, 2$.

(2) $\varepsilon(\Omega_0) = \frac{\varepsilon_1}{\Omega_0}$.

In this case, we have

$$\varepsilon_1 = \frac{\varepsilon_0}{\ln\Delta} \text{ and } R(\Omega) = \frac{\varepsilon_0}{\ln\Delta}[a_2 F_2(\Omega) - a_1 F_1(\Omega)]. \quad (11)$$

(3) $\varepsilon(\Omega_0) = \text{const} = \varepsilon_1$.

In this case, we obtain

$$\varepsilon_1 = \frac{\varepsilon_0}{\Delta - 1} \text{ and } R(\Omega) = \frac{\varepsilon_0}{\Delta - 1}\{\Delta - 1 + \Omega[a_2^2 F_2(\Omega) - a_1^2 F_1(\Omega)]\}. \quad (12)$$

Formulas (10)–(12) thus determine the complex density of a medium with a continuous spectrum of resonance frequencies (or inclusion dimensions) distributed by the above laws. The complex density of such a medium calculated by these formulas was found to differ little from the complex density of a medium with inclusions of one size. The above concentration distribution laws differ primarily in the upward shift that they introduce in the resonance frequency (reducing the dependence of the concentration on the resonance frequency).

Although the continuous spectrum of inclusion dimensions gives a general idea of the frequency dependence of the complex density, such a medium can only be implemented with inclusions of particular dimensions, i.e., on the basis of a discrete spectrum of the latter. In this case, the formula for the complex density can be obtained from Eqs. (6) and (7) by specifying ε as

$$\varepsilon = \varepsilon(\Omega_0)\delta(\Omega_0 - \Omega_{0n}). \quad (13)$$

By substituting Eq. (13) into Eq. (7), we obtain

$$R(\Omega) = \sum_{n=1}^{N} \frac{\varepsilon(\Omega_{0n})\Omega_{0n}^2}{\Omega_{0n}^2 - (1 - i\eta')\Omega^2 + i\chi\Omega\Omega_{0n}}. \quad (14)$$

This formula can be written in a slightly different form as

$$R(\Omega) = \sum_{n=1}^{N} \frac{\varepsilon(\Omega_{0n})}{1 - (1 - i\eta')(\Omega/\Omega_{0n})^2 + i\chi(\Omega/\Omega_{0n})}. \quad (15)$$

This expression contains two systems of parameters: Ω_{0n} and $\varepsilon(\Omega_{0n})$. The values of Ω_{0n} can be specified as a geometrical progression with a geometric ratio a, which corresponds to a uniform distribution on a logarithmic scale. In this case, we have

$$\Omega_{0n} = a\Omega_{0(n-1)}; \quad \Omega_{0n} = a^{(n-1)}; \quad \Delta = a^{(N-1)}.$$

We assume that $\Omega_{01} = 1$. The geometric ratio a can be defined as

$$a = \Delta^{-(N-1)}. \quad (16)$$

At $\Delta = 10$ and $N = 4$, we obtain $a = 2.16$. The utility of this choice will become clear from the following discussion.

It is evident that $\varepsilon(\Omega_{0n})$ must satisfy the relationship

$$\sum_{n=1}^{N} \varepsilon(\Omega_{0n}) \le \varepsilon_0. \quad (17)$$

For distributions $\varepsilon(\Omega_{0n})$ considered above, we obtain

(1) $\varepsilon(\Omega_{0n}) = \dfrac{\varepsilon_1}{\Omega_{0n}^2}$.

Since $\varepsilon_1 \sum_{n=1}^{N} \dfrac{1}{a^{2(n-1)}} = \varepsilon_0$, the formula for a sum of a geometrical progression yields

$$\varepsilon_1 = \varepsilon_0 \frac{(a^2-1)a^{2(N-1)}}{a^{2N}-1}.$$

(2) $\varepsilon(\Omega_{0n}) = \dfrac{\varepsilon_1}{\Omega_{0n}}$.

Likewise, we obtain $\varepsilon_1 = \varepsilon_0 \dfrac{(a-1)a^{N-1}}{a^N-1}$.

(3) $\varepsilon(\Omega_{0n}) = \text{const} = \varepsilon_0$, $\varepsilon_n = \dfrac{\varepsilon_0}{N}$.

Figure 2 illustrates the real part of the complex density and the loss factor of the medium calculated at $N = 4$, $\Delta = 10$, and $a = 2.16$ for discrete-spectrum inclusions.

Figure 2a shows three families of functions with the rubber loss factor as a parameter. Note that, in case 3, the real part of the complex density drops linearly (on a logarithmic scale) with increasing frequency from 1 to 10 and is almost independent of the rubber loss factor. In this case, the loss factor θ (Fig. 2b) is nonmonotonic and also weakly depends on the rubber loss factor. Unlike case 3, in the other two cases, the lower resonance frequencies are to some extent enhanced.

The medium with massive inclusions can be synthesized not only by specifying the concentration as a function of frequency, as we have done above, but also by choosing a special discrete function, so as to provide the required property of the medium. As an example, consider the synthesis of a medium with a constant loss factor $\theta = \theta_0$ in a given frequency range. Let us write the complex density using Eq. (3) with the function R given in the form

$$R(\Omega) = \sum_{n=1}^{N} \frac{\varepsilon_n}{1-(1-i\eta')a^{-2(n-1)}\Omega^2 + i\chi a^{-(n-1)}\Omega}. \quad (18)$$

The problem can be solved in terms of the criterion

$$\frac{1}{K}\sum_{k=1}^{K} |\theta(\Omega_k) - \theta_0| = \min,$$

where Ω_k are the frequencies at which the condition is imposed and $K = 100$ is the number of the frequencies. This criterion minimizes the mean deviation of θ from the required value θ_0 within the given frequency range. The solution algorithm numerically optimizes (by one of the usual methods [17]) the variable parameters ε_n. In this example, $n = 1, 2, 3$, and 4. The feasibility conditions are as follows:

$$\varepsilon_n \geq 0; \quad \varepsilon = \sum_{n=1}^{N} \varepsilon_n \leq \varepsilon_0. \quad (19)$$

Table 1. $\eta = 0.1$, $\Delta = 11$

θ_0	ε_1	ε_2	ε_3	ε_4	ε	δ
0.10	0.0186	0.0152	0.0143	0.0225	0.0706	0.0021
0.15	0.0309	0.0248	0.0223	0.0337	0.1117	0.0031
0.20	0.0457	0.0352	0.0321	0.0449	0.1570	0.0039

The solutions are summarized in Tables 1–3.

The calculations were performed for $\Delta = 11$ and 16; the rubber loss factor $\eta = 0.1$, 0.3, and 0.5; and the feasible loss factor of the medium $\theta_0 = 0.1$, 0.15, and 0.2. In addition to the above quantities, the tables show the total concentration ε and the mean-square deviation δ.

The main conclusion that can be drawn from the data presented in the tables is that, with increasing θ_0, the total concentration ε increases, remaining smaller than its maximal admissible value of $\varepsilon_0 = 0.2$, and that the mean-square deviation δ from the required value θ_0 is less than 0.4% in all cases considered.

Figure 3 illustrates the complex density calculated for $\eta = 0.3$. Figure 4 plots the loss factor on an enlarged scale. The figures clearly show the behavior of θ in the given frequency range. It can be seen that oscillations in the curves become smaller with increasing η, as is also seen from the tables. In essence, we have thus optimized the characteristics shown above in Fig. 2b (case *3*). The method described above can be applied to synthesize media subject to other conditions imposed upon the complex density, but the solution must also satisfy conditions (19).

The most interesting application of the composite materials considered in this paper is their use as sound-absorbing materials for hydroacoustic purposes. Hydroacoustic absorbers should provide a sufficiently high sound absorption and a weak reflection from the absorber–water interface; i.e., their wave impedance should be close to that of water. Such a sound absorber can be synthesized in terms of the criterion of minimal reflectivity over the given frequency range, which allows for both aforementioned requirements.

We will solve the synthesis problem for two cases. In the first case, we assume that the sound absorber is a homogeneous (to be more precise, quasi-homogeneous) layer containing inclusions of various dimensions. In the second case, the sound absorber will have the form of an inhomogeneous layer consisting of a number of sufficiently thin homogeneous layers, each of which contains inclusions of a particular dimension.

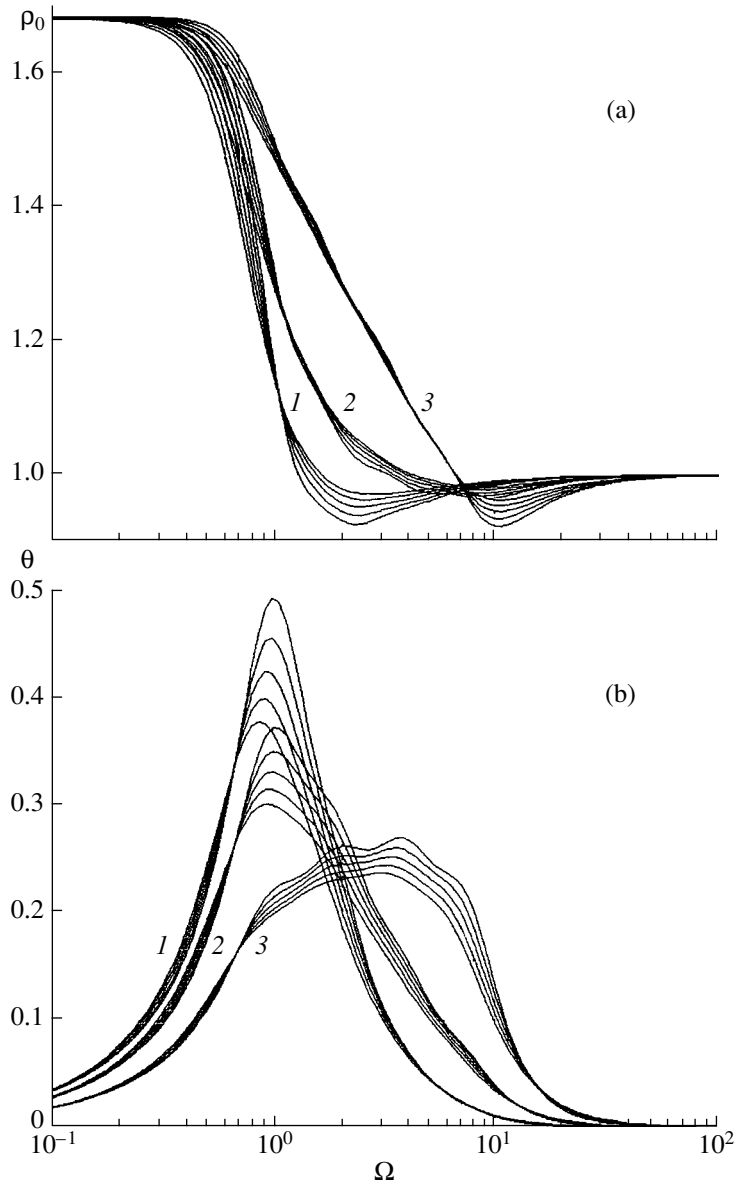

Fig. 2. (a) Real part of the complex density and (b) loss factor of the medium for different functions $\varepsilon(\Omega_{0n})$: (*1*) $(\Omega_{0n}) \sim (\Omega_{0n})^{-2}$, (*2*) $\varepsilon(\Omega_{0n}) \sim (\Omega_{0n})^{-1}$, and (*3*) $\varepsilon(\Omega_{0n}) = \text{const}$.

It is known that the reflection coefficient can be written as

$$V = \frac{Z-1}{Z+1}, \tag{20}$$

where Z is the specific input impedance of the absorber normalized by $(\rho_0 c_0)$ for water. For the absorber in the form of a homogeneous layer, its complex density $\bar{\rho}$ is determined by Eqs. (6) and (18) and its impedance Z is

$$Z = -i\sqrt{\bar{m}}\tan(2\pi L_0\sqrt{\bar{m}}\Omega) \tag{21}$$

for a layer with a zero back loading ($Z_L = 0$) or

$$Z = i\sqrt{\bar{m}}\cot(2\pi L_0\sqrt{\bar{m}}\Omega), \tag{22}$$

Table 2. $\eta = 0.3$, $\Delta = 11$

θ_0	ε_1	ε_2	ε_3	ε_4	ε	δ
0.10	0.0242	0.0190	0.0173	0.0264	0.0869	0.0015
0.15	0.0413	0.0309	0.0277	0.0398	0.1397	0.0023
0.20	0.0627	0.0444	0.0394	0.0533	0.1998	0.0031

Table 3. $\eta = 0.5$, $\Delta = 16$

θ_0	ε_1	ε_2	ε_3	ε_4	ε	δ
0.10	0.267	0.0198	0.0177	0.0283	0.0925	0.00095
0.15	0.0459	0.0325	0.0286	0.0427	0.1497	0.0014
0.20	0.0693	0.0482	0.0397	0.0578	0.2090	0.0020

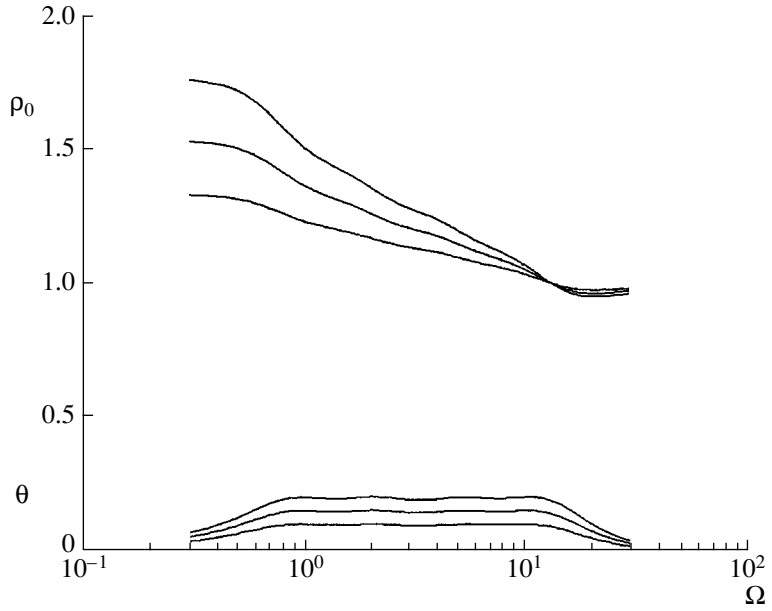

Fig. 3. Complex density of the synthesized material; the loss factor in rubber is equal to 0.3.

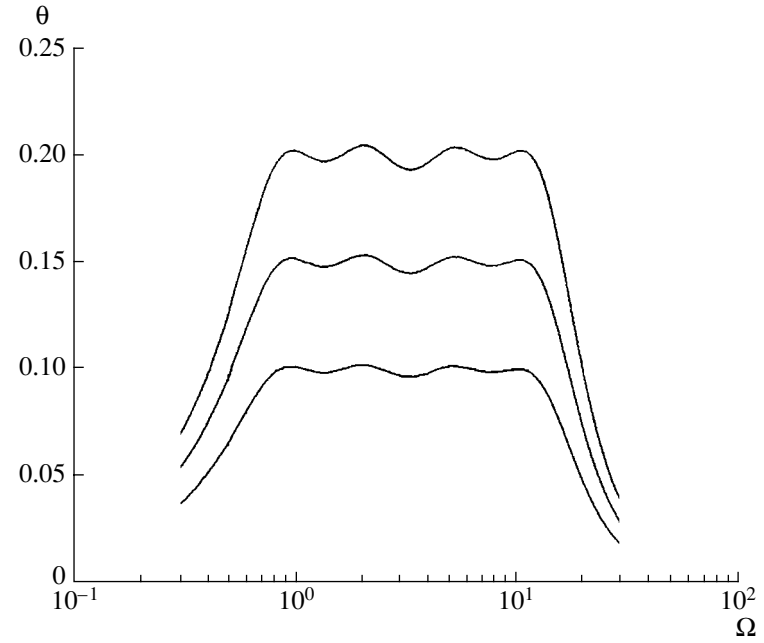

Fig. 4. Loss factor in the medium of Fig. 3 on an enlarged scale.

for a layer with an infinite loading ($Z_L = \infty$). Here,

$$\bar{m} = \frac{\bar{\rho}}{\rho_0}, \quad L_0 = \frac{l}{\lambda_0}, \quad \Omega = \frac{\omega}{\omega_{01}},$$

where l is the layer thickness; λ_0 is the acoustic wavelength in water at the lowest resonance frequency of the inclusions ω_{01}; and $\bar{\rho}$ is determined by Eqs. (3) and (18), in which ε_n are the variable parameters (as above). Note that the parameter L_0 relates the layer thickness in terms of wavelength to the dimensionless resonance frequencies of the inclusions, which allows us to use the dimensionless representation of the results.

We optimize the absorber in terms of the criterion

$$\hat{V} = \frac{1}{K}\sum_{k=1}^{K} |V(\Omega_k)| = \min, \tag{23}$$

which provides the minimal mean reflectivity $\hat{V}$, where the frequencies Ω_k, at which the layer is optimized,

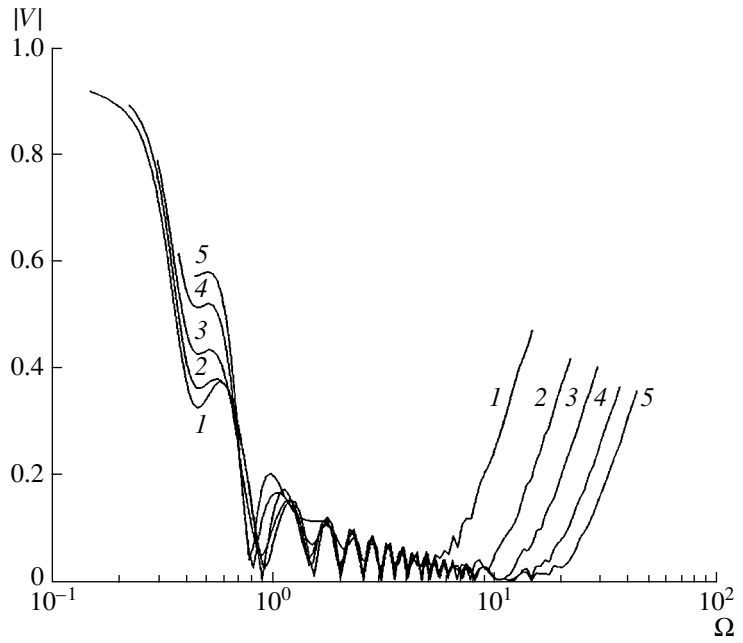

Fig. 5. Reflection coefficient of the synthesized sound absorber for $\eta = 0.3$ and $Z_L = 0$: $L_0 =$ (*1*) 0.5, (*2*) 0.75, (*3*) 1.0, (*4*) 1.25, and (*5*) 1.50.

belong to the interval Ω_{01}–Ω_{0N}, and $K = 100$ is the total number of these frequencies. We use a logarithmic frequency scale, which allows us to emphasize the importance of the lower frequencies of the range. The reflectivity V is determined by Eq. (20) with the use of Eq. (21) or Eq. (22). To satisfy the second feasibility condition of those given by Eqs. (19), a four-layer absorber is synthesized by varying only the first three quantities ε_n, the fourth one being determined as $\varepsilon_4 = \varepsilon_0 - (\varepsilon_1 + \varepsilon_2 + \varepsilon_3)$.

Table 4. $Z_L = 0$

L_0	ε_1	ε_2	ε_3	ε_4	$\hat{V}$
0.50	0.0407	0.0291	0.1041	0.0262	0.1261
0.75	0.0852	0.0736	0.0209	0.0202	0.0724
1.00	0.1351	0.0321	0.0228	0.0150	0.0592
1.25	0.1450	0.0211	0.0203	0.0135	0.0497
1.50	0.1594	0.0103	0.0191	0.0121	0.0457

Table 5. $Z_L = \infty$

L_0	ε_1	ε_2	ε_3	ε_4	$\hat{V}$
0.50	0.0136	0.1377	0.0209	0.0278	0.1114
0.75	0.0997	0.0567	0.0246	0.0191	0.0801
1.00	0.1241	0.0386	0.0.218	0.0155	0.0572
1.25	0.1469	0.0196	0.0206	0.0129	0.0511
1.50	0.1589	0.0116	0.0182	0.0113	0.0451

This choice of ε_n allows one to synthesize the absorber for an arbitrary maximal concentration ε_0.

Since the complex density weakly depends on the loss factor in rubber, we solved the problem only for $\eta = 0.3$. The results are summarized in Tables 4 (for $Z_L = 0$) and 5 (for $Z_L = \infty$) and shown in Fig. 5 (only for $Z_L = 0$).

The results presented above can be used to draw the following conclusions.

The material synthesized is a highly efficient sound absorber: with increasing wave thickness $\hat{V}$ of the layer from 0.5 to 1.5, the reflection coefficient $\hat{V}$ averaged over the frequency range decreases from 0.12 to 0.05, while the bandwidth of effective absorption increases by a factor of approximately 10 to 30. It is essential that the average performance is independent of the type of the load applied to the absorber (results for $Z_L = 0$ and $Z_L = \infty$ are almost the same). The reflectivity curves have the form of the response of a bandpass filter with the ripples caused by the interference of waves reflected from the front and back surfaces of the absorber.

Although the absorber synthesized in the form of a homogeneous layer shows a fairly high efficiency, it is reasonable to synthesize an absorber in the form of an inhomogeneous layer consisting of a number of relatively thin homogeneous layers. Such a study can be conducted primarily with the aim of finding a possibility for designing a thinner absorber than that in the previous case.

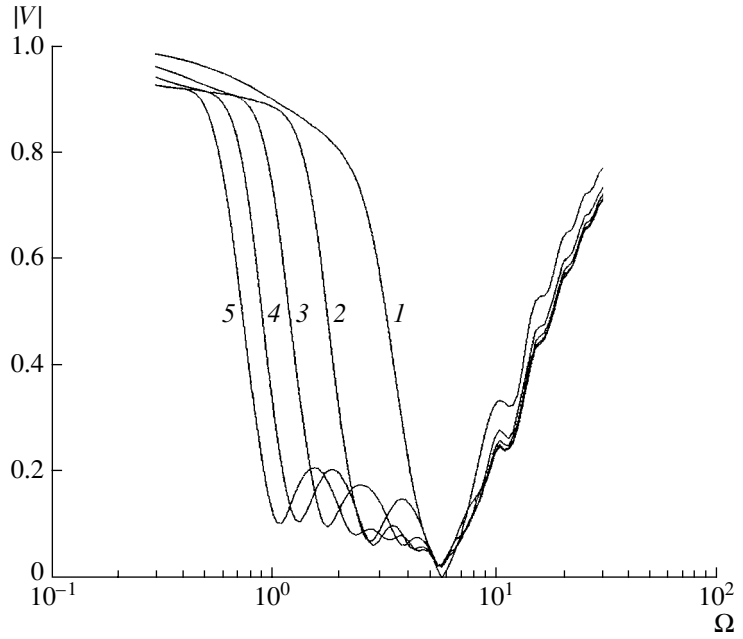

Fig. 6. Reflection coefficient of a layered sound absorber. The thickness of each layer is $L_q = 0.1$. The numbers indicate the total number of layers.

The solution of this optimization problem also relies on Eq. (20), which should be rewritten as

$$V_q = \frac{Z_q - 1}{Z_q + 1}. \tag{24}$$

Here, V_q is the reflection coefficient of the qth layer loaded by $q - 1$ previous layers and Z_q is the corresponding impedance related to the impedance Z_{q-1} through the recurrent relationship

$$Z_q = \frac{-i\sqrt{\overline{m}_q}\tan(2\pi L_q\sqrt{\overline{m}_q}\Omega) + Z_{q-1}}{1 - i\tan(2\pi L_q\sqrt{\overline{m}_q}\Omega)Z_{q-1}(\sqrt{\overline{m}_q})^{-1}}. \tag{25}$$

Here, the notations m and L introduced above refer to the qth layer.

The inhomogeneous (layered) absorber was synthesized using a model in which each layer contains inclusions of a particular dimension that can change from layer to layer. Preliminary calculations showed that the maximal concentration of inclusions ($\varepsilon_0 = 0.2$) must be used in each layer, because the inclusion density is relatively small. The complex density is determined by Eqs. (6) and (7); the optimality criterion for $V = V_q$ is given by Eq. (23) with Ω_{0q} being the variable parameter. The calculations were performed for two layer dimensions: $L_q = 0.1$ and 0.2 at $Z_L = 0$.

Tables 6 and 7 present the dimensionless resonance frequencies Ω_{0q} for each layer, the total number of layers n, and the average reflection coefficient $\widehat{V}$ of the nth layer.

The corresponding frequency behavior of the reflection coefficient is shown in Figs. 6 and 7. The results show that the first (counted from the back surface) layers have higher resonance frequencies, which decrease as the total number of layers increases. Accordingly, the region of high efficiency of the absorber extends toward the lower frequencies, and the average reflection coefficient decreases to 0.11–0.13. Since, in this case, the total absorber thickness L_0 is equal to 0.5 (Table 6) or 0.6 (Table 7), the comparison with the data of Table 4 shows that the layered absorber does not have any advantages over the homogeneous absorber of the same thickness. As follows from the above theoretical study, absorbing materials synthesized as rubberlike media with inclusions of relatively low density feature a rather high efficiency over a wide (about one decade) fre-

Table 6. $L_q = 0.1$

n	1	2	3	4	5
Ω_{0q}	5.93	2.80	1.79	1.31	0.91
$\widehat{V}$	0.4876	0.3009	0.1805	0.1235	0.1067

Table 7. $L_q = 0.2$

n	1	2	3
Ω_{0q}	4.28	1.58	1.40
$\widehat{V}$	0.3342	0.1547	0.1307

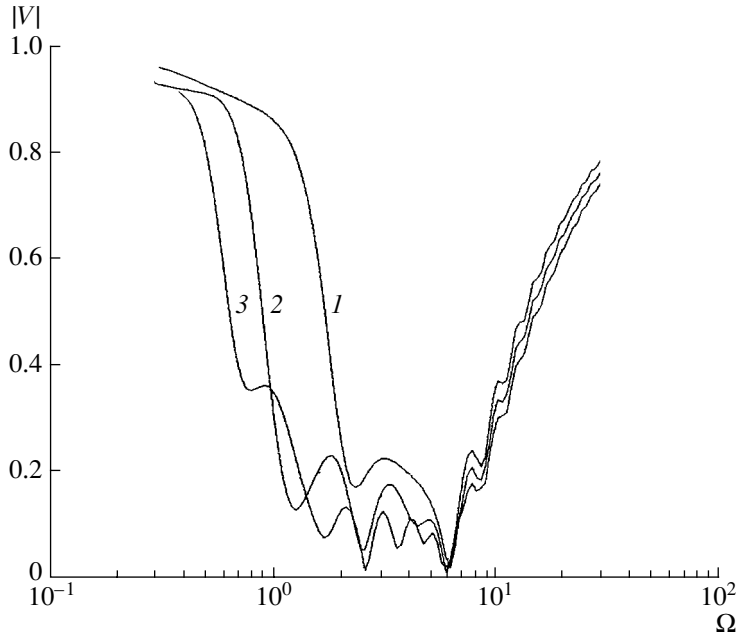

Fig. 7. Same as in Fig. 6 for $L_q = 0.2$.

quency range. At the lowest frequency, their thickness is less than half the sound wavelength in water, which makes them comparable with sound absorbers made with, e.g., lead inclusions [15].

ACKNOWLEDGMENTS

We are grateful to N.A. Dubrovsky for the statement of the problem and useful discussions.

REFERENCES

1. I. A. Chaban, Akust. Zh. **10**, 351 (1964) [Sov. Phys. Acoust. **10**, 298 (1964)].
2. D. V. Sivukhin, Akust. Zh. **1**, 78 (1955) [Sov. Phys. Acoust. **1**, 82 (1955)].
3. M. Viens, Y. Tsukahara, C. K. Jen, and I. D. N. Cheeke, J. Acoust. Soc. Am. **95**, 701 (1994).
4. R. Burridge, M. G. De Hoop, K. Hsu, *et al.*, J. Acoust. Soc. Am. **94**, 2884 (1993).
5. I. A. Chaban, Akust. Zh. **11**, 102 (1965) [Sov. Phys. Acoust. **11**, 81 (1965)].
6. R. N. Viktorova, A. E. Vovk, and V. V. Tyutekin, *Inhomogeneous Acoustic Media with Real Wave Impedance in the Presence of Loss* (Inst. Gidrodin., Novosibirsk, 1992), issue 105.
7. A. E. Vovk, R. N. Viktorova, and T. B. Golikova, in *Proceedings of XI All-Union Acoustical Conference* (Moscow, 1991).
8. V. V. Varadan, S. K. Yarg, and V. K. Varadan, J. Sound Vibr. **159** (3), 403 (1992).
9. V. V. Tyutekin, Akust. Zh. **2**, 295 (1956) [Sov. Phys. Acoust. **2**, 301 (1956)].
10. *Technical Aspects of Sound*, Ed. by E. G. Richardson (Elsevier, Amsterdam, 1953, 1957; Voenizdat, Moscow, 1962), Vols. 1, 2.
11. R. Bobber, *Underwater Electroacoustic Measurements* (Naval Res. Lab., Washington, 1970; Mir, Moscow, 1974).
12. R. N. Viktorova and V. V. Tyutekin, in *Proceedings of VI All-Union Acoustical Conference* (Moscow, 1967).
13. R. N. Viktorova, in *Proceedings of VIII All-Union Acoustical Conference* (Moscow, 1973).
14. M. A. Isakovich, *General Acoustics* (Nauka, Moscow, 1973).
15. R. N. Viktorova and V. V. Tyutekin, Akust. Zh. **44**, 331 (1998) [Acoust. Phys. **44**, 275 (1998)].
16. V. V. Tyutekin, Akust. Zh. **43**, 681 (1997) [Acoust. Phys. **43**, 589 (1997)].
17. V. G. Potemkin, *The MatLab System: Reference Book* (Dialog-MIFI, Moscow 1998).

Translated by A. Khzmalyan

Acoustical Physics, Vol. 48, No. 4, 2002, pp. 467–472. Translated from Akusticheskiĭ Zhurnal, Vol. 48, No. 4, 2002, pp. 533–538.

Effect of Inhomogeneous Acoustic Fields on the Noise Immunity of a Planar Receiving Antenna

V. N. Romanov

Krylov Central Research Institute, Moskovskoe sh. 44, St. Petersburg, 196158 Russia

e-mail: albert@krylov.spb.su

Received April 12, 2001

Abstract—Expressions are obtained for determining the noise immunity of a receiving antenna with a planar aperture under the action of different types of inhomogeneous acoustic fields. The inhomogeneity of these fields is shown to considerably affect the noise immunity of the antenna, which should be taken into account in estimating the antenna efficiency. *© 2002 MAIK "Nauka/Interperiodica".*

Until recently, in the studies of the effect of acoustic fields on receiving antennas, it was assumed that these fields are homogeneous or inhomogeneous throughout the whole acoustic space far from the antenna [1] or they are homogeneous near the antenna in the planes parallel to the plane where the acoustic sources are located [2]. In particular, homogeneous fields result from homogeneous forces acting on structures [2, 3].

However, in recent years, the effect of inhomogeneous fields whose sources are located near the antenna has become the object of interest [4].

This paper considers the effect of a number of inhomogeneous acoustic fields encountered in practice on an antenna with the aim of revealing new features arising in the antenna response in comparison with the case of homogeneous fields.

To simplify the problem, we assume that the antenna has a planar aperture and is composed of point transducers arranged in an array with a spacing shorter than a quarter-wavelength of sound in the surrounding medium. In these conditions, the aperture of the antenna can be considered as continuous and perfectly transparent for sound. We do not introduce temporal delays in separate transducers; as a result, the signal at the antenna output is formed as the sum of signals from its every unit area, and the phase of each term of this sum is governed only by the action of the acoustic field on the corresponding unit area of the aperture.

For such an aperture transparent for sound, the integrator output signal reduced to the aperture surface and expressed in terms of the squared pressure magnitude can be written according to [5] as

$$|P_a|^2 = \frac{1}{S^2}\int\limits_{S_1}\int\limits_{S_2} K(x_1, y_1, x_2, y_2)\,dS_1 dS_2, \qquad (1)$$

where $|P_a|^2$ is the squared magnitude of the acoustic field reduced to the aperture surface, $S_{1,2}$ is the aperture surface, and $K(\ldots)$ is the spatial correlation function of the acoustic field acting on the aperture.

If the acoustic field acting on the aperture is homogeneous in the aperture plane, the correlation function $K(\ldots)$ depends only on the differences in the coordinates on the aperture surface ($x_1 - x_2$ and $y_1 - y_2$). By contrast, if the field is inhomogeneous in the aperture plane, the function $K(\ldots)$ depends on the coordinates x_1, y_1, x_2, and y_2.

If the sound pressure $P(x, y)$ is known for any point of the aperture surface, the correlation function is determined as

$$K(x_1, y_1, x_2, y_2) = M[P(x_1, y_1)P^*(x_2, y_2)], \qquad (2)$$

where * denotes the complex conjugate quantity and $M[\,]$ denotes the mathematical expectation over the space of realizations (in the case under consideration, over the angles of arrival of sound waves).

Consider the following three types of inhomogeneous acoustic fields:

(I) A wave traveling from the source along the plane in which the acoustically transparent aperture is located (Fig. 1)

$$P(x, y) = P_0\left(\frac{1}{R}\right)^n \exp(i\bar{k}\bar{R}), \qquad (3)$$

where P_0 is the pressure at the unit distance from the source. Such a wave is arbitrarily called the quasi-spherical wave. In the case of a perfectly hard plane, $n = 1$, and we deal with a purely spherical wave; in the case of a perfectly soft plane, $n = 2$. Intermediate situations are also possible, and they depend on the relationship between the wave impedance of the surrounding medium and the impedance of the plane.

Since the acoustic pressure varies with distance from the source, this field is an inhomogeneous one.

(II) An acoustic wave produced by a linear obstacle (rib) located on a plate under an incident diffuse field of bending waves (Fig. 2).

1063-7710/02/4804-0467$22.00

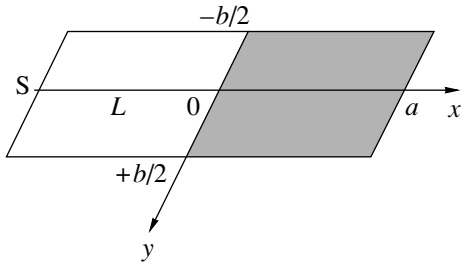

Fig. 1. Reference system for a quasi-spherical wave propagating along the aperture. The source is located at the point S, and the distance between the source and the aperture is L.

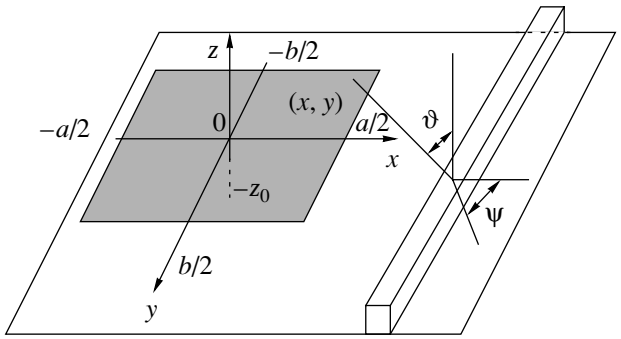

Fig. 2. Reference system for an aperture under the effect of the field of a plate with a stiffening rib. The distance between the aperture and plate planes is z_0, and the distance between the rib and the projection of the aperture center on the plate is L.

According to [6], for frequencies below the critical frequency f_{cr} determined from equating the bending wavelength in the plate to the wavelength in the surrounding medium, the rib driven by a bending wave incident at an angle ψ (see Fig. 2) generates a wave, in which the pressure for $kR > 1$ is given by the expression [2]:

$$P_\psi(x, y, z, \psi) = \frac{-\rho c \dot{W}_\psi}{\sqrt{2\pi kR}\chi_m b\beta^{3/2}} \times \frac{\cos\vartheta[1 - q_1^2\sin^2\psi]^{1/4}}{L_z} L_c \times \exp\left(ik_b y\sin\psi + i\bar{k}\bar{R}\sqrt{1 - q_1^2\sin^2\psi} - i\frac{\pi}{4}\right), \quad (4)$$

where ρc is the wave resistance of the surrounding medium; $\dot{W}_\psi$ is the velocity of oscillations in the bending wave incident on the rib at the angle ψ (Fig. 2); R is the radius vector connecting the rib with the observation point in the plane normal to the line along which the rib is attached to the plate; ϑ is the angle between the normal to the plate at the site of the rib attachment and the radius vector R; $\chi_m = 1$ for the one-side contact of the plate with the surrounding medium; $\chi_m = 2$ for the two-side contact of the plate with the surrounding medium; $b = \rho c/\omega m$ (ω is the angular frequency and m is the mass of the plate per unit area); $\beta = f_{cr}/f$; L_z is the function depending on the parameters of the plate and the angles ϑ and ψ [6]; L_c is the function depending on the parameters of the plate, the mechanical impedances of ribs with respect to the transverse force and the bending momentum, and the angles ϑ and ψ [6]; $q_1 = k_b/k$ (k_b is the wave number of bending waves in the plate); and k is the wave number in the liquid.

As can be seen from the structure of the exponent, only the bending waves incident on the rib at angles $\psi < \arcsin\frac{1}{q_1}$ generate acoustic waves in the liquid; otherwise, a nonwave field is formed in which the pressure decreases with the distance from the plate according to an exponential law.

The critical frequency $\psi_{cr} = \arcsin\frac{1}{q_1}$ depends on the dimensionless wave number of bending waves q_1. The lower the frequency f relative to the critical frequency f_{cr}, the greater the wave number q_1 and, hence, the smaller the angle ψ_{cr}. Thus, for frequencies much lower than f_{cr}, only the bending waves that are almost normally incident on the rib contribute to the sound radiation of the plate with the rib. In this case, a quasi-cylindrical wave propagates in the liquid from the rib and the phase front of this wave is described by the factor $\exp(ik_b y\sin\psi)$.

In accordance with Eq. (4), the acoustic pressure depends on both the radius vector $\bar{R}$ and the angle ϑ; therefore, this field is inhomogeneous.

(III) The nonwave field of bending waves at frequencies $f < f_{cr}$ (Fig. 3).

The bending waves propagating along a plate generate only the nonwave field in the surrounding medium, and the pressure in this field is described by the formula [6]

$$R_H(x, y, z, \psi) = \frac{-i\rho c\dot{W}_\psi}{\sqrt{q_1^2 - 1}}\exp(ik_x x + ik_y y - kz\sqrt{q_1^2 - 1}), \quad (5)$$

where x and y are the coordinates in the plate plane; z is the normal to the plate; and k_x and k_y are the projections of the wave number of bending waves $\bar{k}_b$ on x and y axes, respectively.

The acoustic field described by Eq. (5) is homogeneous.

However, in real shell structures, the vibration energy flux propagating along them forms a quasi-diffuse field of bending waves. This field exhibits a diffuse behavior in the region of the shell bounded by the stiffening ribs. The velocity of oscillation of bending waves in such cells decreases with increasing distance from the source of vibration (e.g., along the x axis) [7].

To take this factor into account, one should multiply Eq. (5) by the factor

$$\exp(-a_f x), \tag{6}$$

where a_f is the coefficient determining the attenuation of vibration along the shell [7]. With allowance for this fact, the nonwave field of bending waves proves to be an inhomogeneous field.

Substituting Eqs. (3), (4), and (5) with allowance for Eq. (6) into Eq. (2), we obtain the correlation function for a fixed propagation direction for either a quasi-spherical wave (the first type of the field) or a bending wave propagating at an angle ψ to the x axis (the second and third types of the field). For the second and third types, the field of bending waves exhibits a diffuse behavior. For this reason, in calculating the correlation function by Eq. (2), one should carry out the integration with respect to the angle ψ from 0 to 2π and multiply the result by $\frac{1}{2\pi}$. Then, substituting the correlation functions in Eq. (1), we determine the squared magnitude of the acoustic pressure reduced to the aperture surface.

In what follows, we consider the changes in the aperture noise immunity normalized by its concentration coefficient Ω:

$$\chi = \frac{|P_{\mathrm{Nr}}|^2}{|P_{\mathrm{a}}|^2 \Omega}, \tag{7}$$

where $|P_{\mathrm{Nr}}|^2$ is the squared magnitude of the pressure measured with a nondirectional receiver positioned at the center of the aperture.

Consider the quantity χ for the field of the first type.

When the source is located far from the aperture, the field at the aperture surface is nearly homogeneous, and the calculation by Eq. (7) yields

$$\chi_{max} = \frac{\pi a}{b[1 - \cos(ka)]}, \tag{8}$$

where a is the size of the aperture along the direction of wave propagation and b is the size of the aperture in the transverse direction.

From Eq. (8), it follows that the maximal aperture immunity occurs for $\cos ka = 1$, i.e., for $ka = 2\pi n$ (n = 1, 2, 3, …). This condition corresponds to the situation when the size of the aperture along the direction of wave propagation measures an even number of half-wavelengths.

In this case, the contributions of the positive and negative half-waves to the output signal of the antenna are mutually canceled and we obtain $|P_{\mathrm{a}}|^2 \longrightarrow 0$ and $\chi \longrightarrow \infty$. The only obstacle to increasing the quantity χ is the scatter in amplitudes and phases of transducers [5], which limits the quantity χ by a value of 30 dB for actual apertures.

The minimal value of the quantity χ occurs for $\cos ka = -1$, i.e., for $ka = \pi(2n + 1)$ (n = 1, 2, 3…). In this case, the size of the aperture along the direction of wave propagation measures an odd number of half-wavelengths and the antenna output signal is formed by a half-wave remaining after the cancellation of other half-waves. Then, we have

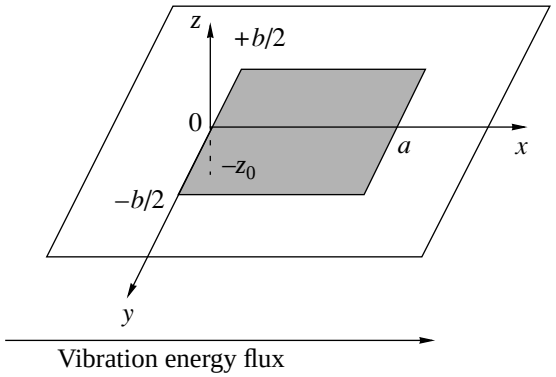

Fig. 3. Reference system for an aperture under the effect of the nonwave field of bending waves in the plate. The distance between the aperture and plate planes is z_0.

$$\chi_{min} = \frac{\pi a}{2b}. \tag{9}$$

For $a = b$, we have $\chi_{min} = \pi/2$ (about 2 dB).

Figures 4 and 5 show the quantity χ calculated for the aperture with $a = b = 4$ m; different curves correspond to the plane wave, the spherical wave with $n = 1$, and the quasi-spherical wave with $n = 2$ propagating along the aperture.

As may be seen, in the case $n = 1$, the maximal noise immunity is between 20 and 30 dB even for a source located far from the antenna ($L/a \sim 5$); i.e., the maximal noise immunity is fairly strongly limited by the incomplete cancellation of the positive and negative half-waves because of the spherical divergence of the wave front.

On the other hand, the minimal noise immunity increases as the source approaches the aperture (L/a = 1). This occurs because, in contrast to the cases of the plane wave and a distant source (L/a = 5), the positive and negative half-waves are partially canceled along the y axis (along the direction perpendicular to the direction of the wave propagation) in the process of the formation of the antenna output signal.

The amplitude of the quasi-spherical wave (n = 2) decays more rapidly with distance between its front and the source as compared to the spherical wave. For this reason, both maximal and minimal noise immunity decrease more substantially, because the positive and negative half-waves are canceled to a lesser extent over the aperture surface, especially when the source is located not far from the aperture.

Now, we consider the noise immunity χ calculated for the second type of inhomogeneous field formed by

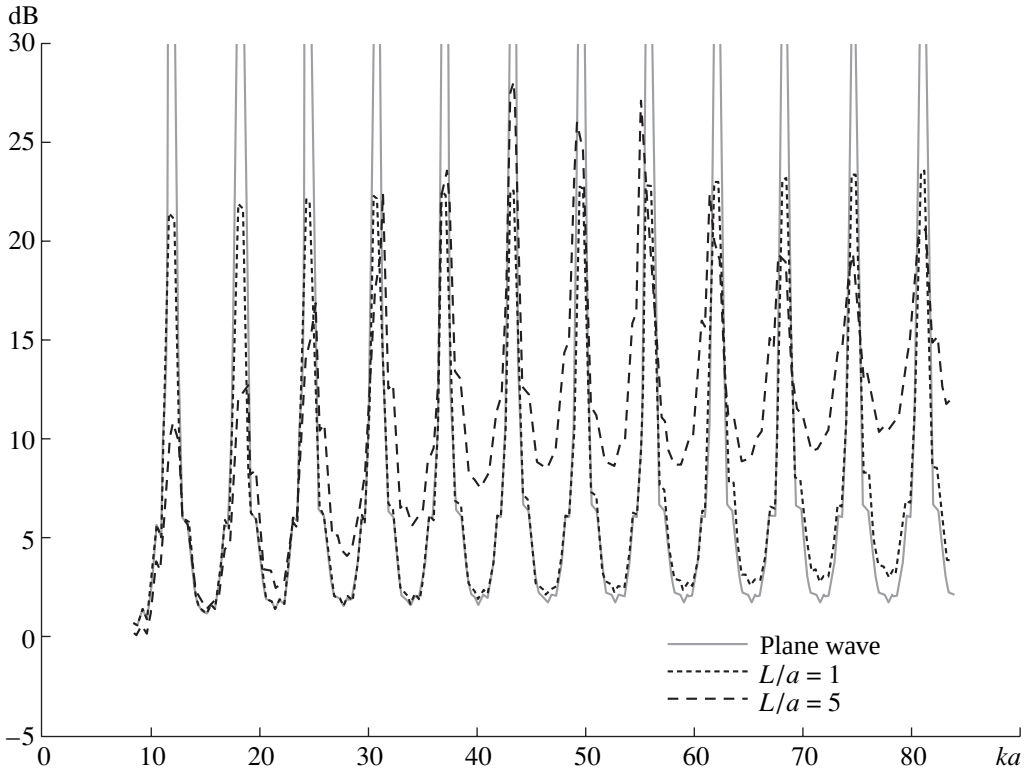

Fig. 4. Noise immunity of the aperture under an incident spherical wave ($n = 1$).

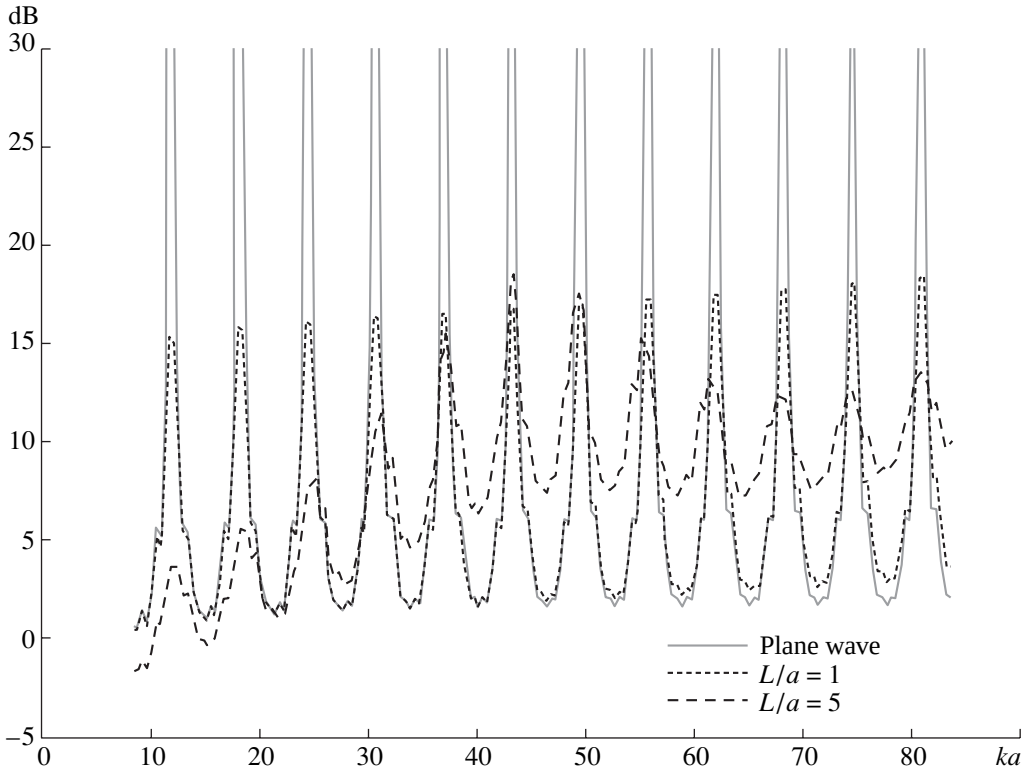

Fig. 5. Noise immunity of the aperture under an incident quasi-spherical wave ($n = 2$).

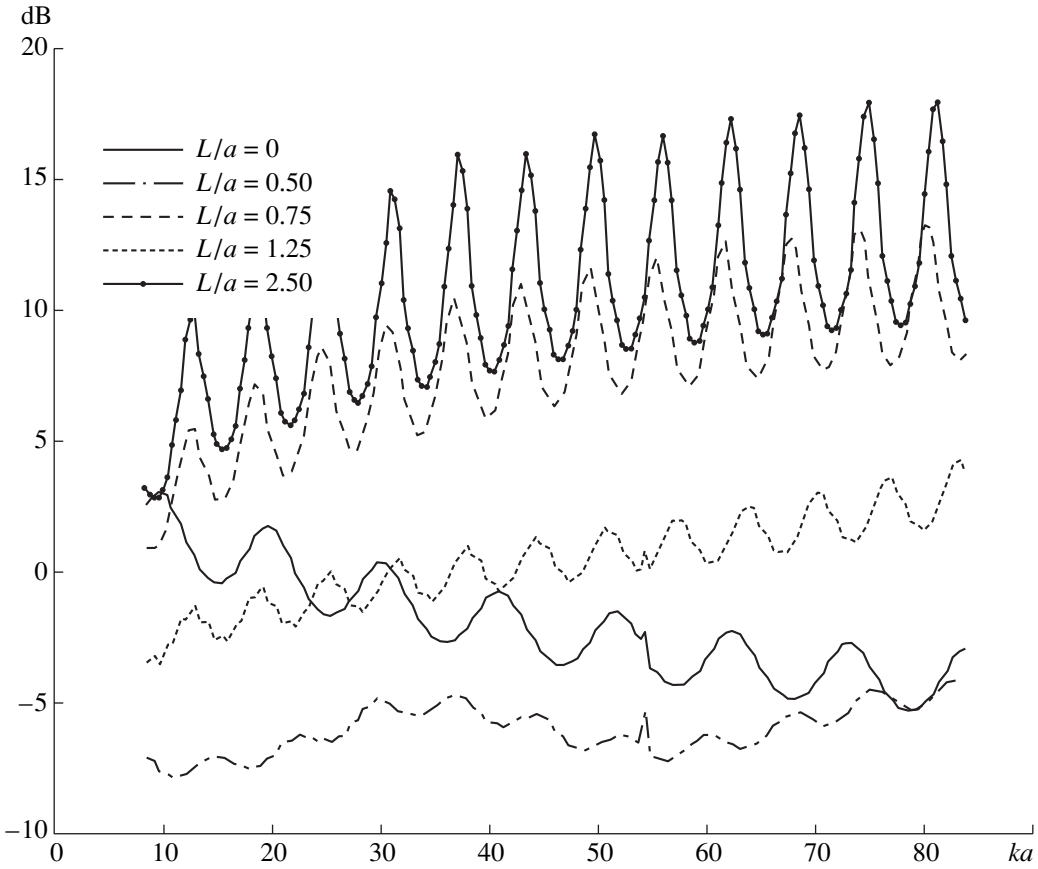

Fig. 6. Noise immunity of the aperture under the effect of the acoustic field of the plate with a stiffening rib.

the plate with a stiffening rib driven by the field of incident bending waves.

Figure 6 shows these results for the aperture with $a = b = 4$ m for different distances between the aperture center and the rib and the distance between the aperture plane and the plate plane $z = 1$ m. The critical frequency of the plate is $f_{cr} = 6000$ Hz; the impedances of the rib relative to the transverse force and the bending momentum are 1000, which means that the rib is relatively massive; and the coefficients are $b = 0.13$ and $\chi = 1$. As may be seen from Fig. 6, the maximal noise immunity of the antenna occurs for relatively large distances between the rib and the aperture.

For the rib located near the boundary of the aperture ($L/a = 0.5$) and, especially, when it is opposite the aperture center ($L/a = 0$), the noise immunity of the aperture rapidly decreases, because the negative and positive half-waves are incompletely canceled over the aperture surface due to the divergence of the wave front from the point where the rib is attached to the plate and due to the directional property of this radiation. The swing of oscillations of the quantity χ also decreases as the rib approaches the aperture center.

For the third type of inhomogeneous field, the quantity χ was calculated for the plate with $f_{cr} = 6000$ Hz, $b = 0.13$, and the distance between the aperture plane and the plate plane $z_0 = 0.5$ m. The size of the aperture was the same as in the previous cases, $a = b = 4$ m. Considering a homogeneous field of bending waves in the limit kq_1a, $kq_1b \gg 1$, we obtain an approximate expression for the minimal values of χ:

$$\chi_{min} = \frac{\pi}{4}\frac{kq_1^3 S}{(a+b)}. \tag{10}$$

From Eq. (10), it follows that the higher the frequency (q_1 decreases), the lower the minimal noise immunity, because the wavelength of bending waves decreases at higher frequencies and the cancellation conditions worsen.

This result is shown in Fig. 7, displaying the curves for the homogeneous field (the vibration W is not damped as the vibration energy propagates from the source along the structure) and the inhomogeneous field (the vibration W is damped; in the calculations, we used $\alpha_f = 0.174(f/1000)^{1/2}$, where f is the frequency).

As can be seen, the noise immunity noticeably decreases in the case of the inhomogeneous field and the swing of oscillations χ also considerably decreases.

Thus, from the investigation described above, it follows that inhomogeneous fields acting on continuous

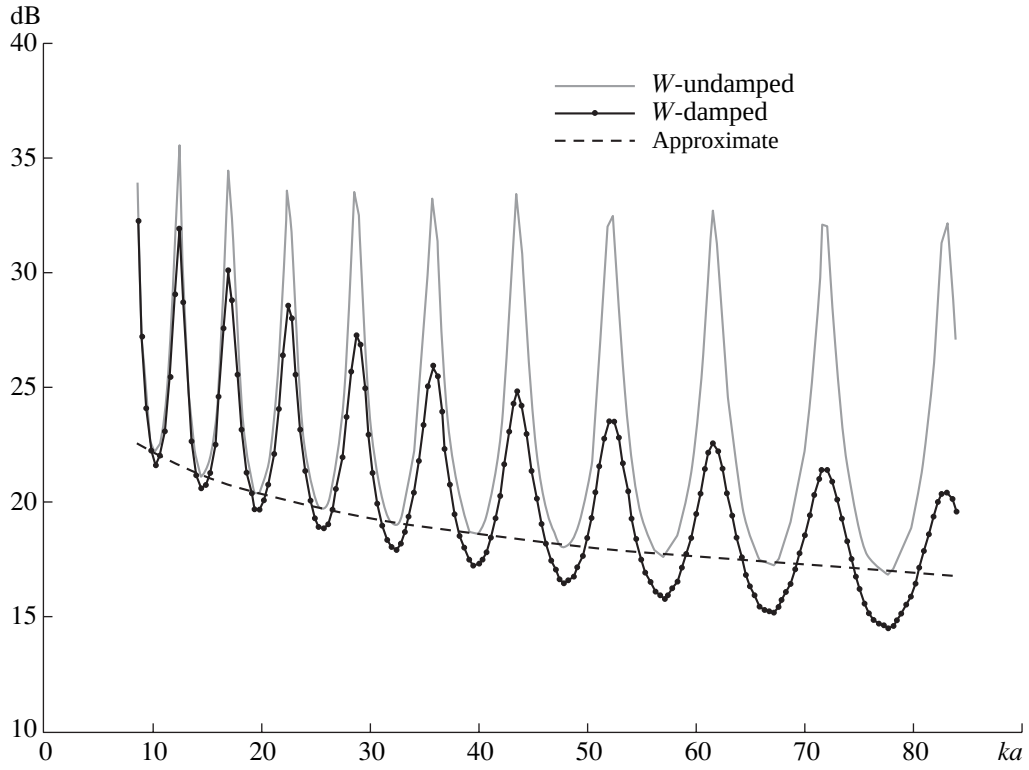

Fig. 7. Noise immunity of the aperture under the effect of the nonwave field of bending waves in the plate.

apertures considerably affect their noise immunity in comparison with the case of homogeneous fields and this effect should be taken into account in estimating the efficiency of such apertures.

REFERENCES

1. M. D. Smaryshev and E. L. Shenderov, Akust. Zh. **31**, 502 (1985) [Sov. Phys. Acoust. **31**, 296 (1985)].
2. E. L. Shenderov, Akust. Zh. **26**, 913 (1980) [Sov. Phys. Acoust. **26**, 514 (1980)].
3. G. Cheng and M. Chui, J. Sound Vibr. **226** (1), 83 (1999).
4. I. G. Bulatov, Akust. Zh. **43**, 762 (1997) [Acoust. Phys. **43**, 663 (1997)].
5. M. D. Smaryshev and Yu. Yu. Dobrovol'skiĭ, *Hydroacoustic Antennas* (Sudostroenie, Leningrad, 1984).
6. V. N. Romanov and V. S. Ivanov, *Sound Generation by Ship Structure Elements* (Sudostroenie, St. Petersburg, 1993).
7. A. S. Nikiforov, *Acoustic Design of Ship Structures* (Sudostroenie, Leningrad, 1990).

Translated by A. Vinogradov

Acoustical Physics, Vol. 48, No. 4, 2002, pp. 473–480. Translated from Akusticheskiĭ Zhurnal, Vol. 48, No. 4, 2002, pp. 539–546.

Studies of the Ocean-Bottom Reflection Coefficient at Angles of Total Internal Reflection

N. V. Studenichnik

Andreev Acoustics Institute, Russian Academy of Sciences, ul. Shvernika 4, Moscow, 117036 Russia

e-mail: bvp@akin.ru

Received July 9, 2001

Abstract—For practical-purpose studies in underwater acoustics, a new method is proposed to determine the bottom reflection coefficient on the basis of multiple bottom–surface reflections. The method allows one to obtain the angular dependence of the bottom reflection coefficient at grazing angles from several degrees to several tens of degrees in the audio and infrasonic frequency bands. The sound field structure is studied in deep-water regions of the Black (2000 m) and Arabian (4000 m) seas at frequencies within 10–400 Hz. For the regions under investigation, the frequency-angular dependence of the reflection coefficient is obtained with the use of the proposed method. The data for the Black Sea are compared with those provided by the conventional method based on the use of single and double bottom and bottom–surface reflections. Experimental data on the values and variations of the bottom reflection coefficient are presented for different deep-water and shallow-water regions of the World Ocean. The presence of shear waves in the bottom sediments is revealed, and the effect of these waves on the frequency-angular dependence of the reflection coefficient is demonstrated. © *2002 MAIK "Nauka/Interperiodica".*

To predict and calculate underwater sound fields at long ranges, it is necessary to know the bottom reflectivity at low audio and infrasonic frequencies for small grazing angles. The conventional technique used for measuring the bottom reflection coefficient is mainly suitable for short distances and, therefore, cannot be applied in long-range studies. The well-known modifications of the conventional technique, which are the only ones that have been put to practice, are based on using single bottom or double bottom–surface reflections [1–3]. These modifications allow one to perform the measurements and obtain the data for a limited range of grazing angles (higher than 10°–15°), mainly at frequencies of several kilohertz. With the conventional technique, due to its technical restrictions, low-frequency and small-angle measurements cannot be performed. Here, on the basis of a large body of experimental data obtained by the author in both shallow- and deep-water regions of the World Ocean, a new method is proposed for studying the bottom reflection coefficient on the basis of multiple bottom–surface reflections. This method allows one to estimate the reflection coefficient at low audio and infrasonic frequencies and at grazing angles from 1°–2° to 30°–40°. The proposed method provides a much higher accuracy of measurements than the conventional one and yields reliable (averaged over the path and the number of reflections) data on the bottom reflectivity in situations that are close to those of practice. In addition, the combinations of frequencies and angles studied here are not considered in the known publications but are the most important for computing long-range sound propagation and evaluating the performance of long-range underwater acoustic systems. The proposed method can be modified for both deep- and shallow-water applications. With this method, underwater explosions are the most advantageous as broadband sound sources.

Numerous experiments on studying the sound fields in deep- and shallow-water regions of the ocean show that the field structure involves signals that are reflected by the surface and bottom from 2–3 to 30–60 times, this number depending on the specific region, range, positions of the source and receiver, sound frequency, parameters of the sediments, relief, and structure of the bottom. A weak reflectivity is often characteristic of offcoast deep-water basins with porous silt sediments or of underwater crests and faults with an extremely rough relief. Such ocean regions are the northern and central parts of the Pacific Ocean, the Philippine Sea, the central part of the Atlantic Ocean (including the regions of Cape Verde and the Canary Islands), the Central Atlantic Range, the abyssal areas of central and southern regions of the Indian Ocean, and other deep-water regions. A high bottom reflectivity is typical of coastal regions with thick, high-density bottom layers and a flat bottom profile. The latter type of regions is represented by ample deep-water areas of the Arabian Sea, the Bay of Bengal in the Indian Ocean, the Norwegian Sea, certain regions of the Mediterranean and Black seas, and some ice-covered areas of the Arctic Ocean. The bottom reflection coefficient ranges from 0.1–0.2 (the Canary Basin and the central regions of the Indian and Pacific oceans) to

1063-7710/02/4804-0473$22.00 © 2002 MAIK "Nauka/Interperiodica"

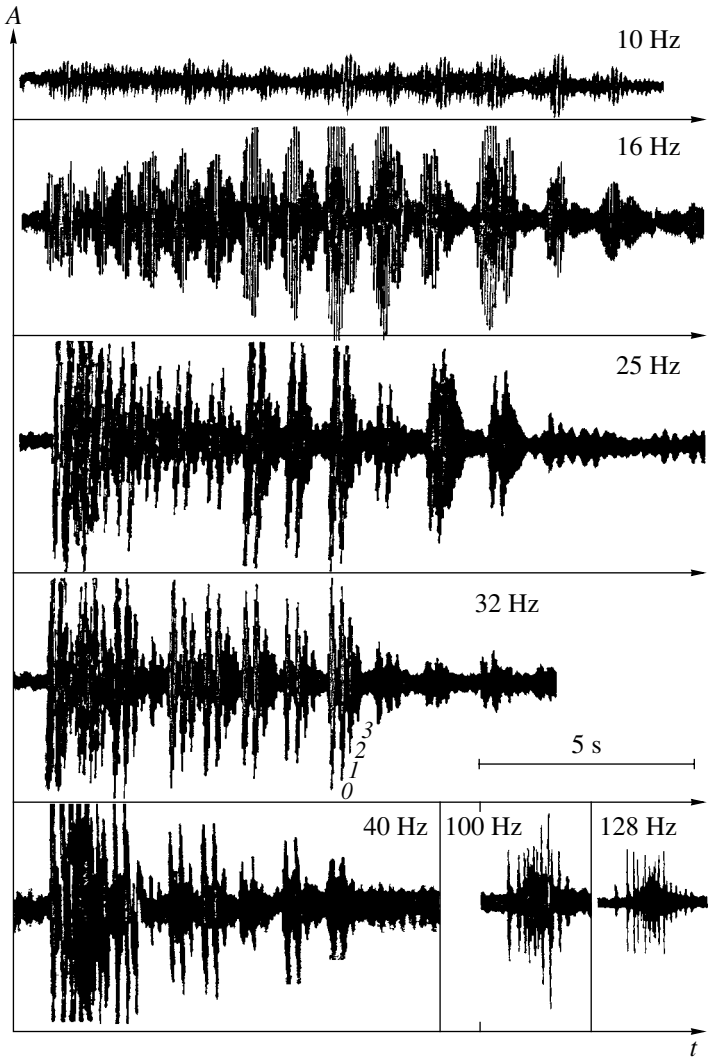

Fig. 1. Dependence of amplitude *A* on time *t* for the sound field generated by an explosive sound source in the Black Sea, at a distance of 140 km, with a sea depth of 2000 m. The frequencies are 10–128 Hz. The source and receiver depths are 35 and 60 m, respectively. For 32 Hz, the following features are indicated: (*0*) the quartet of the shock-wave signals; (*1*) the signal quartet generated by the first gas-bubble oscillation; (*2*) the quartet of the second oscillation; and (*3*) the quartet of the third oscillation. The signal amplitudes are plotted on a linear scale.

0.95–0.98 (the western regions of the Black Sea and the northern regions of the Indian Ocean). In shallow-water sea and ocean regions, the range of the reflection coefficient is even broader. For example, in the 40-m-thick water layer of the South China Sea with a rocky bottom, at a distance of 150 km, explosion-generated signals were received whose amplitudes were 30 dB above the interfering noise at the frequencies 10–200 Hz. The equivalent number of bottom and surface reflections was 1500 at the optimal frequency (125 Hz). In this case, the effective reflection coefficient is 0.9970 to 0.9976, or even 0.9980 if one takes into account the losses caused by reflections from the water–air boundary. To illustrate the aforementioned facts, let us consider some typical structures of the sound field which were obtained in different regions of the World Ocean and included the components refracted in water and the bottom–surface reflections. To this end, we chose two of the aforementioned deep-water regions that differ in their characteristics of the water medium and in the parameters of the bottom sediments. These two regions are the northwestern part of the deep-water basin of the Black Sea and the deep-water plateau of the Arabian Sea in the Indian Ocean.

Figure 1 illustrates the space–time and frequency–power structures of the sound field generated by an explosive sound source in the deep-water basin of the Black Sea with a depth of 2000 m, at a distance of 140 km. The sound field is formed by the refraction components and bottom–surface reflections. The signal records are shown on a linear scale for 1/3-octave

frequency bands. The propagation path 200 km in length passed 100–300 km southeast of the Crimea. The sound speed profile is shown in Fig. 2a. The depth of explosion was 35 m, that of reception was 60 m. The explosive charge was 25 kg in mass. The frequency band of efficient radiation begins from 2–3 Hz. The frequency band under study was 5–300 Hz.

As the plots indicate, up to 20–25 unresolved signal quartets of bottom–surface reflections, along with the refraction components, are present in the sound field structure at frequencies of 10–25 Hz. As the frequency grows, the number of quartets sharply decreases, and, at a frequency of 100 Hz, there are no bottom reflections in the field structure. At this frequency, the sound field is totally formed by the "water" components refracted in deep layers of the sound channel and reflected by the surface. The frequency band within which the rays freely penetrate through the discontinuity layer to the surface is 1.8 to 800 Hz. At low frequencies, each group of bottom–surface reflections consists of 12–16 components that are produced by the signal quartets of the shock wave and two to three oscillations of the gas bubble. A frequency of 32 Hz is most advantageous to detect the quartets of bottom reflections produced by the shock wave (which are not time-resolved) and the signals of three gas-bubble oscillations. At this frequency, one can also determine the parameters of the signals: their time resolution, relative amplitudes, and periods of oscillations.

Because of the extremely strong frequency dependence of bottom reflectivity, the total duration of the refracted and bottom-reflected signals is 15–17 s at frequencies of 10–25 Hz, while it is as small as 1 s at 100 Hz. As the frequency decreases, the duration of the refracted components themselves drops from its maximal value (1.1 s) at high frequencies to nearly zero at frequency of 1.8 Hz, the latter being the critical frequency of the waveguide, which determines the filtering properties of the sound channel. At frequencies of 10, 16, and 32 Hz, the refracted components are protracted to 280, 480, and 610 ms, respectively. For the bottom reflections, these values are 13–17 s; i.e., the bottom-reflected components are 30 to 50 times longer (and more intense) than the refracted ones.

The level ratios in the shock wave and three initial gas-bubble oscillations are 8, 14, and 20 dB at 100 Hz, and 1, 4, and 9 dB at 32 Hz. In the sets of bottom reflections, pronounced maxima and minima are observed that do not correlate in frequencies and grazing angles and can be attributed to the bottom stratification and to the propagation of elastic waves in the sediments. In addition, at frequencies of 10 and 16 Hz, one can notice a dependence of the level of the field components on their arrival times, which is not evident at first glance. In this case, the component amplitudes do not decrease in time when the grazing angle and number of reflections increase. In contrast, they increase to reach their maxima at grazing angles of 15°–24°. At frequencies of 10 and 16 Hz, the interference maxima of bottom reflections are higher than the refracted components: they reach 4–5 and 6–9 dB, respectively. At grazing angles of 24°–30°, the amplitudes of bottom reflections begin to drop steeply: for instance, at 16 Hz, they lose 4–6 dB per consequent reflection, or 0.17–0.25 dB per bounce. As the frequency grows, the starting point of the drop and, hence, that of narrowing of the angle range of power-determining components smoothly shifts towards lower grazing angles. The position of the starting point is governed by the angle of total internal reflection at each frequency and by the parameters of the bottom layers that are responsible for the reflection at this frequency. The corresponding near-bottom grazing angles are 24°–25° at frequencies of 5–25 Hz and 2°–6° at higher frequencies. The sound speed changes from 1506–1507 m/s in the upper bottom layer to 1660 m/s in deeper layers, the sound speed in water being 1505 m/s. The above considerations testify to a

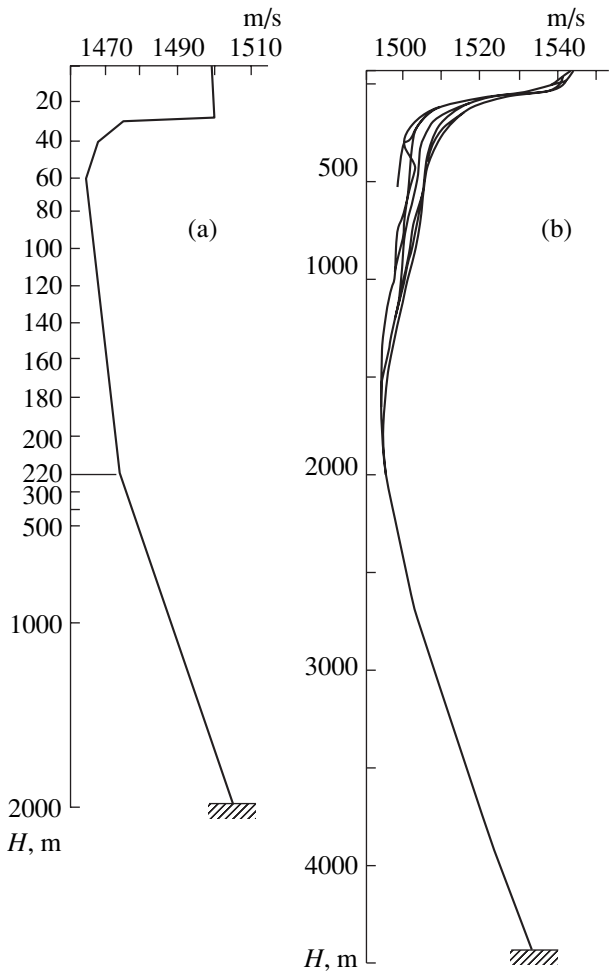

Fig. 2. Sound speed profiles in the (a) Black and (b) Arabian Seas.

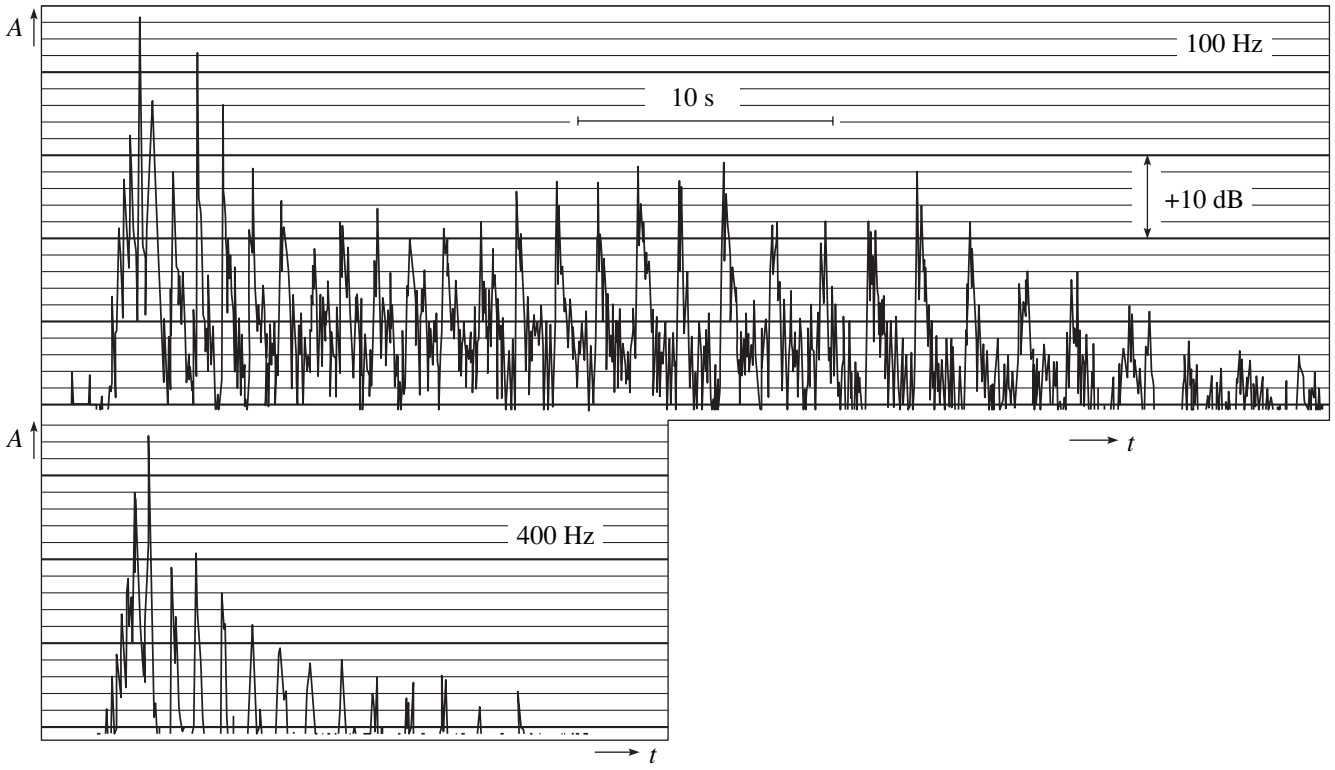

Fig. 3. Same as in Fig. 1 for the Arabian Sea, at a distance of 920 km, with a sea depth of 3800–4500 m. The frequencies are 100 and 400 Hz. The source depth is 600 m, and the receiver depth is 300 m. The signal amplitudes are plotted on a logarithmic scale.

very strong frequency-angular dependence of the bottom reflection coefficient in the ocean region at hand and to a gradient-type dependence of the physical parameters of upper bottom layers on the depth. Hence, in modeling the waveguide to compute the sound fields for a broad frequency band, the parameters of the sound channel (sound speed, bottom density, attenuation coefficient, and sound speed profile if ray-approximation calculations are to be performed) should be specified individually for each frequency.

Figure 3 shows the sound field structure in the Arabian Sea for a distance of 920 km from the source, at frequencies of 100 and 400 Hz. The ocean depth is 3800–4500 m. The sound speed profiles on the 1000-km path are shown in Fig. 2b. The depth of explosions (with a charge mass of 25 kg) is 600 m, the reception depth is 300 m, and the depth of the channel axis is 1700 m. The sound frequencies that are efficiently generated by the explosion start from 20–25 Hz. The signal records are presented on a logarithmic scale, with a 3-mm/s tape speed of a paper-tape recorder. At both frequencies, the systems of the refracted and bottom–surface-reflected signals are well pronounced. The weakly time-resolved arrivals (signal quartets) of 2-s duration, which are first to arrive, are the signals that are refracted in the upper layers of the waveguide and reflected by the bottom, along with purely refracted components propagating in the channel without interacting with the bottom and the surface. The water-path quartets in the first signal group are the last two arrivals with the maximal amplitudes. With the conditions at hand, the mean horizontal velocities of the sound waves that are bottom-reflected at low grazing angles are higher than those of the purely refracted components. As a result, the bottom-reflected–refracted components are first to arrive. Naturally, their levels are lower than those of the water-path components and tend to zero (in accordance with the sharp decrease in the focusing factor) as the grazing angles approach zero. All subsequent arrivals are combined surface–bottom reflections. Their total duration is 17 s at frequency of 400 Hz, and up to 50 s at 100 Hz. The comparison of the frequency–power sound field structures presented in Figs. 1 and 3 shows that, at distance of 920 km in the Arabian Sea, the bottom-reflected signals with 25–30 reflections from the boundaries exist at both frequencies, 100 and 400 Hz, while there is no bottom-reflected component at the 140-km distance in the Black Sea. The amplitudes of the bottom reflections are rather high: they are by as little as 8–20 dB lower than those of the refracted signals. Detailed analysis of the shape of individual components shows that, with a higher number of reflections and, hence, higher grazing angles, the time resolution of the sound field components is better, and one can

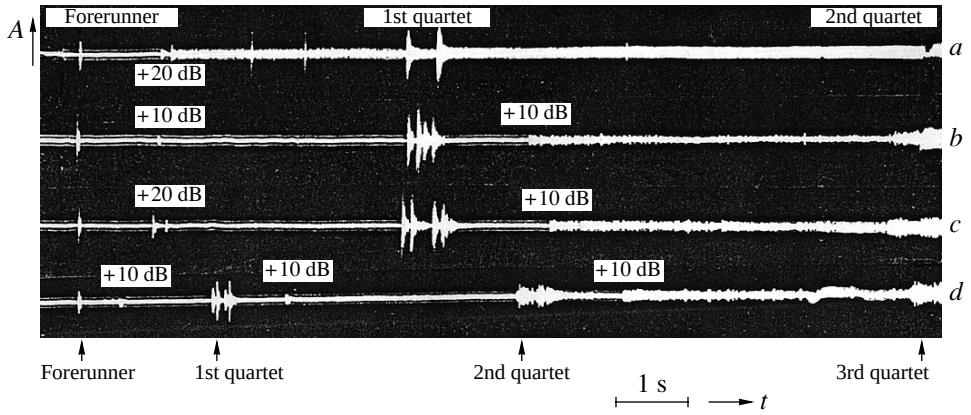

Fig. 4. Same as in Fig. 1 for a near-field zone in the deep-water (5000 m) Canary Basin of the Atlantic Ocean, at a frequency of 3 kHz (the speed of the paper tape is 16.8 mm/s). The distances between the source and receiver are (*a–c*) 4 and (*d*) 20 km. The source depths are (*a*, *b*) 150 and (*d*) 300 m. The receiver depths are (*a*) 10 and (*b–d*) 90 m.

detect separate arrivals in the quartets. In addition, the envelope of the signal system at 100 Hz exhibits a number of amplitude maxima and minima, with level differences of 10–20 dB, which can be related to the angular dependence of the reflection coefficient and are governed by the bottom stratification and shear waves in the sediments. In the maxima, the amplitudes of the bottom reflections are comparable with the amplitudes of the refracted sound waves. As the number of bottom reflections and the related grazing angles increase, the attenuation at 400 Hz also increases and becomes noticeably higher than that at 100 Hz: it is equal to 2–4 dB per bounce.

To estimate the performance and efficiency of the conventional methods of determining the frequency-angular dependence of the bottom reflection coefficient from single (double) reflections, let us consider the sound field structure for typical (but most favorable in the sense of angular resolution) deep-ocean situations. Figure 4 shows the signal records obtained at a frequency of 3 kHz, at distances of 4–20 km (the internal shadow zone), in the Canary Basin of the Atlantic Ocean. The ocean depth was 5000 m. The transmission depths were 150 and 300 m, the reception depths were 10 and 90 m. In the figure, additional gain values are shown relative to the forerunner level, which were applied to the bottom–surface reflections. At all distances, there are isolated signals, which are the first to arrive, and signal quartets of single, double, or triple bottom and bottom–surface reflections. The single arrivals are the diffracted field formed at short distances from the source due to the initial surface reflections of the direct signal. The surface-scattered part of the acoustic energy is captured by the surface sound channel and propagates in it up to long distances. Subsequently, as these components propagate and undergo secondary reflections by the wavy surface (with secondary scattering), they penetrate under the discontinuity layer and constitute the forerunners in the shadow zone. Their amplitudes are strongly decreased and lie much lower than the spherical spread curve. The existence of these components cannot be explained by the classical theory of sound propagation in stratified waveguides and, of course, is not taken into account in the sound field calculations.

With explosion depths of 150 and 300 m and a reception depth of 90 m, the bottom–surface reflections are well resolved in all initial quartets. However, at distances greater than 20–30 km, the resolution of the components in the initial and subsequent quartets fails. With a reception depth of 10 m (even at a frequency of 3 kHz), there is no component resolution in the signal pairs. At the chosen distances and positions of the source and the receiver, the delay times are 5–500 ms, and the relative variations of the amplitudes reach 4–6 dB. The delay time of single reflections is 4 s at a distance of 4 km, with grazing angles of 40°. At a distance of 20 km, the initial quartet is delayed by 1.6 s. The differences in the arrival times are 50 ms within the pairs and 150 ms between the pairs. The grazing angles corresponding to the three quartets are 26°, 45°, and 56°. As the distance increases and becomes closer to the first convergence zone (65–75 km), the grazing angles decrease and tend to zero. At the same time, the delay times and amplitudes in the signal quartets also tend to zero. In such situations, the time resolution of individual components and the solution of any inverse problem are improbable, if feasible at all. Hence, by using the method of single bottom reflections (even with large depths and high frequencies), one fails to approach low grazing angles in determining the bottom reflection coefficient. In subsequent reflections, the conditions of resolving the components in the quartets theoretically become better but, in practice, their resolution is hardly feasible, even with a smooth bottom profile and a calm sea.

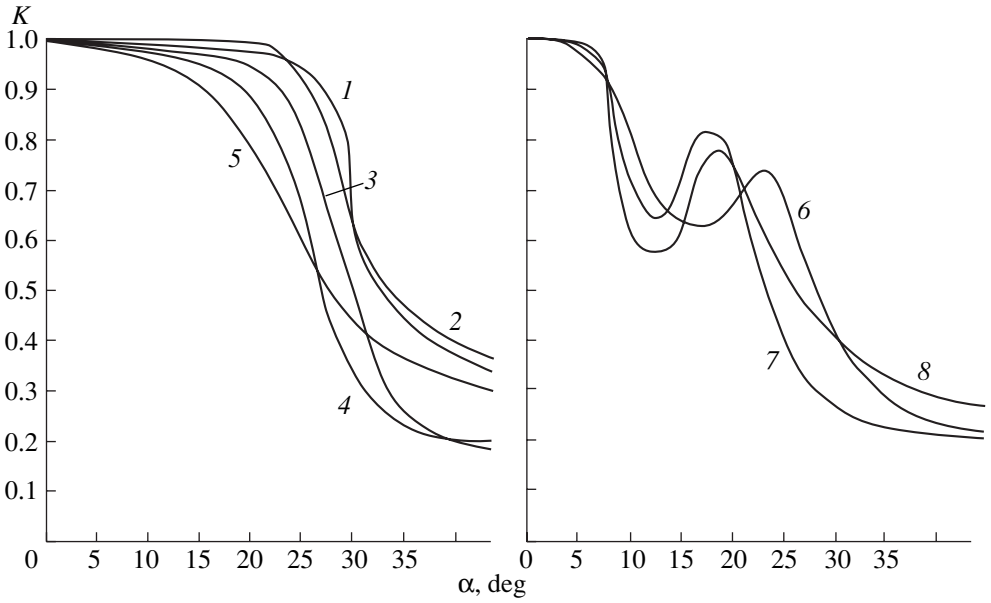

Fig. 5. Frequency-angular dependences of the averaged bottom reflection coefficients for the Black Sea. The dependences are obtained with the method of multiple bottom–surface reflections. Curves *1–8* correspond to the frequencies 10, 15, 25, 32, 40, 64, 100, and 128 Hz, respectively.

The aforementioned examples demonstrate the angular resolution that can be attained with the conventional method of measuring the bottom reflection coefficient by single reflections. When the sea depth is less, the angular resolution of the field components is much worse, and the minimal grazing angles that can be studied increase. In practice, the only way to settle the problem is to use the amplitudes of multiple bottom–surface reflections, which are obtained by averaging the interference oscillations over the frequency of the summed quartets within the filtering band.

The procedure of determining the reflection coefficient consists in that, with the known waveguide parameters (sea depth, sound speed profile, and *a priori* information on the bottom characteristics) and the known relative source and receiver positions, one calculates the time, angular, and power characteristics of the sound field for the interval of grazing angles that is sufficient to identify the field components and to find the frequency-angular dependence of the bottom reflectivity. By comparing the experimental and the calculated component parameters at different points of the path and by determining the number of reflections and the corresponding grazing angles, the signal level is determined (from both experimental and calculated data), to which the levels of all components are to be normalized, and the loss is found for each component in view of the known number of bottom–surface reflections. To exclude additional errors and to obtain the most reliable information on the bottom reflectivity, it is advantageous to perform the experiment at calm sea. If the surface is noticeably wavy, losses in surface reflections at high frequencies can be comparable with losses in bottom reflections, or even higher than those. Upon performing the aforementioned procedures and identifying the components, the reflection coefficient itself is determined from the following relation:

$$K(f, \alpha, n) = [B(R_n/R_0)A]^{1/n},$$

where f is the frequency, α is the grazing angle, n is the number of reflections of the chosen signal, B is the total signal loss in the nth reflection (in view of the normalized signal levels), R_0 is the horizontal distance, R_n is the distance traveled by the signal at a grazing angle α for the nth reflection, and A is the focusing factor for the nth component.

The proposed method allows one to perform the measurements in wide bands of frequencies and grazing angles with a high measurement accuracy.

Figure 5 shows the frequency dependences of the bottom reflection coefficient, which were obtained in the Black Sea at frequencies of 10–128 Hz for the grazing angles from zero to 40°–50°. To obtain these curves, we used records of the signals received at distances of 5 to 180 km. A well-pronounced frequency dependence of the reflection coefficient can be noticed. At low frequencies (up to 30–40 Hz), the reflection coefficient monotonically decreases from unity to 0.20–0.35 at angles of 20°–30°, such behavior being typical of a waterlike half-space with losses (in the absence of shear waves). As the frequency increases, the angles of total internal reflection change from 30°

(which corresponds to a sound speed of 1730 m/s in the sediments) to 8° at frequencies of 60–128 Hz (which corresponds to the 1520-m/s sound speed in the upper bottom layer and the 1505-m/s sound speed in water). At frequencies higher than 60 Hz, a minimum at an angle of 8°–15° occurs in the angular dependence of the reflection coefficient. This minimum can be related to the stratification of the upper sediment layer, such stratification being significant at the frequencies at hand, and to the propagation of shear waves (with velocities of 600–700 m/s) in the consolidated bottom layers, as well as to high losses of longitudinal and shear waves.

Figure 6 serves to compare the data obtained by the proposed method with the reflection coefficient measured by using the conventional method, along with the associated measuring errors. Here, the data of experimenting in the Black Sea are presented for single and double bottom–surface reflections at 5, 10, 32, and 100 Hz. The data agree only at frequencies of 30 Hz and higher. At frequencies of 5–25 Hz, particularly, for grazing angles of 13°–27°, the difference between the two sets of data is substantial. Low values of the reflection coefficient and values that exceed unity are the consequences of inevitable errors and the phenomenon of sound focusing in the water layer and at surface reflections, along with sound refraction in the bulk of sediments. The inaccuracy in the amplitude measurements, which accompany the conventional methods, directly appear in the value of the reflection coefficient. With the method of multiple reflections, such an inaccuracy is much lower or fully eliminated because of the natural averaging of the absolute values of the errors, which, in addition, are normalized to the number of reflections.

Figure 7 shows the angular dependence of the bottom reflection coefficient, which was obtained in the Arabian Sea at frequencies of 100 and 400 Hz for the grazing angles from zero to 20°–25°. The records of the signals received at distances of 300–1000 km were used. Similarly to the Black Sea, a minimum exists at a grazing angle of 5°–15° that is determined by shear waves in the sediments. Judging from the levels of the dips and from the absolute values of the reflection coefficient, the losses of both longitudinal and shear waves are lower in this region. At low frequencies, the velocity of longitudinal waves is 1730 m/s in the Arabian Sea (just as in the Black Sea), the sound speed in water being 1530 m/s. Thus, for these two regions, the difference in the main bottom parameters consists in nothing but the values of losses for longitudinal and shear waves at the frequencies at hand.

The results presented in this paper show how widely different the properties of bottom sediments and, hence, the characteristics of sound fields in different regions of

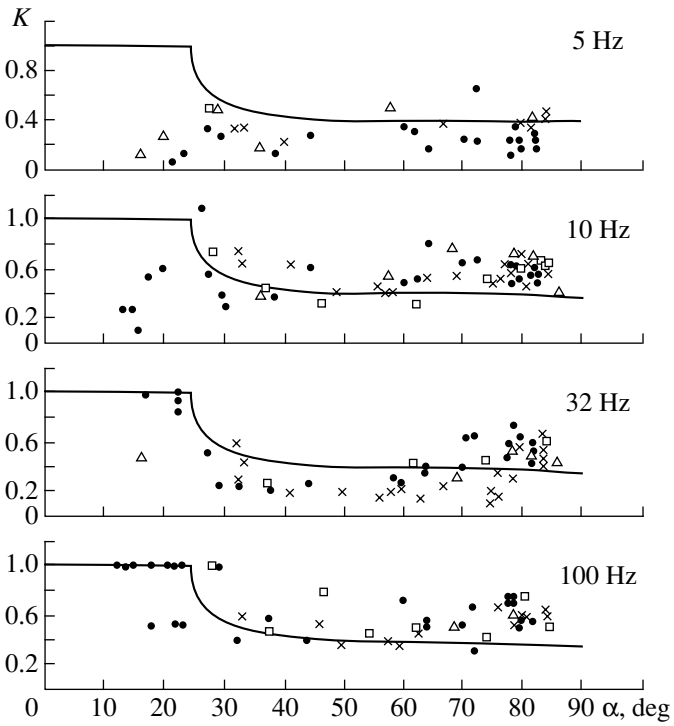

Fig. 6. Angular dependence obtained for the reflection coefficient in the Black Sea from single and double bottom–surface reflections at the grazing angles from 12°–15° to 85°–87°. The frequencies are 5, 10, 32, and 100 Hz. The source depth is 60 m. The solid curve represents the calculated values for a sound speed of 1650 m/s in the bottom. The dots and crosses indicate single and double bottom reflections for the 35-m source depth. The triangles and squares indicate single and double bottom reflections for the 20-m source depth.

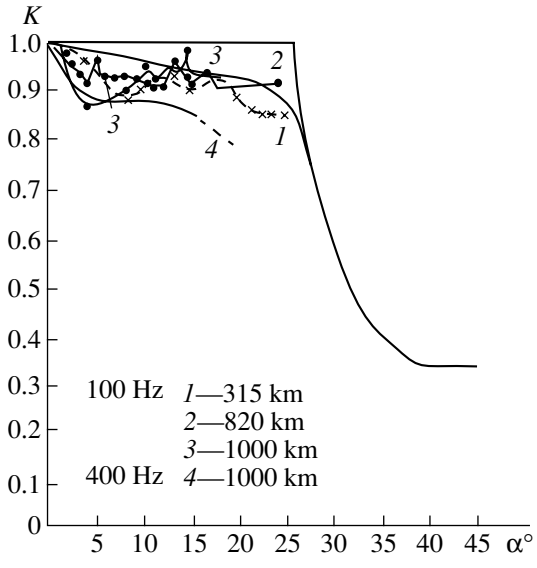

Fig. 7. Angular dependences of the bottom reflection coefficient for the Arabian Sea for frequencies of 100 and 400 Hz. The source and receiver depths are 600 and 300 m, respectively. Curves *1–4* correspond to different distances at which the reflection coefficient was measured.

the World Ocean can be. The aforementioned considerations also demonstrate the importance of choosing and developing the adequate model for the bottom and the entire waveguide to explain the experimental data in a broad frequency band, to predict the sound field characteristics, and to evaluate the performance of various underwater acoustic systems in different ocean regions. In developing the waveguide model, especially in modeling the bottom, one should take into account the bottom stratification, the existence of longitudinal and shear waves with their specific attenuation, the gradients of the sound speed and density in the layers, and, above all, the frequency dependences of the sound speed and attenuation coefficient in the sediments.

ACKNOWLEDGMENTS

This work was supported by the Russian Foundation for Basic Research, project no. 01-02-16636.

REFERENCES

1. L. M. Brekhovskikh, *Waves in Layered Media*, 2nd ed. (Nauka, Moscow, 1973; Academic, New York, 1960).
2. *Acoustics of the Ocean*, Ed. by L. M. Brekhovskikh (Nauka, Moscow, 1974).
3. W. Charles, J. Acoust. Soc. Am. **104**, 1363 (1998).

Translated by E. Kopyl

Acoustical Physics, Vol. 48, No. 4, 2002, pp. 481–485. Translated from Akusticheskiĭ Zhurnal, Vol. 48, No. 4, 2002, pp. 547–551.

A Spherical Acoustic Source in an Ideal Waveguide

B. P. Sharfarets

Kubinskaya ul. 14–17, St. Petersburg, 196128 Russia

e-mail: sharg@mail.rcom.ru

Received June 15, 2001

Abstract—The acoustic field of a spherical source in an ideal waveguide is considered with allowance for the diffraction by the source. The consideration uses the previously obtained results on the diffraction by a spherical source in a halfspace with ideal boundaries. The resultant field is shown to be representable as an infinite sum of the fields of some equivalent sources. The errors that appear when the number of these sources is limited are estimated. The field produced by the sphere in an ideal waveguide is calculated with and without allowance made for the scattering. © *2002 MAIK "Nauka/Interperiodica".*

Scattering by inhomogeneous inclusions in bounded waveguides has been the subject of many publications. Here, we only mention the works cited in the recent paper [1], on the results of which this study is based, and also two other papers [2, 3]: one of them [2] solves the problem of scattering of the field produced by a point source from a transparent layered cylinder (island) in a layered waveguide with ideal boundaries, and the other [3] addresses the sound scattering by a rigid spheroid placed in a layered waveguide under the assumption that the boundaries and inhomogeneities of the medium do not affect the amplitude of the scattered field. The consideration presented below does not use the assumption about the absence of the effect of the boundaries on the scattering amplitude.

An approach to the solution of the problems of the sound diffraction by inhomogeneities located in an ideal halfspace with a plane boundary was considered in the previous publication [1]. Expressions for the amplitude of the field scattered by a perfectly soft sphere in the particular case of a perfectly rigid or soft boundary were obtained within the low-frequency approximation, in particular, when the sphere itself was a source of the primary field. Based on the results obtained in [1], this paper studies the acoustic field produced by such a sphere in an ideal acoustic waveguide with a perfectly soft upper boundary and perfectly rigid lower boundary.

An exact solution to this problem can be obtained by a technique similar to that applied in [1] to the halfspace: it is necessary to sum up all plane waves multiply reflected from the boundaries and scattered from the sphere. However, below, we will obtain a solution in a different way.

As applied to the case when the scattering occurs from the primary source itself, the results obtained in [1] can be interpreted as follows. The sound scattering from the source due to the halfspace boundary is equivalent to the situation with no scattering but with another source whose shape and position coincide with those of the original source and whose field exactly reproduces the scattered field outside the original source. The real source, which creates the primary and scattered fields, is thus replaced by two sources that cause no scattering, but the field they produce outside the original source exactly coincides with the real field. We will characterize these sources by the radiation pattern $D^0(\vartheta, \varphi)$ in free space (the primary source) and by the scattering pattern $D^1(\vartheta, \varphi)$ (the fictitious source of the scattered field). Then, the total field outside the source–scatterer is completely described by an equivalent source with the directional pattern $D(\vartheta, \varphi) = D^0(\vartheta, \varphi) + D^1(\vartheta, \varphi)$. Note that $D^1(\vartheta, \varphi)$ depends not only on frequency, but also on the source depth z_0 and on the conditions at the halfspace boundary.

Let us place the primary source into a homogeneous layer with a perfectly soft upper boundary and perfectly rigid lower boundary. The effect of one boundary, say, of the upper one, is equivalent to that of a source that produces the scattered waves with the pattern $D_0^1(\vartheta, \varphi)$. Similarly, the lower boundary also produces an equivalent source of the scattered waves with the pattern $D_1^1(\vartheta, \varphi)$, which was also obtained in [1]. Here and below, subscripts 0 and 1 indicate that the function D describes the effect of the surface (0) or bottom (1). The field in the waveguide will be described by a resultant source with the pattern $D(\vartheta, \varphi) = D^0(\vartheta, \varphi) + D_0^1(\vartheta, \varphi) + D_1^1(\vartheta, \varphi) = D^0 + D^1$. The process, however, must be iterated. The sources with the patterns D_0^1 and D_1^1 should be considered themselves as primary sources, whose fields will also be scattered from the original

1063-7710/02/4804-0481$22.00 © 2002 MAIK "Nauka/Interperiodica"

(real) source. The source D_0^1 will induce the sources D_{00}^2 and D_{01}^2, while D_1^1 will create sources D_{10}^2 and D_{11}^2. The superscript (in this case, 2) is the number of times the boundaries participate in forming a particular scattering pattern. In turn, D_{00}^2, D_{01}^2, D_{10}^2, and D_{11}^2 will create the sources D_{000}^3 and D_{001}^3, D_{010}^3 and D_{011}^3, D_{100}^3 and D_{101}^3, and D_{110}^3 and D_{111}^3, and so on, the number of sources increasing at each iteration. The pattern of the resultant source will thus be represented by the series (the arguments are omitted)

$$\begin{aligned} D &= D^0 + D_0^1 + D_1^1 + D_{00}^2 + D_{01}^2 + D_{10}^2 + D_{11}^2 \\ &+ D_{000}^3 + D_{001}^3 + D_{010}^3 + D_{011}^3 + D_{100}^3 + D_{101}^3 \\ &+ D_{110}^3 + D_{111}^3 + \ldots = D^0 + D^1 + D^2 + D^3 + \ldots. \end{aligned} \tag{1}$$

As follows from physical considerations, this series must converge. It is only left to determine its convergence rate in each particular case, after which it can be represented as a sum of a finite number of terms. Subsequently, the field in the waveguide can be evaluated with allowance for the scattering by the technique described in [4, 5] with the function $D(\vartheta, \varphi)$ of Eq. (1) as the source pattern. In view of the axial symmetry of the problem, the field produced by the directional source in the ideal waveguide under study can be represented as [4, 5]

$$\begin{aligned} u(r, z) &\approx \frac{1}{H}\sqrt{\frac{2\pi}{r}} \\ &\times \sum_{n=1}^{\infty} \frac{D_1(\vartheta_n)e^{j\frac{2n-1}{2H}\pi z_0} - D_2(\vartheta_n)e^{-j\frac{2n-1}{2H}\pi z_0}}{\xi_n^{1/2}} \\ &\times \sin\left(\frac{2n-1}{2H}\pi z\right)e^{j\left(\xi_n r - \frac{\pi}{4}\right)}. \end{aligned} \tag{2}$$

Here, H is the depth of the waveguide; ξ_n are the eigenvalues of the transverse boundary-value problem; $\theta_n = \arctan\left(\xi_n/\frac{2n-1}{2H}\pi\right)$ are the characteristic incidence angles of the normal waves; and $D_1(\theta) = D(\pi - \theta)$ and $D_2(\theta) = D(\theta)$, $\theta \in [0, \pi/2 - j\infty)$, where $D(\theta)$ is given by Eq. (1). Note that the domain of the function $D(\theta)$ is $\theta \in [0, \pi/2 - j\infty)$ and $\theta \in (\pi/2 + j\infty, \pi]$, where z and z_0 are the depths of the receiver and transmitter respectively [2].

Thus, let a spherical source of radius R_0 with the radiation pattern $D^0 \equiv 1$ be placed at a depth of z_0 in an ideal waveguide of height H. Then, according to [1], we have

$$D_0^1(\theta) = \begin{cases} -c_1 - c_2\cos(\pi - \theta) \\ -c_1 + c_2\cos(\theta) \end{cases} \quad \theta \in [0, \pi/2 - j\infty) \tag{3}$$
(effect of the surface),

$$D_1^1(\theta) = \begin{cases} a_1 - a_2\cos(\pi - \theta) \\ a_1 + a_2\cos(\theta) \end{cases} \quad \theta \in [0, \pi/2 - j\infty) \tag{4}$$
(effect of the bottom).

Here, the constants are defined as

$$a_1 = \frac{\frac{2\pi kA}{\alpha}e^{\alpha} + \frac{(2\pi k)^2}{\alpha^4}ABe^{2\alpha}}{1 - \frac{2\pi k}{\alpha}Ae^{\alpha} + \frac{2\pi kB}{\alpha^3}e^{\alpha}(\alpha^2 - 2\alpha + 2) - \frac{(2\pi k)^2}{\alpha^4}ABe^{2\alpha}}, \tag{5}$$

$$a_2 = \frac{\frac{2\pi k}{\alpha^2}Be^{\alpha}(1 - \alpha)}{1 - \frac{2\pi k}{\alpha}Ae^{\alpha} + \frac{2\pi kB}{\alpha^3}e^{\alpha}(\alpha^2 - 2\alpha + 2) - \frac{(2\pi k)^2}{\alpha^4}ABe^{2\alpha}}, \tag{6}$$

where $\alpha = j2k(H - z_0)$, and

$$c_1 = \frac{\frac{2\pi kA}{\alpha}e^{\alpha} - \frac{(2\pi k)^2}{\alpha^4}ABe^{2\alpha}}{1 + \frac{2\pi k}{\alpha}Ae^{\alpha} - \frac{2\pi kB}{\alpha^3}e^{\alpha}(\alpha^2 - 2\alpha + 2) - \frac{(2\pi k)^2}{\alpha^4}ABe^{2\alpha}}, \tag{7}$$

$$c_2 = \frac{\frac{2\pi k}{\alpha^2}Be^{\alpha}(1 - \alpha)}{1 + \frac{2\pi k}{\alpha}Ae^{\alpha} - \frac{2\pi kB}{\alpha^3}e^{\alpha}(\alpha^2 - 2\alpha + 2) - \frac{(2\pi k)^2}{\alpha^4}ABe^{2\alpha}}, \tag{8}$$

and $\alpha = j2kz_0$. The constants A and B are determined by properties of the sphere as a scatterer. Then, the total pattern $D_0^1 + D_1^1$ has the form

$$\begin{aligned} D^1(\theta) &= D_0^1(\theta) + D_1^1(\theta) \\ &= \begin{cases} (a_1 - c_1) - (a_2 + c_2)\cos(\pi - \theta) \\ (a_1 - c_1) + (a_2 + c_2)\cos\theta \end{cases} \quad \theta \in [0, \pi/2 - j\infty). \end{aligned} \tag{9}$$

As follows from Eq. (9), the pattern D^1 of the secondary-wave source is the sum of a constant and a cosine term with the amplitude $a_2 + c_2$. To find the

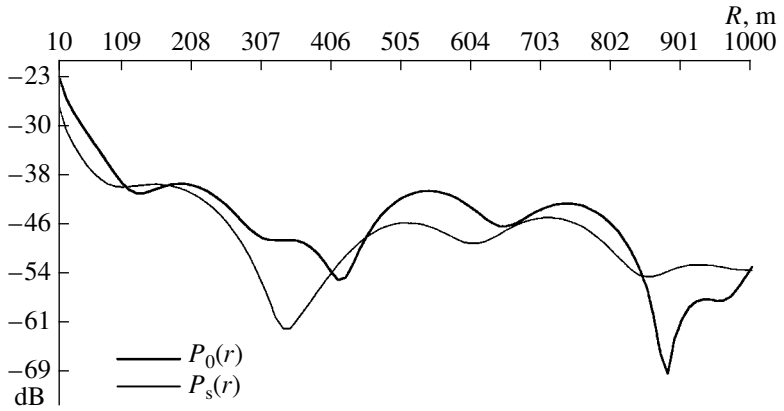

Fig. 1. Dependences $P_0(r)$ and $P_s(r)$ for F = 25 Hz and R_0 = 8 m.

source pattern $D^2 = D_{00}^2 + D_0^2 + D_{10}^2 + D_{11}^2$, it is necessary to substitute the components of Eq. (9) for unity on the right-hand side of integral equation (26) of the cited paper [1]. For example, to find D_{00}^2, it is necessary to substitute $-c_1 - c_2\cos(\theta)$ on the right-hand side of this equation. The pattern D_{00}^2 will have the same structure $D_{00}^2 = -c_1' - c_2'\cos(\theta)$, the order of smallness of these constants however becoming higher: $c_i' = O(|c_i|^2)$. The situation with the remaining components of D^2 is similar. Note that the analysis of the decay of coefficients in Eqs. (5)–(8) with increasing distance from the reflecting boundary shows that their asymptotic behavior is the same. The structure of the component patterns of D^3 is the same: a sum of a constant and a product of another constant by the function $\cos(\theta)$; however, the order of smallness of these constants becomes higher by one, and so on. For example, the order of smallness of the coefficients of the component patterns of D^n is equal to n with respect to the initial coefficients a_i and c_i, i = 1, 2. Thus, series (1) is majorized by the series $D = 1 + q + q^2 + q^3 + \ldots$, where $q = 4|\max(a_i, c_i)|$ and a_i and c_i are the same as in Eq. (9). Hence, if series (1) is truncated to a finite sum $D \approx D^0 + D^1$, where $D^0 = 1$ and D^1 is given by Eq. (9), the error will be strictly less than $\varepsilon = q^2/(1 - q)$. Then, if q is known and its value is admissible, series (1) can be truncated to the finite sum $D \approx D^0 + D^1$.

To analyze q, we calculated coefficients (5)–(8) as functions of frequency, radius of the sphere, and distance between the boundary and the center of the sphere (from Eqs. (5) and (6) for the rigid boundary and from Eqs. (7) and (8) for the soft boundary). The results for which $q \le 0.4$ (i.e., the coefficients a_i and c_i in Eq. (9) are equal to or less than 0.1) are summarized in the table.

The table gives the distances between the boundary and the center of the sphere; beyond them, all coefficients a_i and c_i are equal to or less than 0.1. The error in calculating the pattern as $D \approx D^0 + D^1$ will not exceed 26.6%.

We developed a program that calculates the acoustic pressure as a function of the horizontal distance, $P_S(r)$, from Eq. (2). Figures 1–6 show $P_S(r)$ calculated from Eq. (2) with $D_1(\theta) = 1 + (a_1 - c_1) - (a_2 + c_2)\cos\theta$ and $D_2(\theta) = 1 + (a_1 - c_1) + (a_2 + c_2)\cos\theta$ for various frequencies F and sphere radii R_0. For the sake of comparison, these figures also show the function $P_0(r)$ that corresponds to no scattering from the source, i.e., to the case $D_1(\theta) = D_2(\theta) = 1$ [note that, in this case, the error in calculating the pattern as $D \approx D^0$ is $\varepsilon = q/(1 - q)$]. All plots are calculated for H = 100 m, z = 45 m, and z_0 = 50 m. By comparing the functions plotted in each of these figures, one can estimate the degree of the field disturbance due to the scattering. The plots show that the disturbance is usually smaller than expected, because the quantity q is overestimated.

The technique proposed above can be used to obtain formulas describing different scatterers and waveguides.

It should also be noted that, when obtaining the above results, it was significant that Eq. (2) could be

Table

R_0, m \ F, Hz	10	25	50	75	100
10	250	285	750	1000	2000
5	120	125	130	300	400
4	90	100	110	180	300
2.5	60	70	75	100	105
2	45	60	63	80	82
1	28	30	32	48	51

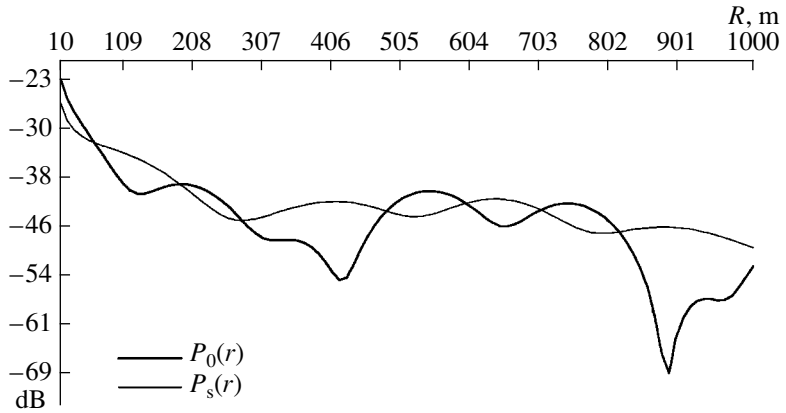

Fig. 2. Dependences $P_0(r)$ and $P_s(r)$ for F = 25 Hz and R_0 = 10 m.

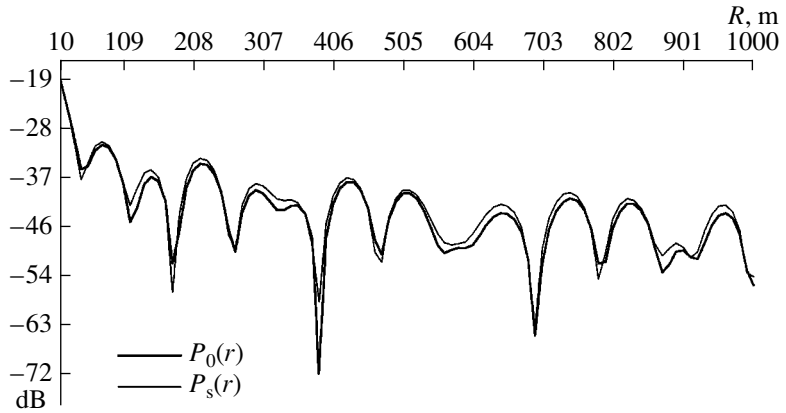

Fig. 3. Dependences $P_0(r)$ and $P_s(r)$ for F = 50 Hz and R_0 = 4 m.

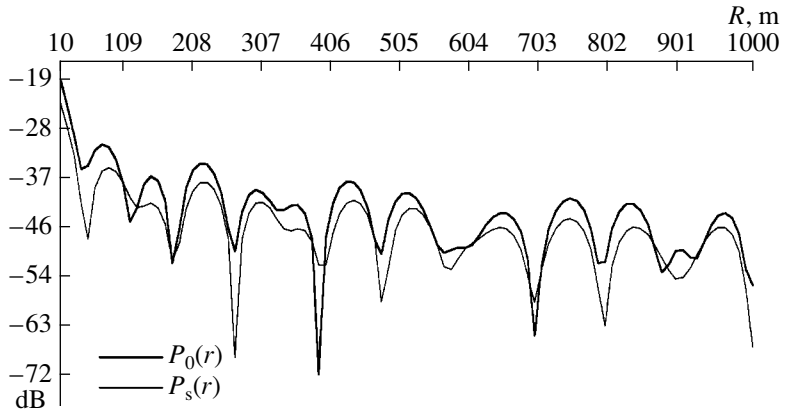

Fig. 4. Dependences $P_0(r)$ and $P_s(r)$ for F = 50 Hz and R_0 = 8 m.

used to calculate the field produced by a source whose pattern could be represented by Eq. (9) for angles θ both greater and smaller than $\pi/2$. For example, expressions for the field of an extended source, which were obtained in [6] by the Green function method, would be inapplicable in this case.

The results obtained above for a source that is a scatterer itself can easily be extended to a passive scatterer

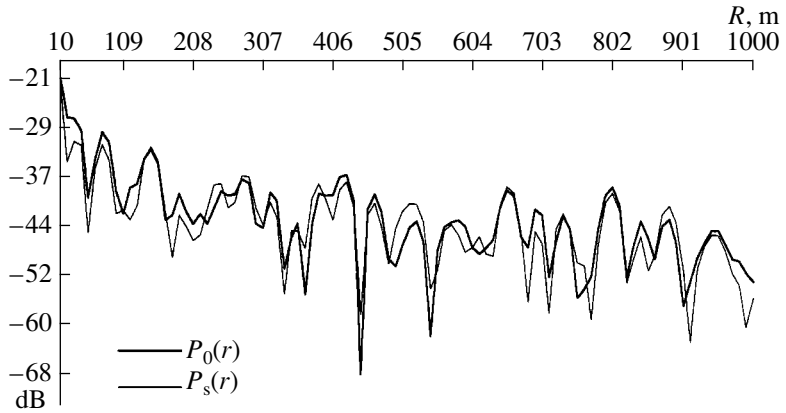

Fig. 5. Dependences $P_0(r)$ and $P_s(r)$ for F = 80 Hz and R_0 = 4 m.

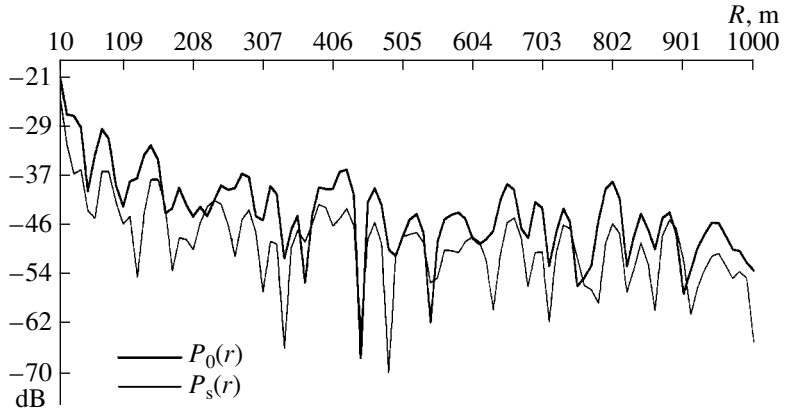

Fig. 6. Dependences $P_0(r)$ and $P_s(r)$ for F = 80 Hz and R_0 = 6 m.

that does not produce the primary field. The calculations in this case are even simpler.

REFERENCES

1. A. V. Zatserkovnyĭ, V. A. Sergeev, and B. P. Sharfarets, Akust. Zh. **47**, 650 (2001) [Acoust. Phys. **47**, 565 (2001)].
2. G. Athanassoulis and A. Prospathopoulos, J. Acoust. Soc. Am. **107**, 2406 (2000).
3. V. A. Grigor'ev, B. G. Katsnel'son, V. M. Kuz'kin, and V. G. Petnikov, Akust. Zh. **47**, 44 (2001) [Acoust. Phys. **47**, 35 (2001)].
4. B. P. Sharfarets, Akust. Zh. **31**, 119 (1985) [Sov. Phys. Acoust. **31**, 68 (1985)].
5. B. P. Sharfarets, Akust. Zh. **35**, 132 (1989) [Sov. Phys. Acoust. **35**, 79 (1989)].
6. B. P. Sharfarets, Akust. Zh. **37**, 794 (1991) [Sov. Phys. Acoust. **37**, 414 (1991)].

Translated by A. Khzmalyan

Acoustical Physics, Vol. 48, No. 4, 2002, pp. 486–493. Translated from Akusticheskiĭ Zhurnal, Vol. 48, No. 4, 2002, pp. 552–559.

CONFERENCES AND MEETINGS

XI Session of the Russian Acoustical Society

The XI Session of the Russian Acoustical Society was held in Moscow on November 19–23, 2001. The scope of the session covered a wide range of problems of modern acoustics, and the participants of the session included acousticians from almost all regions of Russia. Considerable interest was aroused among the participants by the section "Speech Acoustics and Acoustic Problems of Applied Linguistics." The editorial board of *Acoustical Physics* decided to publish part of the papers presented at this section and devoted to the most topical problems of this promising field of research. This issue contains three such papers, and other papers concerned with this subject will appear in the following issues. They were not additionally refereed before publishing.

Linguistic Knowledge and New Technologies[1]

R. K. Potapova

Moscow State Linguistic University, ul. Ostozhenka 38, Moscow, 119992 Russia
e-mail: potapova@linguanet.ru

Abstract—Modern language studies are characterized by a variety of forms, ways, and methods of their development. In this connection, it is necessary to specify the problem of the development of their internal differentiation and classification, which lead to the formation of specific areas knowledge. An example of such an area is speechology—a field of science belonging to fundamental, theoretical, and applied linguistics. © *2002 MAIK "Nauka/Interperiodica".*

Intensification of the integration processes in science characterizes one of the central features of the modern scientific progress. Hence, the problem of the synthesis of scientific knowledge and an interdisciplinary interaction of sciences becomes of primary importance. The rise and development of speechology on the basis of phonetics, phonology, physiology, psychology, electronics, communication engineering, new information technologies, etc., represents an example of an interdisciplinarity exchange of scientific achievements and an interconnected development of many scientific directions.

Speechology, as the special area of linguistic knowledge, has come into being fairly recently. An essential contribution to the successful development of the above-stated interdisciplinary field of knowledge was made by various research groups working both in our country and abroad.

Speechologists participate in solving problems that are of direct economic and defensive importance [1]. The following problems are being developed by experts in this field of knowledge: automatic recognition and understanding of speech; artificial intelligence; effective dialogue in natural man–computer language; automatic control systems; analysis and synthesis of speech; variance of human speech in the act of communication; paralinguistic characteristics of speech; methods of determining the quality of communication channels for connected speech; methods of automatic quality control and transfer of speech through communication channels; perception of acoustic and phonetic features of speech elements in the presence of noise and distortion in communication channels; interlanguage interference regarding sound and intonation structure; cybernetic systems of speech dialogue; hardware–software means for objectification of control in the process of computer-assisted second language learning and the detection of foreign language simulation; interaction of verbal and nonverbal components in the act of communication; functional and system-typological research of languages in Russia, the Commonwealth of Independent States of the former USSR (CIS), and other countries; information retrieval systems; speaker identification and verification of speaker systems and the emotional status of speaker systems.

For the solution of the aforementioned problems, it is necessary to use linguistic knowledge carrying the necessary information on the object and environment under investigation with reference to various aspects of

[1] This paper was submitted by the author in English.

1063-7710/02/4804-0486$22.00

science, industry, defense, protection of intellectual and other property, security, etc.

In this connection, special importance is assumed by applied linguistics engaged in the development of computer systems functioning on the basis of natural language: systems of automatic recognition and understanding of speech (both written and oral), natural language interface systems, systems simulating natural abilities of humans, linguistic components of expert systems, lingware of information retrieval systems, automated translation systems, automated lexicographic systems, etc. [2, 3].

Man–machine communication by means of speech is economical, effective, and convenient. Modern systems of speech recognition (including those for military purposes) contain various language levels, each of them carrying its functional load: acoustic, parametric, lexical, syntactic, semantic, and pragmatic levels. The purpose of modern systems of speech recognition is to use the maximal amount of nonacoustic information, especially information of higher (semantic and pragmatic) levels.

Speech recognition based on the analysis of an acoustic signal requires a detailed acoustic characteristic of the signal. The identification of specific words requires the allocation of additional phonetic subclasses inside the generalized classes, so that, in the end, the hierarchy of phonetic classes has the form of a binary tree of decisions. The procedure of constructing an optimal tree of decisions made on the basis of a generalized classification is proposed.

At the first stage, the terminal chains, i.e., the minimal phonetic classes necessary for the identification of all words of the dictionary, are constructed. In choosing the terminal chains, the following criteria are used: a set of phonetic oppositions must correspond to the simplest acoustic means; the result should be the minimal number of phonetic oppositions.

At the second stage of the decision tree formation, the integration of the two low-level classes (beginning from the terminal classes) into one higher level class is performed, and so on, up to the level of the generalized classes.

The enhancement of the degree of speech recognition is achieved by two methods based on the following procedures: (a) the development of a more perfect phonetic system consisting of contextual variants of phonemes and probable contexts obtained as a result of relevant classification and (b) the adaptation in relation to the phonetic models of training, which uses maximal general information.

The method using the contextual acoustic variants of phonemes is based on the correction of the speech realization of phonemes depending on the subsequent vowel (or consonant), while the method of training by means of maximal general information uses the language model of parts of speech and a multilevel strategy of decoding. The application of each of these methods separately raises the efficiency of recognition in comparison with the existing methods, and the combination of the two offered methods is characterized by maximal efficiency.

Speech recognition using the dynamic transformation of phonemic patterns, which takes into account the acoustic (phonetic) environment, is based on a method developed with the use of the data on the variability of acoustic realizations caused by the sound co-articulation effect in speech flow. The method is intended for recognition systems with a large dictionary and with the use of phonemic patterns. The main principle underlying the construction of this system is the dynamic transformation of phonemic patterns depending on the acoustic–phonetic context of the coarticulating parameters.

In the development of automatic speech recognition systems, the use of models based on Markov chains is productive. The given model includes four basic components: the extraction and the analysis of differential features, acoustic–phonetic decoding, lexical analysis, and syntactic analysis.

There are methods of recognition based on key words. At each stage, the list of key words is defined. Each word is represented by means of phonetic transcription, which is either given directly or can be received from grapheme transcription with the help of a grapheme–phoneme transcriptor used in the process of text–speech synthesis (TTS). The system correlates each word in the list with part of a phonemic matrix, and if the number of correlations is high enough, the word is recognized. The task at the pragmatic level is the recognition of one or several key words at each stage of the dialogue.

There are a number of efficient dialogue systems [4]. For example, the KEAL dialogue system is intended for performing specific tasks (such as information inquiry, order, or input). The mode of the dialogue is defined by a user question. Each functional cycle of the system includes the input and reception of an oral message, the formation of an answer, the performance of actions determined by the answer, and the transition to the following cycle.

The traditional version of this system consists of the following modules: a phonetic analyzer, a phonetic word detector, an acoustic word detector, a syntactic analyzer, an interpreter of the analysis, a prosodic segmentation program, a phonetic–spelling transcription program, a speech generator, and a dialogue device.

The phonetic analyzer allows one to change from a real speech signal to its phonetic representation. Each segment extracted by the phonetic analyzer corresponds to a set of ordered answers arranged in the order of their decreasing probability. The set of answers is

called the phonetic spectrum of a phrase. The phonetic analysis is carried out step by step: at the first stage, the coding of a sound signal in digital form is performed by a vocoder. At the second stage, the segmentation of the digital signal is performed, and at the last stage, phonemes are identified. The central part of the system is the dialogue device, which performs two functions: first, it determines what types of phrases have the greatest probability of being pronounced by the operator according to the dialogue context and, second, it decides what kind of communication the dialogue will compose (information inquiry, answer to a question, etc.).

There also exists a multipurpose system of speech recognition. This system can be easily adapted without substantial modification to a variety of applications in the field of man–computer dialogue. The transfer of information in the given system can be divided into levels as follows: (1) during the dialogue, a small database allows one to carry out communications between models at the highest level; (2) the common analytical base has a set of language constants which are used in the recognition process. The prosodic analyzer, whose functioning is based on the assumption about the significant modifications of the fundamental frequency, is of special interest.

The systems most advanced and best suited to the modern requirements on the automated recognition systems are the DRAGON systems. For example, the DRAGON DICTATE system recognizes discrete speech utterances separated from each other by a pause. In a dialogue with the DRAGON DICTATE, an inexperienced user pronounces 15 words per minute and an experienced user, up to 60 words. The TANGORA system (IBM) can be ascribed to the class of similar systems with a speech input. This system recognizes a dictionary of 20000 words and word collocations pronounced separately. The advantage of the given system is speaker-independent recognition. The user adaptation is realized within 20 min. The VIA VOICE system (IBM) is a recent achievement [12]. The VIA VOICE has the ability to learn 64000 to 260000 words and fits any user. The technological development of the majority of modern systems of speech synthesis is based on one of three approaches:

(1) the synthesis consists in the reproduction of a preliminarily coded speech wave;

(2) the voice tract is modeled, and this model is controlled via parameters whose values are obtained on the basis of the analysis of the input text;

(3) the linear predictive coding (LPC) method is used, in which the control is performed by the preliminarily obtained parameters that are not "evaluated" from the input text and are segmented from the speech wave.

The charges on synthesizer development depend on the method used. In the case of a preliminarily coded speech signal, each new utterance should be coded and sent to the memory of the device. Hence, the cost of synthesis directly depends on the cost of the page stored in the memory device and the length of the text.

The cost of the synthesis based on the LPC method depends on the same parameters, but, since in this case the model is controlled and the speech does not directly depend on the input text in each specific case, the cost of memory is lower (up to two orders of magnitude). The cost of the synthesis based on the control of certain acoustic (or articulatory) parameters of speech practically does not depend on the length of the text and the cost of memory.

The basic part of the charges falls onto those modules of the program which concern the rules and deviations from the rules of spelling, the phonology, and the phonetics of the language of the input text. For each specific language, these modules should be created anew.

The classical base of acoustic parameters is represented by the data received from the formant speech analysis, including the information concerning the formant frequencies, the frequency and amplitude of the pulse voice generator, and the amplitude and frequency of the noise generator. The complexity of the task can not be simplified so as to use only the phonetic alphabet (e.g., cannot be reduced to establishing a conformity between spelling and phonetic transcription). It is necessary to note that the existing alphabets are of insufficiently high qualitaty to provide a satisfactory synthesis. Therefore, the development of additional criteria is necessary in creating the rules for the letter–sound transformation.

The development of software for the microprocessor controlling the synthesizer represents a three-step process.

First, it is necessary to receive the description of the pronunciation (segmental and suprasegmental information) of the language under consideration.

Second, this description should be formulated as a set of rules.

Third, these rules should be maximally economical.

The analysis of a speech signal on the basis of a linear prediction consists of the decomposition of its spectrum into two components: the smoothed spectrum represented as the model of a spectrum whose characteristic contains only poles, and the spectrum of the function of excitation containing the information on the prediction error. In an ideal case, the order of the filter should be chosen so that the signal of the prediction error represents an uncorrelated sequence in the case of nonvocalized sounds or a sequence of pulses following at regular intervals with the period of the fundamental tone for vocalized sounds.

In some applications of a linear prediction, where a detailed behavior of the spectrum of both vocalized and

nonvocalized sounds is of interest (in particular, in the synthesis of speech), it is necessary to examine a range of frequencies from 0 up to 10 kHz. To guarantee a high degree of coordination of the smoothed spectrum, it is necessary to choose a sampling frequency no lower than 20 kHz and then to use an inverse filter whose order is no less than 20.

Since, in practice, the exact spectral representation of nonvocalized sounds does not require the large number of factors necessary for vocalized speech, it is expedient to analyze separately the low-frequency and high-frequency ranges with a smaller quantity of factors allowing, nevertheless, an exact description of the spectrum.

To obtain good results with the help of a linear prediction, it is important to take into account the analyzed ratios and their dependence on the choice of the method, the sampling frequency, the order of the model, the type of the temporary window, and the preemphasis of a signal.

The existing difference between natural and synthesized speech obtained on the basis of the linear prediction methods is partially determined by the limitations of the model having only poles, which is most essential for nasal sounds. Therefore, it is expedient to use the polar model of a linear prediction including zeros into it. In using the LPC method, all selected spectral parameters of a speech signal are included in the values of the coefficients evaluated automatically during the analysis of speech. The advantages of using the LPC method in the synthesis of speech are mainly related to a more accessible and completely automated procedure of analysis and, also, a less complex structure in comparison with other methods.

The application of the LPC-method with the inclusion of formant parameters allows one to obtain better (more naturally sounding) synthesized speech. The application of the special program of coding the linguistic units and characteristics on the basis of TMS in combination with the LPC method allows one to generate a better speech.

Characterizing the role of linguistics in the development of expert systems (ES), it is necessary to emphasize that the basis of an expert system is formed by the extensive stock of knowledge about a specific area. Such an approach to designing systems on the basis of the use of knowledge represents a revolutionary change with consequences of a revolutionary nature, because the traditional formula DATA + ALGORITHM $\longrightarrow$ PROGRAM is replaced with a new architecture relying on the knowledge base and a "logical-conclusion machine," so that we now have KNOWLEDGE + CONCLUSION $\longrightarrow$ SYSTEM.

If, for first-generation ESs, it was important to obtain plausible reasoning; today, the problem of the self-training of expert systems is urgent. Any ES should contain a knowledge base, a logical-conclusion machine, a linguistics processor, and an explanation interface. The knowledge base contains the facts, statements, and rules. The facts represent the short-term information: they can change, e.g., during a discourse. The rules represent more long-term information, i.e., how to derive new facts or hypotheses from the known ones. The knowledge base has a wide array of creative possibilities, as it actively tries to fill in the missing information.

The linguistics processor performs the dialogue interaction with the user (expert) in the language natural to him (natural language, professional language, diagram language, tactile influence, etc.).

The purpose of the interaction component is as follows:

(a) to organize the user–expert system dialogue, i.e., to distribute the functions of the dialogue participants during the cooperative performance of the task;

(b) to carry out the processing of a separate message in view of the current condition of the dialogue, i.e., to carry out the transformation of the message from the natural language form to the form of internal representation or inverse transformation.

The importance of explanations in the ES is caused by a number of factors. First, one can hardly expect that users will know all of the opportunities and understand all of the actions of the ES. Second, the importance is caused by the fact that the ESs are intended for use in illegibly formalized areas, i.e., for tasks having no algorithmic solutions. Under the conditions of the absence of a theory that could guarantee the accuracy of the results, it is necessary to develop the means for giving the users the opportunity to test the reliability of the methods and the knowledge used by the ES for decision making.

According to the general ES circuit, the following knowledge is required for its proper functioning:

(1) the knowledge of the solution process for a given task, i.e., the managing knowledge used by the interpreter;

(2) the knowledge of the language of the dialogue and the method of organization of the dialogue that are used by the linguistics processor;

(3) the knowledge of the method of representation and updating of the knowledge used by the knowledge acquisition component;

(4) the supporting structural and managing knowledge used by the explanatory component.

The dependence of the knowledge structure on the requirements of the user is represented as follows:

—What kind of task with what kind of data does the user want to perform?

—What are the preferred ways and methods of task performance?

—What restrictions on the number of results and methods for their acquisition should be imposed to achieve the desired results?

—What language should be used and how should the dialogue be organized?

—What degree of generality/specification of knowledge about the problem area is accessible to the user?

—What are the purposes of the user?

The whole variety of models of the knowledge representation can be divided into two types: logical and heuristic. The basis of the logical models of knowledge representation is the concept of a formal system. Examples of formal theories can be the calculations of predicates and any specific system of productions. The use of calculating predicates has become especially intensive after the creation of powerful search procedures for a conclusion: the method of resolutions and the inverse method. These methods were enriched by heuristic procedures, which have considerably increased the efficiency of acquiring a conclusion. The methods listed above are systems of a deductive type, i.e., they use the model of obtaining a conclusion from the given system of premises by means of a fixed set of output rules.

The further development of predicate systems are systems of an inductive type in which the output rules are derived by the system on the basis of the processing of a finite number of training examples.

In logical models of knowledge representation, the relations existing between several units of knowledge are expressed only by the means that are represented by syntactic rules of the formal system used. Unlike formal models, heuristic models have various means for transmitting specific features of one or another problem area. For this reason, heuristic models surpass the logical in both adequate representation of the problem area and the efficiency of the output rules in use. In ESs, it is possible to ascribe the network, frame, and productive models to heuristic models.

To illustrate the use of linguistic knowledge for applied purposes, we present some examples of ESs.

(1) **Airline information service systems.** The voice inquiry in these automatic systems concerns the reservation of tickets and flight schedules. The input language of the system is spoken English, but it is limited by the given topic. The output speech includes mainly words of the input language.

(2) **Electronic cash devices with spoken language input commands for calculations.** The input language is determined by the type of operations. The system is supplied with a visual feedback.

(3) **Air traffic control.** The input language is completely defined by a technical sublanguage; however, the deviations in pronunciation while under a high level of stress are taken into account. This task is extremely important but also extremely complicated, because it is necessary to work in real time in the presence of noise with a high reliability (no lower than the reliability of a human controller).

(4) **Check of rocket readiness.** The user enters the information into the computer about the condition of different rocket units and answers the questions of the machine analyzing this information. In comparison with other systems, in this system, man and machine seem to interchange roles. A semantically limited language and a specially trained speaker are used.

(5) **Medical information (e.g., illness data) dictating system.** The system does not include diagnosing but is connected with it. The input language is connected speech, but it mainly consists of short phrases containing compressed information about the illness.

(6) **Voice input of information of artificial intelligence—modeling of human behavior in an unfamiliar environment, taking decisions, etc.** The input language is colloquial English (preferably, brief simple sentences). A wide semantic model is used. The speech output is absent. The requirements of a real time scale are eliminated.

(7) **Inventory task.** The user, moving in a room, says the names of the objects he finds. The speech input provides hands-free operation in order to move the objects and to make necessary measurements. For higher reliability, the items of information on the arrangement of objects are included in the system.

(8) **Control of robot behavior by oral commands.** Speech control is especially attractive when man and robot perform joint tasks.

The BBN company is engaged in developing the system of speech understanding, SPEECHLIS. The language of the LUNAR information-retrieval system (which enabled one to analyze samples of lunar rock obtained from the space flight of Appolo-11) is used as the language of this system. The LUNAR system answers questions such as “What is the average concentration of rubidium in high-alkali samples?” Or perceives commands such as “Print the list of the potassium/rubidium ratios for the samples of rock containing no silicon.” The first dictionary structure of the LUNAR system contained about 3500 words, and the grammar of the language was a subset of general English grammar.

Let us discuss one more example of a system of speech understanding, which, at the beginning, was developed by the SPC company (Santa-Monica, California) and, at the final stage, by Stanford Research Institute. The basic difference of the Voice Controlled Data Management System (VCDMS) from other systems, such as SPEECHLIS, HWIM, and HEARSAY-II, consists in that it is based on the syntax of spontaneous English dialogue, which allows one to use very short elliptical constructions in the dialogue with this system. VCDMS used the problem-oriented language of access to information retrieval system of the data about the

underwater fleet of the USA, Great Britain, and the USSR. The main volume of the dictionary included 450 words. The system was able to remember the information on the earlier pronounced phrases and to decode the current phrases on the basis of the results of recognition of the previous utterances. In VCDMS, in the interpretation of sentences, the artificial intelligence ideology is used most intensively.

The general VCDMS structure includes three basic components: (1) the acoustic–phonetic processor, which provides the formation of a data array containing the information on the phonetic structure of the utterance; (2) the procedure of lexical comparison, which makes comparisons of the predicted words on the basis of the syllabic level by using the acoustic–phonological rules; and (3) the linguistic processor, which contains the grammar analysis (parsing) unit and the dialogue level control unit (discourse level controller) including the model of the user and the semantic memory. The speech signal was limited to a frequency of 9 kHz and was supplied to the 12-digit A/D converter, where it was quantized with a frequency of 20 kHz. Then, the digitized speech was passed through the D/A converter, and the resulting analog speech was transmitted through three bandpass filters with the passbands 150–900, 990–2200, and 2000–5000 Hz. At intervals of 10 ms, two parameters were taken from the filters: the maximal amplitude and the number of zero cross values. The resulting six parameters were used for primary acoustic marking of every 10-ms segment. The system takes into account that various contextual words predicted by the thematic memory "grow old" from sentence to sentence, and the probability of their usage decreases. If the probability of the predicted word decreases below a predetermined threshold, this word drops out of consideration for some time. In VCDMS, all these operations are performed by the dialogue unit (Discourse), which is the most original part of the system. The procedures that realize the Discourse are based on the *study of the dialogue between people jointly carrying out some work*. The influence of the context on the character of the dialogue is found and formalized, and two kinds of contextual influence are considered. The global context provides one kind of restrictions in the interpretation of the utterance. These restrictions are used in the identification of the group of a noun. The second kind of restrictions is related to the current context of the adjacent utterances. They are used in the interpretation of reduced and elliptical expressions and, in particular, add additional fragments to a reduced utterance.

At the moment, the main work on constructing large systems capable of recognizing speech is concentrated at IBM, Sperry Univac, and some other companies. This research acquires a more and more applied character. At Bell Laboratories, the development of systems for the recognition of both isolated sentences and connected speech is in progress, while IBM and Sperry Univac work mainly with connected speech. As a rule, the information on the syntax and semantics of natural problem-oriented language is not used in these systems of speech recognition. The input phrases intended for the analysis do not contain stylistic mistakes, omissions, interjections, false inserts, etc.

Thus, lingua-cybernetics, considered as the science studying the general laws of reception, storage, transfer, and transformation of linguistic information in complex controlling and controlled systems, covers not only technical, but also biological and social systems.

Lingua-cybernetic systems of the future, intended for performance of a wide class of management functions and realized by computers, should have some special properties characteristic of control systems existing in living organisms.

Devices developed to this day in many respects rank below humans, although they already are beginning to perform some functions of human intelligence.

Modern computers can perceive and processes various information (numerical, symbolic, etc.), including the information necessary for the creation of images of the environment. In this connection, the branch of cybernetics connected with language and speech becomes of special importance. Its development is being planned today and is stimulated by the advanced level of new information technologies.

The recognition, synthesis, coding, and decoding of speech should play an important role in the multimedia community of the future with easy-to-operate man–machine interfaces. The systems of speech recognition include not only systems capable of distinguishing messages, but also systems that recognize individual speakers. Services using these systems will include the selection of voice, the access to and control of a database, clauses, various ordering services, dictation and editing, automated translation, telecommunication, safety control, digital communication, help for the handicapped (for example, help in reading for the blind and in speaking for mute persons). The most promising area for the application of speech technologies lies in telecommunications. Some technologies will play a major role in this communication revolution, but the development of speech becomes one of the key points. Owing to the synthesis of speech and technology of recognition, telephone booths will be used as personal terminals for communication with computer systems. It is expected that, in the future, the speaker recognition technique will be widely used as a method of identity verification in banking, domestic service, information services, etc.

The systems of speech recognition should be robust and should be able to distinguish connected speech. It is necessary to develop methods that are stable against changes in voice, physical status of a speaker, manner of speaking, and additional background noise, as well

as to characteristics of a local network, telephone network, microphones, etc. For such systems, it is also important to impose restrictions on tasks and the dictionary. To solve these problems, the development of automated adaptation techniques is necessary. One of the major problems is the detection and normalization (adaptation) of individual characteristics of the human voice.

Recently, research in the field of recognition (identification and verification) of a speaker are directed toward the development of new approaches and technologies that include text-independent methods of recognition based on vector quantization and Markov chains, normalization of parameters and distance, and model adaptation.

The problems of speech recognition include dynamic spectral characteristics, robustness, adaptation–normalization techniques, language modeling, the use of acoustic and perceptual restrictions, and the approach to recognition of spontaneous speech on the basis of detection.

In spite of the fact that the research in recognition, synthesis, and indexing of speech are mainly carried out independently of each other, an increasing interaction between these aspects can be observed. The necessity of research into the human brain will grow according to the need for solving the fundamental problems of recognition and synthesis of speech. Man–machine communication by means of spoken language is effective and convenient. Moreover, plenty of research is being carried out in the field of automatic speech recognition by computer. The results of this research show that the automatic recognition and understanding of speech is rather complicated, except when the dictionary of the words to be recognized is limited. The purpose of modern systems of recognition and understanding of speech is the maximal use of nonacoustic information and, especially, higher-level information, i.e., semantic and pragmatic data. For the purposes of an effective utilization of linguistic information, at the input level one must have only those sentences which describe a certain limited object domain.

Spoken language is one of the fastest forms of dialogue. In addition, speech allows one to communicate simultaneously in various forms. One of the basic factors that stimulated the use of speech devices is their ability to carry out dialogue in industrial areas and in other fields of special communications.

One of the priority directions of modern speechology is forensic phonetics in the field of phonoscopics. The range of problems is characterized by reference not only to oral, but also to written speech. Concerning the latter, an example is a computer program developed for the detection of plagiarism and the proof of authorship. The basic program is the automated comparative analysis of lexicosyntactic features of texts.

The modern status of forensic phonetics is characterized by the presence of three basic directions: *examination of material by subjects who are not professional experts; methodological problems in the field of speaker identification; and technological means for the processing (analysis) of speech and the interpretation of the resulting data*.

The methodological direction covers such problems as the strategy of the development of special questionnaires for experts; a mathematical base for solving the problem of processing the acoustic data and the correlation between the latter and the identified attributes; the relation between perceptive-acoustic and acoustic methods of estimating the fundamental frequency (F_0), the average values of formants (F_n), etc.; study of the techniques for masking a voice; taking into account the characteristics of communication channels (orthophone, telephone, digital) in practical criminality examination; specificity of the expert activity working with material in a foreign language (one example is the Albanian language in Macedonia in the context of material examination by Austrian experts); the problem of the dependence of acoustic–phonetic parameters on a number of extralinguistic factors (background noise; alcoholic and other kinds of intoxication; characteristics of the transfer tract; degree of the physical stress of the speaker, e.g., after running various distances; etc.); the study of the influence of the compression and coding of a speech signal on individual attributes of a voice; the value of the information about the specificity of consonantism and vocalism that is received as a result of perceptive-phonetic analysis; etc.

The technological direction (processing of a speech signal and the interpretation of data) includes the development of a linguistic database for an electronic encyclopedia intended for expert phonoscopists with reference to Russian and covering various theoretical areas, as well as practical recommendations for its usage [6]. In addition, the development of the basic principles and procedures used for phonogram enhancement in technically difficult cases and also the development of technology for speech filtration are being continued.

In summary, it is possible to conclude that the development of modern speechology and applied linguistics [7–9] is characterized by the following directions: the stochastic speech model, new information technologies, semantic networks in real-time dialogue systems, multimodal approach, statistical and combined methods of processing of a speech material and stochastic concepts of speech understanding, neural networks in real-time dialogue systems, remote training on the basis of the hypertext approach and new information technologies (multimedia systems, Internet, e-mail, electronic encyclopedias [10], etc.), the concatenative concept of text–speech transformation, multipurpose expert speech systems, formation of speech databases and speechological knowledge, multilingual systems of

recognition and understanding of speech with the use of various communication channels and inclusion of elements of automated translation, and the development of systems for the identification of a speaker and his physical and emotional status.

REFERENCES

1. R. K. Potapova, *Voice Control by Robot* (Radio i Svyaz', Moscow, 1989).
2. R. K. Potapova, *Introduction to Linguistic Cybernetics* (MGLU, Moscow, 1990).
3. R. K. Potapova, *Mysteries of Modern Centaur. Voice Interaction between a Man and a Machine* (Radio i Svyaz', Moscow, 1992).
4. R. K. Potapova, *Technologies of Natural Language Processing in Science and Industry* (INION Ross. Akad. Nauk, Moscow, 1992).
5. R. K. Potapova, *Speech: Communication, Information, Cybernetics* (Radio i Svyaz', Moscow, 1997).
6. R. K. Potapova, *Linguistic Provision of Electron Encyclopedia for an Expert-Phonoscopist* (MSR-FONO-É, 1999), CD-ROM.
7. R. K. Potapova, in *Proceedings of X Session of the Russian Acoustical Society* (Moscow, 2000), Vol. 2.
8. S. Furui, in *Proceedings of SPECOM'98* (St. Petersburg, 1998).
9. V. Galunov and V. Taubkin, in *Proceedings of SPECOM'99* (Moscow, 1999).
10. R. K. Potapova, in *Proceedings of SPECOM'99* (Moscow, 1999).
11. *Via Voice-98, 99. IBM* (1998; 1999).
12. *Via Voice-Millennium Edition. IBM* (2000).

Acoustical Physics, Vol. 48, No. 4, 2002, pp. 494–496. Translated from Akusticheskiĭ Zhurnal, Vol. 48, No. 4, 2002, pp. 560–562.

CONFERENCES AND MEETINGS

Two-Layer Model for the Formation of States of the Hidden Markov Chains

A. V. Agranovskiĭ, M. Yu. Zulkarneev, and D. A. Lednov

GP KB Spetsvuzavtomatika, Gazetnyĭ per. 51, Rostov-on-Don, 344007 Russia

e-mail: lednov@rnd.runnet.ru

Abstract—Procedures for the formation of states of the hidden Markov models are described. Formant amplitudes and frequencies are used as state features. The training strategy is presented that allows one to calculate the parameters of conditional probabilities of the generation of a given formant set by a given hidden state with the help of the maximum likelihood method. © *2002 MAIK "Nauka/Interperiodica".*

First, we briefly describe the general model of a random signal generated by a chain of hidden random events [1]. Let several hidden random events s_i $i = 1\ldots M$ from a set Ω generate a random process x_t whose values are measured at discrete, equally spaced instants t and belong to a finite set Ξ. The change of events s_i in time is the Markov process specified by the matrix of conditional probabilities R with the elements $r_{ij}(t) = r(h_t = s_i | h_{t-1} = s_j; t)$, where h_t is the current state of the chain of events. If the state of the hidden process is known, the properties of the observed process X are given by the conditional probability $\psi(x_i | X_{t-k}^t; s \in \Omega)$, where X_{t-k}^t is the sequence of the random process ordinates, i.e., $X_{t-k}^t = x_{t-1}, x_{t-2}, \ldots, x_{t-k}$. The conditional probabilities $\psi(x_t | X_{t-k}^t; s \in \Omega)$ can be specified in the parametric form $\psi(x_t | X_{t-k}^t; q_s)$, where q_s is the n-dimensional vector of parameters characterizing the effect of the state s on the formation of the observed process (the determination of this vector is equivalent to the determination of the state s).

In practice, the concept of hidden random processes appeared very fruitful for analyzing the data of experimental observations. In the field of speech recognition, this concept added the variety of hidden Markov models and the hierarchical composition approach of dynamic programing (the HCDP-approach) by Vintsyuk. In line with these advancements, there are a number of practical problems whose solutions require higher accuracy. Examples of such problems are the choice of the class of functions specifying the conditional probabilities $\psi(x_t | X_{t-k}^t; q_s)$, the segmentation, and the estimation of parameters of conditional probabilities (training).

Representation of the conditional probability $\psi(x_t | X_{t-k}^t; q_s)$ used in the general model of a signal is inconvenient for analyzing and processing speech signals, because the instantaneous signal amplitude is known to carry no information about the phonetic composition of speech. To make the representation more convenient, we explicitly include the formant composition of sound in the arguments of the conditional probability: $\psi(\{(A, \omega)\}_t^{N_t} | \Theta_{t-k}^t; q_s)$, where $\{(A, \omega)\}_t^{N_t}$ is a set composed of N_t amplitudes A and frequencies ω of the sound formats at the instant t and $\Theta_{t-k}^t = \{(A, \omega)\}_t^{N_{t-1}}$, $\{(A, \omega)\}_{t-1}^{N_{t-2}}, \ldots, \{(A, \omega)\}_{t-k}^{N_{t-k}}$.

Thus, the general model describing the properties of the speech signal requires the specification of the following elements: $\Lambda = (\Omega, R, \Psi)$, where Ψ is the set of conditional probabilities $\psi(\{(A, \omega)\}_t^{N_t} | \Theta_{t-k}^t; q_s)$ specified for every state s.

The further determination of the properties of the conditional probabilities $\psi(\{(A, \omega)\}_t^{N_t} | \Theta_{t-k}^t; q_s)$ needs some additional information about the preliminary processing of the speech signal.

The method of determination of the formant parameters has been described in an earlier paper [2]. Here, we briefly outline its main concept. The sequence of readings of a speech signal is segmented into a subsequence of spectral windows in which the Fourier spectra are calculated. The spectra obtained are smoothed out using the fifth-order Butterworth filter with a cutoff frequency of 360 Hz. The recursive Butterworth filter is known to induce a nonlinear phase shift, which can be removed using the method of opposing filtration. In the latter method, the data are first processed with a linear filter and, then, the resulting data are processed with the same filter in the inverse order [3]. As a result of this processing, we obtain a smoothed spectrum with harmonics in the form $F_t[n\Delta\omega]$, where t is the number of the segment on which the spectrum was obtained, n is

1063-7710/02/4804-0494$22.00

the number of a spectral harmonic, and $\Delta\omega$ is the spectral error. We approximate the harmonics of the smoothed spectrum $F_t[n\Delta\omega]$ by a sum of Gaussian functions. The parameters of the Gaussian functions, namely, the amplitude and the frequency, are considered as the formant characteristics. This way, we find the instantaneous positions of the formants.

Now, we obtain the dynamic characteristics of the formants, or, in other words, we find the formant trajectories. The basis of the method for obtaining the formant trajectories was described in [4]. Here, we describe this method in detail because of the use of some additional operations.

Let a sequence of sets of formants $\{(A, \omega)\}_1^{N_1}$, $\{(A, \omega)\}_2^{N_2}$, …, $\{(A, \omega)\}_k^{N_k}$ be obtained as a result of the approximation of a spectral sequence. Compare two adjacent sets, $L_t = \{(A, m)\}_t^{N_t}$ and $L_{t+1} = \{(A, m)\}_{t+1}^{N_{t+1}}$.

For a pair of parameters in the sets L_t and L_{t+1}, we introduce the probability measure of similarity

$$P_{ij} = \frac{1}{2\pi\sigma_m\sigma_A} \times \exp\left\{-\frac{(A_j^{(t)} - A_i^{(t+1)})^2}{2\sigma_A^2} - \frac{(\omega_j^{(t)} - \omega_i^{(t+1)})^2}{2\sigma_m^2}\right\}.$$

This formula assumes that A and ω are independent random quantities governed by the Gaussian distribution, σ_A and σ_ω are the variances of the corresponding quantities (the model parameters), and i and j are the order numbers of parameters in the corresponding sets L_t and L_{t+1}.

Below, we will assume that every pair (A, m) observed in a set can either appear, or disappear, or be continued to the following set. To reveal the behavior of a given pair of parameters, one should maximize the matrix P.

Let us maximize the matrix P. With this aim, we find the maximal element and assume that its position corresponds to the ith row and jth column. In this column and row, we replace all elements with zeros except for the maximal element, thus obtaining a new matrix P'. With the matrix P', we perform the same operation. The process is repeated until all rows or columns are exhausted. At every step of the process, we store the value of the maximal element and its position in the matrix. If the maximal element value appears below the preset threshold, we replace the corresponding matrix element with zero. If the matrix is not a square one, redundant rows (columns) will remain. In fact, this means that the number of parameter pairs in the set L_t is greater (less) than the number of parameter pairs in the set L_{t+1}. In the maximized matrix, a row composed of zeros will correspond to the parameter pairs that disappeared or appeared.

If the sequence of sets $L_t, L_{t+1}, \ldots, L_{t+n}$ includes a sequence of parameter pairs $\{(A, \omega)_t, (A, \omega)_{t+1}, \ldots, (A, \omega)_{t+n}\}$ (one pair in each set) such that a nonzero element of the maximized matrix exists for arbitrary adjacent pairs of this sequence, this sequence of parameter pairs will be called the formant trajectory.

Calculations of the formant trajectories for solitary pronounced phonemes showed that the observed trajectories have two undesirable features: random discontinuities and fluctuations, which appear because of the instability of the speech-tract state during the phoneme pronunciation and also because of the errors introduced by the measuring instruments and algorithms. The elimination of these random discontinuities and fluctuations would considerably simplify the observed dynamic pattern of formants.

The following algorithm is used for eliminating the random discontinuities of trajectories. Let trajectory 1 composed of points $\{y_1, y_2, \ldots, y_g\}$ lying to the left of the trajectory 2 composed of points $\{y_{g+m}, y_{g+m+1}, \ldots, y_{g+m+d}\}$ (the parameter y can be replaced with either the amplitude or the frequency of the formants), where m is the time interval between the end of trajectory 1 and the beginning of trajectory 2. We consider the discontinuity between trajectories 1 and 2 as eliminated when the following conditions are satisfied:

$$m < D, \quad \left|(g+m)\frac{6\sum_{i=1}^{g} iy_i}{g(g+1)(2g+1)} + \frac{1}{g}\sum_{i=1}^{g} y_i\right| < \varepsilon, \quad \left|g\frac{6\sum_{i=1}^{d} iy_{g+m+i}}{d(d+1)(2d+1)} + \frac{1}{d}\sum_{i=1}^{d} y_{g+m+i}\right| < \varepsilon. \tag{1}$$

In essence, these conditions impose limitations on the slopes of the lines approximating trajectories 1 and 2. If conditions (1) are satisfied, the end point of trajectory 1 is connected with the starting point of trajectory 2 by a line. Random fluctuations along the trajectory are removed using the method of moving average.

We represent the conditional probability $\psi(\{A, \omega)\}_t^{N_t}|\Theta_{t-k}^t; q_s)$ in the form

$$\psi(\{(A, \omega)\}_t^{N_t}\big|\Theta_{t-k}^t; q_s) = \sum_{i=1}^{N_t} \varphi((A, \omega)_t^i\big|W_t^i; a^s)\phi((A, \omega)_t^{i\in j}\big|Y_{t-k}^{i\in j}; b^s), \tag{2}$$

where $W_t^i = \{(A, \omega)_t^1, \ldots, (A, \omega)_t^{i-1}, (A, \omega)_t^{i+1}, \ldots, (A, \omega)_t^{N_t}\}$ and $Y_{t-k}^{i\in j} = \{(A, \omega)_{t-1}^{i\in j}, (A, \omega)_{t-2}^{i\in j}, \ldots, (A, \omega)_{t-k}^{i\in j}\}$.

Representation (2) describes two types of conditional dependences: (a) the function $\varphi((A, \omega)_t^i|W_t^i; a^s)$ describes the probability of the appearance of the ith formant depending on the surrounding formants at the cur-

rent instant, this function being independent of the index of the trajectory in which the formant i is incorporated; (b) the function $\phi((A, \omega)_t^{i \in j} | Y_{t-k}^{i \in j}; b^s)$ describes the probability of the appearance of the ith formant in the jth trajectory of the speech signal.

We specify the conditional probability of the first type by the function

$$\varphi((A, \omega)^i | W^i; a^s, c^s) = \frac{1}{2\pi a_{0_s} c_{0_s}} \exp\left\{ -\frac{\left(\omega_t - \sum_{j=1}^{N} a_j^s \omega_j\right)^2}{2a_{0_s}^2} - \frac{\left(A_t - \sum_{j=1}^{N} c_j^s A_j\right)^2}{2c_{0_s}^2} \right\}, \quad (3)$$

where for brevity we omit the temporal index.

The conditional probability of the second type will be specified by the function similar to function (3):

$$\phi((A, \omega)_t | Y_{t-k}; b^s, d^s) = \frac{1}{2\pi b_{0_s} d_{0_s}} \times \exp\left\{ -\frac{\left(\omega_t - \sum_{j=1}^{k} b_j^s \omega_{t-j}\right)^2}{2b_{0_s}^2} - \frac{\left(A_t - \sum_{j=1}^{k} d_j^s A_{t-j}\right)^2}{2d_{0_s}^2} \right\}. \quad (4)$$

The parameters a^s, b^s, c^s, and d^s determine the state s. To obtain these parameters, we use the following training strategy. Assume that the structure of each pronounced syllable of the consonant–vowel (c–v) type has the form 0c–c–cv–v–v0; i.e., the syllable is generated by five different hidden states. The segmentation procedure suggested in [5] makes it possible to divide the syllable into the required number of nonoverlapping acoustic segments.

Let ρ_s acoustic segments correspond to the hidden state in the training sample. With the use of the maximum likelihood method, which consists in the minimization of the functionals

$$\sum_{t=t_0}^{t_1} \sum_{g=1}^{\rho_s} \ln\phi((A, \omega)_t^g | Y_{t-k}^g; b^s, d^s) = \min,$$

$$\sum_{t=t_0}^{t_1} \sum_{g=1}^{\rho_s} \ln\phi((A, \omega)_{tt}^g | W_{tt}^g; b^s, d^s) = \min,$$

we determine the required parameters of the hidden state. Here, t_0 and t_1 are the boundaries of the speech segment that includes the realization of the hidden state.

REFERENCES

1. V. V. Mottl' and I. B. Muchnik, *Hidden Markov Models in the Structural Analysis of Signals* (Fizmatlit, Moscow, 1999).
2. A. V. Agranovskiĭ, D. A. Lednov, and S. A. Repalov, Telekommunikatsii, No. 6, 3 (2000).
3. R. W. Hamming, *Digital Filters* (Prentice-Hall, Englewood Cliffs, New Jersey, 1977; Sovetskoe Radio, Moscow, 1980).
4. D. A. Lednov and A. V. Agranovsky, in *Proceedings of SPECOM'97* (Cluj-Napoca, Romania, 1997), p. 95.
5. A. V. Agranovskiĭ, D. A. Lednov, and B. A. Telesnin, Inf. Tekhnol., No. 9, 24 (1998).

Translated by A. Vinogradov

Acoustical Physics, Vol. 48, No. 4, 2002, pp. 497–501. Translated from Akusticheskiĭ Zhurnal, Vol. 48, No. 4, 2002, pp. 563–567.

CONFERENCES AND MEETINGS

Experiment on Investigating the Voice Cords Functioning by the Speech Signal[1]

A. V. Nikolaev

Moscow State Linguistic University, ul. Ostozhenka 38, Moscow, 119992 Russia

e-mail: anikolayev@mail.ru

Abstract—A practical application of linear prediction methods for calculating the pulse function that models the functioning of vocal cords is described. Some characteristics of the pulses of this function enable one to draw some conclusions about the speaker's individual features (and, possibly, about the quality of sound). The first part of the paper is devoted to the theoretical background of the described method. The second part presents a detailed algorithm of the program realization of the method in the MATLAB 5.2 environment and analyzes the results of the experiment made on Russian vowels. © *2002 MAIK "Nauka/Interperiodica".*

This paper reviews the results of the practical application of a poorly investigated method for modeling voice-source functioning by the speech signal. The method allows one to calculate the function approximately describing the form of the fundamental tone pulses. The algorithm is developed on the basis of the linear speech production model described by the equation

$$x(n) = a_1^* x(n+1) + \ldots + a_p^* x(n+p) + h(n), \quad (1)$$

where $\mathbf{x} = \{x(n), \ldots, x(n+p)\}$ represents the speech signal samples; $h(n)$ represents the discrete values of the voice source excitation function (i.e., it describes the functioning of the vocal cords); and $\mathbf{a} = \{a_1, a_2, \ldots, a_p\}$ is the vector of the linear prediction coefficients of the backward prognosis, which characterize the resonance properties of the speech tract.

A researcher can operate only with the values of the speech signal samples $\mathbf{x} = (x(n)\ldots x(n+p))$. The excitation function $h(n)$ is unknown. Therefore, in evaluating the coefficients $\mathbf{a} = \{a_1, a_2, \ldots, a_p\}$, the excitation function is set equal to zero and is replaced in Eq. (1) by discrepancies. Using then the least-squares method, we arrive at the following matrix:

$$\mathbf{R} \cdot \mathbf{a} = \mathbf{b}, \quad (2)$$

where $\mathbf{R} = \{\mathbf{r}_{km}\}$ is the covariance matrix of size pxp with the elements calculated as

$$\mathbf{r}_{km} = \sum_i x(k+i)^* x(m+i), \quad k, m = 1, 2, \ldots, p, \quad (3)$$

where $\mathbf{a} = \{a_1, a_2, \ldots, a_p$ is the column vector with the desired values of the line prediction coefficients and $\mathbf{b} = \{b_1, b_2, \ldots, b_p\}$ is the vector of the free terms

$$\mathbf{b}_k = \sum_i x(k+i)^* x(i), \quad k, m = 1, 2, \ldots, p. \quad (4)$$

Since the number of unknown elements of vector **a** is equal to the order of the matrix, the desired coefficients can be found using one of the known methods. In addition, matrix **R** can be used for modeling the functioning of the vocal cords. As shown in [1, 2], the determinant of the matrix formed by the above method represents a pulse train in which the pulses appear in the regions of the disclosure of the vocal cords, i.e., the pulses are "synchronous" with the fundamental tone of the speech signal. We can assert that the determinant of such a matrix represents a convenient function for approximating the excitation function $h(n)$.

Let us denote this function as $M_p(n)$, where p is the matrix order. Each of the values of this function can be set in correspondence with the values of $x(n)$. Starting with this sample of the speech signal, we can form a vector of length $(N + p - 1)$, where N is the length of the analysis window and p is the order of the matrix **R**. Thus, the cycle variable i used in forming the matrix elements takes values from n to $(n + N + p - 1)$.

During the experiment, the results were presented in a graphical window. Each window consisted of two parts: upper and lower. The oscillogram (i.e., the values $x(n)$ of the speech signal samples) was displayed in the upper part, while the lower part was used for displaying the changes in the values of the function $M_p(n)$.

[1] This paper was submitted by the author in English.

1063-7710/02/4804-0497$22.00 © 2002 MAIK "Nauka/Interperiodica"

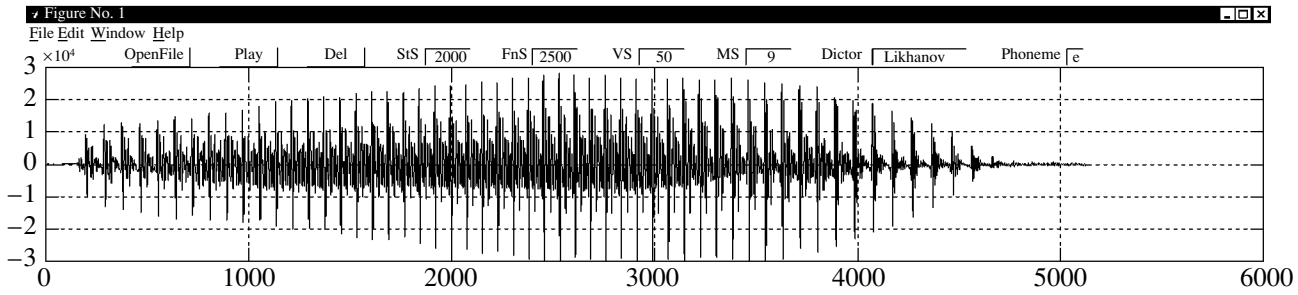

Fig. 1.

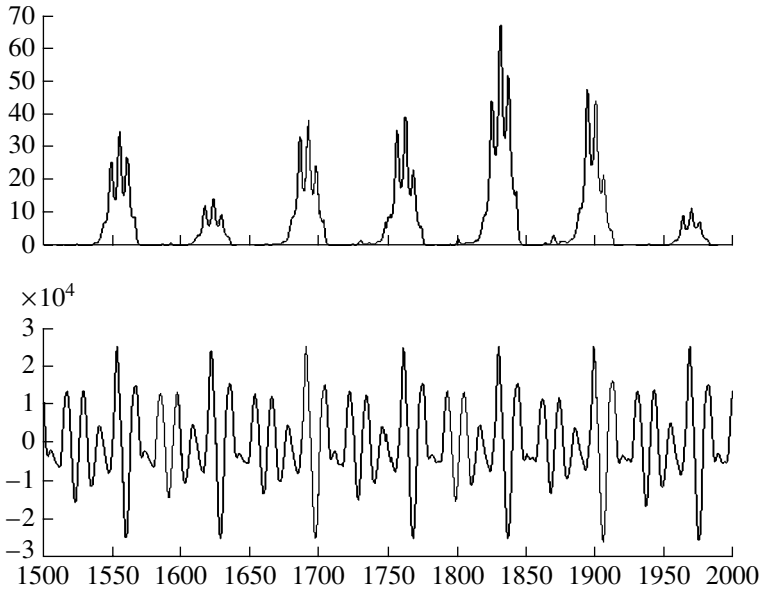

Fig. 2. Speaker E., sound [a].

The method under discussion was realized in the MATLAB 5.2 environment. We investigated four stationary Russian vowels: [и], [ы], [у], [э], [(о)], and [а], pronounced by seven speakers: three men and four women, from 20 to 30 years old. The sounds were input in a PC with Windows 98 via a sound card. The sampling rate was 12 kHz with 16 bits per sample.

The program works as follows. The speech signal samples are read to form a one-dimensional array, which is displayed on the screen, so that the user can choose the region he is interested in (see Fig. 1).

Before processing, the signal is filtered through a digital FIR-filter with a passband from 300 Hz to 3400 kHz. Then, for every discrete time moment j from the chosen region, the program forms a one-dimensional array consisting of the values of the speech signal $\{x(j), \ldots, x(j+N+p-1)\}$. Each array is processed in the following way:

(i) The array is normalized by the average value.

(ii) A matrix $\mathbf{R} = \{\mathbf{r}_{km}\}$ of size pxp is formed from the array elements on the basis of Eq. (3).

(iii) The determinant of the matrix is calculated.

(iv) The determinant value is stored in a one-dimension array.

This procedure is repeated in cycle for every discrete time moment of the chosen range. Thus, we obtain a one-dimensional array storing the values of the function $M_p(n)$. The length of this array is equal to the length of the chosen region. Finally, the program displays two graphs: the speech signal samples from the chosen region (the lower graph) and the corresponding values of the function $M_p(n)$ (the upper graph).

Analyzing the graphs of the function $M_p(n)$ obtained for different speakers and speech sounds, we arrive at the following question: what factors determine the form of its pulses? Can we believe that this function retains both the individual features of the speaker and the features common for the same sound pronounced by different speakers (although the latter idea contradicts the linear model of speech production, which declares the independence of the speech-source functioning from the resonance parameters of the speech tract)? Can we,

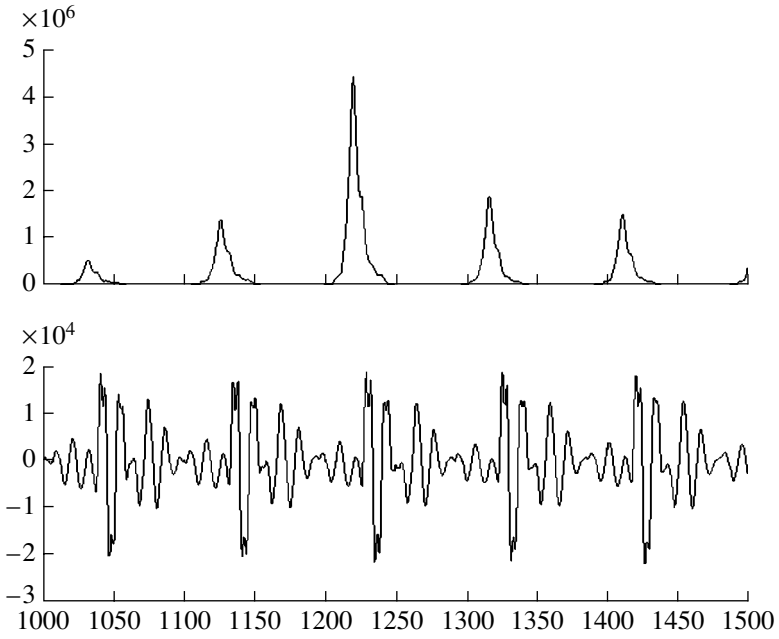

Fig. 3. Speaker N., sound [a].

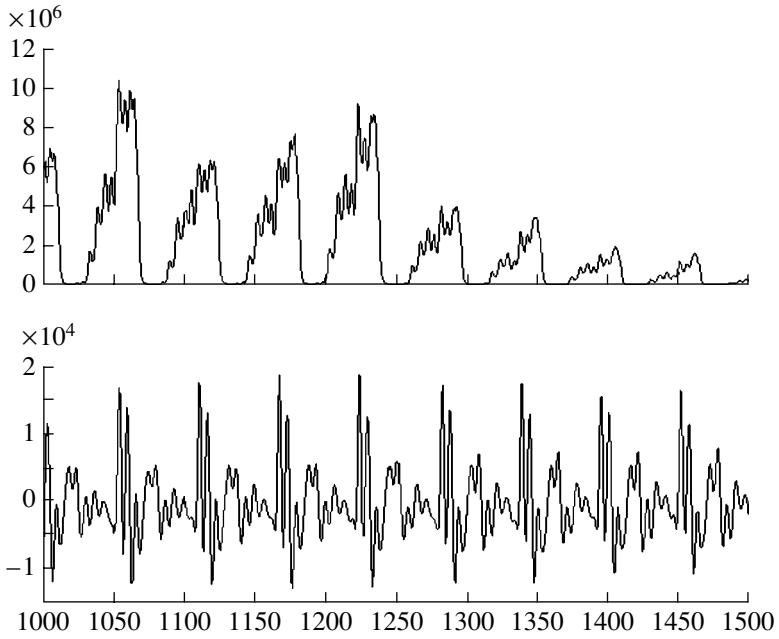

Fig. 4. Speaker E., sound [e].

consequently, use the information about the form of the pulses in solving the problems of speaker identification and speech recognition?

Figures 2–7 show the graphs for two speakers, E. and N., both men, who pronounced the Russian sounds [a], [e], and [o]. The fundamental frequency of speaker E. was 200 Hz and of speaker N., 150 Hz. Comparing the graphs of the excitation function $M_p(n)$ of these two speakers, one can clearly see their individual differences. In particular, the pulses of the excitation function of speaker N. have an evident symmetrical form with one peak at the vowels [a] (Fig. 3) and [(o)] (Fig. 7). The pulses of speaker E. at these vowels (Figs. 2, 6) are nonsymmetrical and have several peaks. The pulses of speaker N. at the sound [e] (Fig. 5) are also nonsym-

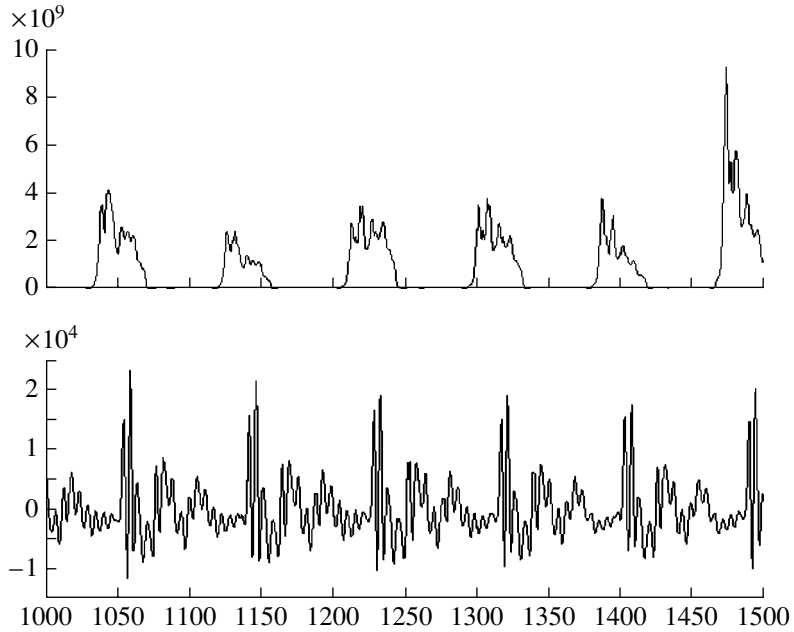

Fig. 5. Speaker N., sound [e].

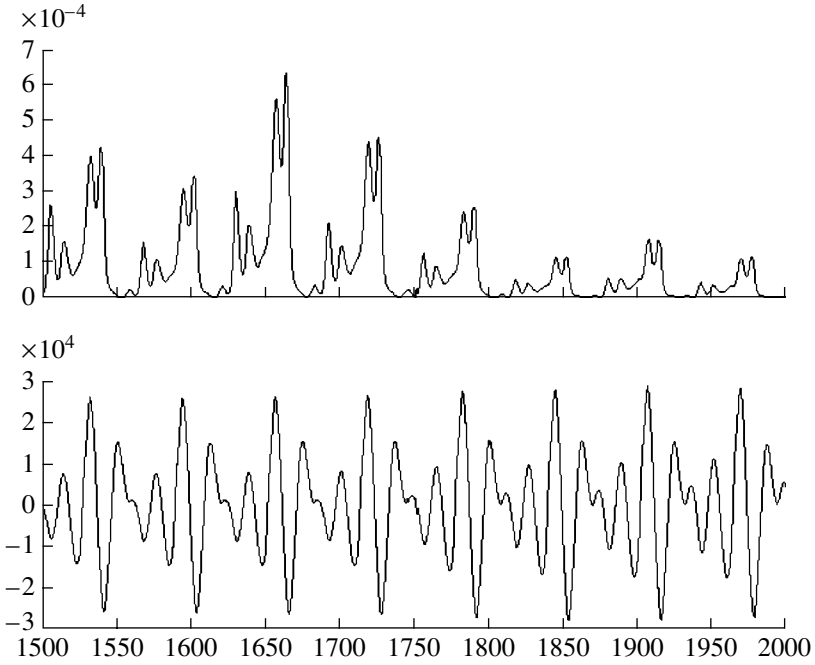

Fig. 6. Speaker E., sound [o].

metrical, but they again differ noticeably from the pulses of speaker E. at the same sound (Fig. 4). The pulses of N. have a slight slope on the right-hand side, whereas the pulses of E., on the left-hand side.

It is much more difficult to single out the features that characterize each vowel (if it is possible at all in view of the aforementioned assumption that functioning of the voice source does not depend on the resonance parameters of the speech tract). Still, from Figs. 2 and 3, one can see that the pulses at the sound [a] have an obviously greater porosity, as compared to the two other sounds in both speakers.

Unfortunately, the size of this paper does not allow us to present more graphs. Analyzing them, we could

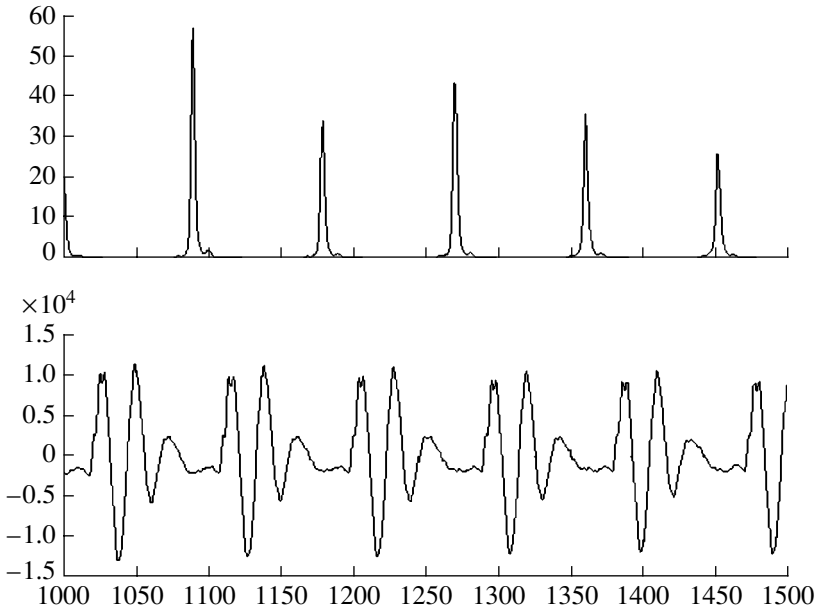

Fig. 7. Speaker N., sound [o].

find that the pulses have also other features characterizing both the speaker and the sound. In addition, one should take into account that we have obtained only preliminary results, which are insufficient for serious conclusions. At the moment, we face the task of a more thorough and deeper development of the described algorithm. Nevertheless, there is no doubt that the method described above has demonstrated its potentialities, and it seems to be promising for application in different areas of digital signal processing.

REFERENCES

1. A. N. Sobakin, Akust. Zh. **18**, 106 (1972) [Sov. Phys. Acoust. **18**, 84 (1972)].
2. A. N. Sobakin, in *Modern Speech Technologies* (Geos, Moscow, 1999), pp. 47–50.

Acoustical Physics, Vol. 48, No. 4, 2002, pp. 502–504. Translated from Akusticheskiĭ Zhurnal, Vol. 48, No. 4, 2002, pp. 568–570.

CHRONICLE

In Memory of Leonid Mikhaĭlovich Lyamshev (August 30, 1928–March 28, 2002)

Leonid Mikhaĭlovich Lyamshev—one of the founders of modern acoustics, editor-in-chief of *Akusticheskiĭ zhurnal* (*Acoustical Physics*), chairman of the Scientific Council on Acoustics of the Russian Academy of Sciences, head of a department of the Andreev Acoustics Institute, doctor of science (phys.–math.), professor, and winner of the USSR State Award—passed away.

Lyamshev's contribution to science is great. It is characterized not only by the new, rapidly progressing directions of research founded by Lyamshev, the monographs and papers written by him, and the results of his scientific and organizational activities, but also by several generations of students educated by Lyamshev, many of whom have grown into prominent scientists. Personally, Lyamshev was a researcher totally devoted to science and an exceptionally honest and respectable man.

Lyamshev grew up in a family of teachers. After he graduated from secondary school with a gold medal and, then, from the Moscow Electrotechnical Institute of Communication, he became (in 1951) a postgraduate student of the Lebedev Physical Institute of the Academy of Sciences of the USSR. At that time, he began his intensive and fruitful research in physical acoustics, which had never been interrupted within more than half a century. The first problem that attracted Lyamshev's attention was reflection and scattering of sound from finite elastic plates and shells in liquid. Already the first results obtained by Lyamshev showed his individual style, which was characterized by a combination of an exact mathematical description of the phenomenon under investigation and its profound physical interpretation with a solid substantiation and a high reliability of the results. During the first years of his work in science, Lyamshev discovered and described the nonspecular reflection of sound from plates performing longitudinal vibrations, the resonance scattering of sound from shells in liquid, and some other phenomena, which formed the basis of an extended field of research in modern acoustics: the studies of the scattering of sound from elastic bodies. Currently, this direction of research is represented by more than a thousand publications including several monographs. The results obtained by Lyamshev in the early 1950s formed the subject of both his candidate dissertation (1954) and his first monograph: L.M. Lyamshev, *Sound Reflection from Thin Plates and Shells in Liquid* (Akad. Nauk SSSR, Moscow, 1955).

Another problem that attracted Lyamshev's attention at that time was the reciprocity principle. In acoustics, this principle was first formulated by Helmholtz in the middle of the 19th century. Fifty years later, Rayleigh presented its mathematical proof for the case of discrete systems with a finite number of degrees of freedom. Within another fifty years, Lyamshev gave a rigorous mathematical proof of the reciprocity principle for arbitrary continuous linear media containing arbitrary numbers of elastic bodies, screens, and boundaries: L.M. Lyamshev, "On the Problem of the Reciprocity Principle in Acoustics," *Doklady Akad. Nauk*, vol. 125, no. 6 (1959) (see also other publications on this issue). The results presented in this paper remain the most general among hundreds of publications concerned with the subject. Since the reciprocity principle

1063-7710/02/4804-0502$22.00

is widely used for solving practical problems, the paper by Lyamshev is one of those most frequently cited in the literature on acoustics.

The next direction of research developed by Lyamshev was the scattering and radiation of sound in a moving medium. The topical problems associated with this subject lie at the boundary between acoustics and hydrodynamics and are characterized by extreme complexity. However, Lyamshev's studies in this area were also successful, and he obtained a series of important fundamental results. Among them, the most significant achievement is the development of the theory of hydrodynamic flow noise. Lyamshev studied in detail the effect of the physical and structural parameters of a body in a flow on the sound component of the flow noise. The series of experimental and theoretical studies carried out by Lyamshev and his students (who had already appeared at Lyamshev's laboratory at that time), together with his colleagues from the Acoustic Institute and other institutions, played a crucial role in the improvement of the design of low-noise vessels. In 1964, Lyamshev received his doctoral degree and published a number of key papers on flow noise, including "Acoustics of a Controlled Boundary Layer," *Vestnik Akad. Nauk SSSR*, no. 7, 1973. One more fundamental paper by Lyamshev was published later: "Determination of Impedance in Acoustics of Moving Media," *Doklady Akad. Nauk SSSR*, vol. 261, no. 1 (1981). The generalization of the notion of impedance, which was proposed in this paper, allowed the transfer of all results from acoustics of stationary media, including the Fresnel reflection formulas, to acoustics of moving layered media without introducing any changes.

In the early 1970s, Lyamshev initiated and began the development of an entirely new direction of research: laser acoustics. It originates from the effect of sound generation in liquid by laser (optical) radiation. Together with his colleagues and students, Lyamshev developed the theory of sound generation by a laser beam, carried out experiments, and proposed new solutions to practical problems. In particular, he proposed and experimentally substantiated the method of remote laser-acoustic sounding of the hydrosphere, in which lasers were used for both generation and detection of sound. In 1989, Lyamshev published the monograph *Laser Thermooptical Excitation of Sound* (Nauka, Moscow, 1989) where he described and analyzed the results obtained by that time in laser optics. The laser-acoustic studies carried out by Lyamshev gained worldwide recognition. Today, this area of research is a promising and rapidly progressing branch of modern physics.

The problem that was addressed by Lyamshev and his colleagues in the 1980s was adjacent to the aforementioned phenomenon: they considered sound generation by penetrating radiation. The studies of the radiation-acoustic effects that accompany the interaction of single particles or particle beams with matter open up new promising possibilities for visualizing and controlling the internal regions of opaque materials in biology (radiation-acoustic microscopy), geology (neutrino-acoustic sounding of the Earth), astrophysics (detection of cosmic neutrinos), etc. Lyamshev's publications concerned with this field of research include a skillfully written monograph, which will certainly have an impact on following generations of scientists: L.M. Lyamshev, *Radiation Acoustics* (Nauka–Fizmatlit, Moscow, 1996).

In recent years, Lyamshev developed one more new direction of research: fractal acoustics. He was one of the first to realize the important role of fractals in acoustics. He showed that many acoustic objects and processes possess fractal properties, the consideration of which makes it possible to explain many anomalous experimental facts related to the radiation, propagation, and scattering of sound waves. For example, the specific spectral shape of reverberation observed in the sea was explained by the fractal properties of the wavy sea surface: L.M. Lyamshev, "On the Fractal Nature of Sea Surface Reverberation," *Akusticheskiĭ zhurnal* (*Acoustical Physics*), vol. 47, no. 2 (2001). Owing to Lyamshev's effort, fractal acoustics has gained acceptance as one of the most promising directions of research in modern acoustics.

Lyamshev had been deeply involved in organizational activities in science. He devoted much of his energy to the development of *Akusticheskiĭ zhurnal* (*Acoustical Physics*). Starting from 1963, he had been the deputy editor-in-chief and from 1987, editor-in chief of this journal. His attitude toward the authors who presented their papers for publication was benevolent, as well as demanding. Lyamshev paid very much attention to his work in the journal. The high scientific level and prestige of the journal are to a great extent due to Lyamshev's supervision. In 1973, Lyamshev became chairman of the Scientific Council on Acoustics of the Russian Academy of Sciences, and he held this post until the last days of his life. The Andreev Acoustics Institute played an important role in the life of Lyamshev. Since the day the institute was established (1954), Lyamshev worked there together with Yu.M. Sukharevskiĭ, L.M. Brekhovskikh, G.D. Malyuzhinets, M.A. Isakovich, and other well-known scientists. At this institute, he advanced from junior researcher to first deputy director. Over many years, including the last few, he headed the department of the institute that was he himself organized. Lyamshev received the title of professor in 1969, he was a winner of the State Award (1985), a bearer of the Order of the October Revolution (1972), and a member of the Russian Academy of Natural Sciences (since 1992).

The name of Lyamshev is well known outside Russia, and not only from his publications. He was twice elected member of the International Commission on Acoustics

(1975–1981 and 1994–1998). He was a member of the Council of the Federation of Acoustical Societies of Europe (1984–1997) and received the title of Honorary Member of the International Institute of Acoustics and Vibration (1999). He took part in many International Congresses on Acoustics and conferences where he gave plenary and invited talks. He also gave lectures at universities of Europe, United States, Japan, and China.

Today, acoustics has suffered a bereavement. However, the ideas put forward by Lyamshev will be developed further by the next generation of acousticians. As for those who were lucky to be acquainted with Leonid Mikhaĭlovich Lyamshev, they will forever keep in their hearts the memory of this excellent scientist and wonderful person.

Translated by E. Golyamina

Acoustical Physics, Vol. 48, No. 4, 2002, pp. 505–506. Translated from Akusticheskiĭ Zhurnal, Vol. 48, No. 4, 2002, pp. 571–572.

CHRONICLE

Yuriĭ Pavlovich Lysanov (On His 80th Birthday)

February 23, 2002, marked the 80th birthday of Yuriĭ Pavlovich Lysanov, leading researcher of the Andreev Acoustics Institute, professor, Doctor of Physics and Mathematics, and laureate of the USSR State Award.

Lysanov graduated from Perm State University in 1952. His first research project was concerned with the scattering of electromagnetic waves from a rough surface. It was carried out at the Acoustical Laboratory of the Lebedev Institute of Physics of the Academy of Sciences of the USSR when Lysanov was a graduate student. After graduation, Lysanov became a postgraduate student at the Lebedev Institute of Physics. In 1955, he completed his postgraduate courses and started working as a researcher in ocean acoustics and in related fields of geophysics.

Lysanov carried out comprehensive studies of the propagation, scattering, and diffraction of waves in the ocean. He is the author of more than 150 scientific publications and 12 inventions and the author and coauthor of six monographs. The monograph *Theoretical Fundamentals of Ocean Acoustics* (1982), written by Lysanov together with L.M. Brekhovskikh, has gained wide recognition among the scientific community. This monograph has seen two editions in English (1982 and 1991) and is often cited in leading scientific publications. Studies of the sound scattering in the ocean are described in another monograph, *Ocean Acoustics*, written by Lysanov together with a group of authors. These studies brought him the USSR State Award in Science and Engineering in 1976.

Lysanov was the first to derive an exact integral equation for the field scattered from a rough surface and to obtain its approximate solution. The method of the integral equation proposed by Lysanov covers the methods of small perturbations and Kirchhoff approximations as limiting cases and, what is especially important, takes into account the multiple scattering of waves. Lysanov substantially contributed to the development of the methods of wave diffraction by surfaces with nonuniform impedances. In this connection, one should note the new modification of the Rayleigh method for describing the resonance phenomena in the conditions of propagation of a grazing wave. In collaboration with Yu.Yu. Popov, Lysanov revealed a new type of creeping waves propagating around a rough sphere.

Another direction of Lysanov's research is related to sound propagation in irregular waveguides with rough boundaries. Lysanov obtained and studied the decay law and the angular spectra of the coherent and incoherent components of an acoustic field in the case of long-range propagation in a surface sound channel in the conditions of multiple scattering from a rough ocean surface. He developed the theory of prereverberation of sound in the ocean and proposed an unconventional method for solving the problem of normal wave excitation in an irregular waveguide with inseparable variables in the Helmholtz equation.

A large group of Lysanov's works is concerned with studying the scattering of sound from the ocean bottom. In this area, an approximate theory was developed for describing the strong time fluctuations of sound signals scattered from the ocean bottom in the case of a moving transmitting–receiving system. The spectral and correlation characteristics of the fluctuations were studied for different kinds of transmission, velocities of motion, and parameters of roughness and inhomogene-

1063-7710/02/4804-0505$22.00 © 2002 MAIK "Nauka/Interperiodica"

ities of the bottom relief. The main conclusions of this theory were confirmed by a large body of data obtained from full-scale experiments in the ocean. The aforementioned theoretical results formed the basis for the acoustic methods of determining the parameters of the bottom relief and the inhomogeneities of the underwater ground, as well as for the new correlation methods of determining the velocities of motion and displacement of a ship relative to the bottom. Geoacoustic bottom models were developed for both shallow-water and deep-water regions of the ocean. The most interesting results were obtained for shallow seas. The statistical model developed for the upper sediment layer with allowance for the anisotropy of volume inhomogeneities provided the first adequate theoretical interpretation for ample experimental data on the backscattering of sound. Lysanov is a coauthor of the acoustic method developed for iron-manganese concretion prospecting and exploration at the bottom of a deep ocean.

One more group of Lysanov's works is related to studying the effect of regular and random inhomogeneities of the sea medium on sound scattering by a rough ocean surface.

Lysanov made an important contribution to the study of the effects of intrathermocline vortex lenses and the fine structure of hydrophysical fields on an acoustic field in the ocean. He showed that these factors considerably affect the spatial structure of an acoustic field.

In recent years, Lysanov concentrated on the long-range propagation of acoustic signals generated by underwater earthquakes and low-frequency sound attenuation in the ocean. Together with L.M. Lyamshev, he described the fractal properties of random volume inhomogeneities, which determine the attenuation of sound in the course of its propagation in an underwater sound channel. For these studies, the two authors received the prize from the International Academic Publishing Company "Nauka/Interperiodica" for the best publication in *Acoustical Physics* (1998).

Lysanov also made a considerable contribution to the organization of full-scale studies in the ocean: he participated in four expeditions of the research ships *Sergeĭ Vavilov* and *Petr Lebedev*, and three of these expeditions were headed by him.

Since 1962, Lysanov has been involved in tutorial activities in higher educational institutions. Today, he is a professor at the department of Thermohydromechanics of the Ocean at the Moscow Institute of Physics and Technology. He pays much attention to the education of highly trained specialists: one doctoral and 12 candidate dissertations have been prepared under his supervision.

Lysanov is a World War II veteran.

He is deeply involved in scientific-organizational activities. He is a member of the editorial boards of *Izvestiya Akad. Nauk, Atmospheric and Oceanic Physics* and *Oceanology* and a member of the Scientific Council on Acoustics of the Russian Academy of Sciences, the Council of the Russian Acoustical Society, the Scientific and Dissertation councils of the Acoustics Institute, and the Dissertation Council of the General Physics Institute of the Russian Academy of Sciences.

Lysanov takes an active part in international scientific relations. Many times he presented his papers at the International Congresses on Acoustics and at international symposiums.

We wish Yuriĭ Pavlovich Lysanov good health and further success in his creative work.

Translated by E. Golyamina

Acoustical Physics, Vol. 48, No. 4, 2002, pp. 507–508. Translated from Akusticheskiĭ Zhurnal, Vol. 48, No. 4, 2002, pp. 573–574.

CHRONICLE

Romual'd Anatol'evich Vadov (On His 70th Birthday)

December 24, 2001 marked the 70th birthday of Romual'd Anatol'evich Vadov, one of the eldest members of staff of the Andreev Acoustics Institute, senior researcher, and Cand. Sci. (Phys.–Math.).

Vadov joined the staff of the newly founded Acoustics Institute of the Academy of Sciences of the USSR in 1954 after graduating from the Physics Faculty of Leningrad State University.

He started his research activities at the institute mastering and improving the reverberation technique for measuring the sound absorption in liquids and together with experimental studies of the electrolytic relaxation absorption of sound in artificial and natural seawater. Studies of the absorption of sound in the course of its propagation in a marine medium became the main subject of his investigations over many years.

At the end of the 1950s, Vadov conducted a series of laboratory measurements of the coefficient of sound absorption (at frequencies of 30–120 kHz) in seawater and electrolytes. A relation connecting the absorption coefficient at high frequencies with the salinity and temperature of seawater resulted from the generalization of these data. In the first half of the 1960s, he carried out full-scale measurements of the absorption coefficient in several regions of the ocean (which differed in salinity and temperature of water) by using an original technique at frequencies of 8–25 kHz. The results of these measurements proved the validity of the aforementioned relation, and it was recommended for use in the design of new equipment. At the end of 1960s, Vadov developed a new technique and conducted full-scale measurements of the dependence of sound absorption in seawater on hydrostatic pressure.

Starting from the mid-1960s, Vadov conducted active experimental studies of low-frequency (<5–8 kHz) sound attenuation in the case of sound channeling. First of all, he was interested in oceanic regions differing noticeably in salinity and temperature of water, such as the Black, Baltic, and Mediterranean seas. In the middle of the 1980s, Vadov proposed relations for estimating the sound attenuation at frequencies higher than 200–300 Hz. The relations were based on an analysis of experimental data on attenuation obtained in these regions, taking into account the results of theoretical and experimental studies of the low-frequency absorption in seawater which had already been published at that time. At the same time (at the end of 1970s), on the basis of the analysis of underwater acoustic conditions for several tracks investigated by him, he demonstrated that the deviation of the real law of geometrical spread from the cylindrical law in the case of channeling can reach 10–15 dB per 1000 km. This fact explained the anomalously high values of the attenuation coefficient (determined by the deviation of the decay law of the sound field level from the cylindrical law) observed in single experiments at frequencies lower than 200–300 Hz.

Experiments on the channeling of explosion signals were conducted by Vadov in ocean regions with widely different oceanological parameters. The data of these experiments were analyzed not only to determine the attenuation, but also to reveal the regional characteristics of the formation of the time and energy structures of sound fields. Special attention was paid to the experimental studies of the acoustic signal propagation in complex oceanological conditions (at a sharp drop in sea depth in the region of the continental slope or propagation tracks intersecting frontal zones and currents).

1063-7710/02/4804-0507$22.00 © 2002 MAIK "Nauka/Interperiodica"

Since the end of the 1960s, Vadov has mastered computer methods for both the computation of sound fields and the processing of experimental data. With the development of this technology, new, previously impossible opportunities for analyzing the fine structure of sound fields arose. For example, in the mid-1990s, Vadov developed a technique and software for the computer processing of elementary (single-beam) explosion signals that were separated in time for measuring the phase shift in the case of a signal touching a caustic. He conducted such measurements and obtained unexpected results (a measured phase shift was not always a multiple of 90°). This and several other somewhat unexpected but very interesting results of the analysis of experimental data obtained by him have since been physically explained.

Vadov has published about 170 works (scientific reports, articles, and papers presented at scientific conferences and seminars) on the basis of his research. Now, Vadov works on the development of the experimental database "Long-Range Propagation of Sound in the Ocean" with the aim of storing and generalizing this priceless experimental material. The basis for this database is the data of the experiments conducted by Vadov in 18 oceanic expeditions on research vessels of the Acoustics Institute and Naval Hydrographical Service.

Vadov took part in many research and development projects and participated in tests of new devices. His name is well known to the research community of the Acoustics Institute and other research and industrial institutions working in adjacent fields. His work is highly appreciated by the institute administration and the government, which awarded him the Order of Honor and four medals.

Romual'd Anatol'evich Vadov has devoted over 47 years of his life to research in underwater acoustics. He continues to work actively. We wish him good health and new achievements.

Translated by M. Lyamshev

Acoustical Physics, Vol. 48, No. 4, 2002, pp. 509–510. Translated from Akusticheskiĭ Zhurnal, Vol. 48, No. 4, 2002, pp. 575–576.

INFORMATION

St. Petersburg Seminar on Computational and Theoretical Acoustics of the Scientific Council on Acoustics of the Russian Academy of Sciences

In 2001, the St. Petersburg Acoustical Seminar continued its regular work. The seminar sessions were held at the traditional time (Tuesdays, 18:30) in the conference hall of the Institute of Mechanical Engineering Problems, Russian Academy of Sciences (Bol'shoĭ pr. 61, Vasil'evskiĭ Ostrov).

In 2001, the seminar suffered a bereavement. One of the seminar leaders, Honored Scientist and Engineer, Professor Evgeniĭ L'vovich Shenderov passed away. A special session of the seminar was devoted to this sad event. D.P. Kouzov recounted Shenderov's work with the seminar and his role as leader in developing it. A detailed paper describing Shenderov's life and research was presented by M.D. Smaryshev.

Twenty sessions of the seminar were held in 2001. As before, in addition to papers on acoustics, some studies in wave mechanics, which were close to acoustics from the point of view of both the physical processes and the mathematical apparatus, were discussed.

Two papers were concerned with the propagation of surface waves. A.V. Osetrov studied the acoustoelastic effect, i.e., the effect of the residual mechanical stress present in a solid crystalline layered heterostructure on the propagation velocity of surface acoustic waves. A calculation technique generalizing the method of transfer matrices was proposed in the paper, and several anomalous effects related to acoustoelasticity were analyzed (H.-J. Frolich, R. Koch, and E. aChilla took part in the research). A.V. Aref'ev examined the characteristic features of the surface wave propagation in a viscoelastic medium described by the Maxwell–Boltzmann–Volterra model with an arbitrary dependence of parameters on the vertical coordinate. The study was conducted in the framework of the ray approach.

A series of papers was devoted to the problems of acoustic diffraction. In his last report at the seminar, Shenderov presented integral relations generalizing the Helmholtz integral to the case of an arbitrary acoustic medium and demonstrated that, in the case of an inhomogeneous medium, an additional factor depending on the density distribution in the medium appears in the integrand. M.A. Lyalinov constructed a scattering pattern for a plane acoustic wave scattered from a narrow impedance cone with an arbitrary cross section. Using the Kantorovich–Lebedev technique, the problem was reduced to that for a spectral function at a unit sphere with a small orifice cut out by the cone (J.M. Bernard participated in the study). V.V. Zalipaev investigated the short-wave scattering of a plane longitudinal wave from a flat crack in an isotropic elastic medium. The crack edges were assumed to be smooth. He obtained a uniform asymptotics in the vicinity of the caustic and the "light–shadow" boundary. S.V. Romashkin analyzed the transmission of longitudinal and transverse waves through a grating formed by parallel equidistant elastic cylinders for which the breaking of adhesive bonds with the medium at their boundaries is taken into account. The boundary conditions were formulated in the linear slip approximation. Expressions for the reflection and transmission coefficients were obtained and analyzed numerically. A considerable effect of the adhesive bond breaking on the scattering properties of the grating was revealed.

The paper by V.V. Fok and E.L. Shenderov demonstrated an interesting relation between the problems of acoustic diffraction and quantum field theory. The authors found that the problem of quantization of the Teichmuller space (a phase space with a dimension of $2 + 1$ and a constant negative curvature) leads to equations similar to the Malyuzhinets equations obtained for problems of acoustic diffraction in angular domains.

Three seminar sessions were devoted to wave propagation in one-dimensional elastic structures. E.V. Shishkina considered wave propagation in an infinite spiral rod. She took into account all possible types of vibrations and compared the resulting refined theory with the common "rod" model of longitudinal vibrations of a spring. Two reports by S.N. Gavrilov dealt with vibrations of a string located on an elastic base. The source of vibration was a moving inertial concentrated load. He demonstrated that, in this model, natural vibrations localized near an inclusion are possible in the case of a uniform motion of the load. The evolution of vibrations was described for a slowly accelerated load.

Two papers discussed acoustic processes in closed volumes with elastic walls. Yu.A. Lavrov and V.D. Luk'yanov obtained an exact analytical solution to the problem of natural vibrations within a spherical sector with the spherical part of the boundary formed by a thin elastic shell. They conducted a numerical and asymptotic investigation of this solution. O. Al-Arja (Jordan) jointly with Lavrov presented the results of a study of forced acoustic processes in a rectangular

1063-7710/02/4804-0509$22.00

room with perfectly rigid walls and divided into two parts by an elastic screen. The results were based on an exact analytical field representation.

Two reports were devoted to the propagation of flexural-gravity waves in plates floating at the surface of a liquid. M.G. Zhuchkova and Kouzov investigated the transmission of such a wave through a system of rigid supports. The reflection and transmission coefficients, and also the force and moment responses of the supports, were calculated. Yu.A. Mochalova analyzed the vibrations of a plate of a finite width under the effect of a moving load. The calculation was performed in the framework of the theory of shallow water. Resonance velocities of the load movement were discovered at which the plate deflection increases without a limit.

The paper by O.V. Izotova was concerned with the refined theory of a thin plate flexure. The plate was described by the equations of the three-dimensional theory of elasticity and assumed to be rigidly fixed at one part of the lateral surface, while the other part remained free. An asymptotic approximation for the plate flexure under the effect of a transverse load was constructed.

The report by E.I. Kartuzov was devoted to the theoretical solution of the problem on the determination of the distribution of a control load exciting transverse oscillations of an elastic fin to provide its translational motions with maximal thrust. He obtained the amplitude and phase characteristics of the transverse oscillations of the fin and the control load for the optimal modes of operation.

Two papers considered gravity waves at the surface of an incompressible liquid. Mochalova studied water oscillations over a circular punch lying on an elastic base at the bottom of a water basin. It was demonstrated that, at certain values of parameters, eigenfrequencies take place that correspond to localized modes of oscillation. D.A. Indeĭtsev examined the formation of high-amplitude internal waves in a two-layer liquid. These waves result from the formation of a localized mode over a massive platform.

Finally, a paper devoted to the general development of the mathematical apparatus was discussed at the seminar. As is known, integral equations whose kernels depend on the difference between the arguments are widely used in diffraction problems. V.F. Pulyaev introduced integral equations with almost periodic kernels, which represent the generalization of the equations mentioned above. He developed a general theory of their solvability using certain special classes of functions.

More detailed abstracts of papers and other information on the seminar can be found at the website http://mph.phys.spbu.ru/~george/seminar.html.

D. P. Kouzov

Translated by M. Lyamshev